Comenius University in Bratislava

Faculty of Mathematics, Physics and Informatics

Charge asymmetry in top-quark pair production at 13 TeV in proton-proton collisions with the ATLAS experiment

PhD Thesis

Bratislava, 2019 Mgr. Matej Melo

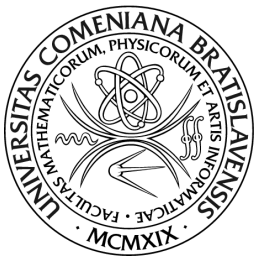

Comenius University in Bratislava
Faculty of Mathematics, Physics and Informatics
Department of Nuclear and Subnuclear Physics

PhD Thesis

Charge asymmetry in top-quark pair production at 13 TeV in proton-proton collisions with the ATLAS experiment

Mgr. Matej Melo

Study program: Nuclear and Subnuclear Physics
Supervisor: Prof. RNDr. Stanislav Tokár, DrSc.
Consultant: Mgr. Pavol Bartoš, PhD.

Bratislava, 2019

Contents

Comenius University in Bratislava
Faculty of Mathematics, Physics and Informatics

THESIS ASSIGNMENT

Name and Surname:	Mgr. Matej Melo
Study programme:	Nuclear and Subnuclear Physics (Single degree study, Ph.D. III. deg., full time form)
Field of Study:	Nuclear And Subnuclear Physics
Type of Thesis:	Dissertation thesis
Language of Thesis:	English
Secondary language:	Slovak

Title: Charge asymmetry in top-quark pair production at 13 TeV in proton-proton collisions with the ATLAS experiment

Annotation: This work requires carrying out a high-level data analysis at the current high energy physics frontier. Firstly, it is necessary to identify top quark events and to reconstruct their kinematics. Two different event topologies are studied - the so-called resolved topology and a topology with highly boosted top quarks. Both topologies are subsequently combined and the charge asymmetry is extracted using the fully bayesian unfolding, which directly includes also systematic uncertainties. Finding the correct unfolding setup, leading to stable results with correctly estimated uncertainties, represents a major challenge in this measurement.

Aim: Measure charge asymmetry in top quark pair production in proton-proton collisions at the centre-of-mass energy of 13 TeV with the ATLAS experiment using full Run 2 dataset.

Literature:
1. M. Beneke et al., Top Quark Physics, Proc. of the Workshop on Standard Model Physics at LHC, CERN 2000-004
2.The ATLAS collaboration, Expected Performance of the ATLAS Experiment, CERN-OPEN-2008-020, Geneva 2009

Comment:

Keywords: top quark, charge asymmetry, fully bayesian unfolding, ATLAS

Tutor:	prof. RNDr. Stanislav Tokár, DrSc.
Consultant:	Mgr. Pavol Bartoš, PhD.
Department:	FMFI.KJFB - Department of Nuclear Physics and Biophysics
Head of department:	prof. RNDr. Stanislav Tokár, DrSc.
Assigned:	25.02.2014

Approved: 25.04.2014 prof. RNDr. Jozef Masarik, DrSc.
Guarantor of Study Programme

.....
Student

.....
Tutor

Univerzita Komenského v Bratislave
Fakulta matematiky, fyziky a informatiky

41866059

ZADANIE ZÁVEREČNEJ PRÁCE

Meno a priezvisko študenta: Mgr. Matej Melo
Študijný program: jadrová a subjadrová fyzika (Jednoodborové štúdium, doktorandské III. st., denná forma)
Študijný odbor: jadrová a subjadrová fyzika
Typ záverečnej práce: dizertačná
Jazyk záverečnej práce: anglický
Sekundárny jazyk: slovenský

Názov: Charge asymmetry in top-quark pair production at 13 TeV in proton-proton collisions with the ATLAS experiment
Nábojová asymetria v produkcii top-kvarkových párov pri 13 TeV v protón-protónových zrážkach na experimente ATLAS

Anotácia: Táto práca požaduje realizáciu náročnej dátovej analýzy na hraniciach možností dnešnej fyziky vysokých energií. Najskôr je potrebné identifikovať top-kvarkové udalosti a zrekonštruovať ich kinematiku. Dve odlišné topológie sú predmetom skúmania - tzv. 'resolved' topológia a tiež topológia s top kvarkmi s vysokou hybnosťou. Obidve topológie sú následne skombinované a nábojová asymetria je spočítana pomocou plne bayesovskej dekonvolúcie, ktorá zahŕňa aj systematické neistoty. Nájdenie správneho nastavenia tejto procedúry, ktoré by viedlo k stabilným výsledkom so správne určenými neistotami, predstavuje hlavnú výzvu tohto merania.

Cieľ: Zmerať nábojovú asymetriu v produkcii top-kvarkových párov z protón-protónových zrážok pri ťažiskovej energii 13 TeV na experimente ATLAS s využitím plnej dátovej vzorky z tzv. Run 2.

Literatúra:
1. M. Beneke et al., Top Quark Physics, Proc. of the Workshop on Standard Model Physics at LHC, CERN 2000-004
2.The ATLAS collaboration, Expected Performance of the ATLAS Experiment, CERN-OPEN-2008-020, Geneva 2009

Poznámka:

Kľúčové slová: top kvark, nábojová asymetria, plne bayesovská dekonvolúcia, ATLAS

Školiteľ: prof. RNDr. Stanislav Tokár, DrSc.
Konzultant: Mgr. Pavol Bartoš, PhD.
Katedra: FMFI.KJFB - Katedra jadrovej fyziky a biofyziky
Vedúci katedry: prof. RNDr. Stanislav Tokár, DrSc.

Dátum zadania: 25.02.2014

Dátum schválenia: 25.04.2014

prof. RNDr. Jozef Masarik, DrSc.
garant študijného programu

Univerzita Komenského v Bratislave
Fakulta matematiky, fyziky a informatiky

....

študent školiteľ

Acknowledgements

Firstly, I would like to thank my supervisor, professor Stanislav Tokár. For eight years he was leading me in my scientific efforts, always willing to help with any problem that I came across. Thanks to him I had a great start of my professional career which I will never forget.

My gratitude belongs also to my consultant Pavol Bartoš, who took the role of the analysis contact person despite having many other important duties. Without his dedication and effort the whole analysis would take much more time and maybe I would even give up. Pavol also showed me an important thing – that it is possible to combine difficult scientific work with a family and several kids.

I also want to thank the whole analysis team. Namely to Oliver because without his programming skills I would be often completely lost. It was him, who solved the most complex computing issues and who showed me how programming should look like. Many thanks also to Barbora for her work in many parts of the analysis. I would like to apologise to her for many hours of strenuous binning optimisation which at the end were found to be useless due to my own mistake. I am grateful to Tomáš for the development of the BDT pairing algorithm and for his willingness to explain me again and again various difficult topics. There are also many others and I am not trying to mention them all, because surely the list would not be complete anyway. Therefore, my thanks belong to everyone in the Bratislava ATLAS team and in the whole ATLAS collaboration – you all showed me how to do perfect scientific work, you accepted my failures and questions and you taught me so much! Similarly, I am grateful to all teachers and lecturers that I met during my studies, particularly to Vojto, who gave me his confidence and showed me how to take responsibility.

However, my studies were not only about physics: I would like to thank my hiking partner Michal for all the beautiful hikes we did together around Geneva. I also want to apologise once again for the troubles and dangers I caused him during our attempt to climb Les Diablerets. I am grateful to Róbert for teaching me how to do fondue. It might seem to be a little thing, but my wife loves it so much! I really enjoyed the long discussions I had with my colleagues, whether they were about physics, society or religion, they were always very inspiring! My thanks belong also to the people from

Slovak catholic mission, who were always very welcoming, and particularly to Marián, who did not hesitate to give us his car when we were in need.

I would like to specially thank my family – my wonderful wife Terezka, my little son Šimon, my parents, my parents-in-law and all my relatives. My wife is for me a solid place, a true home, where I am always loved, accepted and supported. She accepted my business trips to CERN and whenever possible she gladly joined me and helped me as much as possible. Our son Šimon was the main motivation for me to finish, although not in time, but at least without a large delay. It was heartbreaking to leave him and Terezka alone for a few days every week when I had to go to Bratislava and I hope I will be able to compensate for this as soon as possible. My parents are those who grew me up, who always loved and supported me, and they were the first to show me the beauties of maths and physics. Similarly, I have great parents-in-law who also supported us so much. Without their help it would be really difficult, if not impossible, for me to finish my studies. I cannot forget to mention my great siblings – Jakub, Pavol, Milka and Majka, as well as my sisters-in-law Lenka and Lucia. They all helped us so much and, moreover, with them there was always a lot of fun!

Last but not definitely not least, I would like to thank God for all his blessing. It is wonderful to be his child, knowing that he cares and leads me through all the difficulties of life!

Abstract

We report a measurement of the charge asymmetry in top-quark pair production using 139 fb^{-1} of proton-proton collision data collected at the centre-of-mass energy of 13 TeV by the ATLAS experiment. Events are reconstructed in the so-called resolved topology and in a topology with highly boosted top quarks. Both topologies are combined and a fully bayesian unfolding method is used to correct for limited detector acceptance and resolution. The charge asymmetry is measured inclusively and differentially as a function of the top-quark pair mass and longitudinal boost. The measured values are in good agreement with the Standard Model NNLO in QCD + NLO in EW predictions and a non-zero inclusive asymmetry is observed at a 4σ confidence level.

Keywords: top quark, charge asymmetry, fully bayesian unfolding, ATLAS

Abstrakt

Prezentujeme meranie nábojovej asymetrie v produkcii top kvarkových párov s použitím 139 fb^{-1} protón-protónových zrážok pri ťažiskovej energii 13 TeV zozbieraných experimentom ATLAS. Udalosti sú rekonštruované v tzv. resolved topológii a v topológii s vysokými top-kvarkovými hybnosťami. Obidve topológie sú skombinované a metóda plne bayesovskej dekonvolúcie je použitá s cieľom zohľadniť limitované detektorové rozlíšenie a akceptanciu. Nábojová asymetria je odmeraná inkluzívne a diferenciálne ako funkcia hmotnosti a pozdĺžnej hybnosti top-kvarkového páru. Namerané hodnoty sú v dobrej zhode s predpoveďami Štandardného modelu na NNLO v QCD + NLO v EW úrovni a nenulová inkluzívna asymetria je pozorovaná na úrovni spoľahlivosti 4σ.

Kľúčové slová: top kvark, nábojová asymetria, plne bayesovská dekonvolúcia, ATLAS

Introduction

The discovery of the Higgs boson in 2012 by the experiments ATLAS and CMS at the Large Hadron Collider (LHC) was the last big step to complete the Standard Model (SM) theory verification. The SM describes the phenomena of all known elementary particles and the interactions between them. For over 50 years it has demonstrated an unprecedented success in providing theoretical predictions for a huge number of physical experiments and measurements. Up to now there are no significant discrepancies between data and the SM predictions.

Nevertheless, the SM leaves some phenomena unexplained and certainly it is not a complete theory. The existence of the dark matter and the dark energy, the absence of gravitational interaction in the SM and the matter-antimatter asymmetry are among the biggest problems of the SM. Additionally, several of the SM features are considered to be unnatural, e.g. the large number of free parameters or the so-called hierarchy problem.

To solve these problems, a large number of Beyond the Standard Model (BSM) theories have been developed through decades. Most of them, including popular supersymmetry (SUSY), predict the existence of new, yet undiscovered elementary particles. Hence, most of the BSM physics searches focus on direct or indirect signs of possible new particles.

The forward-backward and charge asymmetry ($A_{\mathrm{FB}},\ A_{\mathrm{C}}$) in heavy quark production are among the promising fields for indirect BSM physics searches. These phenomena occur only through higher-order diagrams and they are affected by contributions from not only the SM particles but also from the possible BSM particles. A significant deviation of the observed values from the SM prediction would be a serious evidence of BSM physics.

A number of experiments studying A_{FB} and A_{C} in heavy quark pair (particularly top-quark pair) production has been carried out at the Tevatron by the CDF and DØ experiments and also at the LHC by ATLAS and CMS. The first Tevatron results showed excesses up to 4 standard deviations from the SM predictions and caused a lot of excitement. However, after adding additional data and improving the theoretical predictions the latest Tevatron results are now in a good agreement with the SM.

Similarly, the first LHC results are perfectly compatible with the SM expectations.

The LHC continues to provide new data to further improve the precision and limits of the A_C measurements. The main goal of this PhD thesis is to measure the A_C inclusively and differentially as a function of the top-quark pair mass and longitudinal boost using 139 fb^{-1} of proton-proton collision data collected by the ATLAS experiment at $\sqrt{s} = 13$ TeV.

The SM and the top-quark physics are briefly described in Chapters 1 and 2, respectively. The forward-backward and charge asymmetries are discussed in Chapter 3, where also previous measurements of these quantities are summarised. The ATLAS experiment, together with the LHC, is described in Chapter 4. Chapter 5 provides definitions of the physics objects used in the measurement. In Chapter 6 the data and simulated samples are summarised. Chapter 7 is dedicated to the event selection and reconstruction, and the unfolding procedure is elaborated in Chapter 8. The systematic uncertainties affecting the measurement are summarised in Chapter 9. Finally, the results can be found in Chapter 10.

Chapter 1

Standard Model

The Standard Model (SM) is a theory describing all known elementary particles and the interactions between them: the electromagnetic, weak and strong. Gravitational interaction is not included in the SM. The SM was developed in stages in the 1960s and the 1970s and consists of two main parts: the electroweak (EW) theory [1, 2] unifying the electromagnetic and weak interactions and the quantum chromodynamics (QCD) [3] describing the strong interaction.

1.1 Historical Overview

1.1.1 Electroweak Theory

The first big step towards formulation of a unified theory of electromagnetic and weak interactions was made by Glashow in 1961 [4] by the proposal of a gauge theory based on an $\mathrm{SU}(2) \times \mathrm{U}(1)$ symmetry group. This model predicted an existence of weakly interacting neutral currents mediated by a Z^0 gauge boson, which was added to the previously theorized $W^{\pm}$ bosons and the photon γ^0. With these four gauge bosons it was possible to mathematically describe why the weak interactions violate the parity conservation [5] while the electromagnetic interactions do not. Independently, Salam and Ward proposed a very similar theory in 1964 [6]. Nevertheless, in these gauge theories non-zero masses of the W and Z bosons had to be inserted by hand and there was no theory explaining their origin. Eventually, in 1967 Weinberg [1] and Salam [2] independently managed to incorporate the Higgs mechanism [7, 8] into the Glashow's theory. The Higgs mechanism explained masses of the W and Z boson through spontaneous symmetry breaking and thus completed the EW theory.

Experimentally, the EW theory was largely confirmed in 1973 by the discovery of the weak neutral currents [9] by the Gargamelle experiment [10] at CERN[1]. The W^+ and W^- bosons were discovered in 1983 by the UA1 and UA2 experiments at the

[1] Conseil Européen pour la Recherche Nucléaire, The European Organization for Nuclear Research.

SPS accelerator at CERN in proton-antiproton collisions at $\sqrt{s} = 540$ GeV [11, 12]. After only few months, the same experiments announced also the discovery of the Z boson [13, 14].

1.1.2 Quantum Chromodynamics

A large number of strongly interacting particles discovered in 1950s and 1960s lead to hypotheses that these might actually be compound particles. In 1961 Gell-Mann classified known mesons and baryons according their quantum numbers in a theory known as the 'eightfold way' [15]. This theory succeeded in predicting the existence and properties of the missing Ω^- baryon which was discovered in 1964 [16]. In the same year Gell-Mann proposed [17] existence of three quarks as a fundamental explanation of the 'eightfold way'. Independently, Zweig developed [18] a very similar model. However, these theories required three identical fermions to be in a single quantum state, violating the Pauli exclusion principle [19]. In reaction, Greenberg [20] and Nambu [21] independently proposed an additional quantum number originating from the SU(3) gauge symmetry. At the same time, this would lead also to existence of an octet of gluons as mediators of the strong interaction. The QCD as a field theory was finalised in 1973 [3] and the new quantum number (colour[2]) was recognised as a source of the strong interaction. In the same year there was a discovery of the asymptotic freedom [22, 23], which is together with the colour confinement [24] among the main properties of the QCD.

The QCD theory was largely confirmed in 1979 by the discovery of gluons at the PETRA accelerator at DESY[3] in Hamburg [25].

1.2 Elementary Particles in the Standard Model

In this section the main properties of the SM particles are described. An overview of all known elementary particles is shown in Figure 1.1. Elementary particles can be divided into two main groups: fundamental fermions with spin 1/2 and elementary bosons with integer spins.

Fundamental fermions are sometimes referred to as particles of matter and can be divided into three generations. Between the generations, particles differ by mass and the flavour quantum number, while the other quantum numbers are equal. Only particles of the first generation form the matter in the universe. Particles of the second and third generation existed abundantly in the earliest moments of the universe after the Big Bang but quickly decayed into particles of the first generation. To all elementary fermions there is a corresponding antiparticle with the same properties such as mass

[2]The name 'colour' was chosen due to some similarities with real colour, as will be discussed in Section 1.2.1.
[3]Deutches Elektronen-Synchrotron (German Electron Synchrotron).

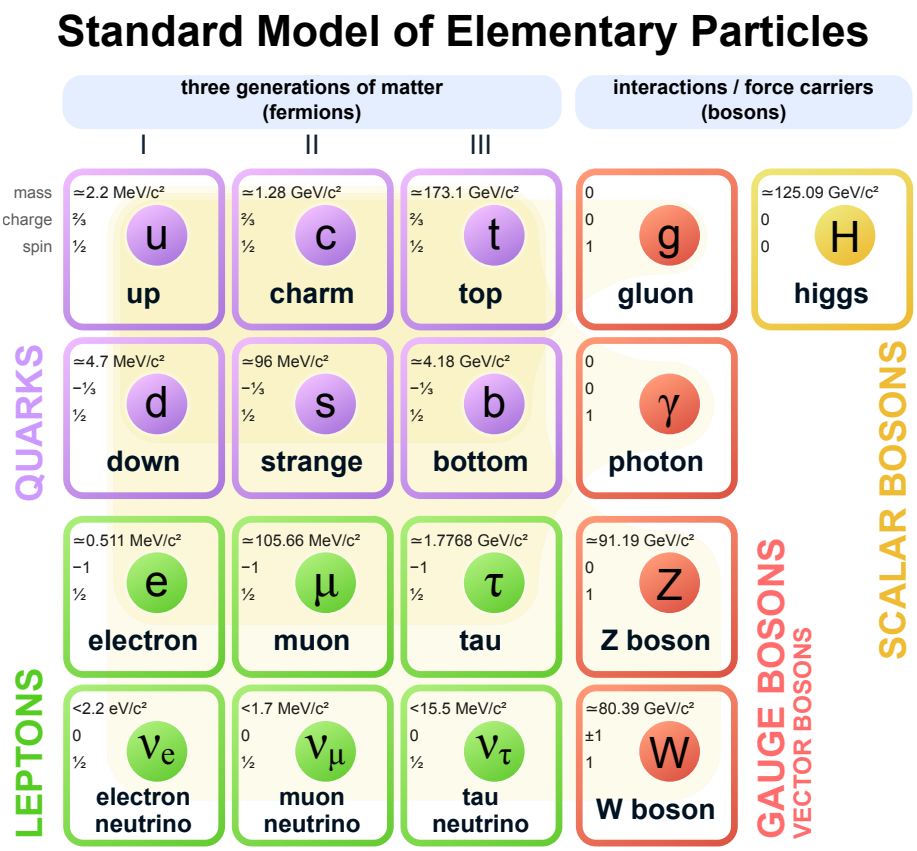

Figure 1.1: Table of elementary particles in the SM.

and decay width, but with inverted quantum numbers and charges. Due to the violation of the baryon symmetry slightly more particles than antiparticles were created after the Big Bang. All antiparticles were annihilated in interactions with particles and only the excessive particles form the universe. Nevertheless, particles of the second and third generation, as well as antiparticles, can still be produced in high energy collisions, e.g. in particle accelerators.

Fundamental fermions can be classified into quarks and leptons, depending on how they interact. Quarks carry colour charge and interact via the strong interaction while leptons have no colour. All fundamental fermions interact via the electroweak interaction.

Bosons in the SM can be divided into gauge (vector) bosons with spin one and the scalar Higgs boson with spin zero. Gauge bosons mediate interactions: electromagnetic interaction is mediated by photons γ^0, weak interaction by the $W^{\pm}$ and Z^0 bosons and strong interaction is mediated by gluons g^0. The Higgs boson is a quantum excitation of the Higgs field, related to the mechanism through which particles acquire mass.

1.2.1 Quarks and Hadrons

Quarks are strongly interacting fermions. Strong interaction exhibits a property of colour confinement [24] and quarks cannot be isolated. Instead, quarks form hadrons – colourless bound states of two or three valence quarks, called mesons and baryons, respectively. As a first approximation, baryons consist of three quarks (which are in colour states red, green and blue) or three antiquarks (antired, antigreen and antiblue). Mesons are always bound states of a quark and an antiquark with opposite colour charges. The up-type quarks (up, charm and top) have an electric charge[4] of $+2/3$ and the down-type quarks (down, strange, bottom) of $-1/3$. Two up quarks and a down quark form a proton and two down quarks with one up quark form a neutron.

However, all hadrons are rather complex objects with a so-called sea of virtual quark-antiquark pairs generated by gluons mediating the strong interaction between the valence quarks. Valence quarks, sea quarks and gluons are collectively referred to as partons. The inner structure of hadrons can be studied through deep inelastic scattering[5] with leptons. Mostly, the proton structure is studied by interactions with electrons. The resolving power in deep inelastic collisions increases with the momentum transfer Q. The inner structure of a proton is then described by the so-called parton distribution functions (PDFs) $f(x, Q^2)$ which are proportionate to probability densities to find a parton carrying the proton momentum fraction x at a squared energy scale Q^2. The PDFs are typically presented normalised so that $\sum_i \int x f_i(x, Q^2) \mathrm{d}x = 1$, where i stands for different partons (gluons and different quark flavours), as shown in Figure 1.2. At low Q^2 values the valence quarks are dominant while at high Q^2 a large fraction of the proton momentum is carried by other partons, the sea quarks and mainly gluons.

Protons and neutrons are the only stable hadrons[6] and form the nuclei of all atoms in the universe. All other hadrons are unstable and depending on their quark composition they can decay weakly, strongly and also electromagnetically. The hadron lifetimes range from $\approx 10^{-24}$ s to $\approx 10^{-8}$ s [26]. Typically, hadrons decaying strongly and electromagnetically have shorter lifetime by several orders of magnitude than those decaying only through the weak interaction.

The up, down and strange quarks are collectively referred to as light quarks while charm, bottom and top quarks are denoted as heavy quarks. Light hadrons are hadrons without any heavy valence quark and the whole QCD theory was developed by studying

[4] Throughout this thesis all values of electric charge are in units of the elementary electric charge, $e = 1.602176634 \times 10^{-19}$ C.

[5] In deep inelastic collisions hadrons no longer interact as single particles. Instead, the scattering occurs on the individual partons which interact as free particles.

[6] Neutrons are stable only when bound in an atomic nucleus, otherwise they are subject to β^- decay with a lifetime of ≈ 880 s [27].

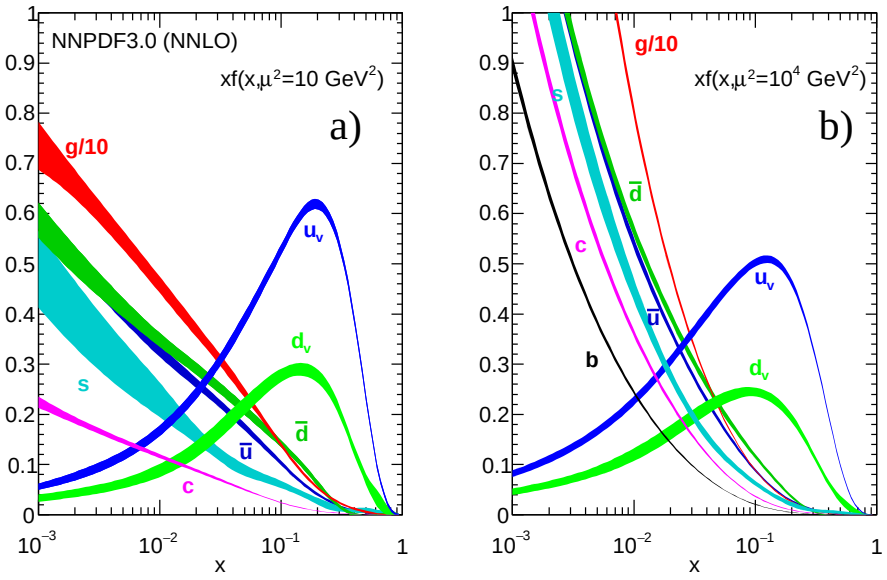

Figure 1.2: Proton parton distribution functions multiplied by the proton momentum fraction x at $Q^2(=\mu^2)$ values of 10 GeV^2 and 10000 GeV^2. The figure is taken from Ref. [26].

their properties. In 1974, two experiments in Brookhaven and at SLAC[7] independently proved the existence of the fourth quark by discovering the J/Ψ meson, bound state of the charm and anticharm quarks [28, 29]. The fifth quark, the bottom quark, was discovered in 1977 at Fermilab[8] [30] in Chicago. Finally, the top quark was discovered in 1995 [31, 32] by the CDF [33] and DØ [34] experiments at the Tevatron [35] collider at Fermilab. The top quark is the only quark that decays before hadronisation and there are no hadrons with a valence top quark. The top quark properties are described in detail in Chapter 2.

As a consequence of the colour confinement, strongly interacting particles (quarks and gluons) manifest themselves in high energy physics (HEP) experiments as showers of hadrons, so-called jets [36]. Jets can be labelled depending on which particle was the primary source of the hadron shower, e.g. gluon jets, light jets, c-jets or b-jets. From the experimental point of view it is very challenging to determine the flavour of the primary particle from the topology of the hadron shower. However, there are some signatures than can increase the probability of correct jet tagging. For example, many mesons containing a valence b quark have a lifetime sufficient to travel a non-negligible distance in the detector tracking system before decaying. As a consequence, many b-jets have a so called secondary vertex within the jet, which corresponds to the point where the short-lived b-hadron decayed.

[7] Stanford Linear Accelerator Center.
[8] Fermi National Accelerator Laboratory.

1.2.2 Leptons

Leptons can be divided into charged leptons (electron e, muon μ and tau τ) with electric charge of -1 and neutrinos, which are not electrically charged and interact only via the weak interaction.

The electron was discovered as a first fermion already in 1897 by Thomson [37] and the corresponding antiparticle, the positron, was discovered in 1932 by Anderson [38]. Electrons are present in all atoms and have a very small mass of only around 511 keV[9] [26]. As a consequence, electrons are often ultrarelativistic[10] in HEP experiments which can be used for their identification by Cherenkov [39] or transition radiation [40] detectors.

Muons are $\approx$ 200-times heavier than electrons and were discovered in 1930s. Muons decay via the weak interaction and have a lifetime of around 2.2 µs [26], see Figure 1.3. In the conditions at HEP experiments muons are considered stable. Due to relatively large mass muons have very small ionization losses when passing through the detector material. This can be used for their identification, since they are the only particles (except neutrinos) which can penetrate through calorimeters.

The tau lepton τ was discovered in 1977 at SLAC [41]. Tau leptons have a mass of around 1.8 GeV and thus can decay also into hadrons with a branching ratio $\mathcal{BR} \approx 65\%$ [26]. The leptonic decays are suppressed, with $\mathcal{BR} \approx 18\%$ and $\mathcal{BR} \approx 17\%$ for decays into muon and electron, respectively. With a mean lifetime of around 2.9×10^{-13} s [26] the tau leptons are challenging from the experimental point of view and can be observed only indirectly through their decay products.

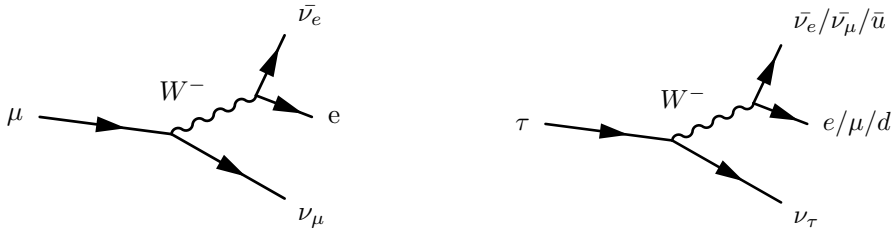

(a) Muon decay. (b) Tau decay.

Figure 1.3: Feynman diagrams for muon and tau decays.

The existence of neutrinos was hypothesized in 1930s in an attempt to explain the continuous energy spectrum in beta decays. Although initially considered undetectable, the electron neutrino ν_e was discovered in 1956 using inverse beta decay and a large neutrino flux from a nuclear reactor [42]. The muon neutrino ν_μ was detected in 1962 [43] and the tau neutrino ν_τ wasn't observed until 2000 when its discovery was announced by the DONUT experiment at Fermilab [44].

[9] Throughout this thesis natural units $\hbar = c = 1$ are used.
[10] $p \gg m$.

The SM initially predicted massless neutrinos, but the phenomenon of neutrino oscillations discovered in 1998 [45] suggests they do have mass, although below the detection limits of the current experiments ($\lesssim 2$ eV for ν_e [26]). Neutrinos interact only weakly and are difficult to study experimentally due to extremely small cross-sections. The dedicated neutrino experiments are often very large in volume to increase the probability of neutrino interactions, e.g. the IceCube [46] and Baikal [47] experiments. In HEP experiments neutrinos manifest themselves indirectly as missing momentum in the transverse plane.

1.2.3 Gauge Bosons

Photons γ are mediators of the electromagnetic interaction. The connection between light and electromagnetism was for the first time proposed by Maxwell in 1865 [48]. In 1905, Einstein suggested [49] that some phenomena such as the photoelectric effect could be explained by the existence of discrete light quanta, which seemed to be contradicting the generally accepted wave theory of light. The corpuscular nature of light was confirmed by a series of experiments conducted by Millikan [50]. In 1927, Dirac developed a quantum theory in which electromagnetic interaction was performed through emission and absorption of radiation [51]. The quantum electrodynamics (QED) as a quantum theory of electromagnetism was finalised in late 1940s by the understanding of the renormalisation procedure [52]. Photons are massless and in the HEP experiments they lose most of their energy by creating electron-positron pairs and thus forming an electromagnetic particle shower.

The mediators of the weak interaction, the $W^{\pm}$ and Z^0 bosons, were discovered in 1983 [11–14], as mentioned already in Section 1.1.1. Precise properties of the W and Z bosons, such as cross section, mass, decay width, branching ratios, couplings to fermions etc., were extensively studied at the LEP [53] electron-positron collider at CERN without observing any significant deviations from the SM predictions [54, 55]. The W and Z bosons are among the heaviest elementary particles, with masses of approximately 80.4 and 91.2 GeV, respectively [26]. Both bosons have a very large decay width of approximately 2.1 and 2.5 GeV for the W and Z bosons, respectively [26], and can be observed only through their decay products.

The W boson decays either leptonically to charged lepton and the corresponding antineutrino with a $\mathcal{BR} \approx 11\%$ for each lepton flavour, or hadronically into quark and an antiquark with a $\mathcal{BR} \approx 68\%$ [26]. The probabilities of decaying into certain quark and antiquark flavours are defined by the Cabbibo-Kobayashi-Maskawa (CKM) matrix, sometimes referred to as quark mixing matrix [26, 56, 57]. In short, the probabilities that the W boson decays into quarks of the same generation (e.g. $u\bar{d}$ or $c\bar{s}$) are much larger than the probabilities of decaying into quarks belonging to different generations

(e.g. $u\bar{b}$ or $c\bar{d}$). The top quark is the only quark which is kinematically forbidden to appear in the W boson decay.

The Z boson decays into fermion-antifermion pairs where both decay products have to be of the same flavour. All fermions are kinematically allowed, except the massive top quark. The hadronic decay mode is the dominant one with a total $\mathcal{BR} \approx 70\%$, followed by the decay into neutrinos with a $\mathcal{BR} \approx 20\%$ [26], which is invisible for the HEP experiments. The decay into charged leptons has an overall $\mathcal{BR} \approx 10\%$ and the probabilities of decaying into the individual lepton flavours are approximately equal.

Gluons, the massless gauge bosons related to the strong interactions, are specific due to the fact that they are coloured – they carry the charge of the interaction they mediate. The QCD theory with an SU(3) colour symmetry leads to an octet of gluons having linearly independent combinations of colours and anticolours.

The SM allows for the existence of the so-called glueballs, colourless bound states of two or three gluons [58]. From the experimental point of view, search for glueballs is very challenging since they are expected to behave similarly to neutral mesons. There are some experiments claiming the observation of glueballs at energies in range of $\approx 0.5 - 3$ GeV [59, 60] but these measurements were not yet confirmed and the existence of glueballs remains an open question of the QCD theory.

1.2.4 Higgs Boson

In 2012 the ATLAS [61] and CMS [62] experiments at the LHC at CERN announced the discovery of a particle with properties as expected for the Higgs boson, the last missing SM particle [63, 64]. Higgs boson with mass of around 125 GeV [26] is a quantum excitation of the Higgs field, which is special by having non-zero vacuum expectation value, $\nu = 246$ GeV [26]. Gauge bosons gain mass through the Higgs mechanism [7, 8] and fermions gain mass proportionately to their Yukawa coupling to the Higgs field. The values of the Yukawa couplings are spread over several orders of magnitude – the top quark is approximately 10^5 times more massive than the electron. Finally, the Higgs boson also gains mass by the self-interaction with its own field.

Width a decay width of around 4 MeV [26] the Higgs boson can be studied only through its decay products. The most important decay modes are summarized in Figure 1.4. From the experimental point of view, some of the decay channels including the dominant $H \to b\bar{b}$ are very challenging due to large background from other processes. For the discovery of the Higgs boson and for the most precise measurements of the Higgs boson properties the $H \to \gamma\gamma$ and $H \to ZZ \to \ell^+\ell^-\ell^+\ell^-$ decay channels are used.

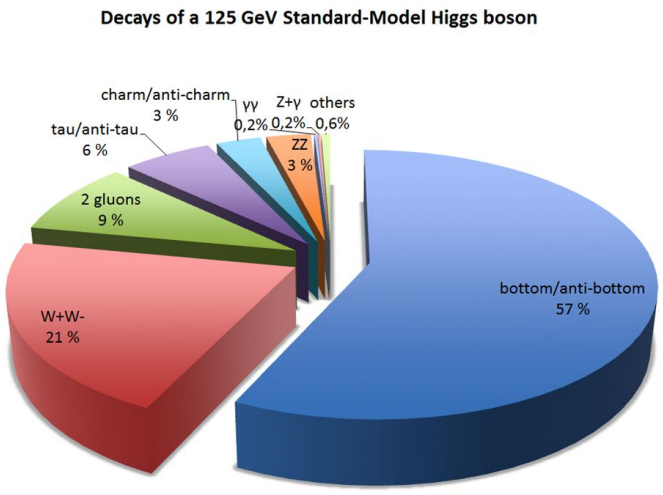

Figure 1.4: Higgs boson decay modes and branching ratios.

1.3 Beyond the Standard Model

Through decades, hundreds or even thousands of measurements were carried out in order to test the SM predictions. Out of these, vast majority demonstrated perfect agreement between the theory and experiments. Nevertheless, despite tremendous success of the SM predictions, it is generally accepted that the SM is not a complete theory.

1.3.1 Problems of the Standard Model

In this section the most important problems of the SM are briefly described.

Gravity. There is no quantum theory of gravity and no connection between the SM and the general theory of relativity [65].

Dark Matter and Dark Energy. Cosmological observations, such as galaxy rotation curves [66] and gravitational lensing [67], suggest the existence of the so-called dark matter [68]. Dark matter is expected to account for around 22% of the total energy in the universe (Figure 1.5) and the SM has no explanation for its origin. Moreover, the so-called dark energy is expected to be responsible for the inflation of the universe [69]. The dark energy contributes by around 70% to the total energy in the universe but very little is known about its nature.

Matter-Antimatter Asymmetry. To explain the relatively large asymmetry between matter and antimatter in the early stages of the universe the three Sakharov conditions

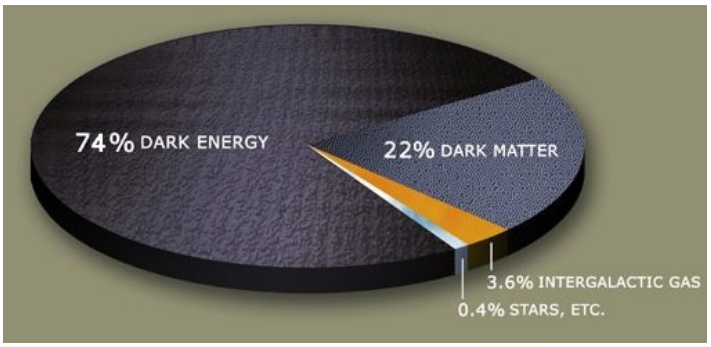

Figure 1.5: Energy distribution in the universe. The SM explains only around 4%.

have to be fullfilled [70]. These include baryon number violation which is not allowed in the SM.

Theoretical Problems. Several properties of the SM are considered unnatural, e.g. quantum corrections to the Higgs boson mass are about 10^{17} times larger than actual Higgs boson mass. The corrections can be removed by renormalisation procedure but 'fine tuning' is required since Higgs boson mass is obtained as a result of subtraction of two numbers of the order of 10^{19} (the so-called hierarchy problem [71]). The SM has also a large number of free parameters, up to 26 in the 'full' version with neutrino masses and strong CP violation. The SM is also incapable of unifying the fundamental interactions.

1.3.2 Beyond the Standard Model Theories

A large number of various theories has been developed in order to solve the problems mentioned above. In general, vast majority of the BSM theories predict the existence of new, yet undiscovered elementary particles. In this section only some of the most promising ideas are mentioned.

Supersymmetry. The supersymmetric theories (SUSY) [72, 73] propose a new symmetry between fermions and bosons. To each of the SM fermions and bosons there would be a superpartner, boson and fermion, respectively. Due to spontaneous breaking of the supersymmetry the superparticles would differ in mass from their SM partners. The SUSY is capable of explaining the dark matter, it elegantly solves the hierarchy problem and achieves a unification of the fundamental interactions at the scale of the grand unification energy of $\Lambda_{\mathrm{GUT}} = 10^{16}$ GeV. One of the disadvantages of the SUSY is that even in the so-called Minimal Supersymmetric Standard Model (MSSM) it contains even much more free parameters (> 100) than the SM. Before launching the LHC the SUSY was among the most promising BSM theories, but since no superparticles

were discovered it has recently become less popular.

Extra Dimensions. A number of BSM models utilise the idea of the existence of more than 3+1 dimensions which form the observed spacetime. The new dimensions might be compactified – circular and very small – and thus not directly observable. For the first time this idea was introduced by Kaluza in 1921 in an attempt to unify gravity and electromagnetism [74]. In 1926 Klein added a quantum interpretation to the Kaluza's theory and suggested the properties of the compactified fifth dimension [75]. Other ideas work with relatively large (up to 1 mm) extra dimensions (LED) and explain the weakness of gravity as a consequence of its penetration into the extra dimensions [76]. The LED theories predict the existence of micro black holes that could be created at the LHC; however, no such evidence was observed and the experiments strongly constrain the LED scenarios. String theories, which consider elementary particles as one-dimensional objects instead of point-like particles, also work with multiple dimensions, e.g. the M-theory considers 11 dimensions [77].

Technicolour and Compositeness A number of theories are based on the idea that at least some of the SM particles might not be elementary, but composite particles made of even smaller building blocks. The technicolour theories [78] propose an alternative to the Higgs mechanism by introducing a new gauge interaction and new fermions. According to the technicolour models there would be no elementary Higgs boson and thus no hierarchy problem. Although the Higgs-like boson was discovered in 2012, the technicolour models are able to incorporate this particle and are not yet completely ruled out. Another set of theories, the preon models, attempt to describe all of the SM particles as composite particles made of even smaller particles that would be truly elementary, the so-called preons [79].

Chapter 2

Top Quark

The very large mass of the top quark of around 173 GeV [26] and the Yukawa coupling $y_t \approx 1$ indicate that the top quark might have a special role in the SM and possibly also in the theories beyond the SM. The question of the vacuum stability [80] is also directly linked to the top-quark mass. The top-quark decay width $\Gamma_t = 1.32$ GeV [81] is much larger than the $\Lambda_{\mathrm{QCD}} \approx 200$ MeV scale related to hadronisation. Thus, the top quark decay can be safely described in perturbative theory and the top quark properties such as spin information are directly passed to the decay products, offering a unique opportunity to study a 'bare' quark.

2.1 Top Quark Production

Neglecting very rare processes, top quarks can be experimentally produced either individually (single top) or in top-antitop pairs. The top-quark pair production via strong interaction has a significantly higher cross section at both the Tevatron and the LHC. The electroweak single top quark production is challenging not only due to smaller cross section but also due to large contamination from background processes.

2.1.1 Top-Quark Pair Production

The theoretical value for the top-quark pair production cross section in proton-proton collisions at $\sqrt{s} = 13$ TeV is $\sigma_{t\bar{t}} = 832^{+40}_{-46}$ pb, assuming the top-quark mass $m_{\mathrm{top}} = 172.5$ GeV [82, 83]. It has been calculated at next-to-next-to leading order (NNLO) in QCD including next-to-next-to leading logarithmic (NNLL) soft gluon terms. The uncertainty originates from variations of the factorisation and renormalisation scales, as well as from PDFs. A dependence of the $t\bar{t}$ pair cross section as a function of the centre-of-mass (CM) energy is shown in Figure 2.1. The top-quark pair cross section measurements [84–87] are in good agreement with the SM predictions.

There are two dominant top-quark pair production modes at hadron colliders: the

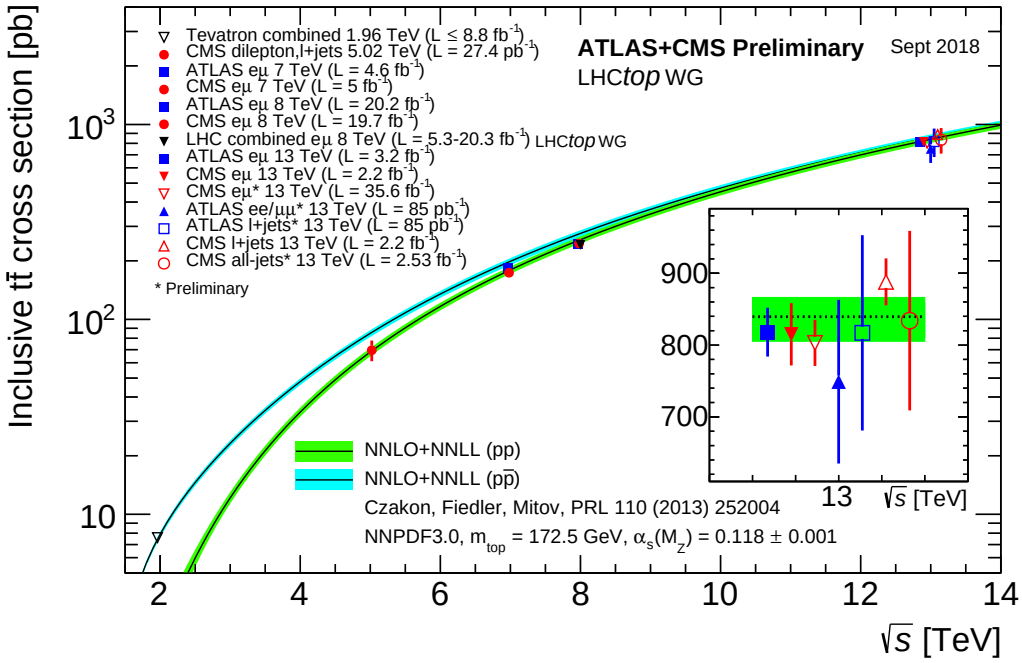

Figure 2.1: Overview of the LHC and Tevatron top-quark pair cross section as a function of the centre-of-mass (CM) energy. The measurements are compared to the theoretical predictions and measurements at the same CM energy are slightly offset for clarity. The figure is taken from Ref. [88].

quark-antiquark annihilation $q\bar{q} \to t\bar{t}$ and the gluon fusion $gg \to t\bar{t}$. At the Tevatron in proton-antiproton collisions at $\sqrt{s} = 1.96$ TeV the quark-antiquark annihilation was largely dominating and the gluon fusion contributed by only $\approx 15\%$. In the proton-proton collisions at higher CM energies at the LHC it is the other way around, with $\approx 90\%$ of the $t\bar{t}$ events being created by the gluon fusion and only around 10% through the quark-antiquark annihilation at $\sqrt{s} = 13$ TeV. A small fraction of $t\bar{t}$ pairs is also created through gluon excitation, the higher-order quark-gluon interaction $qg \to t\bar{t}X$. The Feynman diagrams of the leading order (LO) $t\bar{t}$ production are shown in Figure 2.2.

2.1.2 Single Top Quark Production

The electroweak single top quark production was observed for the first time in 2009 by the by the CDF and DØ experiments [89, 90]. There are three main single top quark production channels: the t-channel, the Wt-channel and the s-channel. Examples of the corresponding LO Feynman diagrams are shown in Figure 2.3. In the t-channel, an initial state b quark exchanges a virtual W boson with a light quark and transforms into the top quark. The Wt-channel is an associated production of the W boson and the top quark. Finally, the s-channel is a production of the top quark and the $\bar{b}$ quark through an intermediate W boson. Various BSM theories predict different effects in

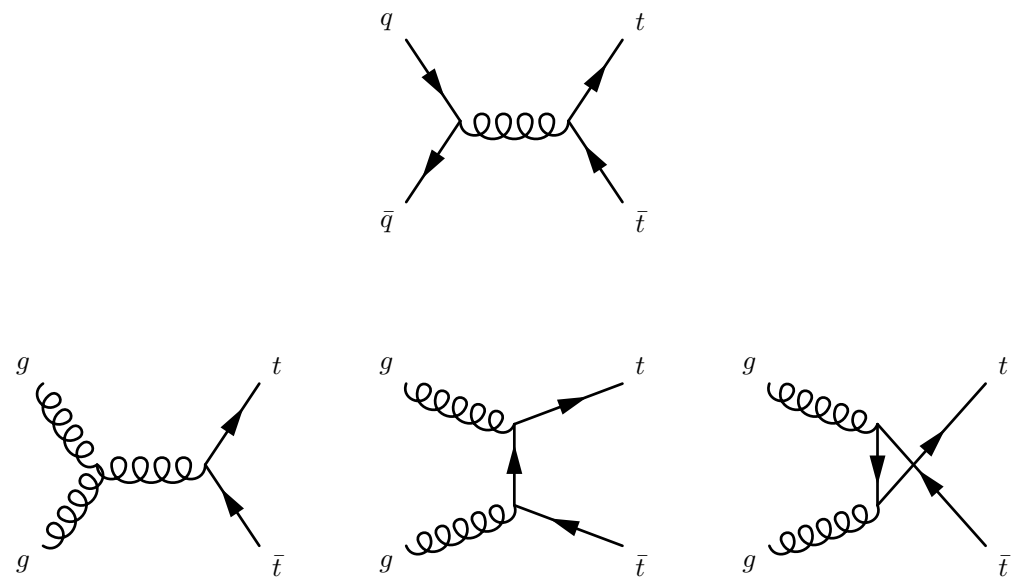

Figure 2.2: The LO Feymnan $t\bar{t}$ production diagrams. Quark-antiquark annihilation (top) and gluon fusion (bottom).

the individual production channels [91] which motivates their precision measurements. Single top quark production also offers a possibility to measure directly the $|V_{tb}|$ element of the CKM matrix.

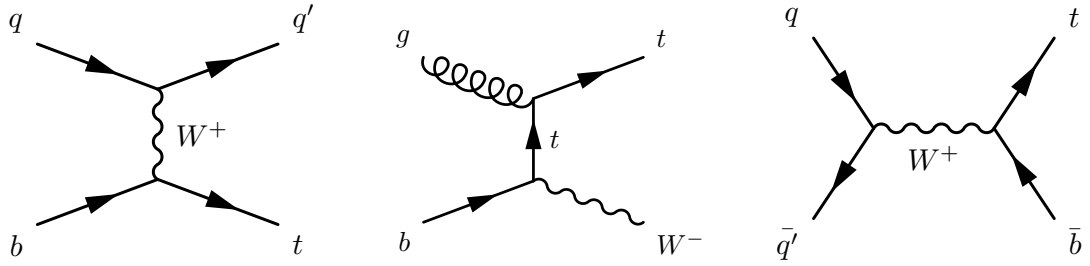

Figure 2.3: Examples of the LO single top quark production Feynman diagrams. The t-channel (left), the Wt-channel (middle) and the s-channel (right).

Assuming the top-quark mass $m_t = 172.5$ GeV the total (single top and single antitop) production cross sections in pp collisions at $\sqrt{s} = 13$ TeV at approximate NNLO in QCD are 217^{+9}_{-8} pb, 72 ± 4 pb and 10.3 ± 0.4 pb for the t-, Wt- and s-channels, respectively [82, 83]. An overview of the single top quark production cross section measurements is presented in Figure 2.4.

2.2 Top Quark Decay

According to the quark mixing CKM matrix [26, 56, 57] the top quark decays into a W boson and a b quark with a probability of $\approx 99.8\%$. The other possibilities are the

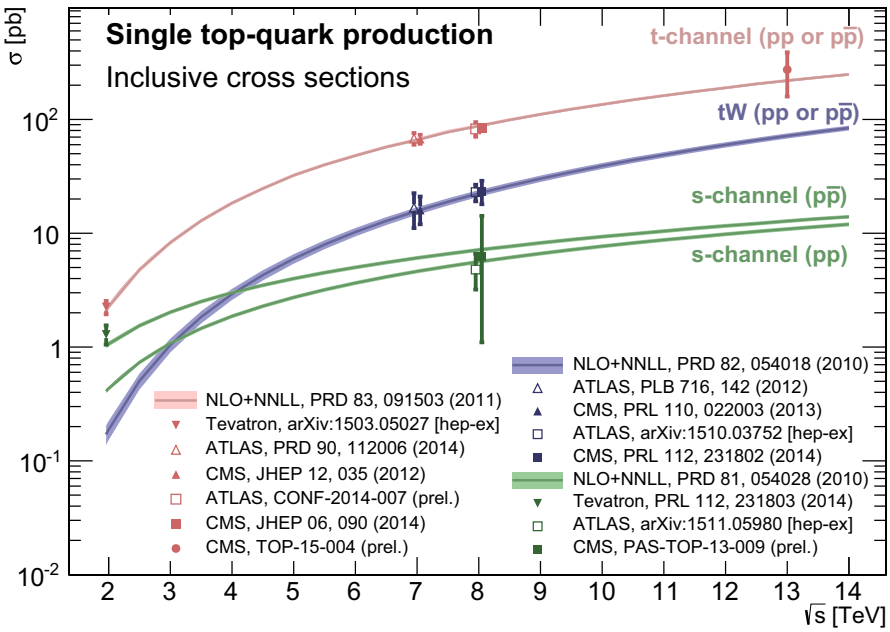

Figure 2.4: Overview of the LHC and Tevatron single top-quark cross section as a function of the CM energy. The measurements are compared to the theory predictions and measurements at the same CM energy are slightly offset for clarity. The figure is taken from Ref. [92].

decays into the W boson and the s quark or the W boson and the d quark. However, these are bellow detection limits of the current experiments and typically are neglected.

Depending on the decay of the two W bosons, there are three main decay channels in top-quark pair events: the all-hadronic channel with $\mathcal{BR} \approx 45.7\%$, the lepton+jets (single lepton) channel with $\mathcal{BR} \approx 43.8\%$ and the dilepton channel with $\mathcal{BR} \approx 10.5\%$ [56]. Graphically, the $t\bar{t}$ branching ratios are shown in Figure 2.5.

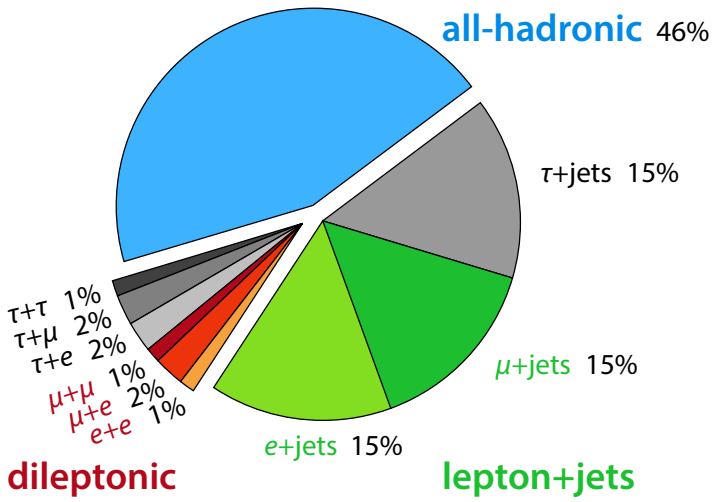

Figure 2.5: Top-quark pair decay channels and the corresponding branching ratios.

2.2.1 All-Hadronic Channel

In the all-hadronic channel both W bosons decay hadronically into $q\bar{q}$ pairs: $t\bar{t} \to W^+bW^-\bar{b} \to b\bar{b}q\bar{q}q\bar{q}$. With the $\mathcal{BR} \approx 45.7\%$ it is the dominating decay channel but at the same time it is challenging from the experimental point of view.

If the $t\bar{t}$ invariant mass is not very high ($m(t\bar{t}) \lesssim 1$ TeV) each quark can be experimentally observed as a jet. This corresponds to the so-called *resolved* all-hadronic topology, shown in Figure 2.6. Even in an ideal case when the six final state quarks are observed as six jets it is very challenging to assign them correctly to the corresponding top quarks. Additionally, experiments have to cope with many background multijet processes that are difficult to distinguish from the all-hadronic $t\bar{t}$ final state. Nevertheless, several measurements were successfully performed in the all-hadronic $t\bar{t}$ decay channel using the resolved topology, e.g. top-quark mass measurements by the ATLAS and CMS experiments [93, 94].

An interesting alternative is the so-called *boosted* topology which can be used to study $t\bar{t}$ pairs with high invariant mass ($m(t\bar{t}) \gtrsim 750$ GeV). If the top quarks are produced with large momenta, the top quark decay products are collimated and instead of six jets two back-to-back 'large' jets might be observed. In the boosted all-hadronic topology there is no problem with combinatorial background and with the advanced boosted top tagging techniques [95] it is also possible to reduce the background from QCD processes to an acceptable level. However, at the LHC at $\sqrt{s} = 13$ TeV the number of $t\bar{t}$ events passing the boosted event selection is by an order of magnitude smaller than the number of events passing the resolved event selection and the boosted all-hadronic measurements suffer from large statistical uncertainties. An example of a measurement using the all-hadronic boosted event selection can be found in Ref. [96].

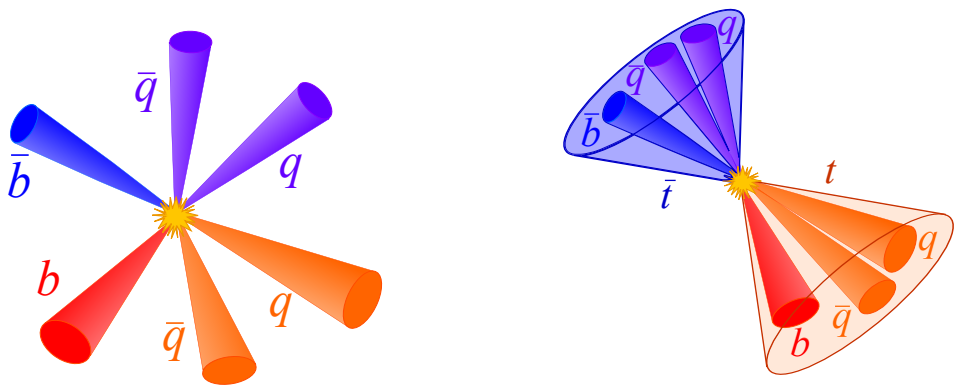

(a) Resolved all-hadronic topology.

(b) Boosted all-hadronic topology.

Figure 2.6: Two of the possible experimental signatures of the all-hadronic $t\bar{t}$ decay channel: The resolved all-hadronic topology (left) and the boosted all-hadronic topology (right).

2.2.2 Lepton+Jets Channel

In the lepton+jets (ℓ+jets) channel, sometimes also called single lepton channel, one W boson decays hadronically and the second W boson decays into leptons: $t\bar{t} \rightarrow W^+bW^-\bar{b} \rightarrow b\bar{b}q\bar{q}\ell\bar{\nu}_\ell$. The charged lepton ℓ in principle might be either electron, muon or tau. However, the tau lepton is unstable with a very short lifetime and mostly decays into hadrons, as discussed in Section 1.2.2. Experiments typically do not attempt to reconstruct hadronically decaying tau leptons and throughout this thesis the ℓ stands for either electron or muon, although it also might be a decay product of the tau lepton.

For many measurements the ℓ+jets channel is the most important decay channel in which the smallest uncertainties on the measured quantities can be obtained and it is also the decay channel which is investigated in this thesis. The ℓ+jets channel benefits from large branching ratio, $\mathcal{BR} \approx 43.8\%$. At the same time, the isolated lepton together with missing transverse momentum are important signatures that strongly suppress multijet background processes.

Similarly to the all-hadronic channel, the ℓ+jets events can be also reconstructed in either resolved or boosted topology. Both topologies are shown in Figure 2.7. The resolved topology has a larger acceptance but cannot be used to study $t\bar{t}$ events with large invariant mass; for the boosted topology it is the other way around. Typically, above ≈ 1 TeV it is more efficient to reconstruct $t\bar{t}$ events in the boosted topology.

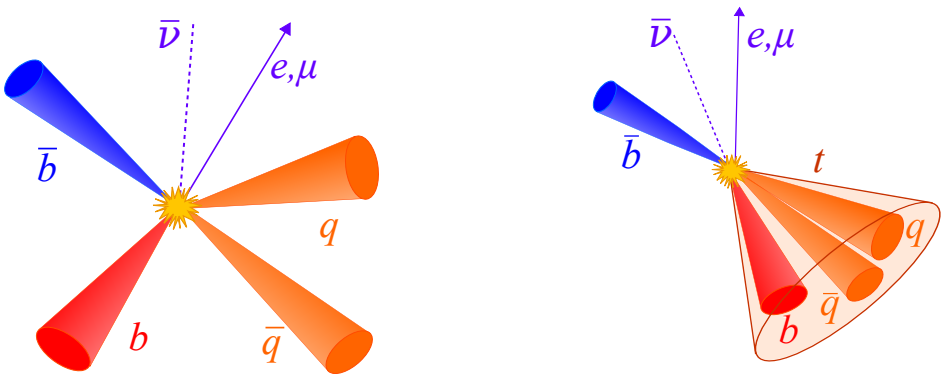

(a) Resolved ℓ+jets topology.

(b) Boosted ℓ+jets topology.

Figure 2.7: Two of the possible experimental signatures of the ℓ+jets $t\bar{t}$ decay channel: The resolved ℓ+jets topology (left) and the boosted ℓ+jets topology (right). Neutrino is observed indirectly as missing momentum in the transverse plane.

In the resolved topology it is necessary to cope with the combinatorial background when assigning the jets to the corresponding top quarks, but the problem is much simplified with respect to the all-hadronic channel. In both topologies it is also necessary to reconstruct the neutrino kinematics. Algorithms which can be used for the event reconstruction in the ℓ+jets channel are described in detail in Section 7.2.

2.2.3 Dilepton Channel

In the dilepton channel both W bosons decay into leptons: $t\bar{t} \to W^+bW^-\bar{b} \to b\bar{b}\ell\bar{\nu}_\ell\ell\bar{\nu}_\ell$, where ℓ stands for electron or muon, although the leptons also might be decay products of the tau lepton. Depending on the lepton flavours the dilepton channel can be divided into three sub-channels: e^+e^-, $\mu^+\mu^-$ and $e^+\mu^-/e^-\mu^+$, typically simplified to ee, $\mu\mu$ and $e\mu$ channels. The $e\mu$ channel is the most important from the experimental point of view, since requiring different lepton flavours almost completely removes the Z+jets background processes which represent the dominant background contribution in the same-flavour dilepton channels.

Measurements in the dilepton channel with a total $\mathcal{BR} \approx 10.5\%$ typically suffer from larger statistical uncertainties. On the other hand, the background contamination is relatively small, particularly in the $e\mu$ channel, and the combinatorial background is also very small in comparison to the ℓ+jets or the all-hadronic channel. The major challenge in reconstruction of the $t\bar{t}$ pairs in the dilepton decay channel is caused by the presence of two neutrinos.

An example of an ideal experimental signature of a dilepton $t\bar{t}$ event is shown in Figure 2.8.

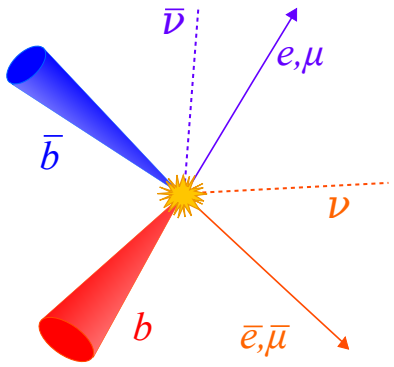

Figure 2.8: One of the possible experimental signatures of the dilepton $t\bar{t}$ decay channel. Neutrinos are observed indirectly as missing momentum in the transverse plane.

2.3 Top Quark Properties

The discovery of the top quark in 1995 [31, 32] by the CDF [33] and DØ [34] experiments was followed by a large effort to precisely measure its properties. In this section we briefly mention measurements of the most important top quark properties. Additionally, the top-quark charge asymmetry is discussed in detail in Chapter 3.

2.3.1 Top-Quark Charge

The top quark was generally accepted as the SM quark with charge $+2/3$ since its discovery in 1995, but an alternative explanation suggested that it actually might be an exotic quark with charge $-4/3$ [97]. The CDF and DØ experiments disfavoured the exotic model [98, 99], but the definitive exclusion of the exotic model at 5 σ confidence level (CL) was made by the ATLAS collaboration only in 2013 when the top-quark charge was measured to be $0.64 \pm 0.02(\text{stat.}) \pm 0.08(\text{syst.})$ [100].

2.3.2 Top-Quark Mass

The top quark is the most massive SM particle with Yukawa coupling $y_t \approx 1$. Precise top-quark mass measurements provide an opportunity for stringent tests of the overall consistency of the SM.

Before we continue, it is necessary to mention that there is some ambiguity in understanding of what exactly the top-quark mass is. The direct top-quark mass measurements search for the exact position of the peak in the invariant mass of the top quark decay products, typically by comparing the data distributions with simulated templates [101, 102]. However, the top quark decay products carry colour and are affected by hadronisation, therefore their final invariant mass is not well defined from the theoretical point of view. The top-quark pole mass has a better physical meaning, it is defined as a real part of the pole in the top quark propagator where all self energy corrections are taken into account. Top-quark pole mass can be experimentally estimated indirectly, e.g. by comparing the top-quark pair cross section to the theoretical predictions [84]. The difference between these two definitions is expected to be of the order of 1 GeV [103].

An overview of the direct LHC top-quark mass measurements can be found in Figure 2.9. Both the current ATLAS combination with $m_{\text{top}} = 173.69 \pm 0.48$ GeV [102] and the CMS combination with $m_{\text{top}} = 172.44 \pm 0.48$ GeV [104] have already significantly smaller total uncertainties than the world average from 2014 with $m_{\text{top}} = 173.34 \pm 0.76$ GeV [105]. The current top-quark pole mass world combination yields 173.2 ± 0.9 GeV [26].

The top-quark mass is related to the mass of the Higgs and the W bosons and precise measurements of these properties provide a stringent test of the SM predictions. An example of an electroweak fit with constraints on the top-quark and W-boson masses from the SM predictions is shown in Figure 2.10 and is discussed in Ref. [106]. So far the direct mass measurements of the top quark, the W boson and the Higgs boson are in good agreement with each other and with the SM predictions.

The question of the vacuum stability [80, 107] is also directly linked to the top-quark and Higgs-boson masses and is among the motivations for precise top-quark

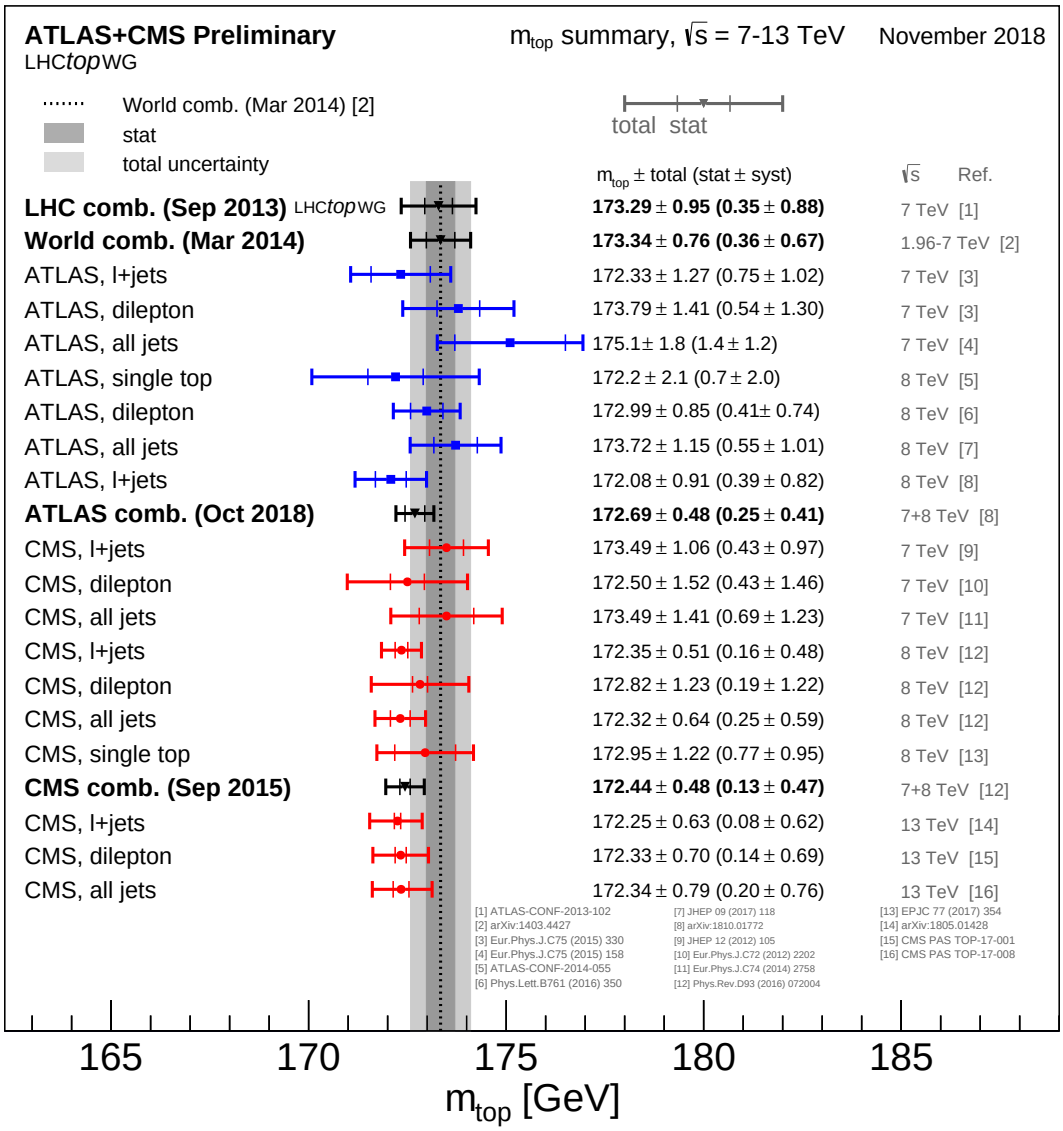

Figure 2.9: Summary of the direct top-quark mass LHC measurements, compared to the world combination [26]. The figure is taken from Ref. [88].

mass measurements. If our vacuum is not in a global energy minimum, there would be a possibility of quantum tunnelling into the global energy minimum, modifying masses of all elementary particles and completely changing the universe.

The current measurements indicate that the universe might be stable or metastable with a lifetime significantly larger than the age of the universe, see Figure 2.11. Nevertheless, BSM physics could completely change the picture [108].

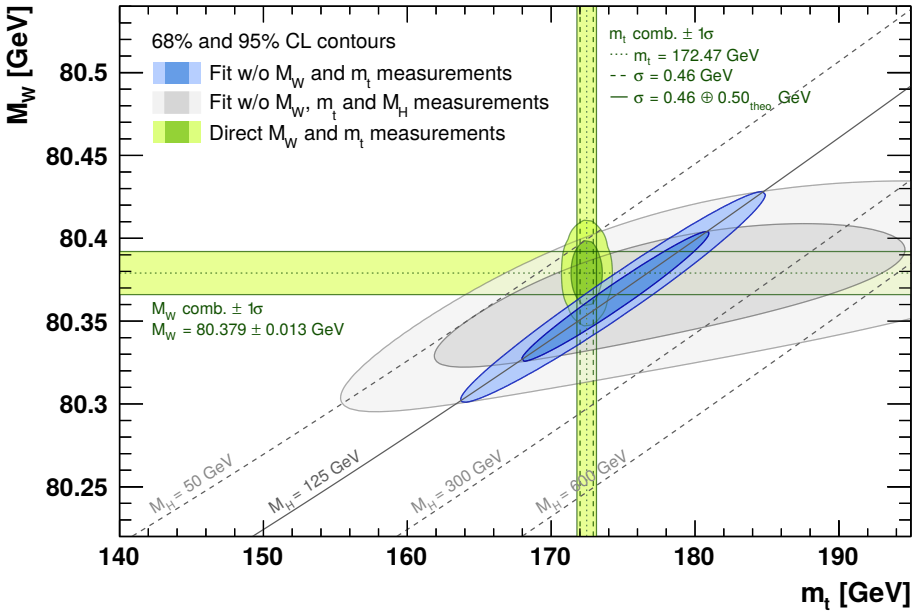

Figure 2.10: Scans of the top-quark mass versus W boson mass for the electroweak fit including and excluding the Higgs boson mass measurement, in blue and grey, respectively. Direct top-quark and W mass measurements are also shown (green). The figure is taken from Ref. [106].

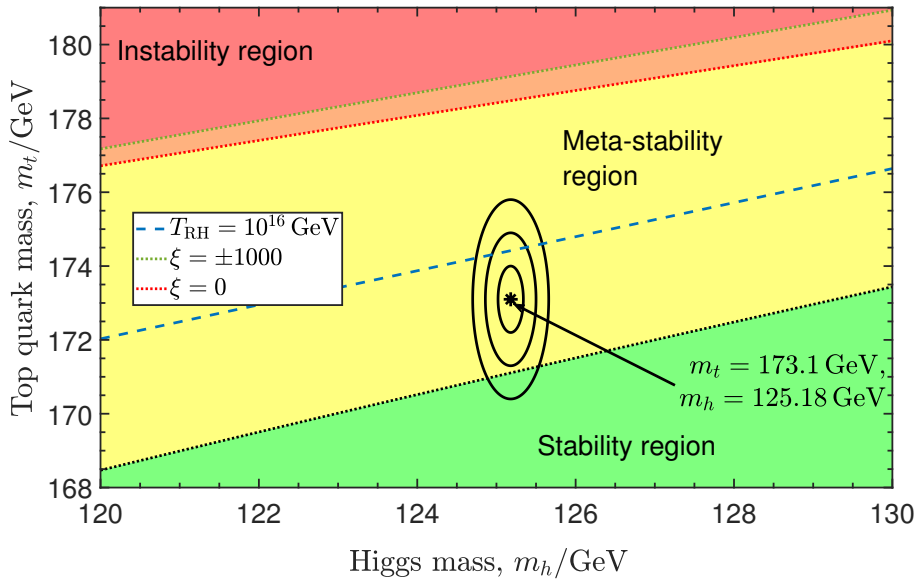

Figure 2.11: Stability diagram of the SM vacuum in the pole masses of the top quark and the Higgs boson. The ellipses correspond to 1, 2 and 3 σ deviations from the values reported in Ref. [26]. The figure is taken from Ref. [107].

2.3.3 Top-Quark Decay Width

The large top-quark mass implies a very short lifetime and a large top-quark decay width $\Gamma_t = 1.32$ GeV [81]. However, if there are new BSM top quark decay channels, the top-quark decay width would differ from the SM prediction. The most precise top-quark decay width measurement carried out by the CMS collaboration achieved $\Gamma_t = 1.36 \pm 0.02(\text{stat.})^{+0.14}_{-0.11}(\text{syst.})$ GeV [109]. However, this was an indirect measurement which used some of the SM predictions. The ATLAS experiment performed a direct measurement using a template fit and obtained $\Gamma_t = 1.76 \pm 0.33(\text{stat.})^{+0.79}_{-0.68}(\text{syst.})$ GeV [110], which is consistent with the SM prediction.

2.3.4 Top-Quark Spin Correlation

The top-quark lifetime is by about two orders of magnitude shorter than the spin decorrelation time [111] and the spin information is transferred directly to the top quark decay products. Experimentally, this can be measured via the angular distributions of the top quark decay products, particularly via the difference in azimuthal angles between the two charged leptons in the dilepton decay channel. The first observation of the correlation in top-quark pair events in 2012 by the ATLAS and CMS experiments [112, 113] was followed by a large effort to measure this property precisely due to its sensitivity to BSM physics. The most recent ATLAS preliminary measurement using 36.1 fb^{-1} of pp collision data at $\sqrt{s} = 13$ TeV deviates from the SM prediction by 3.2 standard deviations [114].

Chapter 3

Top-Quark Charge Asymmetry

The charge asymmetry in heavy quark pair production is a phenomenon predicted by the SM, occurring through higher-order diagrams [115–121]. The charge asymmetry manifests itself through different differential cross sections of the heavy quarks and antiquarks. As a consequence, the probabilities of the final state quarks to be produced in forward/backward directions in the CM frame are not equal. This is illustrated in Figure 3.1 where the final state particles are heavy quarks Q and $\bar{Q}$ and the initial state particles are light quarks q and $\bar{q}$. The forward direction is given by the direction of the incoming light quark q and the backward direction is defined complementary.

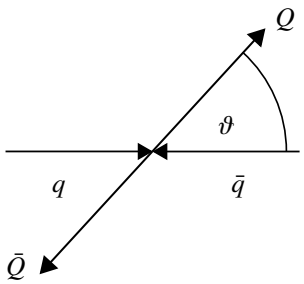

Figure 3.1: Forward heavy quark production, given by the condition $\cos\theta > 0$.

The definition of the asymmetry in the CM frame is then given by the production cross-sections of the heavy quark Q:

$$A = \frac{\sigma(\cos\theta > 0) - \sigma(\cos\theta < 0)}{\sigma(\cos\theta > 0) + \sigma(\cos\theta < 0)}, \tag{3.1}$$

where the angle θ is explained in Figure 3.1.

3.1 Origin of the Charge Asymmetry

There are two main heavy quark production processes at hadron colliders, the gluon fusion $gg \to Q\bar{Q}$ and quark-antiquark annihilation $q\bar{q} \to Q\bar{Q}$. A small contribution is

also due to higher-order flavour excitation, i.e. $q(\bar{q})g \to Q\bar{Q}X$, where X stands for an additional final state particle.

In the case of the $t\bar{t}$ production, at the Tevatron in $p\bar{p}$ collisions the $q\bar{q}$ annihilation was dominating ($\approx$ 85%), followed by the gluon fusion ($\approx$ 15%). At the LHC at $\sqrt{s}$ = 13 TeV it is the other way around, the gluon fusion is largely dominating and only around 10% of the $t\bar{t}$ events are created through $q\bar{q}$ annihilation. A small fraction of about 2% of $t\bar{t}$ events is produced through flavour excitation.

The gluon fusion does not contribute to the charge asymmetry, it is symmetric in all orders of the perturbative QCD theory. The $q\bar{q}$ annihilation is also symmetric in the leading-order (LO). However, if the higher-order diagrams are also taken into account, the top-quark and antitop-quark differential cross sections become different, leading to a non-zero charge asymmetry. The Feynman diagrams which are most important for the charge asymmetry are shown in Figure 3.2.

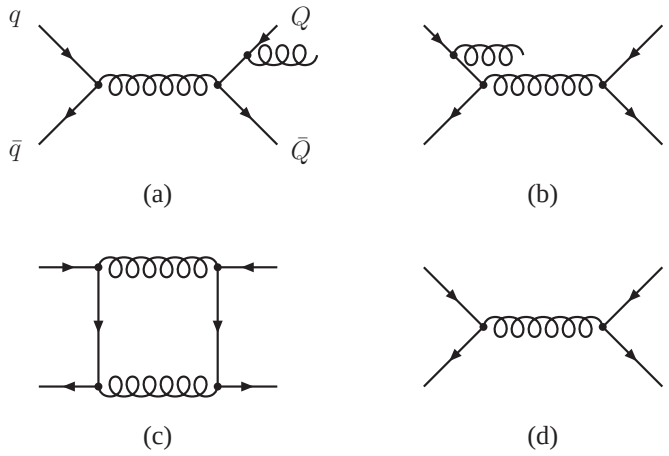

Figure 3.2: Quark-antiquark annihilation Feynman diagrams contributing to the charge asymmetry. The final (a) and initial (b) state radiation, the box (c) and the LO diagram (d).

The interference of the initial and final state radiation leads to a negative contribution to the asymmetry, while the interference of the LO and the box diagrams is dominant and contributes positively. The flavour excitation diagrams shown in Figure 3.3 also slightly affect the asymmetry. Finally, the interference of the $q\bar{q}$ annihilation diagrams with electroweak processes $q\bar{q} \to Z/\gamma^* \to Q\bar{Q}$ contributes positively to the charge asymmetry. The ratio of the electroweak and QCD contributions to the asymmetry is up to 20% in the high $t\bar{t}$ mass region [115, 117, 122]. The energy dependence of the contributions by individual processes is shown in Figure 3.4.

BSM theories can modify the expected asymmetry due to additional diagrams in which a new particle is exchanged, e.g. axigluons [123, 124], heavy Z bosons [125], or coloured Kaluza-Klein gluon excitations [126]. The charge asymmetry measurements can constrain the parameter space of the BSM theories. A significant deviation of the

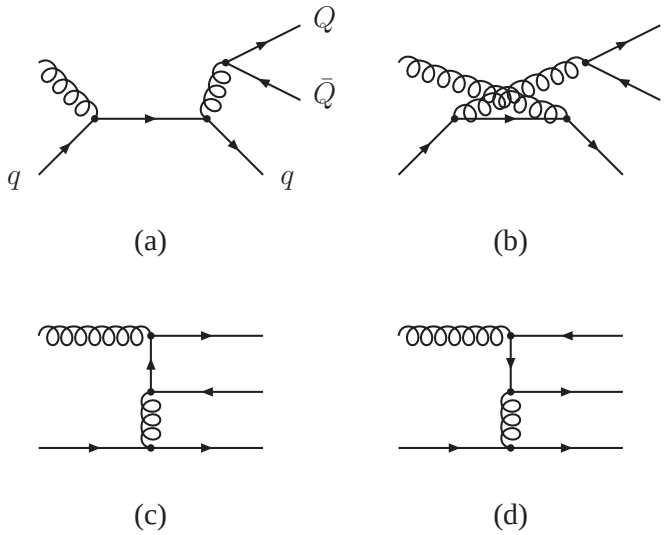

Figure 3.3: Origin of the A_{FB} in heavy quark production through flavour excitation.

measured asymmetry from the SM prediction would be considered as an evidence of BSM physics.

3.2 Charge Asymmetry at Hadron Colliders

Conditions in the hadron colliders do not allow to measure the charge asymmetry using the definition from Equation (3.1). The interacting partons have different longitudinal momenta and the laboratory frame is not identical with the CM frame as it would be in the case of e^+e^- colliders. To describe the top-quark asymmetry at hadron colliders, rapidity y is used instead of the polar angle θ:

$$y = \frac{1}{2} \ln \frac{E + p_z}{E - p_z}, \tag{3.2}$$

where E is the energy of the final state particle and p_z is the longitudinal momentum. It is clear that in the CM system the condition $\cos\theta > 0$ ($\cos\theta < 0$) is the same as $y > 0$ ($y < 0$). Additionally, due to the momentum conservation $y_Q = -y_{\bar{Q}}$ and the rapidity difference

$$\Delta y = y_Q - y_{\bar{Q}} \tag{3.3}$$

is Lorentz invariant under the boosts along the z-axis. As a consequence, a new definition of the charge asymmetry, typically referred to as forward-backward asymmetry A_{FB}, can be defined:

$$A_{\mathrm{FB}}^{Q\bar{Q}} = \frac{N(\Delta y > 0) - N(\Delta y < 0)}{N(\Delta y > 0) + N(\Delta y < 0)}, \tag{3.4}$$

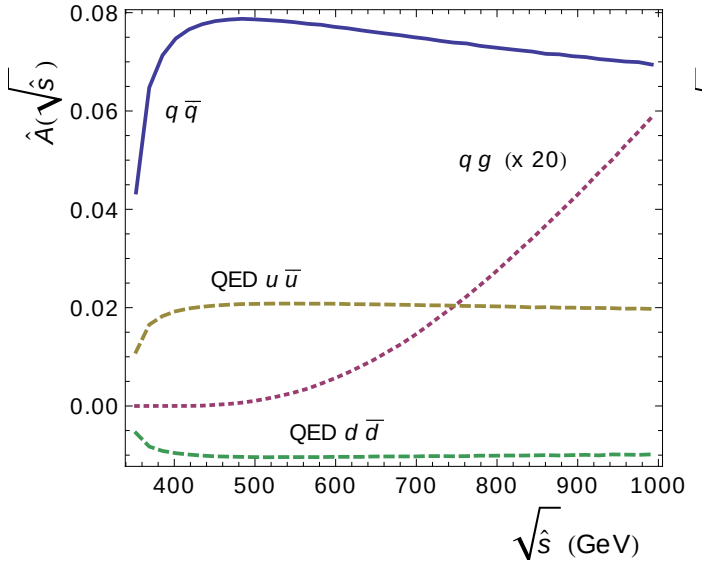

Figure 3.4: Contributions from various processes to the asymmetry defined in (3.1) as a function of the CM energy. The figure is taken from Ref. [122].

which is completely equivalent to the CM system definition (3.1) and can be measured in the laboratory frame.

The definition from Equation (3.4) was largely used in the Tevatron measurements, where the significant direction was given by the direction of the incident (anti)proton. However, in the symmetric LHC pp collisions it is not possible to use this definition, since the direction of the incident (anti)quark is unknown. On the other hand, in pp collisions the antiquarks are always sea quarks, while the quarks are usually valence quarks. Sea quarks typically carry lower momentum fraction than the valence quarks, therefore in the LHC collisions the $q\bar{q}$ system is mostly boosted in the direction of the incident quark, see Figure 3.5. This enables to define a complementary forward-central charge asymmetry A_{C} which can be measured at the LHC:

$$A_{\mathrm{C}}^{Q\bar{Q}} = \frac{N(\Delta|y| > 0) - N(\Delta|y| < 0)}{N(\Delta|y| > 0) + N(\Delta|y| < 0)}, \tag{3.5}$$

where $\Delta|y|$ is given by

$$\Delta|y| = |y_Q| - |y_{\bar{Q}}|. \tag{3.6}$$

Both $A_{\mathrm{FB}}^{Q\bar{Q}}$ and $A_{\mathrm{C}}^{Q\bar{Q}}$ require full reconstruction of the heavy quark four-momenta, which can be challenging in the case of $t\bar{t}$ events. If the top-quark pair decays in the dilepton channel, it is possible to calculate the dilepton asymmetry using only the kinematics of the charged leptons, which typically can be measured very precisely. The dilepton asymmetry in $t\bar{t}$ events is largely correlated with the top-quark asymmetry. Since the electron and muon rest masses are much smaller than their typical energies

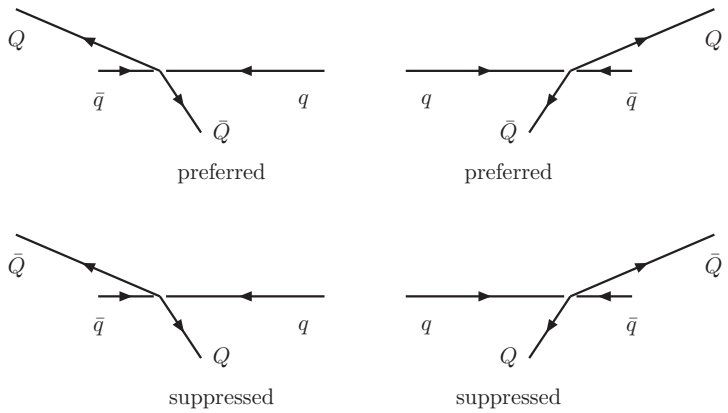

Figure 3.5: Preferred and suppressed configurations at the LHC assuming positive charge asymmetry.

in $t\bar{t}$ events, the rapidity y can be replaced by the pseudorapidity $\eta = -\ln\tan\left(\frac{\theta}{2}\right)$. The forward-backward dilepton asymmetry is then defined as

$$A_{\mathrm{FB}}^{\ell\ell} = \frac{N(\Delta\eta > 0) - N(\Delta\eta < 0)}{N(\Delta\eta > 0) + N(\Delta\eta < 0)}, \tag{3.7}$$

where

$$\Delta\eta = \eta_{\ell^+} - \eta_{\ell^-}. \tag{3.8}$$

Similarly, the dilepton charge asymmetry can be defined as

$$A_{\mathrm{C}}^{\ell\ell} = \frac{N(\Delta|\eta| > 0) - N(\Delta|\eta| < 0)}{N(\Delta|\eta| > 0) + N(\Delta|\eta| < 0)}, \tag{3.9}$$

where

$$\Delta|\eta| = |\eta_{\ell^+}| - |\eta_{\ell^-}|. \tag{3.10}$$

It is also possible to define a single lepton asymmetry using the lepton charge q:

$$A_{\mathrm{FB}}^{\ell} = \frac{N(q \times \eta > 0) - N(q \times \eta < 0)}{N(q \times \eta > 0) + N(q \times \eta < 0)}. \tag{3.11}$$

In the dilepton top quark decay channel, the single lepton asymmetry is largely correlated with the dilepton asymmetry [127, 128]. On the other hand, this definition can be used also in the ℓ+jets decay channel.

This is not a comprehensive list of all possible asymmetries that origin from the single physical phenomenon defined in Equation (3.1), although vast majority of experiments use one of the approaches mentioned above. There are also proposals of a combined top-lepton charge asymmetry or even single lepton charge asymmetry in ℓ+jets events [129]. Different observable is used also in the proposal for the LHCb [130] experiment to measure top-quark charge asymmetry in the very forward region [131].

3.3 Experimental Challenges of the Charge Asymmetry Measurements

At the LHC the main challenge of the A_C measurements is related to the large dilution caused by the gluon fusion $Q\bar{Q}$ production. As a consequence, the expected inclusive A_C is small, around 0.6% in $t\bar{t}$ events from pp collisions at $\sqrt{s} = 13$ TeV [132]. On the other hand, there are several possibilities to enhance it by using various kinematic requirements.

The fraction of $Q\bar{Q}$ pairs created through $q\bar{q}$ annihilation increases with the invariant mass of the $Q\bar{Q}$ pair, therefore higher asymmetries can be observed in the high invariant mass regions. The gluon fusion can be suppressed also by requiring higher longitudinal momentum of the $Q\bar{Q}$ system, since this is typical for the $q\bar{q}$ annihilation where the valence quark typically carries much larger momentum fraction than the antiquark from the proton sea. Another interesting possibility is to require a limit on the maximum transverse momentum of the $Q\bar{Q}$ pair system, which suppresses events where the gluon emission in the initial or final state created an additional jet. The contribution from the interference of the initial and final state radiation to the top-quark asymmetry is negative, therefore this requirement significantly enhances the asymmetry [122].

In the case of the $b\bar{b}$ events, the asymmetry can be calculated directly using Equation (3.5), assuming that it is possible to identify which jet was initiated by the b ($\bar{b}$) quark. When using $t\bar{t}$ events, it is necessary to reconstruct both top quarks from their decay products. In the case of high $t\bar{t}$ invariant mass the top quarks must be reconstructed in the boosted topology, discussed in Section 2.2. The top (antitop) quark is typically identified by the charge of the isolated lepton from the $t\bar{t}$ decay, unless it is a measurement in the all-hadronic channel. In that case some modification of the jet charge technique [133] can be used.

A more detailed discussion of the top-quark asymmetry measurements at hadron collider experiments can be found in Refs. [122, 134].

3.4 Previous Top-Quark Asymmetry Measurements

3.4.1 Tevatron A_{FB} Measurements

The forward-backward asymmetry in the top-quark pair production has been extensively studied by the CDF and DØ experiments at the Tevatron collider. The large fraction of $q\bar{q}$ annihilation, as well as the fact that protons were collided with antiprotons, made the Tevatron an ideal environment for the A_{FB} measurements. First results by both experiments in the ℓ+jets channel using 5 fb^{-1} of $p\bar{p}$ data at $\sqrt{s} = 1.96$ TeV [135, 136] measured an asymmetry inconsistent with the then-existing

SM predictions [137] by more than 3 standard deviations. These measurements brought a large attention to the problematic of the top-quark asymmetry and were followed by a large effort to deeper understand this subject from both the theoretical and experimental point of view.

Subsequent A_{FB} Tevatron measurements benefited from the full Run II $p\bar{p}$ dataset and refined analysis techniques were used to minimise the total uncertainty. The asymmetry was studied by both CDF and DØ experiments in the ℓ+jets and dilepton decay channels and different observables and definitions of the asymmetry were investigated. The $A_{\mathrm{FB}}^{t\bar{t}}$ measurements are reported in Refs. [138–141], the A_{FB}^{ℓ} observable measurements can be found in Refs. [127, 128, 142, 143] and the dilepton asymmetry $A_{\mathrm{FB}}^{\ell\ell}$ measurements are reported in Refs. [127, 128].

At the same time there was a significant improvement in the theoretical understanding of the A_{FB}. Recent calculations [119–121] include NNLO and even approximate N^{3}LO QCD corrections, as well as the NLO electroweak contribution. These corrections are larger than previously expected and almost double the previous inclusive prediction at NLO in QCD. As a consequence, the CDF and DØ measurements are now consistent with the current SM predictions.

The final Tevatron A_{FB} combination is presented in Ref. [144] and an overview of all Tevatron top-quark inclusive asymmetry measurements including the theoretical predictions is shown in Figure 3.6. The Tevatron combination of mass-dependent $A_{\mathrm{FB}}^{t\bar{t}}$ measurements is shown in Figure 3.7. At the Tevatron, the precision of the A_{FB} measurements was limited by the statistical uncertainties.

3.4.2 LHC A_{C} Measurements

The LHC experiments benefit from an unprecedented amount of top quark events and due to larger collision energy they can study kinematic regions which were not accessible at the Tevatron. On the other hand, the top-quark asymmetry measurements are much more challenging than at the Tevatron, as discussed in Section 3.3. The higher the collision energy, the larger is the fraction of top-quark pair production via gluon fusion which dilutes the top-quark asymmetry.

The ATLAS and CMS experiments at the Large Hadron Collider (LHC) have performed inclusive and differential measurements of the top-quark charge asymmetry in Run 1 at $\sqrt{s} = 7$ TeV and $\sqrt{s} = 8$ TeV. Both experiments focused on the ℓ+jets and dilepton channels.

Using the $\sqrt{s} = 7$ TeV pp collision data the $A_{\mathrm{C}}^{t\bar{t}}$ was measured in the ℓ+jets channel [145, 146] and the dependencies of the asymmetry on the $t\bar{t}$ mass, transverse momentum p_{T}, boost along the z-axis β_z and the absolute value of the rapidity of the top-quark pair system $|y|$ were also studied. In the dilepton channel both $A_{\mathrm{C}}^{t\bar{t}}$ and $A_{\mathrm{C}}^{\ell\ell}$

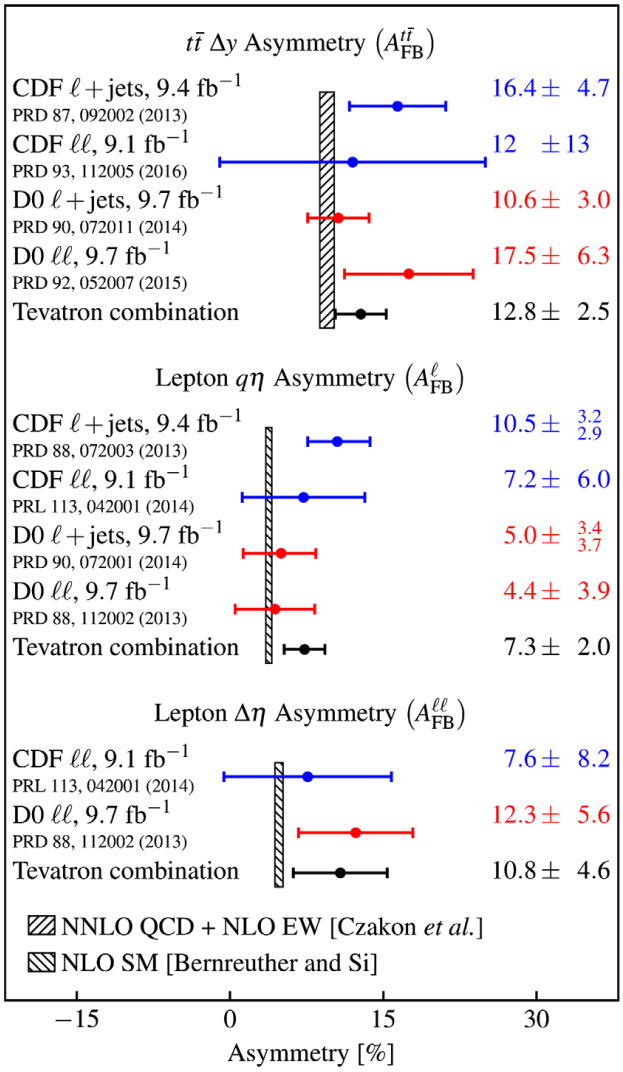

Figure 3.6: Summary of the Tevatron top-quark asymmetry measurements [127,128,138–143]. The figure is taken from Ref. [144].

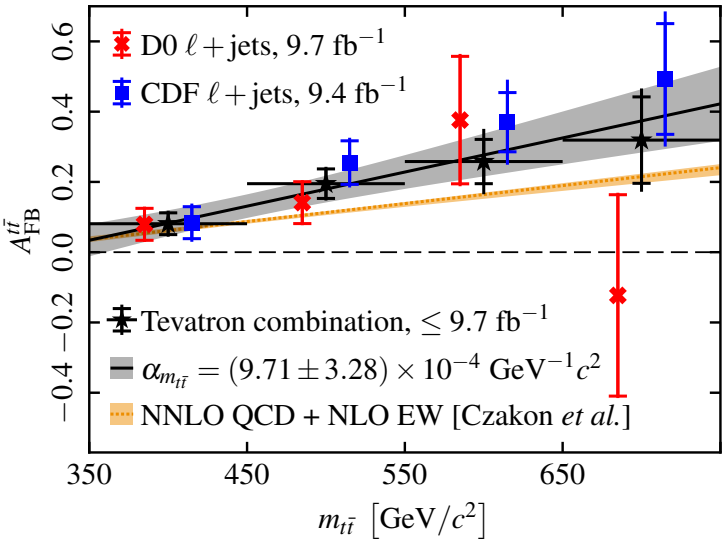

Figure 3.7: Combined CDF+DØ forward-backward asymmetry as a function of the $t\bar{t}$ mass in comparison with the SM theoretical prediction. The figure is taken from Ref. [144].

were measured by both experiments [147, 148]. An overview of the top-quark asymmetry measurements at $\sqrt{s} = 7$ including the combination of the ATLAS and CMS results [149] is shown in Figure 3.8.

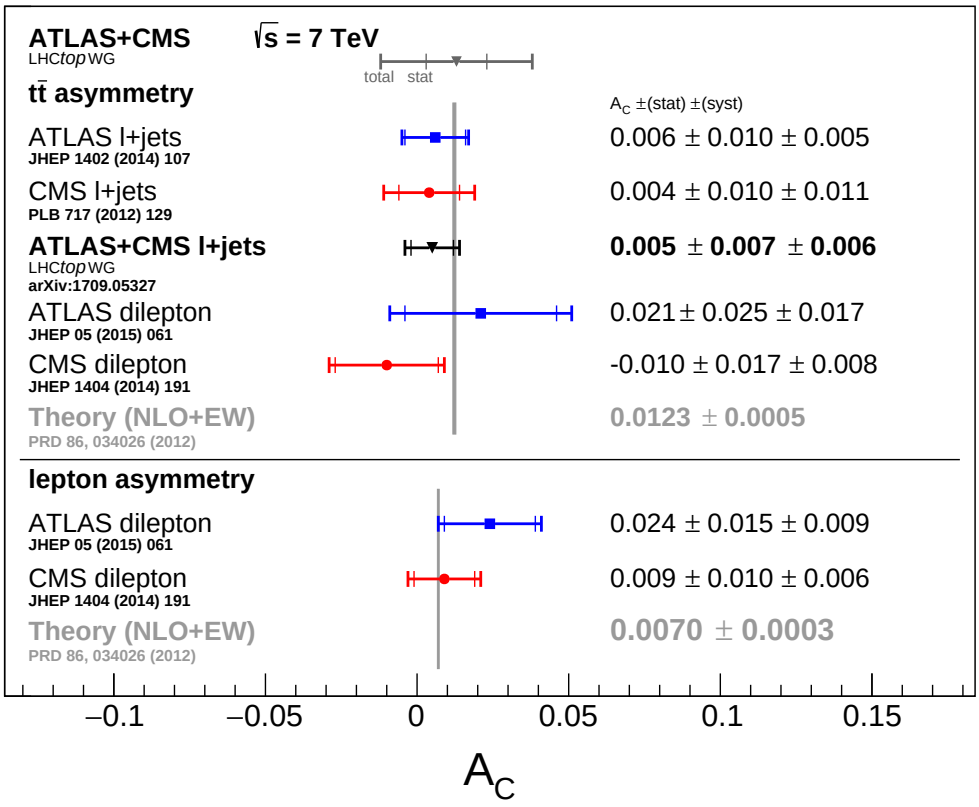

Figure 3.8: Summary of the top-quark inclusive charge asymmetry measurements by the ATLAS and CMS experiments using $\sqrt{s} = 7$ TeV pp collision data [145–149]. The figure is taken from Ref. [88].

The $\sqrt{s} = 8$ TeV charge asymmetry measurements were performed in the ℓ+jets channel [150, 151] and in the dilepton channel [152, 153]. In all cases also differential measurements were carried out, mostly as a function of the top-quark pair mass, p_{T}, β_z and $|y|$. In the dilepton channel also the dilepton charge asymmetry was calculated. ATLAS additionally performed a fiducial ($|\Delta|y|| < 2$ and $m(t\bar{t}) > 750$ GeV) measurement in the ℓ+jets channel in the boosted regime [154] and CMS performed a measurement in the ℓ+jets channel using a template method [155]. An overview of the top-quark asymmetry measurements at $\sqrt{s} = 8$ TeV including the combination of the ATLAS and CMS results [149] is shown in Figure 3.9. A combination of differential $A_{\mathrm{C}}^{t\bar{t}}$ measurements as a function of $t\bar{t}$ mass is presented in Figure 3.10

All of the ATLAS and CMS charge asymmetry measurements are consistent with the SM predictions. Despite the unprecedented amount of top-quark pairs the total uncertainties are mostly dominated by the statistical uncertainties. Nevertheless, even with limited precision the LHC Run 1 top-quark asymmetry measurements constrain

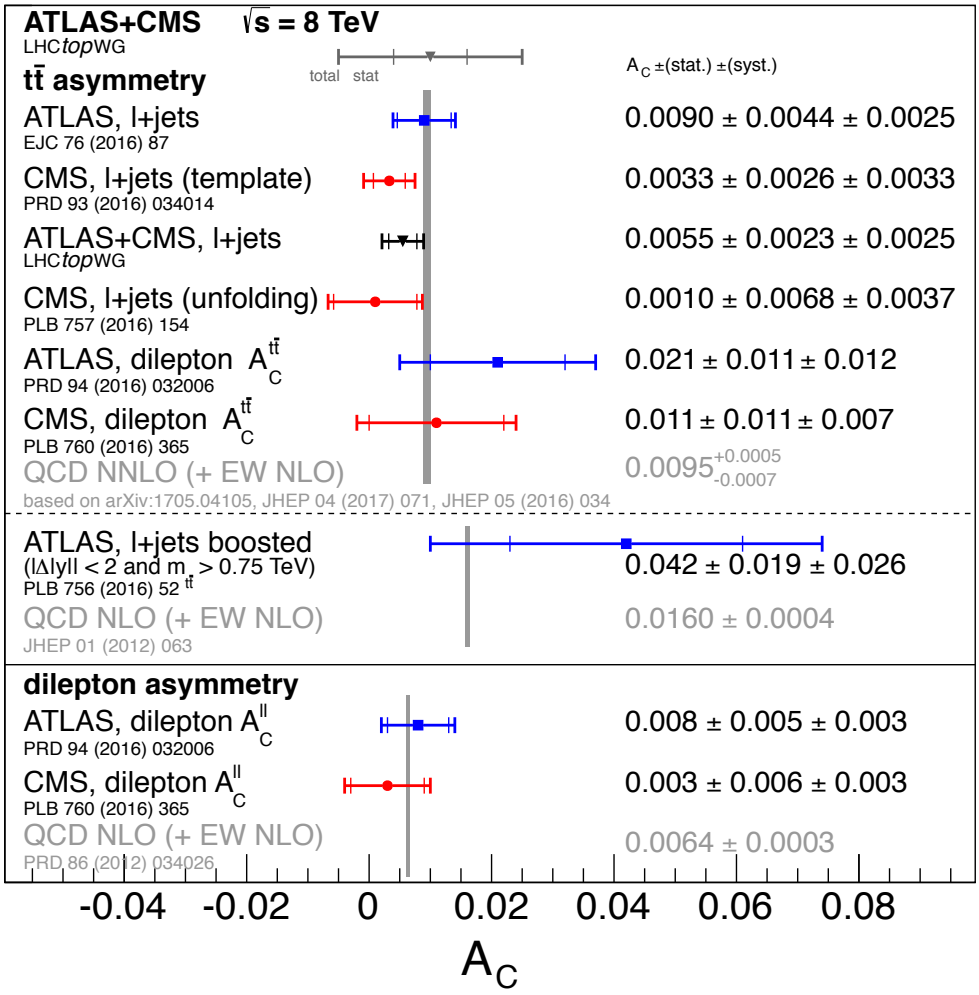

Figure 3.9: Summary of the top-quark inclusive charge asymmetry measurements by the ATLAS and CMS experiments using $\sqrt{s} = 8$ TeV pp collision data [149–155]. The figure is taken from Ref. [88].

parameter space of several BSM scenarios as shown in Figure 3.11.

In the LHC Run 2 at $\sqrt{s} = 13$ TeV there is currently only one measurement of the top-quark charge and dilepton asymmetries with 35.9 fb^{-1} of pp collision data as a part of the top-quark differential cross section measurement in the dilepton decay channel by the CMS experiment [157]. The measured asymmetries are found to be consistent with the SM predictions.

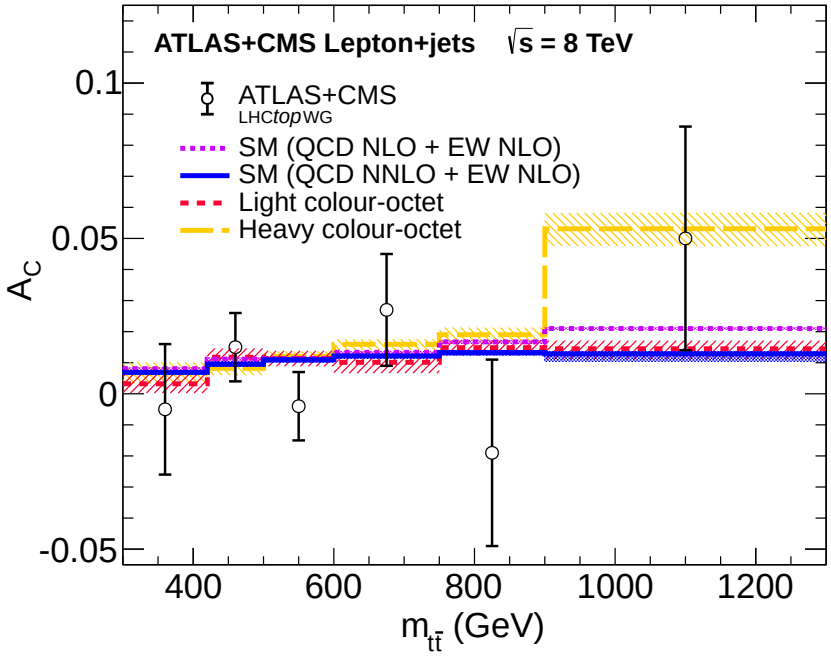

Figure 3.10: Combined ATLAS+CMS charge asymmetry as a function of the $t\bar{t}$ mass in comparison with the SM theoretical predictions and two versions of a colour-octet model [156]. The figure is taken from Ref. [149].

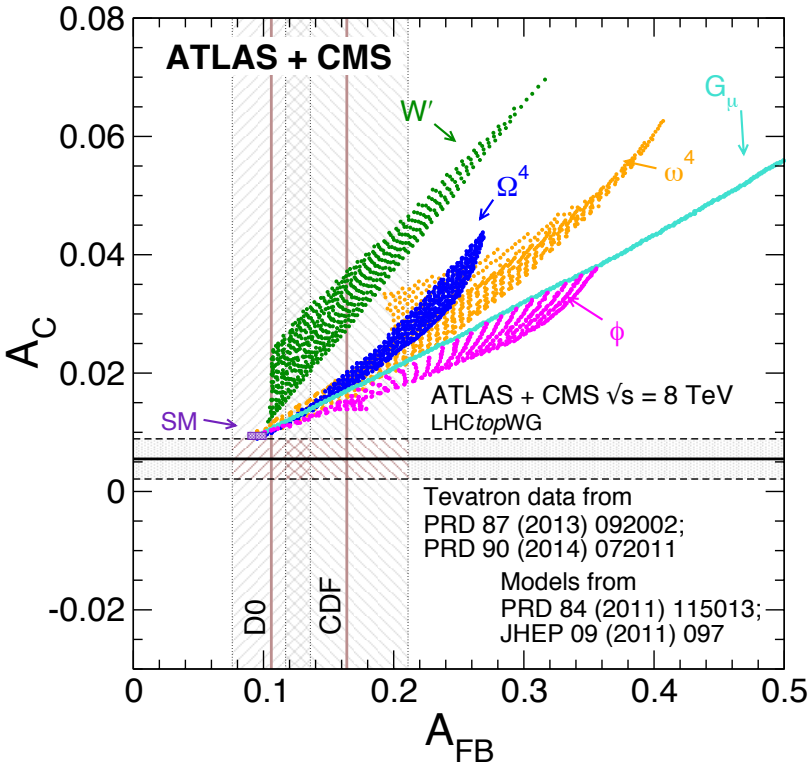

Figure 3.11: Measured inclusive charge asymmetry A_{C} at the LHC at $\sqrt{s} = 8$ TeV (horizontal line) versus forward-backward asymmetries A_{FB} (vertical lines) at the Tevatron, compared with the SM prediction and with predictions incorporating various potential BSM contributions. The figure is taken from Ref. [149].

3.5 Asymmetry in $b\bar{b}$ and $c\bar{c}$ Pair Production

Analogously to the asymmetry in $t\bar{t}$ events one can define forward-backward and charge asymmetry in bottom or charm quark pair production. In the SM the sources of the asymmetries are similar in all cases, but at the same time these processes are complementary and their sensitivity to the BSM physics might be different.

Forward-backward asymmetry in these events has been largely studied already at the SLAC and LEP colliders, especially at the Z boson pole in order to measure precisely the effective weak mixing angle $\sin^2\theta_W$ [55]. After interesting results in the top-quark asymmetry the CDF experiment at the Tevatron conducted A_{FB} measurements in $b\bar{b}$ production [158, 159] and excluded a 200 GeV axigluon model. The DØ experiment measured A_{FB} in $B^{\pm}$ mesons [160] and $\Lambda_b^0(\bar{\Lambda}_b^0)$ baryons [161]. These measurements were discussed in Ref. [162] and no significant deviation from the SM has been found.

Charge asymmetry in bottom and charm quark pair production is very challenging at the LHC. The fraction of gluon fusion is even larger than in the case of $t\bar{t}$ events and it is difficult to separate these processes from background events. So far only LHCb, experiment dedicated to b physics, measured charge asymmetry in $b\bar{b}$ events [163]. This result is found to be in agreement with the SM prediction.

Chapter 4

The LHC and the ATLAS Experiment

The ATLAS (A Toroidal LHC ApparatuS) experiment [61, 164] is one of the four main particle physics experiments located at the Large Hadron Collider (LHC) [165, 166] at CERN in Geneva, Switzerland. The ATLAS collaboration which built and now runs the detector was formed in 1992. In 2019 more than 3000 physicists and engineers from about 181 institutions in 38 countries were involved.

4.1 The Large Hadron Collider

The LHC is currently the world's largest and most powerful particle accelerator located at CERN in the 27 km long circular underground tunnel on the France-Switzerland border near Geneva. It has been designed to collide two opposing particle beams of either protons with maximum collision energy of $\sqrt{s} = 14$ TeV or heavy ions with $\sqrt{s} = 2.8$ TeV per nucleon. The designed maximum instantaneous luminosity of the LHC is 10^{-34} cm^{-2}s^{-1}. These unprecedented parameters were chosen in order to maximise the possibility of discovering rare processes such as the Higgs boson production and potential BSM physics, as well as to deliver large number of events for precision measurements.

Bunches of particles interact at four interaction points along the collider which correspond to the positions of the four main particle detectors (experiments): ATLAS, CMS [62], ALICE [167] and LHCb [130]. ATLAS and CMS are both designed as multipurpose detectors aiming for high-luminosity precision measurements. Although their goal is the same, both are designed and operated by independent collaborations which provides an important possibility of having independent and cross-checking measurements. The ALICE experiment is optimised to study QCD physics in lead-lead ion collisions, e.g. properties of the quark-gluon plasma. LHCb is an experiment dedicated to B-physics and precise CP-violation measurements. Three smaller experiments are also located in the LHC tunnel: TOTEM [168], LHCf [169] and MoEDAL [170]. The TOTEM and LHCf experiments are focusing on forward physics and are located close

to the beampipe on either side of CMS and ATLAS, respectively. MoEDAL is located near LHCb and is searching for hypothetical magnetic monopoles [171].

4.1.1 Acceleration Process

A whole set of accelerators (Figure 4.1) is involved in the LHC acceleration process. Protons are obtained from molecular hydrogen by breaking the molecules into individual atoms and stripping the electrons. Afterwards they are passed into the linear accelerator LINAC2 [172] and a small circular accelerator Proton Synchrotron Booster (PSB) [173] which has four separate rings. In each ring one bunch of approximately 10^{11} protons is accelerated by electric fields until it reaches energy 1.4 GeV per proton, while bending magnets are used to keep the beam on the circular trajectory. Bunches are then sent into the Proton Synchrotron (PS) [174] and Super Proton Synchrotron (SPS) [175] with circumference of 628 m and 7 km, respectively. In the PS energy of 25 GeV per proton is reached and in SPS it is 450 GeV per proton.

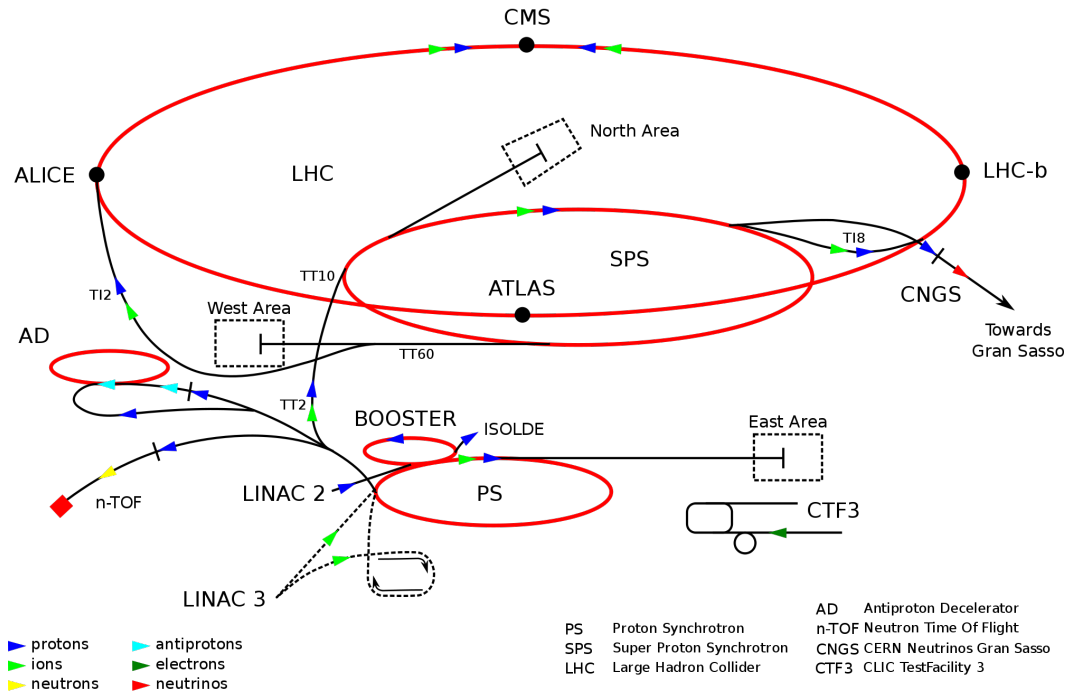

Figure 4.1: CERN accelerator complex.

After acceleration in the SPS the proton bunches are injected into the LHC, half of them in one beampipe and half in the second one, running in the opposite direction. Maximum of 2808 bunches with nominal bunch spacing of 25 ns can be injected into each of the two proton beams. Unlike the SPS and smaller accelerators, the LHC has superconducting niobium-titanium magnets with a magnetic field of 8.3 T (Figure 4.2). Together 1232 dipole magnets are used for bending the beam and another hundreds of quadrupole, sextupole and octupole magnets are used to focus the beam. Huge

cryogenic system with 700 m^3 of liquid helium is needed to cool down the magnets to the superconducting temperature of 1.9 K. The cryogenic system must deal with heat load from synchrotron radiation, beam induced wall currents, electron cloud accompanying the beam and unavoidable beam losses. Increased temperature can lead to loss of superconductivity (so-called *quench*) and, due to the further heating of the liquid helium, this can severe damage both the magnet and the cryogenic system. To avoid this, a quench protection system [176] is installed, which is in emergency responsible for bringing the superconductive elements to zero current safely.

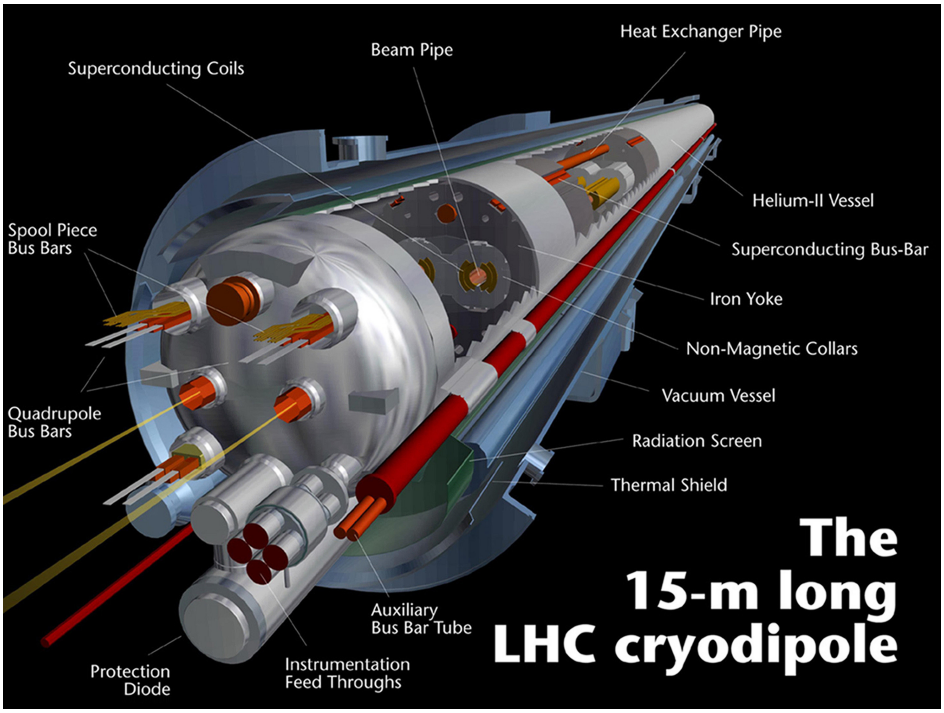

Figure 4.2: The computer-generated cut-away view of the LHC dipole magnet including the vacuum vessel with insulation and cryogenic system. © CERN.

When the accelerated particles reach the final energy, magnets near the interaction points modify the trajectories of the opposing beams so that they cross and start to collide. Typically tens of protons collide per each bunch crossing, while most of them do not interact at all and they continue to circulate for several hours, until the luminosity of the bunches becomes too small. The rest of the beam is deflected by a fast kicker magnet into the beam dump tunnel, where it is diluted and absorbed in a well shielded graphite beam dump block. This happens also every time when the beam becomes unstable and potentially dangerous. Typically, the whole run from LHC filling to beam dump is repeated from one to several times in 24 hours.

4.1.2 Operation and Performance of the LHC

The early operation tests of the LHC were largely affected by an accident which occurred on September 8th, 2008 [177]. Faulty electrical connection between magnets was identified as a main problem and caused an electric arc that damaged the cryogenic system. Several tons of helium escaped explosively and caused a damage of 53 LHC magnets. This incident delayed the LHC physics programme by more than one year.

First proton-proton collisions took place in November 2009. The first period of LHC physics research program, the Run 1, started in 2010, when around 45 pb^{-1} of pp data at $\sqrt{s} = 7$ TeV has been delivered to the experiments and first runs with lead ions were also carried out. In 2011 the integrated luminosity increased by two orders of magnitude to around 5.5 fb^{-1} at 7 TeV. In 2012 the collision energy was increased to 8 TeV and with around 23 fb^{-1} of pp data the LHC successfully completed the Run 1. The main success of the Run 1 was the Higgs boson discovery, which was firstly announced on July 4th, 2012 by both the ATLAS and CMS experiments [63, 64].

During 2013 and 2014 a first long shutdown (LS1) took place at the LHC. A whole series of renovation was carried out on both the accelerator chain and the experiments in order to reach higher collision energy and luminosity. These included also the consolidation of the interconnections between the LHC magnets which caused the accident in 2008.

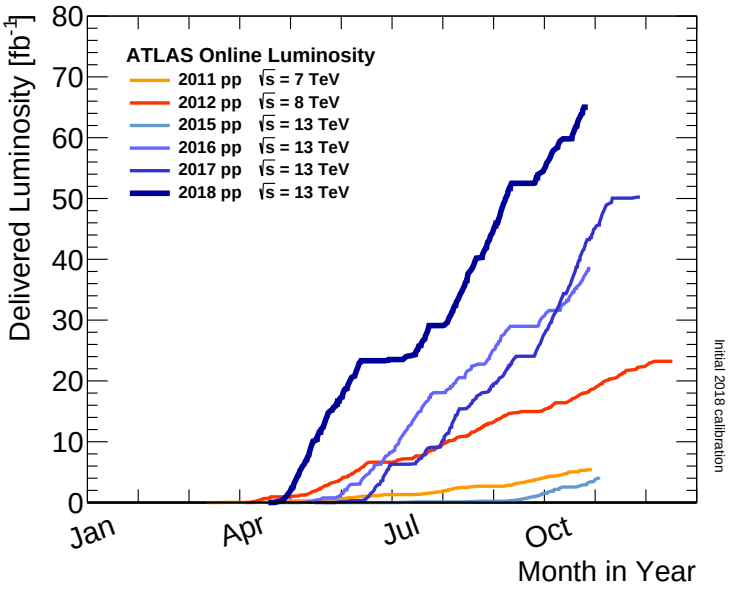

Figure 4.3: The integrated luminosity delivered to the ATLAS experiment by the LHC (pp data only). The end of the year is typically dedicated to ion collisions and during the winter there is a year end technical shutdown. The improving performance of the LHC is apparent from the increase in energy and luminosity over the years. The figure is taken from Ref. [178].

The Run 2 has begun in 2015 when the LHC started to collide protons at a record high 13 TeV collision energy. In overall, around 4 fb^{-1} of pp data has been collected in 2015 and around 40 fb^{-1}, 50 fb^{-1} and 65 fb^{-1} in 2016, 2017 and 2018, respectively (Figure 4.3). This is an unprecedented amount of data which provides a great opportunity to make precision measurements and search for BSM physics. At the end of 2018, just before the second long shutdown (LS2), around 155 fb^{-1} of 13 TeV pp data was delivered to the experiments. This is more than previously expected, thanks to the very good overall performance of the LHC. The maximum instantaneous luminosity in 2017 and 2018 was already two times higher than the designed value of 10^{-34} $\text{cm}^{-2}\text{s}^{-1}$.

No new data will be delivered until the Run 3 will start in 2021 with record-breaking 14 TeV collision energy.

4.2 ATLAS Detector

4.2.1 Physics Requirements and Detector Overview

The ATLAS detector [61, 164] is a multipurpose particle physics device operating at one of the beam interaction points of the LHC. Together with the CMS experiment the ATLAS is aiming for high-luminosity precision measurements and searches for a whole scale of BSM particles. High acceptance, precise particle identification and high energy and momentum resolution are among the basic physics requirements for the ATLAS construction. Additionally, radiation hardness of the ATLAS components is a necessity and the electronics must be fast enough to cope with huge amount of data and pile-up[1] from background collisions.

ATLAS has a cylindrical shape with length of 44 m, diameter of 25 m and axis identical with the beamline. The experiment covers almost an entire solid angle around the nominal interaction point in the centre and is forward-backward symmetric. It consists of several layers of detectors (Figure 4.4), concentrically disposed around the beampipe forming the ATLAS barrel. Perpendicularly to the barrel detectors there are so-called end-caps, enclosing the experiment from both sides. The total assembly weight of all ATLAS components is around 7000 tons.

According to their function the detector components can be divided into several major parts: the Inner Detector (ID), the Calorimeters, the Muon Spectrometer (MS) and the Magnet System. Additionally, ATLAS is equipped with powerful Trigger System used for online event selection and background rejection.

In ATLAS detector a right-handed Cartesian coordinate system is used with the origin at the nominal interaction point. The z-axis is identical with the LHC beamline, the x-axis points towards centre of the LHC ring and the y-axis points upward. Pseu-

[1] Typically, tens of protons collide per bunch crossing and usually only one collision is interesting from the experimental point of view. The rest is referred to as pile-up.

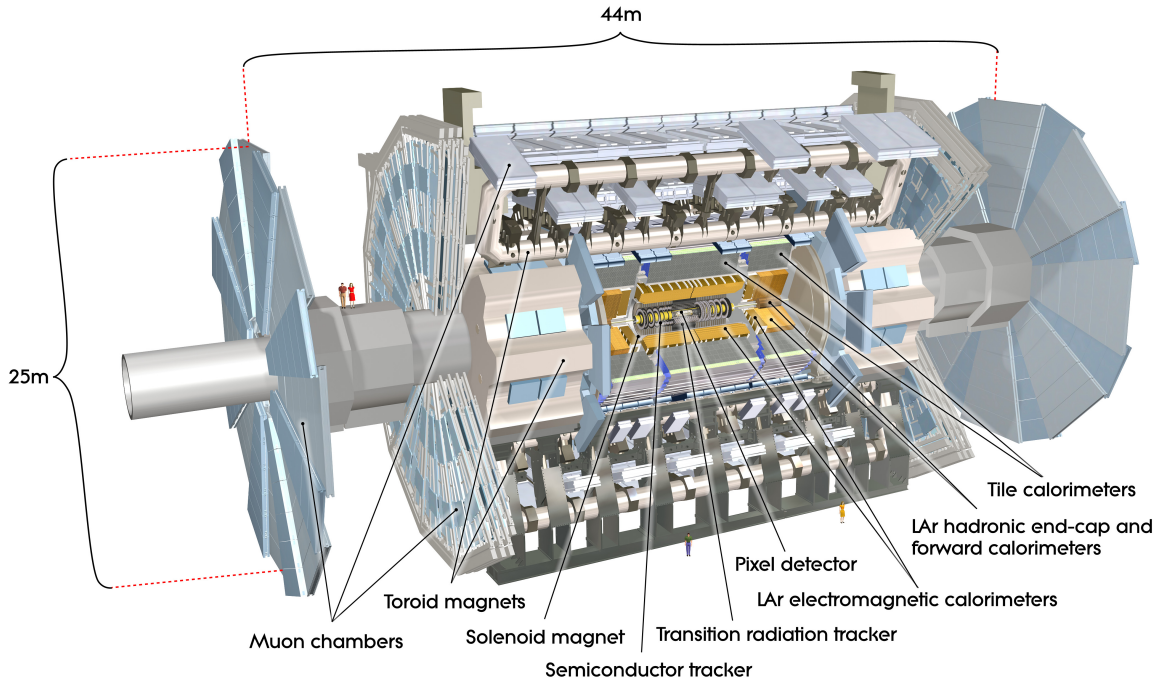

Figure 4.4: The computer-generated cut-away view of the ATLAS experiment. © CERN.

dorapidity η is defined as $\eta = -\ln(\tan(\theta/2))$, where the polar angle θ is measured with respect to the beam axis. Azimuthal angle ϕ is measured with respect to the x-axis with positive (negative) values corresponding to the top (bottom) part of the detector. Distance in the pseudorapidity-azimuthal space is defined as $\Delta R = \sqrt{\eta^2 + \phi^2}$.

4.2.2 Inner Detector

The basic function of the ID [179] is to precisely track charged particles produced in collisions at the interaction point. A computer generated image of the ID is presented in Figure 4.5. The ID starts right next to the beampipe and extends to the radius of approximately 1.1 m, with length of 6.2 m. The whole ID is placed inside of a thin superconducting solenoid magnet, which provides nearly uniform 2 T magnetic field. From the observed curvature of the charged particles it is possible to estimate the electric charge and momentum of particles. The designed momentum resolution in the plane perpendicular to the beam axis is given by formula:

$$\frac{\sigma_{p_\mathrm{T}}}{p_\mathrm{T}} = 0.05\% \times p_\mathrm{T} \oplus 1\%, \tag{4.1}$$

with p_T in GeV. The ID covers the pseudorapidity range $|\eta| < 2.5$ and it consists of three main parts: the Pixel Tracker, the Semiconductor Tracker (SCT) and the Transition Radiation Tracker (TRT).

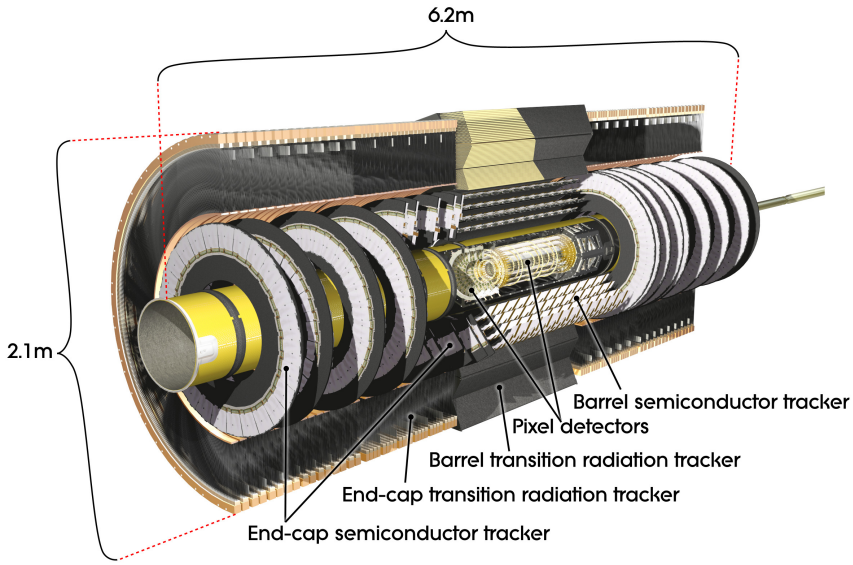

Figure 4.5: The cut-away view of the ATLAS inner detector. © CERN.

Pixel Tracker. The innermost part of the ID consists of three layers of silicon pixel detectors. They are designed to withstand huge radiation near the interaction point, while they must perform extremely precise tracking. The smallest unit that can be read out is the pixel with size of 50 by 400 µm. Additionally, during the LS1 a new beampipe with smaller radius was mounted and a 4-th layer of pixel detectors, the Insertable B-Layer (IBL) [180], was inserted inside the existing pixel tracker. The IBL has even smaller pixels (50 by 250 µm) and it was designed to improve track reconstruction at 13 TeV energy and higher luminosity. The whole pixel detector has more than 80 million readout channels, which is about 50% of the total readout channels of the whole experiment.

Semiconductor Tracker. The microstrip SCT is the middle component of the ID. It works on similar principles as the pixel detector, but it has long narrow strips rather than pixels and covers much larger area. Each strip measures 80 µm by 6-12 cm. There are four double layers of these strips in the barrel while the end-caps have a few more. The SCT readout has over 6 million channels.

Transition Radiation Tracker. The TRT is the outer component of the ID. It is a combination of a so-called *straw* detector and a transition radiation detector. The detecting elements are drift tubes (straws), each four millimetres in diameter and up to 1.5 m long. A thin wire passes through the straw axis and there is a voltage difference of 1500 V between the straws and the wires. When a charged particle passes, it ionises the xenon gas mixture inside the straw. The produced electrons are collected on the anode wire, generating the current pulse (signal) on the wire.

Additionally, materials with highly varying refraction indices between the straws cause ultra-relativistic charged particles to produce transition radiation [40] and leave much stronger signals in some of the straws. This process is typical for very light particles like electrons and positrons, therefore very strong signals in the straws might be used for their identification. The TRT has over 300 thousands of straws and spatial resolution of around 200 µm.

4.2.3 Calorimeters

The calorimeter system (Figure 4.6) surrounds the solenoid magnet and the ID. The main purpose of the calorimeters is to measure the particle energies by absorbing them. The ATLAS experiment uses sampling calorimeters, which consist of several layers of high-density absorbent material. Between these layers the energy of the particle shower is sampled which makes possible to infer the energy of the original particle. The calorimeter system covers the pseudorapidity range $|\eta| \leq 4.9$ and consists of two main parts: the inner Liquid Argon Calorimeter (LAr) and the outer Tile Calorimeter (TileCal).

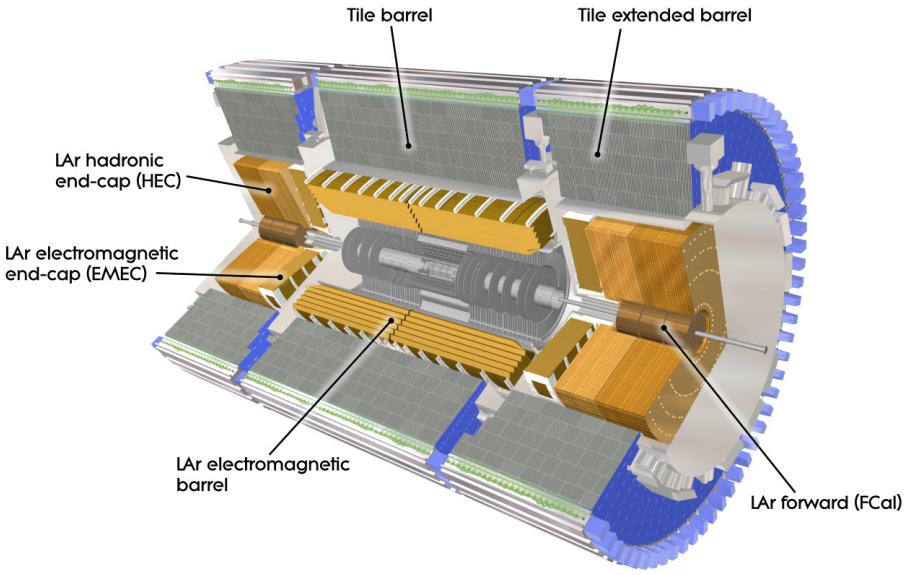

Figure 4.6: The cut-away view of the ATLAS calorimeter system. © CERN.

Liquid Argon Calorimeter. The LAr [181] has three main parts: the Electromagnetic Calorimeter (ECal), the Hadronic End-Cap (HEC) and the Forward Calorimeter (FCal). The main function of the ECal is to completely absorb photons, electrons and positrons and measure their energies[2]. The ECal consists of several accordion shaped

[2]Hadrons also deposit some energy in ECal but in general they are not absorbed there.

layers of lead absorbers with liquid argon as a sampling material. The electromagnetic shower ionises atoms in liquid argon and the collected electrons produce a signal. Signals from different layers are used to estimate the energy of the original particles. Liquid argon was chosen due to the fast drift of the charged particles and radiation hardness. To keep it in liquid form the whole LAr is placed inside of a cryostat which cools it down to -185 °C. The ECal has a detailed segmentation $\Delta\eta \times \Delta\phi = 0.025 \times 0.025$ which provides very good spatial resolution. The target energy resolution of the ECal is given by the formula

$$\frac{\sigma_E}{E} = \frac{0.1}{\sqrt{E}} \oplus 0.007 \oplus \frac{0.17}{E}, \tag{4.2}$$

with energy E in GeV.

The HEC is a part of the Hadronic Calorimeter (HCal), which is composed of the HEC, FCal and the Tile Calorimeter. The main function of the HEC is to measure the energy of quarks and hadrons by absorbing the hadronic showers (jets) in the forward region $1.5 < |\eta| < 3.2$. Geometry differs from the ECal and copper is used instead of lead to absorb the hadronic shower.

The FCal is used to measure jets and missing E_{T} in the very forward region $3.1 < |\eta| < 4.9$ and completes the almost full solid angle calorimeter coverage. Copper and tungsten are used as absorbers in this very high radiation environment.

Tile Calorimeter. The TileCal [182] spans the central pseudorapidity region $|\eta| < 1.7$ and forms the main part of the HCal. The TileCal consists of a central part and two "extended barrels". Steel layers are used as an absorbent material and plastic scintillating tiles are used for energy sampling. The amount of light produced in scintillators is a measure of the hadron shower energy.

The TileCal has 8 m in diameter and total length of 12 m, but it is much less precise than the ECal, with segmentation only around $\Delta\eta \times \Delta\phi = 0.1 \times 0.1$. The energy resolution is also worse:

$$\frac{\sigma_E}{E} = \frac{0.5}{\sqrt{E}} \oplus 0.03, \tag{4.3}$$

with energy E in GeV.

4.2.4 Muon Spectrometer

Muons are the only particles (except neutrinos) which in general are not absorbed in the calorimeters[3]. A large Muon Spectrometer system (Figure 4.7) [183] is used to precisely measure the muon momentum, independently from the inner detector momentum measurements. The MS is placed in a toroidal magnetic field which ensures

[3]Muons with low momentum ($p_{\mathrm{T}} < 5$ GeV) might be completely absorbed in the calorimeters.

an almost homogeneous transverse momentum resolution across the pseudorapidity range. The target transverse momentum resolution varies from 3% at 100 GeV up to 10% at $p_{\mathrm{T}} = 1$ TeV. The MS covers the pseudorapidity range $|\eta| < 2.7$ and consists of four main parts: the Monitored Drift Tubes (MDT), the Cathode Strip Chambers (CSC), the Resistive Plate Chambers (RPC) and the Thin Gap Chambers (TGC).

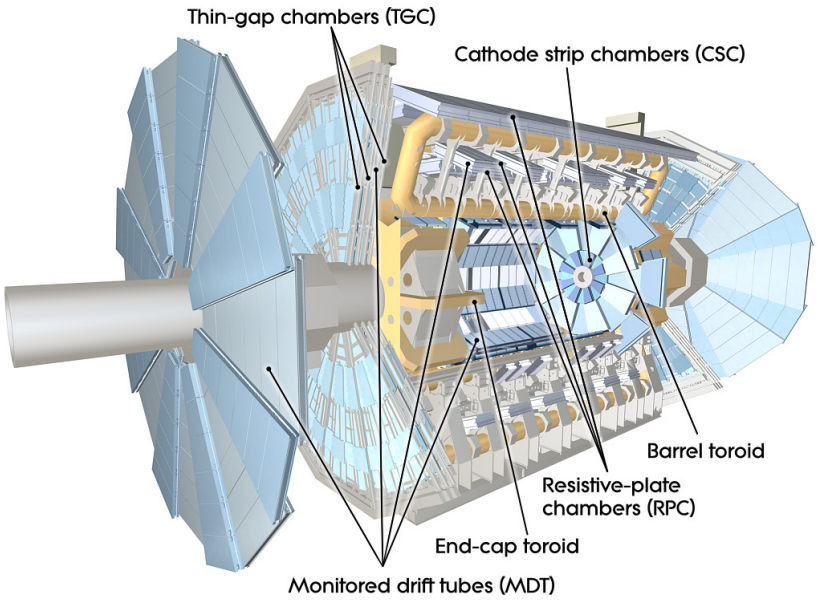

Figure 4.7: The cut-away view of the muon spectrometer. © CERN.

Monitored Drift Tubes. The MDT chambers consist of three or four layers of drift tubes with 3 cm in diameter, filled with Ar-CO_2 gas, with a 50 µm anode wire in the middle at a potential of 3270 V. They are extremely precise, with spatial resolution of around 50 µm. The MDT are the main detectors for precise muon position measurements and cover most of the MS acceptance.

Cathode Strip Chambers. The CSC are multiwire proportional chambers with segmented cathode. The position of the passing muon is measured by the centre-of-gravity of the induced charge on the cathode strips. The CSC are used for precise measurements of the muon trajectories in the end-cap regions with high muon flux due to their high granularity and very good spatial resolution.

Resistive Plate Chambers. The RPC also work on the principle of gas ionization detection. The active volume is formed by two resistive electrodes separated by 2 mm insulating spacers. When a charged particle enters this volume and ionises the gas, very strong uniform electric field produces an avalanche multiplication of electrons. The readout is done by charge induction in metal strips placed on both electrodes.

The RPC are less accurate but very fast, therefore they are used as a first level trigger in the barrel region. They are assembled together with MDTs and they provide the second coordinate not measured by the MDT chambers.

Thin Gap Chambers. The TGC are multiwire proportional chambers. Their function is similar to the RPC, they are fast but less precise. The TGC work as a first level trigger in the end-cap regions and they are also assembled in combination with the MDT chambers.

4.2.5 Magnet System

The ATLAS magnet system [184] is necessary for particle momentum and electric charge measurements. It consists of three main parts: the Central Solenoid, the Barrel Toroid and the End-Cap Toroids.

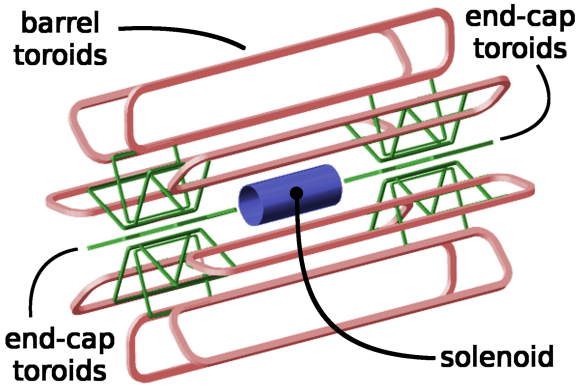

Figure 4.8: The ATLAS magnet system scheme. © CERN.

Central Solenoid. The central superconducting solenoid is assembled around the ID in order to provide a nearly homogeneous 2 T magnetic field. This enables to measure precisely momentum of the charged particles in the ID. The ATLAS solenoid is thin to absorb as little particle energy as possible and shares the same cryostat with the LAr to reach superconductivity.

Barrel Toroid. The barrel toroid system consists of 8 superconducting air-core coils, each 25 m long and 5 m wide. They provide a 4 T magnetic field, although less homogeneous than the central solenoid field. The whole system weights 830 t and enables precise muon momentum measurements in the MS.

End-cap Toroids. The end-cap toroids work similarly as the barrel toroid system. Eight superconducting coils in each end-cap are assembled inside an insulation vacuum

vessel that is 5 m wide and 11 m in diameter. Each of the two end-cap toroid systems weights 240 t.

4.2.6 Trigger System

The event rate at full ATLAS performance is ≈ 40 MHz but the potentially interesting events are expected to appear at a rate of ≈ 1 kHz only. The ATLAS trigger system was therefore developed for real-time event selection and consists of two main parts: The Level-1 Trigger (LVL1) [185] and the High Level Trigger (HLT) [186].

Level-1 Trigger The LVL1 is hardware based and works online. The LVL1 uses only a subset of information from the calorimeters and from the muon trigger detectors, RPC and TGC. It is very fast with latency around 2.5 µs and it reduces the event flow to around 100 kHz. The LVL1 also selects regions of interests (RoIs), which are further analysed by the HLT.

High Level Trigger The HLT is software based and uses fast algorithms running mostly in RoIs to select interesting events offline. At this step full detector granularity information is available. The HLT reduces the event flow by a factor of 100 to ≈ 1 kHz with an average latency of around 350 ms.

Correct setup of the trigger requirements is crucial since rejected events are definitively lost. The ATLAS triggers typically require presence of one or several high-p_{T} objects in the event, such as charged leptons and jets, or large missing transverse energy.

4.2.7 Background Radiation and Shielding

The main primary source of background radiation in the ATLAS experiment comes from the proton-proton collisions in the vicinity of the interaction point. Typically there are tens of collisions per bunch crossing and most of the energy from the primary background radiation is deposited in the very forward regions, such as the FCal. Interactions with the detector material or the beampipe itself cause secondary radiation, which illuminates the individual sub-detectors and especially the muon spectrometer end-cap. As a consequence, background radiation may cause many undesirable effects including radiation damage and ageing of the individual components. Higher occupancy may lead to inefficiencies, resolution degradation and the triggers can be also affected by spurious signals. To reduce all these effects a large amount of shielding is used in ATLAS, as shown in Figure 4.9. The total weight of the shielding is almost 3000 t and consists mainly of metal, concrete and plastic material.

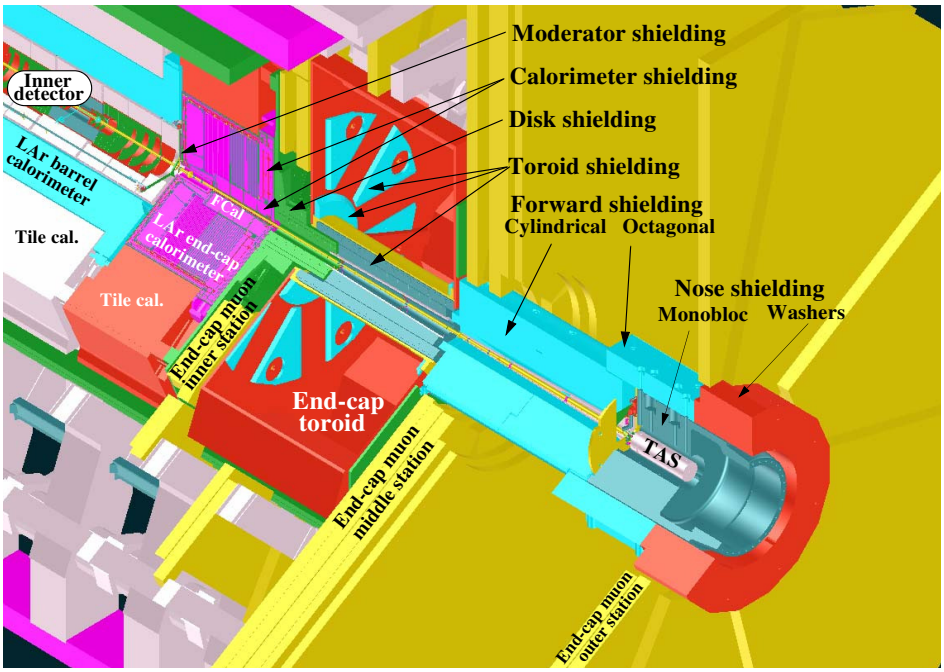

Figure 4.9: The scheme of the shielding used in the ATLAS experiment. © CERN.

The moderator shielding is located between the inner detector and the LAr end-cap and its aim is to reduce the flux of neutrons back-scattered in the LAr towards the ID. It is made of polyethylene enriched with boron to improve radiation hardness. At the very end of the LAr cryostat there are brass calorimeter shielding elements, which are together with the disk shielding responsible for shielding the innermost part of the MS end-cap from background radiation coming from the calorimeters. The toroid shielding is located between the first and second layer of the MS, partially within the toroid end-cap cryostat. It is made of iron, polyethylene with boron and stainless steel; this combination is chosen to absorb neutrons and also the subsequently emitted photons. The outermost forward and nose shielding protect the middle and outer part of the MS from radiation coming from interactions in the beampipe and the so-called Target Absorber Secondary collimator (TAS). TAS is a copper element which is shielding the first quadrupole LHC magnet, but as a consequence it is a significant source of secondary background radiation. Shielding in this very forward region is the most massive and weights hundreds of tonnes. Predominately it is made out of cast iron. Despite the shielding ATLAS has to cope with harsh radiation environment. The annual radiation doses vary from tens of Gy/y in the tile calorimeter to more than 100 kGy/y in the innermost pixel layer and the forward detectors [187].

4.2.8 Operation and Performance of the ATLAS Experiment

In overall, ATLAS data taking efficiency is high and the detector operation is smooth. In Run 2 ATLAS recorded more than 94% of luminosity delivered by the LHC (Figure 4.10). Around 89% of delivered luminosity is good for physics, i.e. all physics objects were reconstructed with good data quality. Similar numbers were obtained also in Run 1.

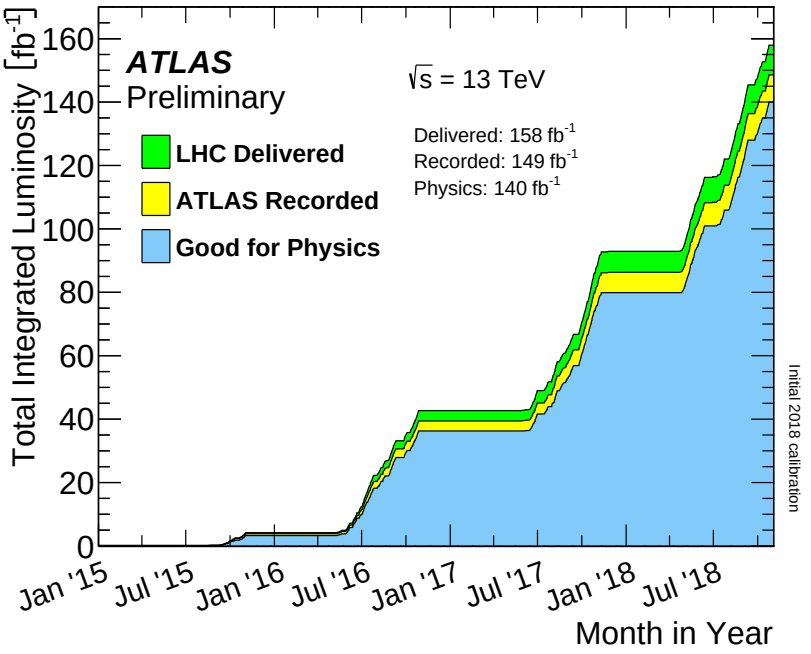

Figure 4.10: Total integrated luminosity and ATLAS data quality in 2015-2018. The figure is taken from Ref. [188].

Chapter 5

Object Definition

In this chapter we define physics objects that are used in the analysis, which include tracks, electrons, muons, jets, b-jets, large-radius (large-R) jets and missing transverse momentum. Additionally, the overlap removal procedure that prevents double counting of a single final state object is described and the definition of the parton-level top quarks is also discussed.

5.1 Tracks

Tracks are not used directly as stand-alone objects in the top-quark charge analysis. However, since tracks are used in definitions of almost all physical objects, the track reconstruction is briefly described.

The track reconstruction starts by assembling clusters using raw data from the pixel and SCT detectors. A charged particle often induces signal in several adjacent pixels and a connected component analysis [189] is used to group neighbouring pixels and strips into clusters. The exact point where the particle crossed the material of the detector is determined using a charge interpolation technique [190]. Thus, a set of points in the three-dimensional space can be obtained.

Sets of three points satisfying various criteria such as momentum and impact parameter requirements are then used to seed the Kalman filter [191] which is used to reconstruct tracks by adding additional points that are compatible with the preliminary trajectories. This approach is very efficient but creates a large number of track candidates including those which are not correct or are partially overlapping.

An ambiguity-solver [192] is used to identify the correct track candidates by calculating a track score using various track properties. For example, if the track intersects a sensitive layer without creating a signal the score is reduced, similarly if the χ^2 of the track fit is poor. Track candidates which do not match basic quality criteria listed in Ref. [192] or have a low score are rejected.

Finally, a high resolution fit is performed on the remaining track candidates using an

advanced neural network algorithm [193] to increase the precision of the reconstructed track properties.

Once the tracks are reconstructed, an iterative vertex finding algorithm is used to reconstruct vertices from at least two tracks [194]. The primary vertex is selected as the one with the largest sum of squared transverse momenta of the associated tracks.

Track impact parameters are usually defined with respect to the beamline and the primary vertex. The *transverse impact parameter* d_0 is the closest approach of the track to the beamline and the *longitudinal impact parameter* z_0 is the z coordinate of the closest approach with respect to the primary vertex [192].

5.2 Electrons

The electron reconstruction procedure [195] is based on reconstructing clusters in the electromagnetic calorimeter which are then associated to the tracks of charged particles reconstructed in the ID .

The sliding-window clustering algorithm [196] is used to identify the ECal clusters. In the barrel (end-caps) 3×7 (5×5) ECal cells are used to reconstruct the ECal clusters, which is equivalent to an area of size $\Delta\eta \times \Delta\phi = 0.075 \times 0.175$ (0.125×0.125).

Tracks loosely matched to the ECal clusters are investigated and required to fulfil certain quality criteria [195]. If there is no track matched to the ECal cluster it is classified as a photon candidate and if there are two oppositely charged tracks it is a candidate for a converted photon. If there is only one track matched it is further investigated as an electron candidate. Electrons are accepted within $|\eta_{\text{cluster}}| < 2.47$ except the transition region between the barrel and the end-cap of the liquid argon calorimeter $1.37 < |\eta_{\text{cluster}}| < 1.52$. Requirements on the impact parameters are also applied: $|d_0|/\sigma(d_0) < 5$ and $|z_0 \sin\theta| < 0.5$ mm.

A multivariate likelihood technique is further implemented to reject fake and non prompt electrons, utilising full track and calorimeter cluster information into a single discriminant [197]. By application of different requirements on the discriminant variable three working points (WP) are defined: `Tight`, `Medium` and `Loose`. The efficiency to identify electrons is the highest when using the `Loose` requirements but the background rejection is highest with the `Tight` WP, as shown in Figure 5.1.

In this analysis, the `Tight` electron identification criteria are used to identify the *tight* electrons and the `Medium` criteria are used for the *loose* electrons. The tight electrons are the nominal ones used in the analysis while the loose are used to estimate multijet background, as described in Section 6.3.

To further suppress non-prompt and fake electrons isolation criteria can be applied. The isolation is studied separately in the tracker and the ECal and various operating points combining requirements on these quantities are defined [197]. In this analysis,

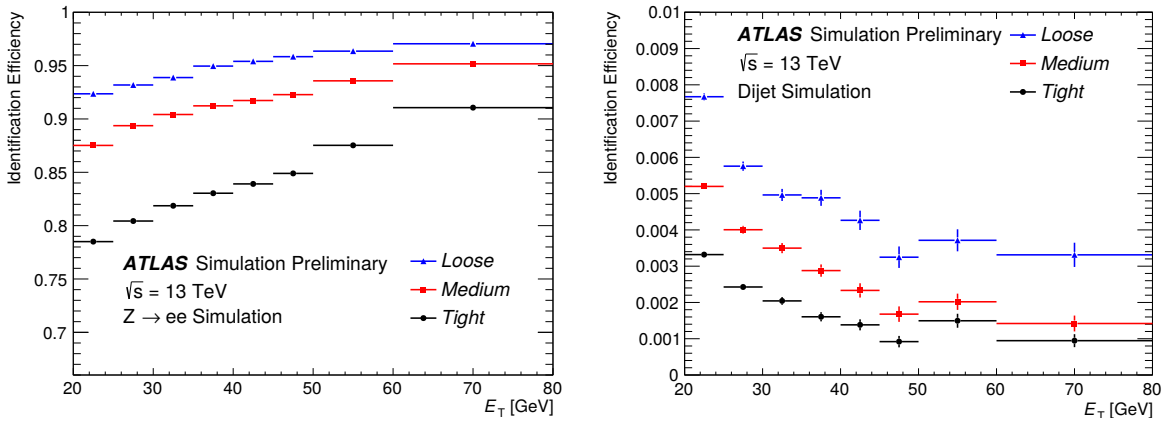

Figure 5.1: The efficiency to identify electrons obtained using $Z \to e^+e^-$ decays (left) and the probability of mis-identifying hadrons as electrons (right). The figure is taken from Ref. [197].

the `Gradient` [197] isolation is applied to the tight electrons while no isolation is required for loose electrons.

Since quality of the electron identification and reconstruction can be slightly different between data and MC, scale factors are applied to correct the discrepancies in the simulation. The scale factors are obtained in well understood processes such as $Z \to e^+e^-$ and $J/\psi \to e^+e^-$ [195].

5.3 Muons

Muons are reconstructed using a unified muon identification chain [198], which combines information from the ID and the MS.

In the MS the reconstruction starts by forming segments in each layer from individual signals from MDT and CSC utilising also information from RPC and TGC. The track candidates are then formed by a combinatorial matching of segments in different layers. Various criteria on the segment quality are introduced and the matching is performed using the relative segment positions and angles. At least two matching segments are required to form a track except in transition regions between the barrel and the end-caps, where even one segment with high quality can be used.

Track candidates are accepted if they fulfil criteria on a global χ^2 fit which combines information from the ID and the MS. In this analysis only muons within $|\eta| < 2.5$ are selected and impact parameter cuts $|d_0|/\sigma(d_0) < 3$ and $|z_0 \sin\theta| < 0.5$ mm are applied.

Similarly to the electron definition, a multivariate likelihood is calculated to suppress non-prompt and fake muons. The momentum and transverse momentum information is compared between the ID and MS and the total χ^2 value is also considered. The `Medium` WP is used in this analysis in tight and loose muon definition and the `Gradient` isolation is additionally applied in tight muons [198]. The `Medium` identifi-

cation efficiency as a function of muon transverse momentum is shown in Figure 5.2. Discrepancies between muon identification and reconstruction in data and simulation are corrected by application of scale factors.

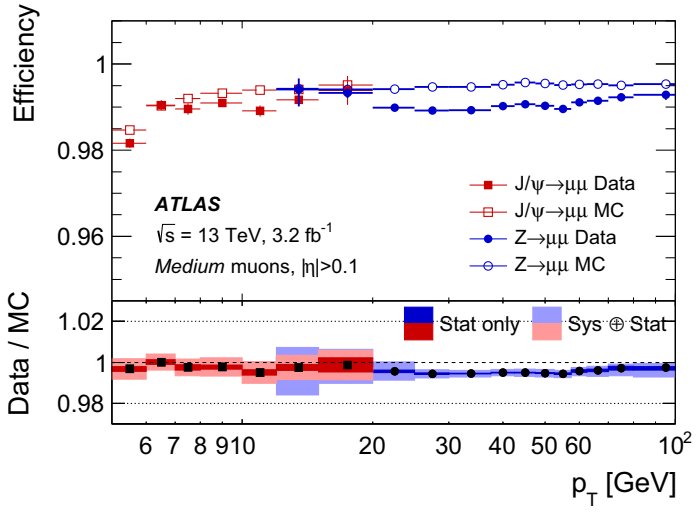

Figure 5.2: The efficiency to identify muons obtained with $Z \to \mu^+\mu^-$ and $J/\psi \to \mu^+\mu^-$ events for data and MC. The figure is taken from Ref. [198].

5.4 Jets

Quarks and gluons are coloured and due to quark confinement they are observed experimentally as showers of hadrons, so-called jets, as discussed already in Section 1.2.1

The jet reconstruction starts in the HCal, where the energy deposits are measured at the electromagnetic (EM) scale from the electromagnetically interacting particles. Subsequently, energy deposits are clustered using topological clustering algorithm [196]. The anti-k_t algorithm [199] with a radius parameter $R = 0.4$ is used to reconstruct *small-R jets* from topological calorimeter clusters. The anti-k_t algorithm satisfies infrared and collinear safety requirements [200], i.e. it is not affected by collinear splitting or soft gluon emissions within the hadron showers and the number of reconstructed jets remains independent of these effects, which are hard to theoretically describe and simulate.

The topological clusters are obtained only from electromagnetically interacting particles and are affected by pile-up, therefore the output jets from the anti-k_t algorithm need a couple of corrections and calibrations in order to get the correct jet kinematic properties [201]. The jet energy is corrected for pile-up effects using a technique based on jet area [202] which subtracts the pile-up contribution (per event) from the jet. Additionally, residual pile-up correction to the jet p_{T} is applied as a function of the number of primary vertices and the number of interactions per bunch crossing.

After the pile-up corrections the jet energy scale (JES) and η calibration based on the PYTHIA [203–205] MC simulation is performed [201]. The average energy response as a function of the η_{det} for jets with different 'truth' energy is shown in Figure 5.3. The energy response is in general lower with increasing η_{det} and in the transition regions between the individual calorimeter sub-detectors. Subsequently, the Global Sequential Calibration (GSC) is applied to correct for residual dependencies of the JES on various jet properties, such as the number of tracks, fraction of jet energy measured in the LAr and in the first layer of the HCal etc. [201].

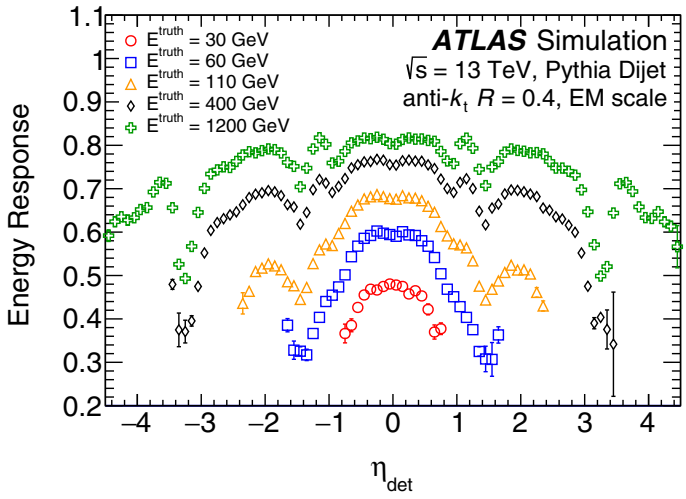

Figure 5.3: The average energy response as a function of the detector η_{det} for jets with different 'truth' energy. The figure is taken from Ref. [201].

Finally, the multivariate Jet Vertex Tagger (JVT) [206] is also used to discriminate jets originating from the primary vertex from jets from pile-up collisions, using the inner detector tracks associated with the jet. In this analysis the JVT discriminant is required to be larger than 0.59 for jets with $p_{\text{T}} < 60$ GeV and all small-R jets are required to be within $|\eta| < 2.5$.

5.5 Large-R Jets

If the hadronically decaying top quark is produced with very large momentum it might be inefficient or even impossible to reconstruct its decay products by searching for three small-R jets. Instead, the hadronic showers are often overlapping and it is more efficient to search for one large jet, further referred to as *large-R jet*.

Despite some similarities with the small-R jets definition and reconstruction there are also many important differences. The advanced local cluster weighting (LCW) scheme [207] is used in order to maximise the information that can be obtained from the cluster shape variables and the anti-k_t algorithm is used with $R = 1.0$. The

large-R jets are even much more sensitive to pile-up contributions and the so-called grooming techniques are usually applied in order to find and throw away pile-up-like constituents of the large-R jet. This analysis utilises the trimming procedure described in Ref. [208]. The idea is that the constituents of the large-R jet are reclustered using the k_t algorithm [209] with a radius parameter R_{sub}. The k_t sub-jets carrying less than a fraction f_{cut} of the large-R jet p_{T} are removed and the large-R jet p_{T} is recalculated from the remaining sub-jets. In this analysis values of $R_{\text{sub}} = 0.2$ and $f_{\text{cut}} = 0.05$ are used and the trimming procedure is illustrated in Figure 5.4.

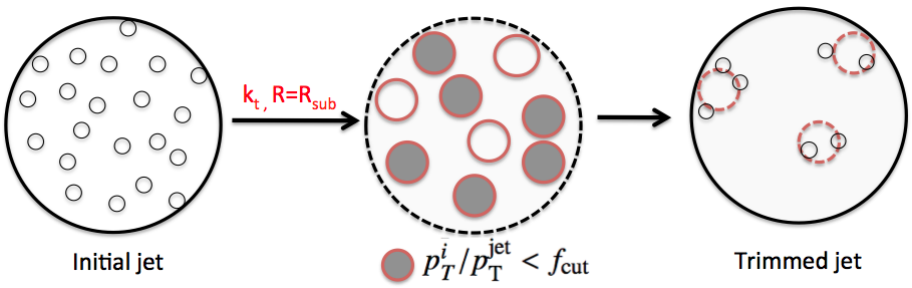

Figure 5.4: Diagram depicting the large-R jet trimming procedure. The figure is taken from Ref. [210].

Similarly to the small-R jets, a set of calibrations is applied to correct the large-R detector response to the 'truth' values.

The large-R jets are further required to have signatures of the hadronic top quark decays and top tagging criteria on the jet mass and the substructure variable τ_{32} [95] are applied. The criteria are chosen in order to obtain 80% efficiency of tagging large-R jets from the hadronic top quark decays.

5.6 *B*-Tagging

Identifying small-R jets initiated by a b quark is important for correct identification and reconstruction of the $t\bar{t}$ events, as well as for background suppression.

A multivariate MV2c10 algorithm [211,212] is used in this analysis to identify b-jets. The MV2c10 algorithm combines inputs from three stand-alone b-tagging algorithms SV1, JetFitter and IP3D with jet p_{T} and η within a boosted decision tree (BDT). All of the three stand-alone algorithms exploit the fact that majority of b-hadrons have a non-negligible decay length and a secondary vertex typically can be reconstructed. The IP3D is track-based and calculates the discriminant from the transverse and longitudinal track impact parameters. Typically, tracks originating from b-hadron decays have large impact parameters while tracks from light jets have impact parameters consistent with zero.

The SV1 and JetFitter are secondary-vertex based. The SV1 algorithm reconstructs a single secondary vertex and various vertex properties such as invariant mass of the vertex, decay length, track multiplicity and the energy fraction[1] are considered. The JetFitter is a topological multi-vertex algorithm based on a modified Kalman filter and reconstructs the full decay topology including possible tertiary vertex which corresponds to the point where the c-hadron decayed. Similarly to the SV1, properties of the vertices are combined into a single discriminant.

The final output of the combined MV2c10 algorithm is a discriminant from -1 to 1 which non-linearly corresponds to a probability that the jet is initiated by a b quark. Jets initiated by a b quark have typically outputs close to 1 and light jets close to -1, as demonstrated in Figure 5.5. In the case of c-jets the situation is more complex, since c-hadrons can also produce secondary vertices with a non-negligible decay length.

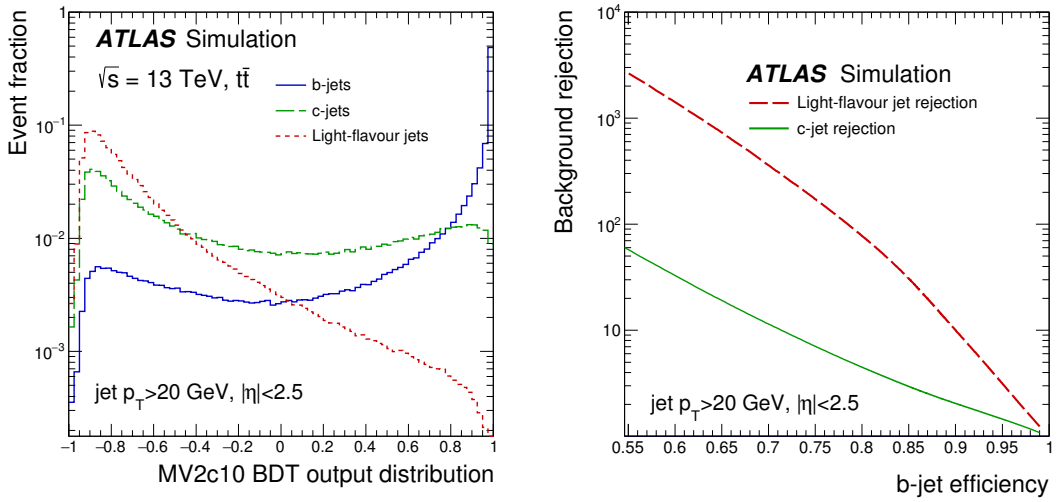

Figure 5.5: The MV2c10 outputs for b-jets, c-jets and light jets (left) and the c-jet and light jet rejection factors as a function of the b-tagging efficiency (right). The figure is taken from Ref. [213].

In this analysis the MV2c10 discriminant is required to be larger than 0.64 in order to consider jets as b-tagged. This threshold corresponds to an inclusive 77% b-jet selection efficiency. The corresponding rejection factors for jets initiated by a c quark, tau lepton, and light quarks are 4, 16, and 113, respectively. To account for mismodelling of selection efficiency of the different quark flavour jets and jets initiated by hadronically decaying tau leptons, per-jet scale factors obtained from $t\bar{t}$ events in data [211, 214] are applied.

[1]The energy fraction in SV1 is defined as the total energy of tracks associated to the vertex to the total energy of all tracks associated to the jet.

5.7 Missing Transverse Momentum

Neutrinos do not interact with the detector material and can be observed only indirectly as missing momentum in the transverse plane with a magnitude $E_{\mathrm{T}}^{\mathrm{miss}}$. The two components E_x^{miss} and E_y^{miss} of $E_{\mathrm{T}}^{\mathrm{miss}}$ are calculated from the transverse momenta of all reconstructed objects - charged leptons, photons and jets [215]. Additionally, a soft term calculated from the ID tracks not associated to any physical object is also considered:

$$E_{x(y)}^{\mathrm{miss}} = E_{x(y)}^{\mathrm{miss},\ell} + E_{x(y)}^{\mathrm{miss},\gamma} + E_{x(y)}^{\mathrm{miss,jets}} + E_{x(y)}^{\mathrm{miss,soft}}. \tag{5.1}$$

The whole procedure is sensitive to pile-up effects which have to be carefully analysed [215]. Calibration is performed using $Z \to \mu^+\mu^-$ events which are expected to have zero $E_{\mathrm{T}}^{\mathrm{miss}}$ and with $W \to \ell\bar{\nu}_\ell$ processes where ℓ stands for electron or muon. Additionally, $t\bar{t}$ events decaying in the ℓ+jets channel are used to study the $E_{\mathrm{T}}^{\mathrm{miss}}$ performance in an environment with higher jet multiplicity.

5.8 Overlap Removal

In order to avoid double counting of single final state objects an overlap removal procedure between electrons, muons and small-R jets is implemented as a sequence of operations:

- Electron candidates sharing a track with a muon candidate are removed.
- If the distance between a small-R jet and an electron candidate is $\Delta R < 0.2$, the jet is dropped. If multiple small-R jets fulfil this requirement, only the closest one is removed.
- If the distance between a small-R jet and an electron candidate is $0.2 < \Delta R < 0.4$, the electron is dropped.
- Jets with less than three tracks found within $\Delta R < 0.2$ of muon candidates are removed.
- Subsequently, muon candidates found within $\Delta R < 0.4$ of jets are removed.

5.9 Parton-Level Top Quark

For the purposes of unfolding it is necessary to define parton-level top quarks in MC simulated samples. In this analysis, the last top (antitop) quark in the 'truth' chain before decay is taken. For the nominal sample this corresponds to the top quarks after FSR, since FSR also affects the charge asymmetry.

Chapter 6

Data and Simulated Samples

In this section the dataset used in the A_C analysis at $\sqrt{s} = 13$ TeV is described. We also discuss how the SM prediction is obtained - the Monte Carlo modelling and a data-driven (DD) technique used to estimate contribution from processes which are difficult to simulate.

6.1 Data Sample

The analysis is carried out using full Run 2 pp collision dataset at $\sqrt{s} = 13$ TeV collected by the ATLAS experiment in 2015-2018. Only data taking periods (so-called *lumiblocks*) in which all sub-detectors were fully operational are used in this analysis. The 'good' lumiblocks are summarised in the so-called *Good Run Lists* (GRLs). The luminosity is measured using the LUCID-2 [216] detector and the corresponding uncertainties are derived following an approach similar to the one described in Ref. [217]. The combined 2015-2018 GRLs correspond to the total integrated luminosity of 139 fb^{-1} with an uncertainty of 1.7%. The breakdown of luminosity values for the individual data taking years is shown in Table 6.1.

Year	GRL $\int L\ \mathrm{d}t$ [fb^{-1}]
2015	3.2±0.1
2016	33.0±0.7
2017	44.3±1.1
2018	58.5±1.2
Total	139.0±2.4

Table 6.1: Integrated luminosities of the GRLs corresponding to the individual data taking years in Run 2, including the total integrated luminosity. The uncertainties are also shown.

The datasets corresponding to the individual data taking years do not differ only in the amount of data collected, but also in the pile-up conditions. While the mean number of interactions per bunch crossing $\langle\mu\rangle$ was 13.4 in 2015, in 2017 it was 37.8

with maximum values of over 70. The pile-up distributions are shown in Figure 6.1. In general, events with larger pile-up are more difficult to reconstruct due to larger number of background collisions causing noise in the tracker and the calorimeters.

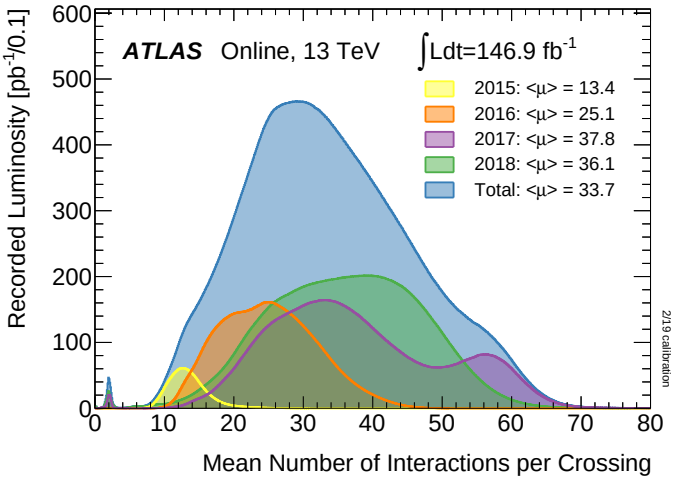

Figure 6.1: Luminosity-weighted distributions of the mean number of interactions per bunch crossing for the 2015-2018 years, as well as for their combination. Full online luminosity recorded by the ATLAS experiment is shown. Figure is taken from Ref. [178].

6.2 Monte Carlo Samples

For several reasons it is very useful, and often even necessary, to simulate the studied physical phenomena according to the predictions of the SM (or some different theory) using the Monte Carlo method. Proper simulations help to validate the agreement between the data and the SM in some well understood, control distributions. At the same time simulations enable to understand the sensitivity of the detection technique to the studied quantity - acceptance, resolution and migrations between the *parton* and the *reconstruction* levels. The obtained information can be used to unfold the measured data to obtain the 'true' distributions, unaffected by the imperfectness of the experiment, as described in detail in Chapter 8.

There are several steps that need to be properly modelled, e.g. the PDFs of the interacting protons, hard scattering and matrix elements, parton showering and hadronisation, pile-up contribution, interaction with the material of the detector and the detector response. Additionally, MC generators use a couple of relatively free parameters which have to be tuned using real data in order to describe the reality in the best possible way.

The simulated samples are generated in three so-called campaigns, corresponding to different pile-up profiles in the individual years of data taking - the `mc16a` corresponds to

the combined 2015 and 2016 datasets and the `mc16d` and `mc16e` campaigns correspond to the 2017 and 2018 datasets, respectively. The campaigns use independent sets of events and can be simply summed to describe the full Run 2 dataset.

In this section we decribe the simulated samples used in this analysis. Some of the features are common between almost all samples. Decays of heavy hadrons are modelled using the EvtGen 1.6.0 [218] generator, with the exception of some of the background samples generated by the Sherpa 2.2 [219] generator. The response of the ATLAS detector is simulated mostly using the Geant4 [220] software, which performs a full simulation of particle showers in the calorimeters. However, this is computationally very demanding and for some samples (mentioned below) the AtlFast-II [221, 222] which applies some approximations is used instead. To model the additional pile-up pp interactions from the same (or close-by) bunch crossing the hard scattering events are overlaid with a set of minimum-bias pp interactions generated using the Pythia 8 [203–205] generator and the MSTW2008LO [223] PDF set.

6.2.1 Signal Modelling

The nominal $t\bar{t}$ signal sample is modelled using the Powheg Box 2 [224–226] matrix element (ME) generator which provides matrix elements at NLO in the QCD with the NNPDF3.0NLO [227] PDF set and the h_{damp}[1] parameter set to 1.5 m_{top} [228]. The ME generator assumes $m_{\text{top}} = 172.5$ GeV and is interfaced with Pythia 8.230 generator for the parton shower (PS) and hadronisation modelling. The NNPDF2.3LO [227] PDF set and A14 [229] set of tuned parameters is applied in hadronisation.

To estimate the uncertainty on the signal modelling alternative signal samples are also generated using different MC generators. The uncertainty on the ME modelling is estimated by comparing the nominal sample with the one where the Powheg Box 2 is replaced by the MadGraph5_aMC@NLO 2.6.0 [230] generator. Similarly, the uncertainty on the PS modelling is estimated by comparing the nominal sample with the one where Pythia 8.230 is replaced by Herwig 7.04 [231, 232] with the H7UE [232] set of tuned parameters and the MMHT2014LO [233] PDF set. Finally, the nominal generator setup with different m_{top} values is used to evaluate the effect of the top quark mass uncertainty. The response of the detector in the alternative signal samples is mostly modelled using the simplified AtlFast-II approach instead of Geant4. Further information about the systematic uncertainties related to the MC modelling can be found in Section 9.2.

All signal $t\bar{t}$ samples, generated at the NLO in QCD, are normalised to the cross section at NNLO in QCD with NNLL soft gluon terms, $\sigma(t\bar{t})_{\text{NNLO+NNLL}} = 832$ pb^{-1} [82, 83], discussed already in Section 2.1.1.

[1] The h_{damp} parameter controls the transverse momentum of the first additional gluon emission beyond the leading-order Feynman diagram in the parton shower.

6.2.2 Background Modelling

In this subsection the generators used to model the important background processes are briefly described. Processes, which are not mentioned here, either belong to the 'multijet' category described in Section 6.3 or they are considered to be negligible and are not taken into account.

Single Top Quark Production. The single top quark production in the t-, Wt- and s-channels is simulated using a similar set of MC generators as in the case of the nominal $t\bar{t}$ signal sample. The POWHEG BOX 2 [224–226, 234–236] at NLO in QCD is interfaced with PYTHIA 8.230 using the A14 set of tuned parameters. Similarly as in the case of the $t\bar{t}$ modelling, alternative MC generators are used to estimate the single top quark modelling uncertainties. The single top quark samples are normalised to the approximate NNLO cross sections [82, 83], discussed in Section 2.1.2.

$t\bar{t}W$, $t\bar{t}Z$ and $t\bar{t}H$. The associated production of the $t\bar{t}$ pair with the W or Z boson (collectively referred to as $t\bar{t}V$) is generated using the MADGRAPH5_AMC@NLO 2.3.3 ME generator at NLO interfaced with PYTHIA 8.210. In the case of the $t\bar{t}H$ production the ME is generated using POWHEG BOX 2 in the `mc16a` and `mc16d` campaigns, while MADGRAPH5_AMC@NLO 2.6.0 is used in the `mc16e` campaign. In all three campaigns the ME generator is interfaced with PYTHIA 8.210. The $t\bar{t}V$ and $t\bar{t}H$ cross sections are calculated at the NLO QCD+EW accuracies [237].

W+jets, Z+jets and Diboson. The V+jets and diboson (WW, ZZ, WZ) production is simulated with the stand-alone SHERPA 2.2 parton shower Monte Carlo generator. The NNPDF3.0NNLO [227] set of PDFs and a dedicated set of tuned parton shower parameters developed by the SHERPA authors are used. The V+jets samples are normalised to the NNLO prediction [238] and the diboson prediction is scaled to the NLO precision [239].

6.3 Data-Driven Background Estimate

The MC modelling is a reliable method of estimating the expected signal and background distributions, but it has some limitations. For example, processes with very large cross sections and at the same time very small acceptanceare particularly challenging to simulate. A very large number of events has to be generated since only a small fraction of them passes the selection criteria. Furthermore, the result is typically very sensitive to even small mis-modelling and is affected by large statistical and systematic uncertainties. An alternative approach is to estimate the contribution of the

particular process using the data-driven (DD) technique which extracts the information directly from the measured data.

In this analysis the challenging background is the fake and non-prompt lepton contribution, further referred to as *multijet* background or '*fakes*'. The fake leptons are mis-identified leptons, typically photons or light hadrons identified as electrons. The non-prompt leptons are genuine, correctly identified leptons, but not originating from the primary vertex. Instead, the non-prompt leptons are created during subsequent interactions, such as heavy hadron decays, photon conversions etc.

To estimate the contribution of the multijet background the DD *matrix method* [240] is used in this analysis. In the matrix method, two categories of events are defined - events that satisfy the so-called loose lepton selection criteria and events that pass the so-called tight lepton requirements. The tight lepton selection is the one used in the measurement itself and events passing the tight selection are a subset of events passing the loose selection. Typically, the loose lepton selection uses e.g. less strict lepton definition and isolation requirements.

In the ℓ+jet $t\bar{t}$ decay channel the number of events in data with one loose (tight) lepton can be written as:

$$N_{\text{loose}} = N_{\text{loose}}^{\text{real}} + N_{\text{loose}}^{\text{fake}} \tag{6.1}$$

and

$$N_{\text{tight}} = N_{\text{tight}}^{\text{real}} + N_{\text{tight}}^{\text{fake}}, \tag{6.2}$$

where $N_{\text{loose}}^{\text{real}}$ ($N_{\text{loose}}^{\text{fake}}$) is the number of events with (without) a real prompt lepton satisfying the loose lepton requirements. Similarly, $N_{\text{tight}}^{\text{real}}$ ($N_{\text{tight}}^{\text{fake}}$) is the number of events with (without) a real prompt lepton satisfying the tight lepton criteria.

The probability of a real prompt lepton satisfying the loose criteria to pass also the tight selection, the *real efficiency* ϵ^{real}, is defined as

$$\epsilon^{\text{real}} = \frac{N_{\text{tight}}^{\text{real}}}{N_{\text{loose}}^{\text{real}}} \tag{6.3}$$

and similarly the *fake efficiency* ϵ^{fake} can be expressed as:

$$\epsilon^{\text{fake}} = \frac{N_{\text{tight}}^{\text{fake}}}{N_{\text{loose}}^{\text{fake}}}. \tag{6.4}$$

The real and fake efficiencies can be measured in data using suitable control regions. The real efficiency ϵ^{real} is typically estimated using the well-understood $Z \to e^+e^-$ and $Z \to \mu^+\mu^-$ processes with the *tag and probe* technique. One lepton is required to pass the tight selection and the second one is used to probe the efficiency of fulfilling the loose and tight criteria. The fake efficiency ϵ^{fake} can be measured using selections that prefer multijet events, e.g. selections requiring low $E_{\text{T}}^{\text{miss}}$ or high lepton impact parameter with

respect to the primary vertex. The contribution from processes containing prompt leptons is estimated using MC and subtracted to obtain pure multijet sample. The fake efficiency ϵ^{fake} is then determined as a ratio between the number of tight and loose events in these regions. Typically, the real and fake efficiencies are parametrised as functions of various kinematic observables and event properties, such as jet and b-jet multiplicities.

Once the real and fake efficiencies are known, it is possible to solve the set of two linear equations (6.1) and (6.2) to get the number of fake lepton events when using the tight selection:

$$N_{\text{tight}}^{\text{fake}} = \frac{\epsilon^{\text{fake}}}{\epsilon^{\text{real}} - \epsilon^{\text{fake}}}(\epsilon^{\text{real}} N_{\text{loose}} - N_{\text{tight}}) \tag{6.5}$$

In practice, a weight is applied to each data event to obtain the multijet distribution. Events passing the tight selection contribute with weight

$$w_{\text{tight}} = \frac{\epsilon^{\text{fake}}(\epsilon^{\text{real}} - 1)}{(\epsilon^{\text{real}} - \epsilon^{\text{fake}})} \tag{6.6}$$

and events that pass only the loose selection and not the tight one are assigned a weight

$$w_{\text{not-tight}} = \frac{\epsilon^{\text{fake}}\epsilon^{\text{real}}}{(\epsilon^{\text{real}} - \epsilon^{\text{fake}})}. \tag{6.7}$$

Since typically $\epsilon^{\text{real}} > \epsilon^{\text{fake}}$, tight events contribute negatively and the contribution from events passing only the loose selection is positive.

6.3.1 Parametrisation Choice

The following parametrisations of real and fake efficiencies were studied: lepton p_{T} and η, distance between the lepton and the closest jet $\Delta R(\ell, jet)$, $\Delta\Phi(\ell, E_{\text{T}}^{\text{miss}})$, leading jet p_{T}, jet multiplicity and b-jet multiplicity. All combinations of two of these variables were also tested. The basic criterion for a good parametrisation is to provide non-negative multijet contributions to all bins in the studied inclusive and differential $\Delta|y|$ distributions and to be in good agreement with data in basic 'control' distributions, such as jet p_{T}, lepton p_{T}, $E_{\text{T}}^{\text{miss}}$ etc. Parametrisations that describe well multijet contributions in both 1 b-tag exclusive and 2 b-tag inclusive signal regions (described in Section 7.1) are preferred.

The optimal parametrisation is chosen independently for the e+jets/μ+jets $t\bar{t}$ decay channel and for the resolved/boosted event topology. Typically, only one or two parametrisations satisfy the criteria above. Out of these, one is picked as a nominal choice and the second one as a 'shape' systematic uncertainty. If only one parametrisation passes the criteria, another parametrisation with the lowest number of negative

$\Delta|y|$ bins is chosen as a systematic uncertainty while the negative bins are set to zero. In all cases the same parametrisation is used for real and fake efficiencies and final choices are summarised in Table 6.2. In the case of the boosted topology in μ+jets events the contribution from multijet background is found to be negligible, well bellow 1%, and is omitted completely.

Channel	ϵ^{real} and ϵ^{fake} parametrisation	
	nominal	alternative
e+jets, resolved/boosted	$p_{\text{T}}^{\text{lead. jet}}$, $\Delta\Phi(\ell, E_{\text{T}}^{\text{miss}})$	p_{T}^{ℓ}, $\Delta\Phi(\ell, E_{\text{T}}^{\text{miss}})$
μ+jets, resolved	p_{T}^{ℓ}, $p_{\text{T}}^{\text{lead. jet}}$	$p_{\text{T}}^{\text{lead. jet}}$, $\Delta\Phi(\ell, E_{\text{T}}^{\text{miss}})$

Table 6.2: Summary of the parametrisations of real and fake efficiencies used to define nominal and alternative (used for determination of systematic uncertainty) multijet distributions.

Chapter 7

Event Selection and Reconstruction

7.1 Event Selection

A set of selection criteria is applied on data satisfying the GRL requirements (see Section 6.1) and simulated samples in order to reconstruct $t\bar{t}$ ℓ+jets events in the resolved and boosted topology, introduced in Section 2.2.2.

7.1.1 Selection Criteria Common to Resolved and Boosted Topologies

The following selection criteria are used to select ℓ+jets events in both resolved and boosted topologies:

- **Primary vertex** with at least two tracks is required. Since typically multiple vertices are present, vertex with the highest $\sum p_{\mathrm{T,track}}^2$, where $p_{\mathrm{T,track}}$ is the transverse momentum of track associated to the vertex, is chosen.
- **Event quality** – to avoid events affected by detector noise criteria on the calorimeter response and on the jet quality must be fulfilled.
- **Single electron/muon trigger** requirements, at least one of the triggers listed in Table 7.1 must be fired. Slightly higher trigger thresholds are used in 2016-2018 data due to larger pile-up contribution.
- **Exactly one electron or muon** matched to the trigger with $p_{\mathrm{T}} > 28$ GeV is required. This value is slightly larger than the lowest trigger thresholds in order to operate at the trigger efficiency plateau. Events containing additional leptons with $p_{\mathrm{T}} > 25$ GeV are rejected.
- **Missing transverse energy and W boson transverse mass (M_{T}^{W})** – in order to suppress fake and non-prompt leptons from multijet background $E_{\mathrm{T}}^{\mathrm{miss}}$ of at least 30 GeV and M_{T}^{W}[1] of at least 30 GeV is required. In the μ+jets channel

[1] $M_{\mathrm{T}}^{W} = \sqrt{2p_{\mathrm{T}}^{\ell}E_{\mathrm{T}}^{\mathrm{miss}}(1-\cos\Delta\phi)}$ where $\Delta\phi$ is the angle between the lepton and $E_{\mathrm{T}}^{\mathrm{miss}}$ in the transverse plane with respect to the beam axis.

Dataset	e+jets	μ+jets
2015	HLT_e24_lhmedium_L1EM20VH HLT_e60_lhmedium HLT_e120_lhloose	HLT_mu20_iloose_L1MU15 HLT_mu50
2016 - 2018	HLT_e26_lhtight_nod0_ivarloose HLT_e60_lhmedium_nod0 HLT_e140_lhloose_nod0	HLT_mu26_ivarmedium HLT_mu50

Table 7.1: Summary of the ATLAS triggers used in the ℓ+jets selection. The `HLT` string in the trigger names stands for high level trigger discussed in Section 4.2.6 and the numbers, e.g. `e24` and `mu50` correspond to different momentum thresholds in GeV. Leptons with lower momentum are required to fulfil more strict likelihood (e.g. `lhmedium`) and isolation (e.g. `ivarloose`) criteria than those with higher momenta. The `nod0` string indicates that no transverse impact parameter requirements are applied and `L1` indicates that also Level-1 trigger requirements have to be fulfilled.

no cut is applied on $E_{\mathrm{T}}^{\mathrm{miss}}$ but $E_{\mathrm{T}}^{\mathrm{miss}} + M_{\mathrm{T}}^{W} > 60$ GeV is required.

- ***B*-tagged jet** – at least one of the small-R jets is required to be b-tagged by the algorithm described in Section 5.6.

7.1.2 Selection Criteria Specific to the Resolved Topology

- **At least 4 small-R jets** with $p_{\mathrm{T}} > 25$ GeV are required.
- **Boosted veto** is implemented in order to remove an overlap between events passing both resolved and boosted criteria. These events are removed from the resolved topology since reconstruction of the top quark four momenta is easier in the boosted topology.
- **Event reconstruction requirements** – the $t\bar{t}$ system is reconstructed using a boosted decision tree (BDT) algorithm, described in detail in Section 7.2. Events are required to have BDT discriminant > 0.3 in order to suppress background processes and combinatorial background due to wrong assignment of jets in $t\bar{t}$ events. This criterion accepts around 52% of $t\bar{t}$ events and only 27% of background events. Further details on the BDT threshold optimisation are provided in Section 7.2.

7.1.3 Selection Criteria Specific to the Boosted Topology

- **At least one small-R jet close to the lepton** with $p_{\mathrm{T}} > 25$ GeV and $\Delta R(\mathrm{jet}, \ell) < 1.5$ is required. If multiple jets satisfy this condition, the one with highest p_{T} is considered for the subsequent reconstruction of the leptonically decaying top quark.

- **At least one top-tagged large-R jet** with $p_{\mathrm{T}} > 350$ GeV and $|\eta| < 2$. In the case of multiple large-R jets satisfying these conditions the one with the highest p_{T} is chosen. Since both top quarks are expected to be back-to-back in the $t\bar{t}$ rest frame, additional requirements related to the large-R jet, isolated lepton and the small-R jet close to the lepton ($\Delta R(\mathrm{jet}, \ell) < 1.5$) are applied: $\Delta\phi(\mathrm{jet}_{R=1.0}, \ell) > 2.3$ and $\Delta R(\mathrm{jet}_{R=1.0}, \mathrm{jet}_{R=0.4}) > 1.5$.
- **Invariant mass of the reconstructed $t\bar{t}$ system** is required to be larger than 500 GeV. This criterion is imposed to remove a negligible fraction ($\approx 0.1\%$) of poorly reconstructed events which pass the boosted selection criteria despite low $t\bar{t}$ mass.

7.1.4 Event Yields

The event yields after the event selection are summarised in Tables 7.2 and 7.3.

Process:	Electron channel		Muon channel	
	1b-excl.	2b-incl.	1b-excl.	2b-incl.
$t\bar{t}$	700000 ± 60000	850000 ± 70000	820000 ± 70000	100000 ± 80000
Single top	41000 ± 6000	22000 ± 4000	48000 ± 7000	27000 ± 5000
W + jets	90000 ± 50000	10000 ± 6000	120000 ± 60000	13000 ± 8000
Z + jets	21000 ± 11000	3300 ± 1800	16000 ± 9000	2800 ± 1600
Diboson	4400 ± 2300	600 ± 400	5200 ± 2800	800 ± 500
$t\bar{t}V$, $t\bar{t}H$	2500 ± 1300	3300 ± 1800	2800 ± 1400	3700 ± 2000
Fakes	71000 ± 35000	36000 ± 18000	18000 ± 9000	11000 ± 6000
Total Prediction	920000 ± 100000	920000 ± 80000	1030000 ± 110000	1050000 ± 90000
Data (139 fb^{-1})	898484	922567	1046553	1086959

Table 7.2: Event yields in the resolved topology, split by the lepton flavour (e, μ) and b-tag multiplicity (1-excl., 2-incl.). Total pre-marginalisation uncertainty is shown.

Process:	Electron channel		Muon channel	
	1b-excl.	2b-incl.	1b-excl	2b-incl.
$t\bar{t}$	24000 ± 4000	36000 ± 5000	25000 ± 4000	39000 ± 6000
Single top	1800 ± 500	1400 ± 600	1900 ± 700	1500 ± 700
W + jets	4400 ± 2400	800 ± 500	5200 ± 2800	1000 ± 500
Z + jets	550 ± 300	120 ± 70	580 ± 320	130 ± 80
Diboson	410 ± 240	100 ± 70	430 ± 250	100 ± 90
$t\bar{t}V$, $t\bar{t}H$	300 ± 180	490 ± 260	280 ± 170	510 ± 290
Fakes‘	3000 ± 1500	2300 ± 1200	∼0.7%	∼0.4%
Total Prediction	35000 ± 6000	41000 ± 6000	34000 ± 6000	42000 ± 6000
Data (139 fb^{-1})	26999	32155	27711	34427

Table 7.3: Event yields in the boosted topology, split by the lepton flavour (e, μ) and b-tag multiplicity (1 excl., 2 incl.). Total pre-marginalisation uncertainty is shown.

7.2 Event Reconstruction

After the event selection it is necessary to reconstruct the top quark four momenta from the reconstructed objects, i.e. jets, lepton and $E_{\mathrm{T}}^{\mathrm{miss}}$. In this section the reconstruction techniques in resolved and boosted topologies are described.

7.2.1 Reconstruction in the Resolved Topology

In the resoled topology the main challenge of the event reconstruction is to correctly assign individual jets to the four quarks from the $t\bar{t}$ decay. Several reconstruction techniques have been studied, including the Kinematic Likelihood Fitter (KLFitter) [241] and the χ^2-pairing technique [242]. However, these techniques were eventually outperformed by an advanced multivariate Boosted Decision Tree (BDT) technique implemented using the `TMVA` package [243]. The BDT reconstruction technique combines information from the KLFitter with various kinematic variables and the b-tagging information into a single discriminant with value from -1 to 1. Each permutation of jet to quark assignment is evaluated and the permutation with the highest score of the BDT discriminant is chosen. Since the number of possible permutations increases with the number of jets as $\sim n!$, only permutations of up to five jets are considered. If there are more than five jets present in the event, the two jets with the highest b-tagging score are taken into account together with three other jets with the highest p_{T}.

The process of optimisation of the individual decision nodes within the BDT using MC samples, in order to maximise the power to discriminate between correct and wrong jet permutations, is called *training*. For the purpose of the BDT training each possible permutation of the jet to quark assignment is flagged as 'signal' or 'background'. Only permutations with four jets correctly assigned within $\Delta R = 0.3$ of the corresponding quarks are considered as signal, other permutations are considered as combinatorial background. Due to the large number of possible permutations the background category is at least by an order of magnitude larger than the signal category. At the same time most of the background permutations can be very easily distinguished from the signal permutations, therefore not all background permutations are considered in the BDT training. The background permutations are divided into four categories by the number of correct jet to quark assignments, from 0 to 3. To train on permutations that are not correct, but which have properties that make them difficult to discriminate from the correct ones, only the permutation with the highest KLFitter event probability[2] is chosen from each background category for the training process. Training on all permutations would spoil the BDT performance due to strongly imbalanced sizes of

[2] KLFitter event probability is calculated from the purely kinematic likelihood given by the KLFitter by adding the b-tagging information and normalisation factors. In this analysis the `kWorkingPoint` b-tagging KLFitter option is used and the top-quark mass is a free parameter.

the signal and background training samples. Furthermore, it is observed that the BDT technique can assign correctly also the background permutations which are easier to reconstruct even if they are not directly included in the training set.

The BDT training is performed separately in the 1-exclusive and 2-inclusive b-tag regions and inclusively in lepton flavours – the electron and muon channels are merged. Together 13 different input variables are used in the BDT. The separation power is defined as:

$$\text{Separation} = \frac{1}{2}\frac{\sum_{i\in\text{bin}}(s_i - b_i)^2}{\sum_{i\in\text{bin}}(s_i + b_i)}, \tag{7.1}$$

where s_i represents the number of signal events in bin i, and b_i represents the number of background events in bin i. It is a measure of power to discriminate signal from background for a given distribution, where signal and background are normalised to the same expected number of events. The full list of input variables with their separation powers can be found in Table 7.4 and the input distributions for signal and background are shown in the Appendix in Figures A.1 and A.2.

Variable	Definition	Separation	
		1 b-excl.	2 b-incl.
m_t^{had}	Reconstructed mass of the hadronically-decaying top quark	24.3%	25.6%
KLFitter $\ln\mathcal{L}$	Logarithm of likelihood from the stand-alone KLFitter	15.5%	16.2%
m_W^{had}	Reconstructed mass of the hadronically-decaying W boson	12.8%	14.0%
b-tag b^{lep}	States if the assumed b-jet from the leptonically-decaying top quark is b-tagged	1.4%	13.4%
b-tag b^{had}	States if the assumed b-jet from the hadronically-decaying top quark is b-tagged	1.2%	12.9%
m_t^{lep}	Reconstructed mass of the leptonically-decaying top quark	14.2%	12.9%
b-tag light jet 1	States if the light jet from W decay with highest b-tag score is b-tagged	6.9%	12.6%
$\Delta R(j_b^{\text{lep}}, \ell)$	ΔR between assumed b-jet from leptonically-decaying top quark and lepton	6.8%	6.7%
$\Delta R(j_{\text{l1}}, j_{\text{l2}})$	ΔR between two assumed light jets from W decay	3.7%	3.6%
$p_{\text{T}}^{\ell b}$	p_{T} of the lepton and assumed b-jet from leptonically-decaying top quark	1.0%	1.4%
Jet multiplicity	Number of jets in an event (for the purpose of correlations with other variables)	1.1%	1.2%
η_t^{had}	η of the hadronically-decaying top quark	0.4%	0.7%
$\Delta R(j_b^{\text{had}}, j_b^{\text{lep}})$	ΔR between two assumed b-jets from $t\bar{t}$ decay	0.8%	0.6%
Total	BDT output (discriminant)	45.1%	58.6%

Table 7.4: Separation power of the individual BDT input variables and of the BDT output discriminant. Input variables are ordered by the separation power in 2 b-incl. region.

During the BDT training process it is important to avoid 'overtraining', i.e. optimisation of decision nodes to properties specific only to the training set, typically statistical fluctuations. To validate the training procedure the MC sample is split into two independent parts, first one is used for training and the second one for testing. The distributions of the BDT output discriminant for both training and testing samples are shown in Figure 7.1. A very good agreement is observed with no signs of BDT overtraining.

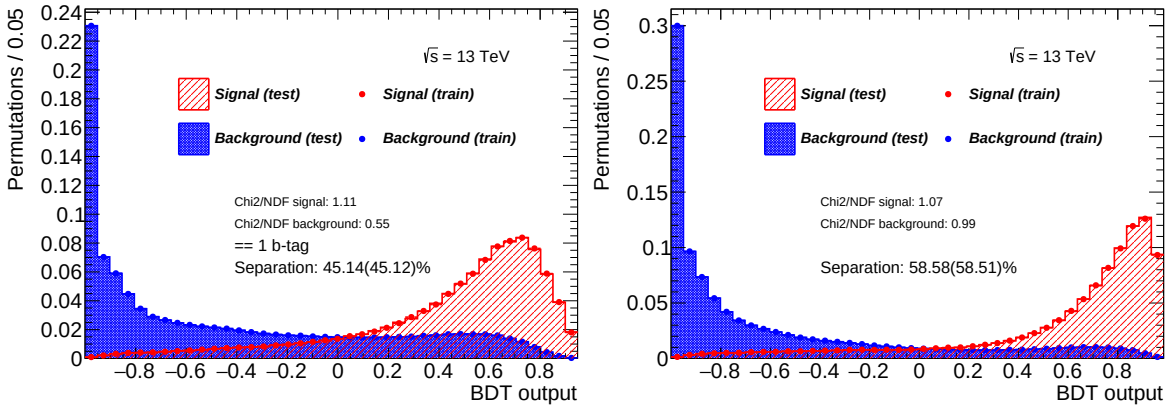

(a) 1 b-tag excl.

(b) 2 b-tag incl.

Figure 7.1: The BDT output distribution in events with exactly 1 b-tagged jet (left) and at least 2 b-tagged jets (right). Electron and muon channels are plotted together. The BDT discriminant is plotted for the training sample (dots) and testing sample (shaded areas).

The observed and predicted distributions of the BDT discriminant of the best permutation after the event selection (but before application of requirements on the BDT discriminant itself) are shown in Figure 7.2. The small mis-modelling is mostly covered by the signal modelling systematic uncertainties. It is also clear that background processes are more likely to have lower BDT discriminant values and that the fraction of background contamination decreases towards higher values of the BDT discriminant.

Different requirements on the minimal value of the BDT discriminant were tested in order to optimise the selection criteria and minimise the unfolded A_C uncertainties. Since in most of the studied kinematic regions the A_C measurement is dominated by statistical uncertainties, these tests were performed without systematic uncertainties and with `mc16a` and `mc16d` MC campaigns only to save computational power. The Asimov[3] datasets corresponding to different BDT tresholds are unfolded[4] and the A_C uncertainties are compared. The unfolded uncertainties depend relatively weakly on the BDT discriminant threshold - looser requirements include more background and badly reconstructed $t\bar{t}$ events, but to some extent this is compensated by larger statis-

[3]The Asimov dataset is constructed from the MC prediction of the signal and background. Thus, the unfolded values are expected to be in perfect agreement with the MC parton-level prediction.

[4]The unfolding procedure is described in detail in Chapter 8.

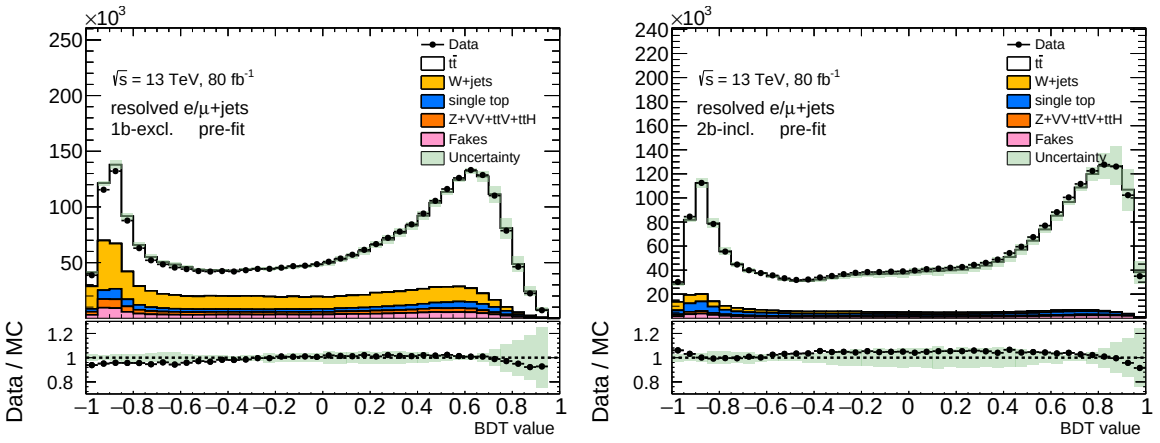

(a) 1 b-tag excl.

(b) 2 b-tag incl.

Figure 7.2: Comparison of the observed and predicted distributions of the BDT output discriminant of the best permutation in events with exactly 1 b-tagged jet (left) and at least 2 b-tagged jets (right). Electron and muon channels are plotted together. Only 2015-2017 data are plotted and the uncertainties include the statistical uncertainties and signal modelling uncertainties (the PS, ME and ISR uncertainties which will be introduced in Chapter 9).

tics of data sample leading to smaller statistical uncertainties. On the contrary, tighter thresholds lead to smaller background contribution and better reconstructed signal events but at some point the sample size becomes too small and the statistical uncertainties too large. In the inclusive case, the optimal threshold on the minimal BDT value is between -0.5 and 0.0, see Table 7.5, while in most of the differential bins it is rather between 0.0 and 0.5 as shown in Tables 7.6 and 7.7. As a compromise, the BDT discriminant of the best permutation is required to be larger than 0.3, which corresponds to $\approx 52\%$ $t\bar{t}$ selection efficiency while only $\approx 27\%$ of background events are kept in the combined 1 b-excl. and 2 b-incl. selection. The introduction of a relatively strict requirement on the BDT discriminant provides several advantages, e.g. the smaller fraction of background events makes the measurement less dependent on the background modelling uncertainties. Additionally, by rejecting badly reconstructed events it is possible to save a significant amount of computational resources.

After choosing the best permutation it is still necessary to reconstruct the neutrino four-momentum using the $E_{\mathrm{T}}^{\mathrm{miss}}$ information and a constraint from the mass of W boson:

$$m_W = (p_\ell + p_\nu)^2, \tag{7.2}$$

where p_ℓ and p_ν are four-momenta of the lepton and the corresponding neutrino, respectively. The p_ν^x and p_ν^y components of the neutrino momentum can be obtained from the magnitude and azimuthal angle of the $E_{\mathrm{T}}^{\mathrm{miss}}$ and the problem can be reduced to a quadratic equation for the p_ν^z. If there are two real solutions, the one which leads

BDT threshold	Inclusive A_C	Signal acc. [%]	Bckg. acc. [%]	Sig./Bckg.
-1.0	0.0036 ± 0.0016	100	100	3.2
-0.5	0.0036 ± 0.0014	79	61	4.1
0.0	0.0036 ± 0.0014	64	40	5.0
0.3	**0.0036 ± 0.0015**	**52**	**27**	**6.1**
0.5	0.0036 ± 0.0015	41	17	7.8
0.7	0.0036 ± 0.0017	22	5	13.0

Table 7.5: Influence of the BDT discriminant threshold on the Asimov unfolded A_C values. The combination of resolved and boosted topologies is studied and only statistical uncertainties with 80 fb^{-1} are presented. The signal and background acceptances in the resolved topology (combined 1 b-excl. and 2 b-incl. regions) are also shown, as well as the total signal to background ratios. The final choice of the BDT threshold is highlighted.

	A_C $(m(t\bar{t}))$				
BDT	[0, 500]	[500, 750]	[750, 1000]	[1000, 1500]	>1500 GeV
-1.0	0.0030 ± 0.0039	0.0040 ± 0.0028	0.0049 ± 0.0074	0.0059 ± 0.0110	0.0102 ± 0.0347
-0.5	0.0030 ± 0.0038	0.0040 ± 0.0026	0.0049 ± 0.0063	0.0060 ± 0.0096	0.0097 ± 0.0312
0.0	0.0030 ± 0.0037	0.0040 ± 0.0025	0.0049 ± 0.0062	0.0060 ± 0.0093	0.0095 ± 0.0297
0.3	**0.0031 ± 0.0037**	**0.0040 ± 0.0026**	**0.0049 ± 0.0062**	**0.0060 ± 0.0092**	**0.0095 ± 0.0297**
0.5	0.0030 ± 0.0038	0.0040 ± 0.0027	0.0049 ± 0.0062	0.0060 ± 0.0094	0.0106 ± 0.0299
0.7	0.0030 ± 0.0044	0.0040 ± 0.0030	0.0049 ± 0.0065	0.0060 ± 0.0095	0.0093 ± 0.0303

Table 7.6: Influence of the BDT discriminant threshold on the Asimov unfolded A_C values in the $m(t\bar{t})$ differential measurement. The combination of resolved and boosted topologies is studied and only statistical uncertainties with 80 fb^{-1} are presented. The final choice of the BDT threshold is highlighted.

to the top-quark mass closest to 172.5 GeV is chosen. In the case of no real solutions, the E_T^{miss} is varied by a minimal amount necessary to obtain a real solution.

7.2.2 Reconstruction in the Boosted Topology

In the boosted topology the four-momentum of the large-R jet satisfying the selection criteria from Section 7.1.3 is taken as an estimate of the four-momentum of the hadronically decaying top quark. The leptonically decaying top quark four-momentum is constructed from the isolated lepton, selected small-R jet close to the lepton and the neutrino four-momentum. The neutrino four-momentum is calculated using the constraint from Equation (7.2), similarly as in the case of the resolved topology. The only difference with respect to the resolved topology is that if there are two real solutions for p_ν^z, the one with minimum $|p_\nu^z|$ is taken.

A_C ($\beta_z(t\bar{t})$)				
BDT	[0, 0.3]	[0.3, 0.6]	[0.6, 0.8]	[0.8, 1.]
-1.0	0.0000 ± 0.0062	0.0014 ± 0.0046	0.0025 ± 0.0040	0.0086 ± 0.0034
-0.5	0.0000 ± 0.0055	0.0014 ± 0.0041	0.0025 ± 0.0037	0.0086 ± 0.0033
0.0	0.0001 ± 0.0053	0.0014 ± 0.0040	0.0025 ± 0.0037	0.0086 ± 0.0034
0.3	**0.0000 ± 0.0052**	**0.0015 ± 0.0040**	**0.0025 ± 0.0038**	**0.0086 ± 0.0035**
0.5	0.0000 ± 0.0052	0.0015 ± 0.0040	0.0025 ± 0.0039	0.0086 ± 0.0037
0.7	0.0000 ± 0.0055	0.0015 ± 0.0043	0.0025 ± 0.0042	0.0086 ± 0.0043

Table 7.7: Influence of the BDT discriminant threshold on the Asimov unfolded A_C values in the $\beta_z(t\bar{t})$ differential measurement. The combination of resolved and boosted topologies is studied and only statistical uncertainties with 80 fb^{-1} are presented. The final choice of the BDT threshold is highlighted.

7.3 Control Distributions

The agreement between the data and the MC prediction is studied in various 'control' distributions, which compare basic event properties such as lepton and jet p_T, reconstructed top-quark p_T etc. The control distributions are plotted separately for the e and μ channels, 1 b-excl. and 2 b-incl. regions and for the resolved and boosted topologies. Here we present a selection of the most important distributions. Distributions with the 1 b-excl. selection are shown in Figures 7.3 – 7.6 and the 2 b-excl. selection is presented in the Appendix in Figures A.3 – A.6. In all cases the data points are compared to the SM prediction and a ratio plot is provided. The green uncertainty band corresponds to the MC statistical and systematic uncertainties, which are described in Chapter 9. The luminosity uncertainty and the signal and background normalisation uncertainties are not included.

In general, a good agreement between data and prediction is observed and the discrepancies are covered by the uncertainties on the SM prediction. In several cases a slight disagreement is related to the known problem with the POWHEG+PYTHIA 8 generators, which predict harder top p_T spectrum [244]. This mis-modelling is observed as a slope in the data/MC agreement in almost all figures showing p_T or E_T^{miss} distributions. The boosted topology selection is efficient only in the high-p_T regime, therefore in this case the mis-modelling is effectively observed as a large normalisation effect of about 20%. The treatment of this normalisation difference in the A_C measurement is discussed in Section 9.2.1.

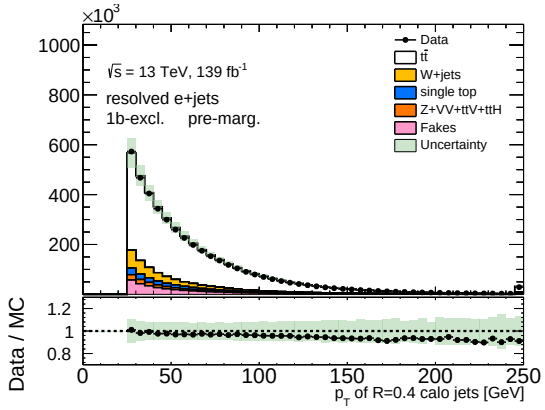

(a) Jet p_{T}.

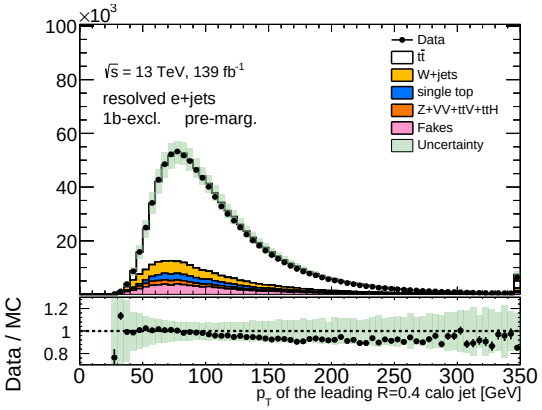

(b) Leading jet p_{T}.

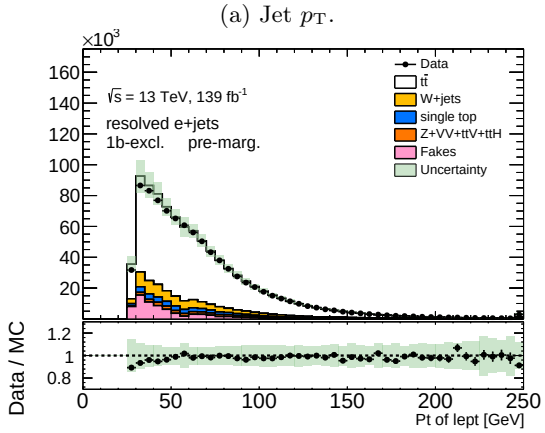

(c) Lepton p_{T}.

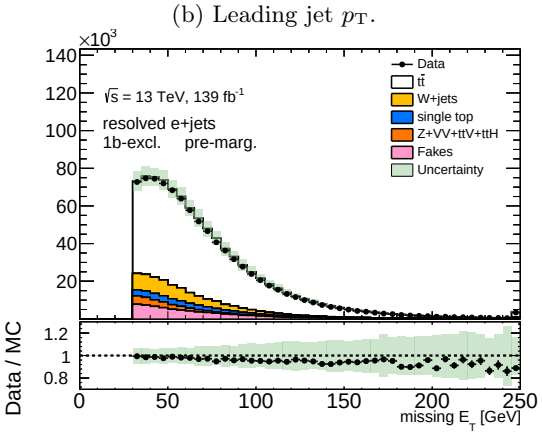

(d) $E_{\mathrm{T}}^{\mathrm{miss}}$.

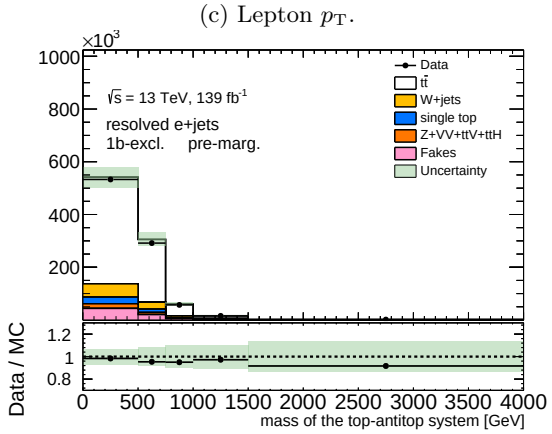

(e) $m(t\bar{t})$.

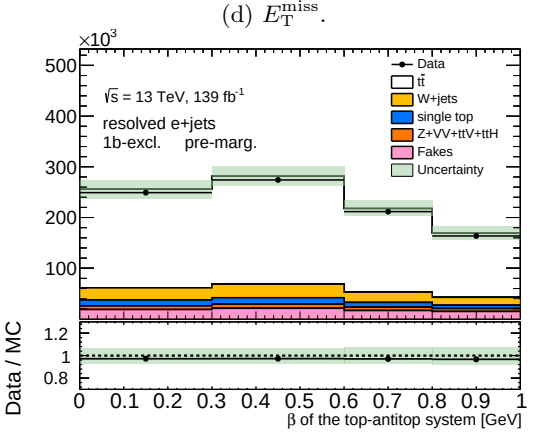

(f) $\beta_{\mathrm{z}}(t\bar{t})$.

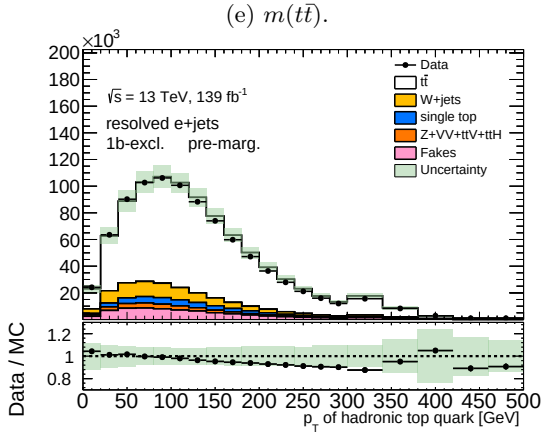

(g) BDT reco. t^{had} p_{T}.

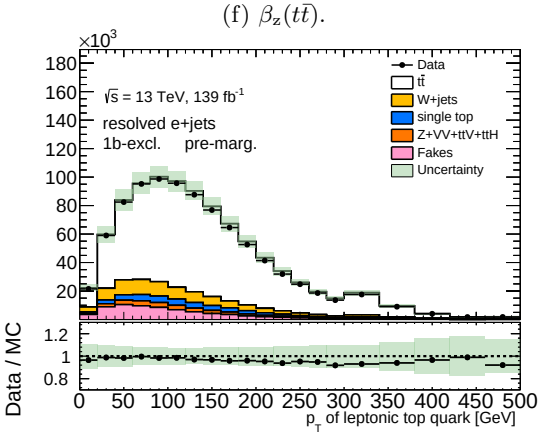

(h) BDT reco. t^{lep} p_{T}.

Figure 7.3: A data to prediction comparison in resolved e+jets channel, 1 excl. b-tag region. The last bin includes overflow events. The green band corresponds to the MC statistical and systematic uncertainties. Luminosity and normalisation uncertainties are not included.

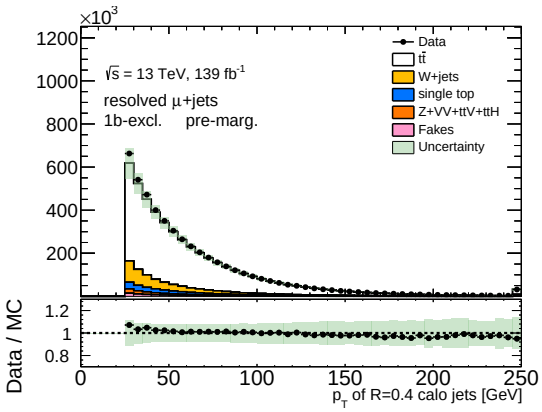

(a) Jet p_{T}.

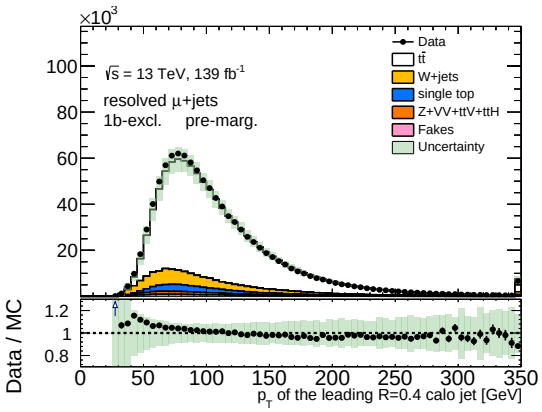

(b) Leading jet p_{T}.

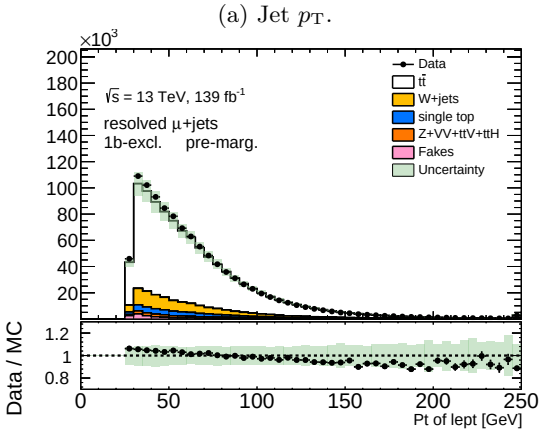

(c) Lepton p_{T}.

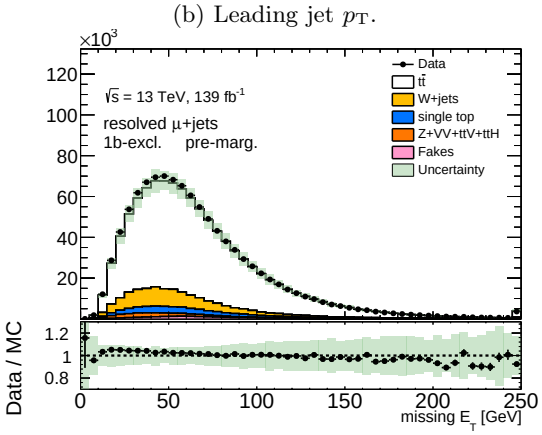

(d) $E_{\mathrm{T}}^{\mathrm{miss}}$.

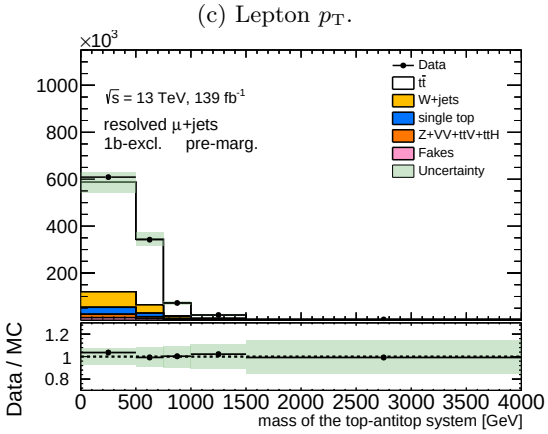

(e) $m(t\bar{t})$.

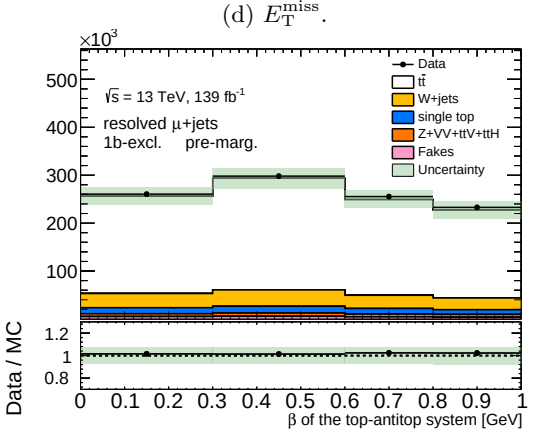

(f) $\beta_{\mathrm{z}}(t\bar{t})$.

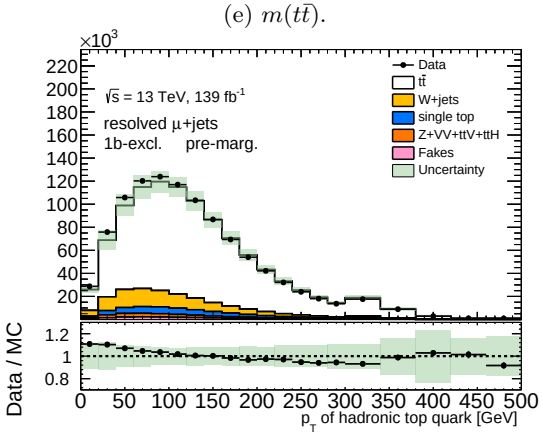

(g) BDT reco. t^{had} p_{T}.

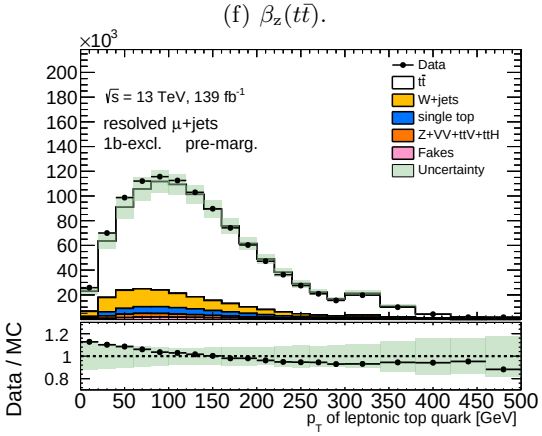

(h) BDT reco. t^{lep} p_{T}.

Figure 7.4: A data to prediction comparison in resolved μ+jets channel, 1 excl. b-tag region. The last bin includes overflow events. The green band corresponds to the MC statistical and systematic uncertainties. Luminosity and normalisation uncertainties are not included.

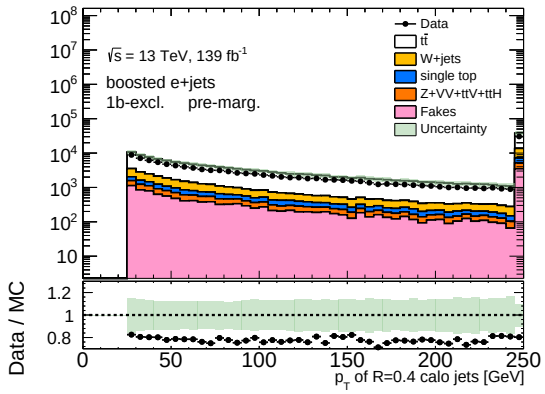

(a) Jet p_{T}.

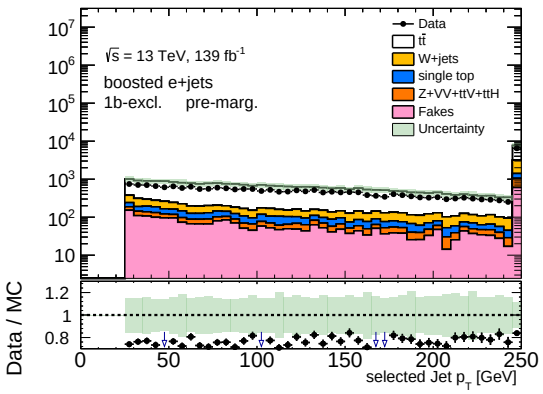

(b) Jet close to the lepton ($\Delta R(\mathrm{jet}, \ell) < 1.5$) p_{T}.

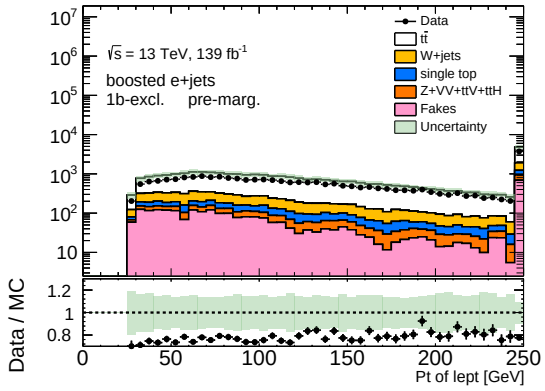

(c) Lepton p_{T}.

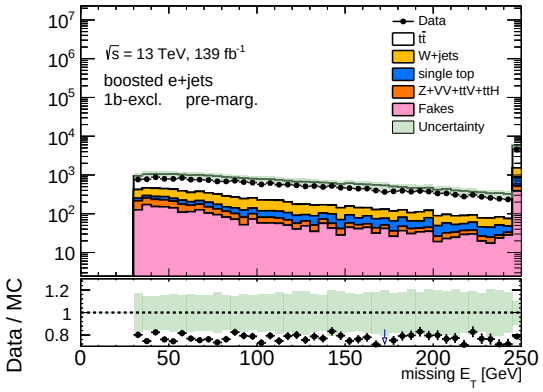

(d) $E_{\mathrm{T}}^{\mathrm{miss}}$.

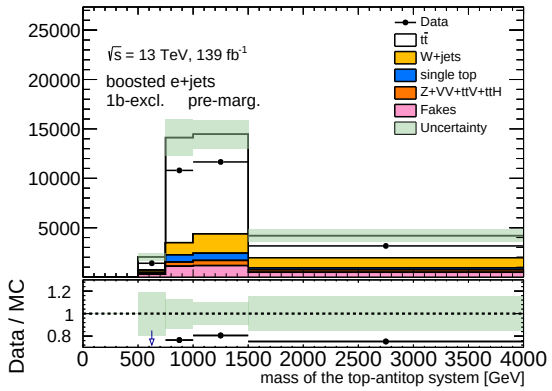

(e) $m(t\bar{t})$.

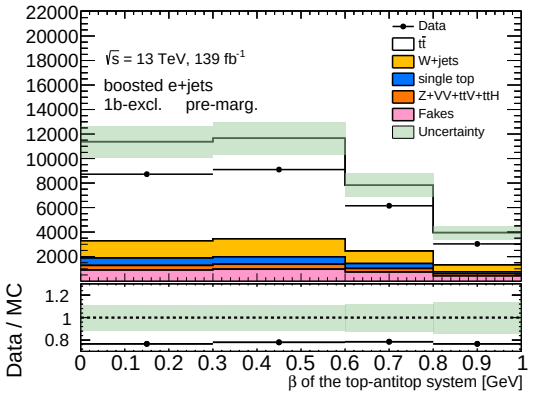

(f) $\beta_{\mathrm{z}}(t\bar{t})$.

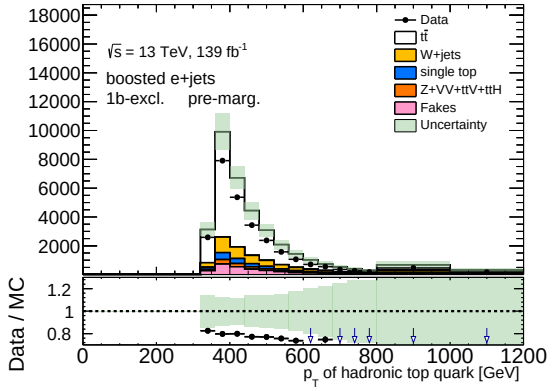

(g) Reco. t^{had} (large-R jet) p_{T}.

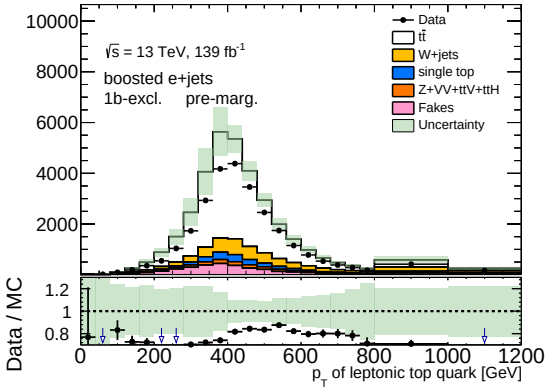

(h) Reco. t^{lep} p_{T}.

Figure 7.5: A data to prediction comparison in boosted e+jets channel, 1 excl. b-tag region. The last bin includes overflow events. The green band corresponds to the MC statistical and systematic uncertainties. Luminosity and normalisation uncertainties are not included.

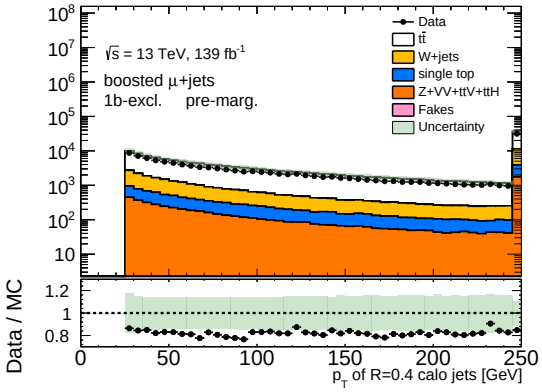

(a) Jet p_{T}.

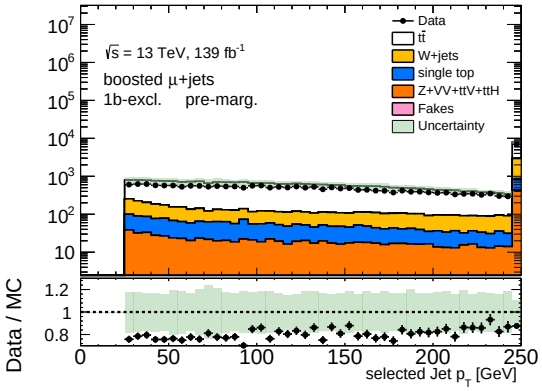

(b) Jet close to the lepton ($\Delta R(\mathrm{jet}, \ell) < 1.5$) p_{T}.

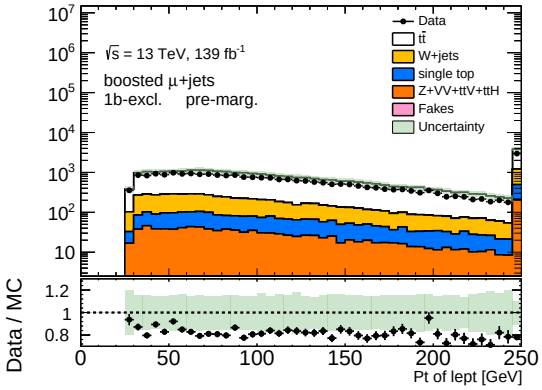

(c) Lepton p_{T}.

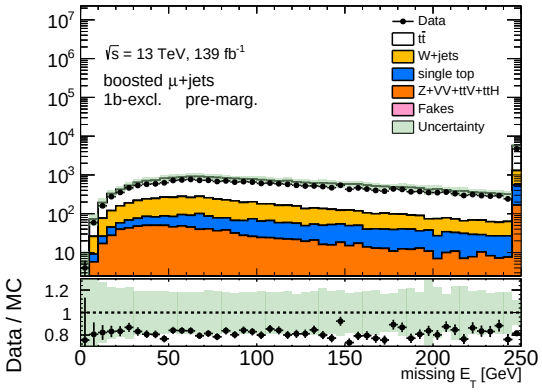

(d) $E_{\mathrm{T}}^{\mathrm{miss}}$.

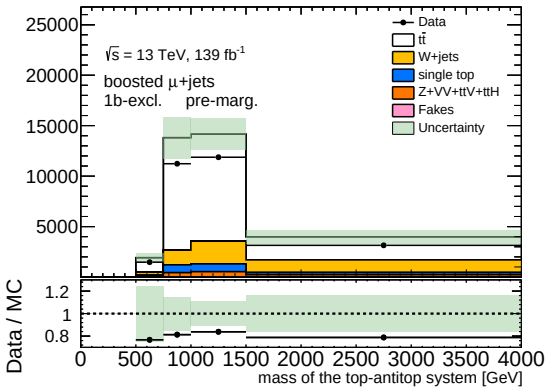

(e) $m(t\bar{t})$.

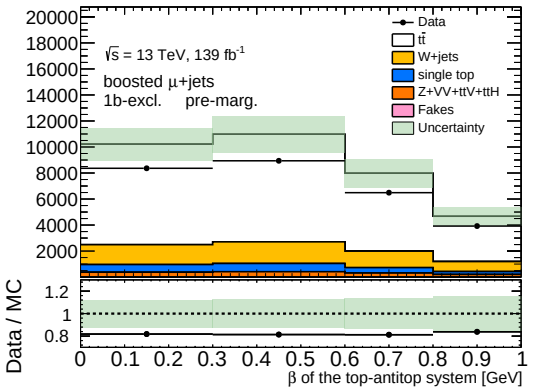

(f) $\beta_{\mathrm{z}}(t\bar{t})$.

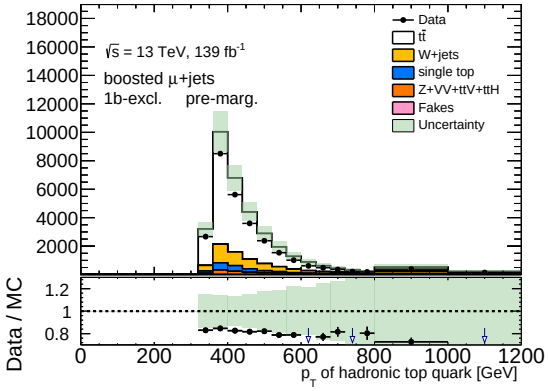

(g) Reco. t^{had} (large-R jet) p_{T}.

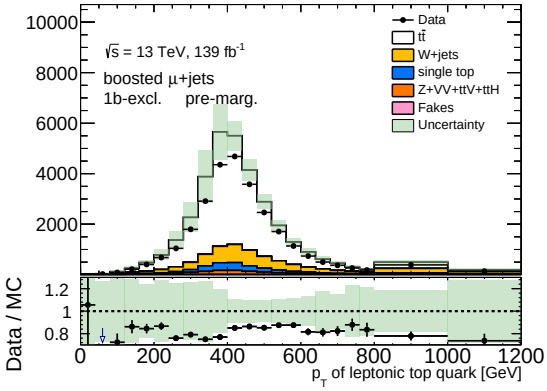

(h) Reco. t^{lep} p_{T}.

Figure 7.6: A data to prediction comparison in boosted μ+jets channel, 1 excl. b-tag region. The last bin includes overflow events. The green band corresponds to the MC statistical and systematic uncertainties. Luminosity and normalisation uncertainties are not included.

Chapter 8

Unfolding

8.1 Introduction

In general, particle detectors are never perfect and the measured quantities are affected by limited acceptance, non-linear detector response, limited energy and momentum resolution etc. Furthermore, event reconstruction (e.g. using methods described in Section 7.2) is not perfect either and further dilutes the studied observable. The directly reconstructed distributions are often referred to as distributions at the *reconstruction level*.

On the contrary, the theoretical predictions are typically detector-independent. One possibility is to calculate the physical quantities at the *parton level* – using directly the kinematic of the particles of interest, even if they are unstable and cannot be observed directly in the experiments. In the context of this analysis this corresponds to calculating the A_{C} directly from the rapidities of the top quarks before decay. The second possibility, referred to as the *particle-level* prediction, is to calculate the quantities of interest from the final state objects that can be actually observed by the experiments. In our case this corresponds to calculating the A_{C} value from the kinematic of leptons and jets from the $t\bar{t}$ decay. Particle-level predictions are often calculated in the 'fiducial' phase space, e.g. in the η acceptance region of the experiment. The main disadvantage of the particle-level predictions is that they are much more model-dependent than the parton-level ones, e.g. due to an ambiguity in the particle-level jet definition. In this analysis the parton-level predictions are used.

The process in which the theoretical quantities and distributions are transformed by the experimental and reconstruction imperfections is referred to as *folding* and the inverse process is known as *unfolding*. Unfolding transforms the reconstruction-level distributions to the parton/particle-level ones and enables to compare the experimental result with the theory and with results from different experiments. In this analysis, the Fully Bayesian Unfolding (FBU) [245] is used to estimate the parton-level charge asymmetry from the reconstruction-level $\Delta|y|$ spectra.

8.2 Fully Bayesian Unfolding Formulation

The FBU is an application of the Bayesian inference to the problem of unfolding: Given the data stored in a histogram with N_r bins ($\mathrm{D} \in \mathbb{N}^{N_r}$) and the response matrix $\mathcal{M} \in \mathbb{R}^{N_r} \times \mathbb{R}^{N_t}$, the question is what is the actual parton-level spectrum with N_t bins ($\tilde{\mathrm{T}} \in \mathbb{R}^{N_t}$). In the terms of the Bayesian inference this corresponds to:

$$P(\mathrm{T}|\mathrm{D}, \mathcal{M}) \propto \mathcal{L}(\mathrm{D}|\mathrm{T}, \mathcal{M})\pi(\mathrm{T}), \tag{8.1}$$

where $P(\mathrm{T}|\mathrm{D}, \mathcal{M})$ is the *posterior* probability of the true spectrum T; $\mathcal{L}(\mathrm{D}|\mathrm{T}, \mathcal{M})$ is the likelihood function of D given T and a *response* matrix $\mathcal{M}$ and $\pi(\mathrm{T})$ is the *prior* probability density for the true spectrum T. In other words, by sampling every possible true spectrum it is possible to obtain a probability density function for the true distributions and in our case also for the A_C itself.

The prior, likelihood, treatment of systematic uncertainties and the process of obtaining the posterior probability density are further described in the following sections.

8.3 Prior

The prior probability density $\pi(\mathrm{T})$ is to be chosen according to what is known about T before the measurement is performed. Typically, this corresponds to a reasonably large range which covers all realistic T distributions. If all possibilities are considered with the same probability, the uninformative prior is used:

$$\pi(\mathrm{T}) \propto \begin{cases} 1 & \text{if } \mathrm{T}_t \in [\mathrm{T}_t^{\mathrm{min}}, \mathrm{T}_t^{\mathrm{max}}], \forall t \in [1, N_t] \\ 0 & \text{otherwise} \end{cases} . \tag{8.2}$$

If some of the possible T distributions are considered to be more probable, this can by added as an additional information to reduce the variance by introducing a small bias towards the preferred truth distributions:

$$\pi(\mathrm{T}) \propto \begin{cases} e^{\alpha S(\mathrm{T})} & \text{if } \mathrm{T}_t \in [\mathrm{T}_t^{\lceil}, \mathrm{T}_t^{\rceil}], \forall t \in [1, N_t] \\ 0 & \text{otherwise} \end{cases} , \tag{8.3}$$

where α is an arbitrary parameter and $S(\mathrm{T})$ is a regularisation function. In this analysis an uninformative prior with $[0, 2\tilde{\mathrm{T}}]$ is used, where $\tilde{\mathrm{T}}$ is the parton-level spectrum of the nominal MC sample.

8.4 Likelihood

The response matrix $\mathcal{M}$ with elements $m_{ij} = \epsilon_{t_j} P(r_i|t_j)$ can be obtained from the MC signal sample and contains two pieces of information:

- ϵ_{t_j} - efficiency for a parton-level event produced in bin t_j to be reconstructed in any bin r.

- $P(r_i|t_j)$ - probability of a parton-level event produced in bin t_j to be observed at the reconstruction level in bin r_i. This is summarised in *migration* matrices. Migration matrices used in this analysis are provided in the Appendix in Figures A.7 – A.9.

Prediction of the reconstruction-level spectrum $\mathrm{R} \in \mathbb{R}^{N_r}$ corresponding to a given parton-level spectrum T is then

$$r_i(\mathrm{T}, \mathcal{M}) = \sum_{j=0}^{N_r} m_{ij} t_j. \tag{8.4}$$

The likelihood is defined by comparing the observed spectrum D with the expected one R; assuming Poisson statistics and background prediction $\mathrm{B} \in \mathbb{R}^{N_r}$:

$$\mathcal{L}(\mathrm{D}|\mathrm{T}, \mathcal{M}, \mathrm{B}) = \prod_{i=1}^{N_r} \frac{(r_i + b_i)^{d_i}}{d_i!} e^{-(r_i+b_i)}. \tag{8.5}$$

8.5 Nuisance Parameter Marginalisation

Treatment of systematic uncertainties is naturally included in the FBU by extending the likelihood with nuisance parameter (NP) terms corresponding to the individual systematic uncertainties. By using this approach it is possible to significantly reduce the total uncertainty, since the correlations between the uncertainties are correctly taken into account. In some cases it is also possible to constrain the systematic uncertainties using information from the data. This feature is unique to the FBU and is the main motivation for using the FBU in the A_{C} measurements.

The marginal likelihood is defined as

$$\mathcal{L}(\mathrm{D}|\mathrm{T}) = \int \mathcal{L}(\mathrm{D}|\mathrm{T}, \theta)\pi(\theta)\mathrm{d}\theta, \tag{8.6}$$

where θ are the nuisance parameters and $\pi(\theta)$ their priors, typically Gaussian distributions G with $\mu = 0$ and $\sigma = 1$. Two main categories of systematic uncertainties are considered:

- Background normalisation uncertainties θ_b which affect only the background predictions.
- Uncertainties related to object identification, reconstruction and calibration θ_s affecting both the signal and the background predictions, $\mathrm{R}(\mathrm{T};\theta_s)$ and $\mathrm{B}(\theta_s,\theta_b)$, respectively.

The signal reconstruction-level prediction is then defined as:

$$r_i(\mathrm{T},\mathcal{M};\theta_s) = r_i(\mathrm{T},\mathcal{M};0)\left(1+\sum_k \theta_s^k \Delta r_i^k\right), \tag{8.7}$$

where Δr_i^k is the systematic variation corresponding to the uncertainty k in the i-th histogram bin.
Similarly, the prediction for each background process:

$$b_i(\theta_s,\theta_b) = b_i(0)(1+\theta_b\Delta b)\left(1+\sum_k \theta_s^k \Delta b_i^k\right), \tag{8.8}$$

where Δb is the uncertainty on the background normalization.
The marginal likelihood can be then rewritten as:

$$\mathcal{L}(\mathrm{D}|\mathrm{T}) = \int \mathcal{L}(\mathrm{D}|\mathrm{R}(\mathrm{T};\theta_s),\mathrm{B}(\theta_s,\theta_b))G(\theta_s)G(\theta_b)\mathrm{d}\theta_s\mathrm{d}\theta_b. \tag{8.9}$$

An example of a marginalised nuisance parameter is shown in Figure 8.1. In this case the NP is *constrained*, i.e. the posterior probability density is narrower than the prior. In practise this means that the corresponding systematic uncertainty was overestimated and by using the statistical power in data it is possible to reduce this uncertainty. Furthermore, the NP is also *pulled* and the central value is shifted. In other words, the corresponding parameter was measured in data and the central value is found to be slightly different than initially predicted.

Nuisance parameter constraints reduce the total uncertainty. At the same time, pulls improve the agreement between data and MC by modifying the prediction according to what can be learned from data. Consequently, in the post-marginalisation distributions better agreement between data and MC is observed and the uncertainties are reduced. This improvement will be clearly observed in Chapter 10 in Figure 10.4.

The possibility of pulling and constraining the systematic uncertainties provides an important advantage, but special caution is also required, especially if relatively large pulls and constraints are observed. Large pulls and constraints might be a result of unphysical spikes in the spectrum of the systematic uncertainty, typically due to statistical fluctuations in the corresponding MC samples. Therefore it is important to validate the post-marginalisation agreement between data and MC in various control

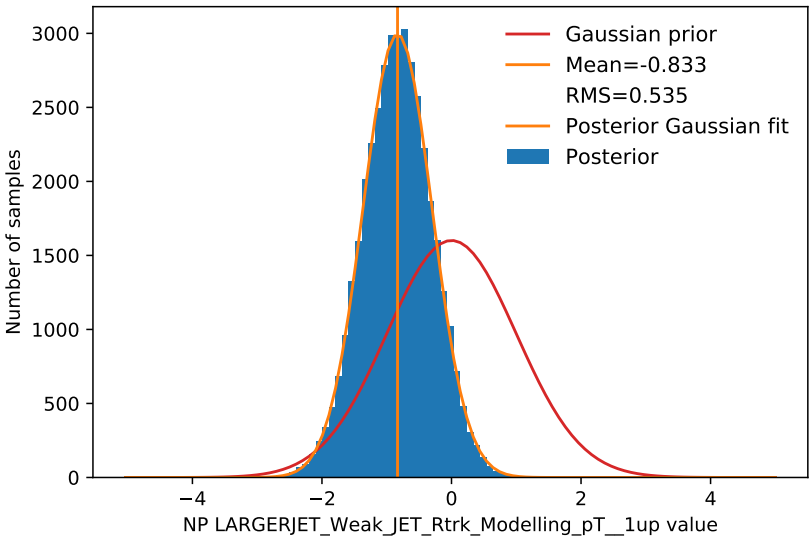

Figure 8.1: Example of a pulled and constrained nuisance parameter. The Gaussian prior is shown in red and the x-axis is in the units of the corresponding RMS. The posterior distribution obtained by sampling is shown in blue and has a perfect Gaussian shape.

distributions, such as those presented in the Appendix in Figures A.20 – A.19.

8.6 Signal Region Combination

Utilisation of orthogonal channels, e.g. regions with different background contamination, helps to constrain the individual systematic uncertainties and thus to reduce the total uncertainty. Having the nuisance parameters common to all channels, the likelihood is:

$$\mathcal{L}(\{\mathrm{D}_1 \cdots \mathrm{D}_{N_{\mathrm{ch}}}\}|\mathrm{T}) = \int \prod_{i=1}^{N_{\mathrm{ch}}} \mathcal{L}(\mathrm{D}_i|\mathrm{T};\theta)G(\theta)\mathrm{d}\theta, \tag{8.10}$$

where N_{ch} is the number of orthogonal channels.

The final posterior probability including systematic uncertainties and multiple orthogonal signal regions can be then written as

$$P(\mathrm{T}|\{\mathrm{D}_1 \cdots \mathrm{D}_{N_{\mathrm{ch}}}\}) = \int \prod_{i=1}^{N_{\mathrm{ch}}} \mathcal{L}\left(\mathrm{D}_i|\mathrm{R}_i(\mathrm{T};\theta_s), \mathrm{B}_i(\theta_s,\theta_b)\right) G(\theta_s)G(\theta_b)\pi(\mathrm{T})\mathrm{d}\theta_s\mathrm{d}\theta_b. \tag{8.11}$$

In this analysis events are split into four signal regions by topology (resolved/boosted) and b-tag multiplicity (1 b-excl./2b-incl.).

8.7 Sampling

The posterior $P(\mathrm{T},\mathrm{D})$ is determined by sampling the (N_t+N_{NP})-dimensional parameter space and by evaluating for each point the product of $\mathcal{L}(\mathrm{D}|\mathrm{T},\mathcal{M})$ and $\pi(\mathrm{T})$, thus performing a numerical integration.

The most simple option is to perform a *grid sampling* - to evaluate $\mathcal{L}(\mathrm{D}|\mathrm{T},\mathcal{M})\pi(\mathrm{T})$ at n_G equally spaced positions along each dimension. However, this leads to $n_G^{N_t+N_{\mathrm{NP}}}$ samples and is extremely inefficient. In practice, advanced techniques specialized for multi-dimensional sampling based on the Markov Chain Monte Carlo method (MCMC) [246] are used within FBU. In this analysis, the No-U-Turn Sampler (NUTS) [247] algorithm is used, based on the Hamiltonian Monte Carlo [248] implemented using the PyMC3 package [249].

The sampler initially performs a tuning sampling, during which it scans the parameter space, adapts the sampling configuration specifically for the studied problem and finds suitable initial values of the individual parameters. Afterwards, the 'main' sampling is performed – each sampling step corresponds to one point in the posterior distributions for each parameter. The posterior distributions contain the full probability density information; the mean of distribution can be afterwards taken as the unfolded estimate and the RMS as the corresponding uncertainty. Similarly, posterior probability density distribution can be obtained for any quantity that is computed from the spectrum, such as the A_{C}:

$$p(A_C|\mathrm{D}) = \int \delta(A_C - A_C(\mathrm{T}))P(\mathrm{T}|\mathrm{D})d\mathrm{T}. \tag{8.12}$$

Effectively, this corresponds to calculating the observable of interest from the bin contents for every single sample.

The numbers of tuning and sampling steps are free parameters of the procedure and various combinations were studied. The PyMC3 package provides self-diagnostic warnings in the case of too small numbers of both tuning and samplings steps. There is no motivation to use a large number of tuning steps, since typically even few hundreds are enough for the algorithm to converge to the region of interest. In this analysis we conservatively used 2500 sampling steps. In general, a larger number of sampling steps increases precision of the method, since more points are used to create the posterior distributions. At the same time the sampling can be very CPU expensive, especially if the number of dimensions is large. In this analysis 10000 sampling steps are used as a compromise and we have shown that with this number of sampling steps the statistical uncertainty from sampling is negligible. Furthermore, both tuning and sampling is performed in four independent chains to take the advantage of multi-core CPUs and the posteriors from 4×10000 steps are then combined. Additionally, the choice of

multiple independent sampling chains offers a possibility to cross-check the agreement of the outputs using the Gelman-Rubin convergence diagnostic [250].

A potential problem of the sampling approach is that due to correlations between the individual bins and nuisance parameters the numerical integration across all dimensions might lead to biased posteriors. Thus, the mean of the posterior distribution for a given parameter might not be exactly equal to the 'true' value of this parameter which corresponds to the mode of the FBU likelihood. This effect has been carefully studied using the Asimov pseudo-data. A completely independent maximum-a-posteriori (MAP) [251] approach is also tested in order to validate the usage of the sampling method in this particular measurement. The MAP finds the mode of the likelihood numerically, but provides only a point estimate which can be biased if the mode is not a good representative of the likelihood distribution. The estimate of the corresponding uncertainty to the MAP estimation is technically challenging and is not performed in this analysis.

A good agreement of the central values is observed between the sampling and MAP approaches, as demonstrated in the plots with nuisance parameter pulls (see Figures 10.1 – 10.3) and in the Asimov A_{C} posteriors presented in the Appendix (Figures A.10 – A.12). The mean of the posterior distributions is therefore used to measure the A_{C} in data.

8.8 Binning Choice and Linearity Tests

An important step in the unfolding optimisation is related to proper choice of binning in the $\Delta|y|$ distributions, as well as in the differential variable in measurements of the A_{C} as a function of $m(t\bar{t})$ and $\beta_{\mathrm{z}}(t\bar{t})$.

In the case of differential measurements, the choice of binning is motivated by physics considerations. Fine binning in $m(t\bar{t})$ is desirable in order to discriminate different physics models. Since many BSM theories predict enhancement of the asymmetry in the very high $m(t\bar{t})$, it is important to set the last bin threshold as high as possible. At high $\beta_z(t\bar{t})$ the fraction of the $q\bar{q}$ annihilation is larger and the asymmetry is enhanced in a model independent way. Taking into account the statistical limitations the following binning is chosen:

- $\beta_z(t\bar{t})$ - 4 bins: $[0, 0.3, 0.6, 0.8, 1]$.
- $m(t\bar{t})$ [GeV] - 5 bins: $[0, 500, 750, 1000, 1500, \infty]$.

Two competing factors determine the choice of the number of bins in the $\Delta|y|$ distribution:

- Smaller number of bins implies smaller relative statistical uncertainties. At least

two bins are necessary to compute A_C (positive and negative side of the $\Delta|y|$ distribution).

- Larger number of bins allows to track the migrations more accurately and thus allows to obtain unbiased estimates. However, only migrations that change the $\Delta|y|$ sign affect the computation of the A_C and these are more likely for small $\Delta|y|$ values. Therefore a fine binning is required in the central $\Delta|y|$ region.

In this analysis four bins in $\Delta|y|$ are used and the same binning is used at both the reconstruction and the parton level in all four signal regions mentioned in Section 8.6. However, the x-value in $\Delta|y|$ binning $[-5, -x, 0, x, 5]$ is optimised separately in the inclusive measurement and in each of the differential bins. The outer bin edges (± 5) are effectively the same as $\pm\infty$, since there are no $t\bar{t}$ events with $\Delta|y|$ values beyond $\approx \pm 4$.

In order to find the optimal x-values in $\Delta|y|$ binning, samples with various parton-level asymmetries are prepared and the unfolding procedure is required to work properly across a range of different parton-level A_C values. In this analysis, the PROTOS [252] generator is used to simulate axigluon (mass of 250 GeV) contribution to the charge asymmetry and the nominal signal sample is subsequently correspondingly reweighted. Parton-level asymmetries of approximately $\pm 1\%$, $\pm 2\%$, $\pm 3\%$ and $\pm 4\%$ are considered. The unfolding response is required to be linear with a slope ≈ 1 and offset ≈ 0 and an example is shown in Figure 8.2. Typically, larger x leads to larger slope and the other way around. Different values of x were tried with a step of 0.1 and after several iterations the one with the best slope and offset values is chosen. The optimal x-values range from 0.3 to 1.0, depending on the differential bin where the measurement is performed. During the optimisation process the unfolding was performed without systematic uncertainties to save computational power. The best option is validated with final configuration with all systematic uncertainties and 300 pseudo-experiments are used to test also the effect of statistical fluctuations in the MC samples. Only negligible differences are found between the slope and offset values in configurations with and without systematic uncertainties. A summary of the binning with the corresponding slope and offset values is shown in Table 8.1. The effect of non-perfect linearity is studied as a systematic uncertainty and will be discussed in Section 9.3.2.

A linear reweighting in which the event weights are modified linearly according to the parton level asymmetry[1] is used as a cross check. This reweighting is not motivated physically, but it provides a rough estimate of an ambiguity in the slope and offset values caused by choosing a specific BSM scenario for the binning optimisation. The differences in the obtained slope values are found to be smaller than 10% in all differential bins and the offset values are very close to 0 in both reweighting scenarios.

[1] $w = 1 + k \times \Delta|y|$, where k is a constant equal to $\pm 10\%$, $\pm 20\%$ and $\pm 30\%$.

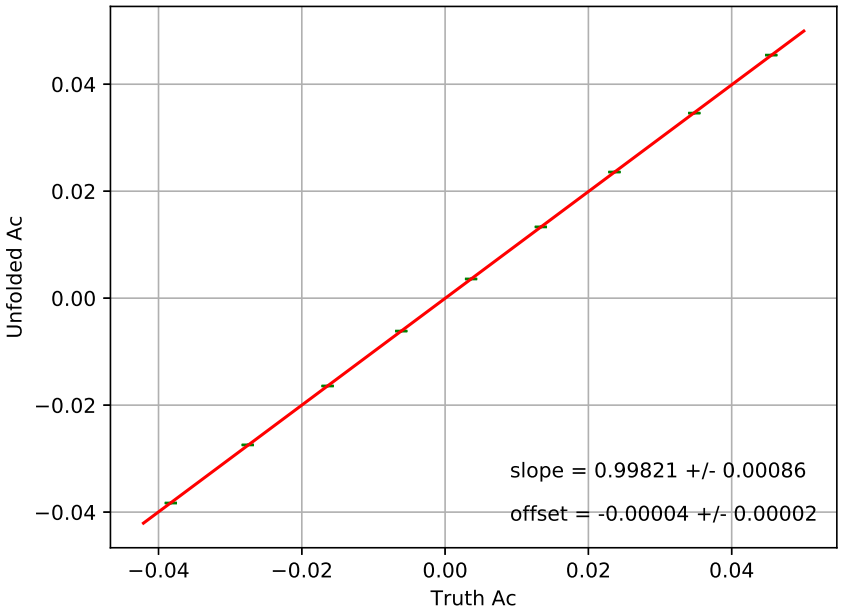

Figure 8.2: Example of a linearity test of the unfolding response in the inclusive case. The full setup with all systematic uncertainties is used and 300 pseudo-experiments are performed.

	$\Delta\|y\|$ binning	Linearity PROTOS	
		slope	offset
inclusive	[-5, -0.5, 0, 0.5, 5]	0.998±0.001	0.0000±0.0000
$m(t\bar{t}) \in$ [0, 500 GeV]	[-5, -0.4, 0, 0.4, 5]	1.001±0.003	0.0001±0.0001
$m(t\bar{t}) \in$ [500, 750]	[-5, -0.6, 0, 0.6, 5]	0.986±0.001	0.0001±0.0000
$m(t\bar{t}) \in$ [750, 1000]	[-5, -1.0, 0, 1.0, 5]	0.997±0.003	0.0002±0.0001
$m(t\bar{t}) \in$ [1000, 1500]	[-5, -0.9, 0, 0.9, 5]	0.998±0.004	-0.0004±0.0002
$m(t\bar{t}) \in$ [1500, ∞]	[-5, -0.9, 0, 0.9, 5]	1.027±0.016	-0.0009±0.0005
$\beta_z(t\bar{t}) \in$ [0.0, 0.3]	[-5, -0.3, 0, 0.3, 5]	1.015±0.006	-0.0001±0.0001
$\beta_z(t\bar{t}) \in$ [0.3, 0.6]	[-5, -0.3, 0, 0.3, 5]	1.007±0.002	0.0002±0.0001
$\beta_z(t\bar{t}) \in$ [0.6, 0.8]	[-5, -0.5, 0, 0.5, 5]	1.012±0.002	-0.0005±0.0001
$\beta_z(t\bar{t}) \in$ [0.8, 1.0]	[-5, -0.7, 0, 0.7, 5]	0.995±0.002	0.0007±0.0001

Table 8.1: Linearity tests of the unfolding response. Binning, slope and offset for the inclusive and differential A_C measurements is shown. Full setup with all systematic uncertainties is used and 300 pseudo-experiments are performed.

Chapter 9

Systematic Uncertainties

In this chapter the individual systematic uncertainties affecting the A_C measurement are described. To each systematic uncertainty a nuisance parameter is assigned, unless specified otherwise, and the effect of systematic uncertainties is embedded directly in the FBU likelihood as described in Section 8.5. Individual systematic uncertainties are considered to be uncorrelated and typically they are either *one-sided* or *two-sided*. In the case of one-sided uncertainties, which include e.g. comparisons with alternative MC generators, the difference between the nominal and alternative distribution is taken as the uncertainty. The two-sided uncertainties, typically affecting various scale factors which can be either a bit larger or smaller, require firstly averaging of the effects of the *up* and *down* variations. All systematic uncertainties are taken as $\pm$ the obtained effect, i.e. all uncertainties are *symmetrised*. Finally, unless specified otherwise, a Gaussian prior with RMS equal to the magnitude of the systematic effect is used as a prior entering the FBU likelihood. Typically, the systematic uncertainties are considered correlated between the individual signal regions discussed in Section 8.6 with few exceptions mentioned below.

9.1 Experimental Uncertainties

In this section, systematic uncertainties originating from the detector and reconstruction imperfections are described.

9.1.1 Luminosity

The luminosity uncertainty affects the normalisation of the MC samples and slightly changes the relative background contributions, since the multijet background is data-driven. As discussed already in Section 6.1, the relative luminosity uncertainty of the combined 2015-2018 dataset is 1.7%.

9.1.2 Pile-up

Scale factors are applied in order to correct for the differences between the pile-up conditions in data and simulated samples. The uncertainties on the corresponding scale factors are considered.

9.1.3 Lepton-Related Uncertainties

Lepton (e, μ) identification, reconstruction, isolation and trigger performance, as well as resolution and momentum scale, differ between data and simulations and scale factors are applied to correct these differences. The scale factors are obtained using the tag and probe technique in well understood decays of the Z boson, J/ψ and W boson into leptons [195, 197, 198]. The uncertainties on these corrections are treated as systematic uncertainties.

9.1.4 Jet Energy Scale

The JES and its uncertainty is estimated from the collision data and MC simulations using techniques described in Ref. [201]. Events with a vector boson and additional jets are used to calibrate jets in the central region. Dijet events are used to calibrate forward jets against the jets in the central region and multijet events are used to calibrate high-p_{T} jets. The measurements are combined and decorrelated into a set of 29 nuisance parameters which have different jet p_{T} and η dependencies [253].

9.1.5 Jet Energy Resolution

The jet energy resolution (JER) is measured separately in data and MC using in situ techniques [253]. The results are further improved by an additional in situ measurement using dijet events and events with γ/Z+jets. The differences between the jet energy resolutions in data and MC are decorrelated into 8 components with different dependencies on the jet p_{T} and η. To estimate the effect on the measurement itself the energy of jets is smeared by these differences and the corresponding $\Delta|y|$ distributions are compared to the nominal ones.

9.1.6 Jet Vertex Tagger

The JVT scale factors are calculated using simulated $Z \to \mu^+\mu^-$ and $t\bar{t}$ events [254]. The corresponding JVT uncertainty includes the uncertainty on the pile-up jet contamination and a systematic uncertainty due to the choice of different MC generators.

9.1.7 Large-R Jet Moment Scale and Resolution

The scales of the detector response for all large-R jet moments (p_{T}, mass, τ_{32} substructure variable [95]) are obtained using a method described in Ref. [255]. The resolution of the detector response is conservatively estimated as a 2% absolute uncertainty on the large-R jet p_{T} and 20% relative uncertainty on large-R jet mass, parametrised in p_{T} and $m_{\mathrm{jet}}/p_{\mathrm{T}}$ [256]. In total, a set of 14 nuisance parameters is used to describe uncertainties on the large-R jet moment scales and resolution.

9.1.8 B-tagging

A set of scale factors correcting different b-tagging efficiencies in data and MC is used and the corresponding uncertainties are propagated through the analysis as systematic uncertainties [211, 214, 257]. These include 9 parameters for b-tagging efficiency as well as 4 parameters for c-tagging and 4 for light quark mis-identification efficiencies, parametrised in jet p_{T} and η. Additionally, 2 parameters are assigned for high p_{T} extrapolated b and c efficiencies.

9.1.9 Missing Transverse Energy Scale and Resolution

The $E_{\mathrm{T}}^{\mathrm{miss}}$ is calculated from several terms corresponding to different types of reconstructed objects, as described in Section 5.7. Uncertainty on each object is evaluated and then propagated to the uncertainty on the $E_{\mathrm{T}}^{\mathrm{miss}}$. Two methods are used to estimate the uncertainty on the soft term that enters the $E_{\mathrm{T}}^{\mathrm{miss}}$ calculation [258]. The individual sources of the uncertainty on $E_{\mathrm{T}}^{\mathrm{miss}}$ are combined into two nuisance parameters for the total uncertainty on the energy scale and resolution of $E_{\mathrm{T}}^{\mathrm{miss}}$.

9.2 Modelling Uncertainties

Signal and background modelling, based on theoretical understanding of the physical processes, is used in the measurement e.g. to create the response matrix and model the background contributions.

9.2.1 Cross Sections and Normalisation

For all processes entering the measurement the normalisation uncertainties are considered. Typically, the normalisation uncertainty corresponds to theoretical cross section uncertainties. In some cases, such as for the multijet data-driven background, a conservative normalisation uncertainty estimate is used instead.

In the case of the $t\bar{t}$ signal, 5.5% uncertainty is considered, which corresponds to the cross section uncertainty discussed in Section 2.1.1. However, this uncertainty is

shown only in some of the control distributions and does not enter the unfolding itself. The reason is that the individual $\Delta|y|$ bins are free parameters, therefore effectively the signal normalisation is also a free parameter.

In the boosted topology a large normalisation mis-modelling is observed and about 20% more events are predicted than actually observed in data, as discussed already in Section 7.3. Since the unfolding is performed in both topologies simultaneously, a boosted normalisation nuisance parameter with flat prior from 0 to 2 is introduced to absorb the normalisation discrepancy.

The single top quark production inclusive cross section uncertainty is 5.3%. The combined 'small background' category, which includes Z+jets, diboson production, $t\bar{t}V$ and $t\bar{t}H$ events, is assigned a normalisation uncertainty of 50%. In the case of the production of the W boson in association with additional jets conservative 50% uncertainty is applied. The W+jets background is the dominant one and since the normalisation might be understood differently between 1 b-excl. and 2 b-incl. regions, this uncertainty is decorrelated between the b-tag regions and two nuisance parameters are introduced. Finally, in the case of the multijet background 50% uncertainty is also considered and in this case it is decorrelated between all 4 signal regions which are split by b-tag multiplicity and event topology. The nuisance parameters corresponding to background normalisations use Gaussian distributions truncated at 0 as priors, instead of full Gaussian curves, in order to forbid negative background contributions.

9.2.2 Matrix Element Modelling

To estimate the uncertainty related to the matrix element (ME) modelling in the $t\bar{t}$ signal the nominal Powheg Box 2 generator is compared to the alternative MadGraph5_aMC@NLO 2.6.0. For the purpose of this comparison both samples are generated with the simplified AtlFast-II simulation of hadron showers. The difference is taken as 'shape-only' and the normalisation effect is removed. This does not underestimate the total uncertainty, since the signal normalisation is effectively a free parameter. The systematic variation is treated as decorrelated between the resolved and boosted topologies, since the agreement of the nominal setup with data might be different in completely different kinematic regions.

The ME modelling uncertainty is estimated in a similar way also for the single top background. However, in this case only one nuisance parameter is introduced and the normalisation effect is also considered.

9.2.3 Parton Shower Modelling

The uncertainty on parton shower and hadronisation modelling (PS) is treated similarly as the ME uncertainty. In this case, the Pythia 8.230 generator is compared to

the alternative HERWIG 7.04, both generated with ATLFAST-II and interfaced to the POWHEG BOX 2. The PS uncertainty in $t\bar{t}$ modelling is taken as shape-only and is decorrelated between the resolved and boosted topologies. In the case of the single top quark background the uncertainty is taken as correlated.

9.2.4 Initial and Final State Radiation

The uncertainties on the effects of initial state radiation (ISR) and final state radiation (FSR) in top quark production are studied using the nominal MC generators, i.e. POWHEG BOX 2 and PYTHIA 8.230. The fast simulation ATLFAST-II is used in the case of ISR and the full GEANT4 for the FSR.

The ISR up variation is estimated using a dedicated MC sample generated with $h_{\text{damp}} = 517.5$ GeV, with renormalisation and factorisation scales $\mu_r = \mu_f = 0.5$ of the nominal scales and with the `Var3cUp` shower tune variation [229]. The ISR down variation is estimated using the nominal sample by application of different event weights, corresponding to $\mu_r = \mu_f = 2.0$ of the nominal scales and to the `Var3cDown` shower tune [229]. The uncertainties are taken as shape-only and decorrelated between resolved and boosted topologies. In the case of the single top quark background the uncertainty is taken as correlated and the normalisation effect is also considered. Both up and down variations are separately tested in the unfolding as one-sided uncertainties and only the more conservative one is chosen it the final setup. The ISR down variations are found to be more conservative.

The FSR uncertainty is calculated in a similar way, by varying the μ_r and μ_f in parton showering and hadronisation by a factor of 2 up and down. The FSR down variation is found to be more conservative in the case of the $t\bar{t}$ signal and for the single top quark background the FSR up is chosen.

9.2.5 Top-Quark Mass

The nominal sample is generated with $m_{\text{top}} = 172.5$ GeV and the effect of the top quark mass uncertainty on the signal modelling is studied using alternative samples generated with $m_{\text{top}} = 172$ GeV and $m_{\text{top}} = 173$ GeV. The systematic effect is taken as shape-only and is decorrelated between resolved and boosted topologies. Both 172 GeV and 173 GeV samples are tested and the more conservative one is chosen as a one-sided uncertainty.

9.2.6 Parton Distribution Functions

The uncertainty on the PDFs is applied only on the signal sample using the PDF4LHC prescriptions [259] which combine the uncertainties of the following PDF sets: CT14

[260], MMHT14 [233] and NNPDF3.0 [227]. The output is a set of 30 nuisance parameters.

9.2.7 Single Top Quark Wt-Channel Interference

Due to the interference of the Wt-channel with the $t\bar{t}$ production it is necessary to remove the overlap using the diagram removal (DR) technique [261]. The alternative diagram subtraction (DS) method [261] is used as an alternative and the difference is taken as a corresponding uncertainty.

9.2.8 W+jets Modelling

A number of scale variations in W+jets background modelling are considered as shape-only uncertainties [262]. The μ_r and μ_f scales are varied up and down by a factor of 2 leading to a two-sided uncertainty. The CKKW scale [263], which controls the ME to PS matching, is varied from 0.75 to 1.5 of the nominal value and the differences are treated as a two-sided uncertainty. Similarly, the parton showering QSF scale [219] is varied from 0.25 to 4.0 of the nominal value.

9.2.9 Multijet Shape

The multijet background is data-driven and therefore not affected by the experimental or modelling uncertainties. An alternative parametrisation is taken as a shape-only uncertainty, as discussed already in Section 6.3.1.

9.3 Unfolding Uncertainties

In addition to all systematic uncertainties mentioned above, two uncertainties are related to the unfolding procedure itself. Consequently, these are not embedded within FBU and no nuisance parameters are assigned. These uncertainties are simply added in quadrature to the total unfolded uncertainty.

9.3.1 Response Matrix Statistical Uncertainty

The response matrix is created using the nominal $t\bar{t}$ MC sample with more than 200 million events. However, the corresponding statistical uncertainties are not negligible. To estimate this uncertainty, 300 pseudo-experiments were performed with the response matrices smeared according the Poisson distribution and the raw number of MC events. The width of the obtained A_C distribution is taken and added in quadrature to the total unfolded uncertainty obtained using the nominal response matrix.

9.3.2 Unfolding Bias

The non-ideal slope and offset of the unfolding response summarised in Table 8.1 leads to a bias in the unfolded values. Since $A_{\mathrm{C}}^{\mathrm{unfolded}} = \mathrm{slope} \times A_{\mathrm{C}}^{\mathrm{true}} + \mathrm{offset}$, the corresponding bias can be expressed as a function of the unfolded asymmetry:

$$\mathrm{Bias} = A_{\mathrm{C}}^{\mathrm{unfolded}} - A_{\mathrm{C}}^{\mathrm{true}} = A_{\mathrm{C}}^{\mathrm{unfolded}} - (A_{\mathrm{C}}^{\mathrm{unfolded}} - \mathrm{offset})/\mathrm{slope}. \tag{9.1}$$

In most cases the bias is found to be negligible.

9.4 Bootstrap Method

The bootstrap method [264] is applied on most of the systematic uncertainties in order to remove unphysical fluctuations due to limited MC sample size. In general, it is not easy to estimate statistical uncertainties of the systematic effects, since both the nominal and shifted distribution are typically largely correlated. For example, if an alternative JES scale is applied, slightly more (or less) events pass the selection criteria, but a vast majority remains the same.

In the bootstrap method, for each of the N events forming the studied distributions n random weights from a Poisson distribution $P(\lambda = 1)$ are generated. Subsequently, n replicas of the nominal and shifted distributions are created by filling them event by event with the corresponding Poisson weights. Run numbers and event numbers are used as a seed for generating the Poisson weights which ensures that the events which are the same in both the nominal and shifted distributions will behave in a correlated way. The relative difference between the nominal and shifted distributions is then calculated in each bin for all n replicas. The mean of the n relative differences is taken as the systematic uncertainty and the corresponding RMS as its statistical component. In this analysis, 500 replicas are used.

Having correctly estimated statistical uncertainties of the systematic uncertainty it is possible to smooth the distribution in order to remove statistically insignificant effects. This is particularly important in the A_{C} measurement with only four $\Delta|y|$ bins in each of the signal regions. Since the expected uncertainties are of the order of $\lessapprox 1\%$, even a small fluctuation in one of the $\Delta|y|$ bins can lead to a relatively large systematic effect. Furthermore, due to the fact that the systematic uncertainties are marginalised within FBU, special caution is required, since large unphysical spikes in the systematic distributions might lead to over-constraining of the corresponding nuisance parameters. Paradoxically, this might lead to underestimation of the systematic effect in other signal regions where the effect might be truly physical.

Due to the fact of having only four $\Delta|y|$ bins in the signal regions the smoothing procedure differs from the one described in Refs. [264] and [265]. A simplified smoothing

procedure is applied: A bin is considered statistically significant if it is inconsistent with zero at more than 2 standard deviations. If at least one of the four bins is significant, all four bins are left unchanged and no smoothing is applied. If no bin is significant, the four bins are combined into one and the same significance criterion is applied. If the bin combination is significant, all four bins are set to the combined value, i.e. only the normalisation effect is kept and the shape is dropped. If the bin combination is still insignificant, all four bins are set to zero.

The bootstrapping method is applied on a majority of systematic uncertainties with some exceptions. It does not make sense to apply it on uncertainties which are statistically significant by definition, e.g. luminosity and normalisation uncertainties. Similarly, uncertainties which are obtained by reweighting of the nominal sample are typically significant by definition, since the nominal and alternative samples are 100% correlated. However, a small effect of statistical fluctuations might be still present if the event weights are very unevenly distributed, which is typical for the FSR uncertainty where the bootstrap method is also applied. In the case of two-sided systematic uncertainties, the up and down variations are bootstrapped independently. The effect of bootstrapping on the systematic uncertainties affecting the $t\bar{t}$ signal sample in the inclusive case is summarised in Figure 9.1.

9.5 Systematic Uncertainty Ranking

Within the FBU all uncertainties are combined in one posterior distribution function of the measured quantity, i.e. in this case the charge asymmetry. In order to assess the relative importance of the individual uncertainties two approaches are used.

The first one, here referred to as the 'stat.-only' approach, is relatively simple. To estimate the relative importance of a particular systematic uncertainty, the Asimov dataset is replaced by the one corresponding to the studied uncertainty (Asimov $\pm$ the syst. effect). Afterwards, these pseudo-data are unfolded without systematic uncertainties, i.e. only the statistical uncertainty is considered. The unfolded A_{C} value is then compared to the one corresponding to the Asimov dataset and the difference is taken as the effect of the systematic uncertainty.

The problem with the 'stat.-only' approach is that it does not take into account correlations between other systematic uncertainties, neither it considers possible constraining of the studied uncertainty by the FBU. A more realistic approach, here referred to as 'full-syst.', is to unfold the pseudo-data using all systematic uncertainties, except the one which is analysed. While the former approach represents the effect of stand-alone systematic uncertainties before combining them within the FBU, the latter one represents the effect of the uncertainty in the particular setup used in the A_{C} analysis.

Ranking of the 20 most important uncertainties affecting the inclusive A_C measurement is shown in Figures 9.2 and 9.3 for the 20 most important uncertainties. Corresponding plots with the full set of uncertainties can be found in the Appendix, Figures A.13 and A.14. In the case of the 'stat.-only' approach also a naively calculated total uncertainty from the squares of the individual components is shown. In the case of the 'full-syst.' method, the full unfolded uncertainty is shown. The statistical uncertainty is found to be the dominant one not only in the differential measurement, but also in the inclusive case. A vast majority of uncertainties is found to contribute only negligibly to the total uncertainty.

9.6 Pruning

The multi-dimensional sampling in FBU is computationally expensive due to the large number of nuisance parameters. However, the majority of systematic uncertainties contribute only negligibly to the uncertainty of the measured A_C, as demonstrated in the Appendix in Figures A.13 and A.14. Some of the systematic uncertainties are small enough to be completely neglected, at least in some of the signal regions or in some backgrounds, By simplifying the systematic model it is possible to obtain not only an improvement of the computational time, but also a more numerically stable setup, cleaned from unnecessary nuisance parameters.

A pruning procedure is implemented in order to remove negligible nuisance parameters. Since the A_C value is affected more by the shape of the systematic uncertainties and less by the normalisation effects, these effects are handled separately and different pruning criteria are used to remove the shape/normalisation of each systematic uncertainty. If at least one of the bins in the shape distribution of the systematic uncertainty has a relative effect larger than the threshold, the shape is kept, otherwise it is dropped (set to the nominal). Similarly, if the overall relative normalisation effect of the systematic uncertainty is smaller than the threshold, the normalisation is dropped. The signal regions are processed separately and one systematic uncertainty can be kept in some regions and removed in the others. All differential bins in one signal region are studied together. If both the shape and normalisation effects for a particular systematic uncertainty are dropped in all signal regions for both the signal and background distributions, the corresponding nuisance parameter is removed completely.

In order to find the optimal pruning thresholds a number of combinations of relative shape and normalisation thresholds are tested, as demonstrated in Tables 9.1 – 9.3. The main criterion is that the unfolded uncertainty at the fourth decimal digit should change at most by 1, which approximately corresponds to the rounding uncertainty at the last decimal digit of the quoted results. It was also checked if the uncertainties which were found to be high in the systematic ranking plots are not removed completely.

The effect of pruning on the systematic uncertainties affecting the $t\bar{t}$ signal sample in the inclusive case is summarised in Figure 9.4.

norm	shape	Asimov unfolded A_C
0.0000	0.0000	0.00360 ± 0.00151
0.0010	0.0004	0.00361 ± 0.00145
0.0025	0.0005	0.00359 ± 0.00145
0.0030	0.0006	0.00361 ± 0.00144
0.0050	0.0010	0.00363 ± 0.00147
0.0060	**0.0020**	**0.00361 ± 0.00140**
0.0070	0.0030	0.00362 ± 0.00136
true A_C		0.00362 ± 0.00006

Table 9.1: Summary of different pruning thresholds tested for the inclusive A_C measurement. The final option is highlighted.

thresholds		Asimov unfolded A_C			
norm	shape	$\beta_z(t\bar{t}) \in [0, 0.3]$	$\beta_z(t\bar{t}) \in [0.3, 0.6]$	$\beta_z(t\bar{t}) \in [0.6, 0.8]$	$\beta_z(t\bar{t}) \in [0.8, 1.0]$
0.0000	0.0000	0.0001 ± 0.0050	0.0015 ± 0.0038	0.0022 ± 0.0043	0.0092 ± 0.0049
0.0010	0.0004	0.0001 ± 0.0050	0.0015 ± 0.0038	0.0021 ± 0.0043	0.0092 ± 0.0048
0.0025	0.0005	0.0001 ± 0.0049	0.0015 ± 0.0038	0.0021 ± 0.0043	0.0092 ± 0.0048
0.0030	**0.0006**	**0.0001 ± 0.0049**	**0.0016 ± 0.0038**	**0.0021 ± 0.0042**	**0.0092 ± 0.0048**
0.0050	0.0010	0.0001 ± 0.0045	0.0016 ± 0.0037	0.0022 ± 0.0042	0.0092 ± 0.0047
0.0060	0.0020	0.0002 ± 0.0049	0.0015 ± 0.0037	0.0023 ± 0.0042	0.0091 ± 0.0047
0.0070	0.0030	0.0002 ± 0.0051	0.0016 ± 0.0037	0.0024 ± 0.0041	0.0091 ± 0.0046
true A_C		0.0001 ± 0.0001	0.0014 ± 0.0002	0.0026 ± 0.0001	0.0086 ± 0.0001

Table 9.2: Summary of the different pruning thresholds applied for the differential $\beta_z(t\bar{t})$ A_C measurement. The final option is highlighted.

thresholds		Asimov unfolded A_C				
norm.	shape	[0, 500 GeV]	[500, 750]	[750, 1000]	[1000, 1500]	> 1500
0.0000	0.0000	0.0028± 0.0042	0.0042± 0.0028	0.0046 ± 0.0063	0.0063 ± 0.0079	0.0111 ± 0.0282
0.0010	0.0004	0.0028± 0.0042	0.0042± 0.0028	0.0047 ± 0.0063	0.0063 ± 0.0079	0.0113 ± 0.0280
0.0025	0.0005	0.0028± 0.0042	0.0042± 0.0028	0.0046 ± 0.0063	0.0063 ± 0.0079	0.0110 ± 0.0281
0.0030	0.0006	0.0028± 0.0042	0.0042± 0.0029	0.0047 ± 0.0063	0.0063 ± 0.0079	0.0111 ± 0.0281
0.0050	**0.0010**	**0.0028± 0.0042**	**0.0042± 0.0028**	**0.0046 ± 0.0063**	**0.0063 ± 0.0079**	**0.0112 ± 0.0281**
0.0060	0.0020	0.0029± 0.0042	0.0042± 0.0028	0.0046 ± 0.0063	0.0062 ± 0.0079	0.0111 ± 0.0279
0.0070	0.0030	0.0029± 0.0041	0.0042± 0.0028	0.0047 ± 0.0063	0.0062 ± 0.0079	0.0113 ± 0.0279
true A_C		0.0031± 0.0001	0.0041± 0.0001	0.0049 ± 0.0003	0.0061 ± 0.0005	0.0100 ± 0.0012

Table 9.3: Summary of the different pruning thresholds applied for the differential $m(t\bar{t})$ A_C measurement. The final option is highlighted.

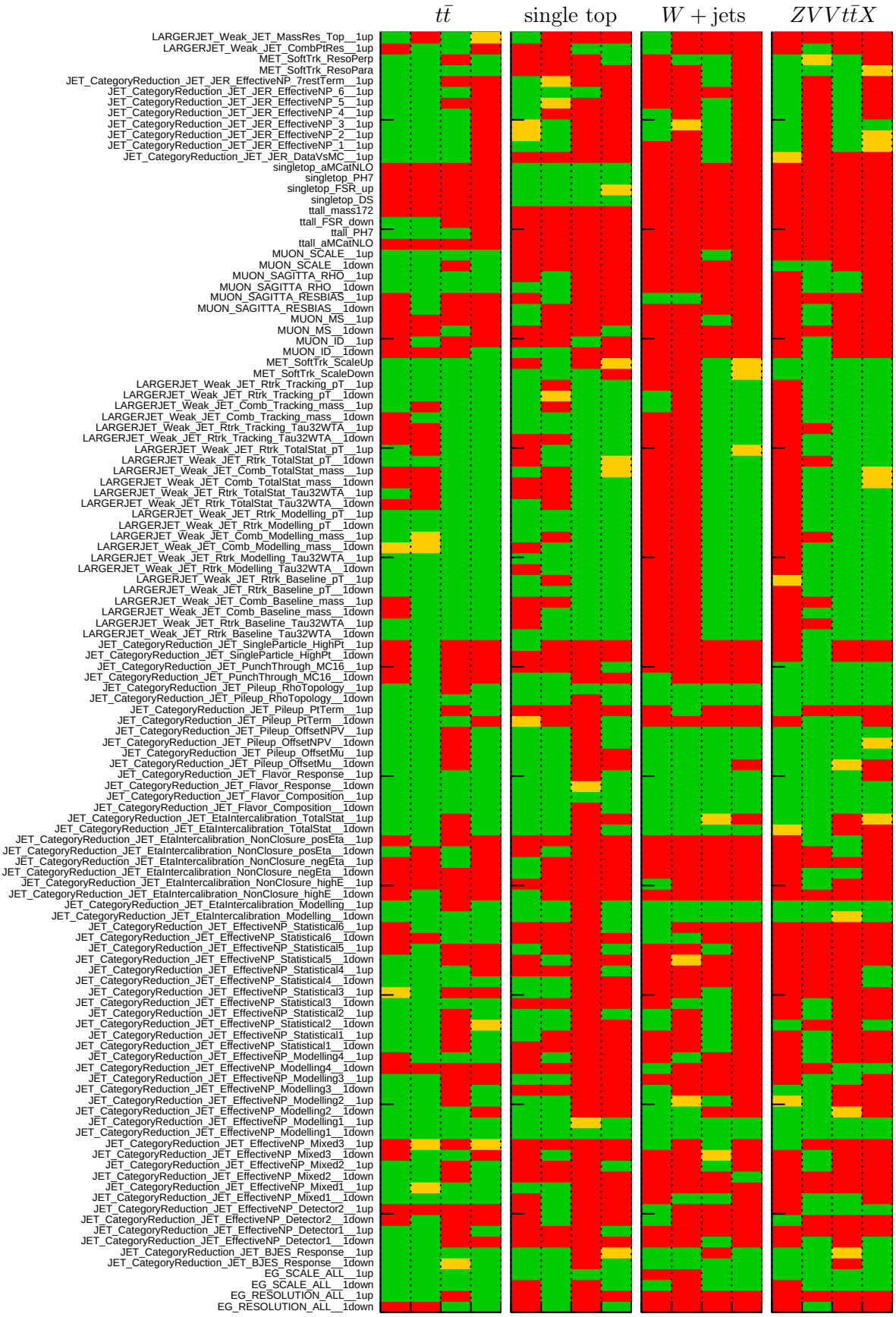

Figure 9.1: Effect of bootstrapping on syst. uncertainties affecting the signal and background processes in the inclusive measurement. In each process, the four columns correspond to four signal regions, from left to right: resolved (1 b-excl./2 b-incl.) and boosted (1 b-excl./2 b-incl.). Red cells indicate the uncertainty is removed by bootstrapping, yellow that shape is removed and green correspond to no modifications.

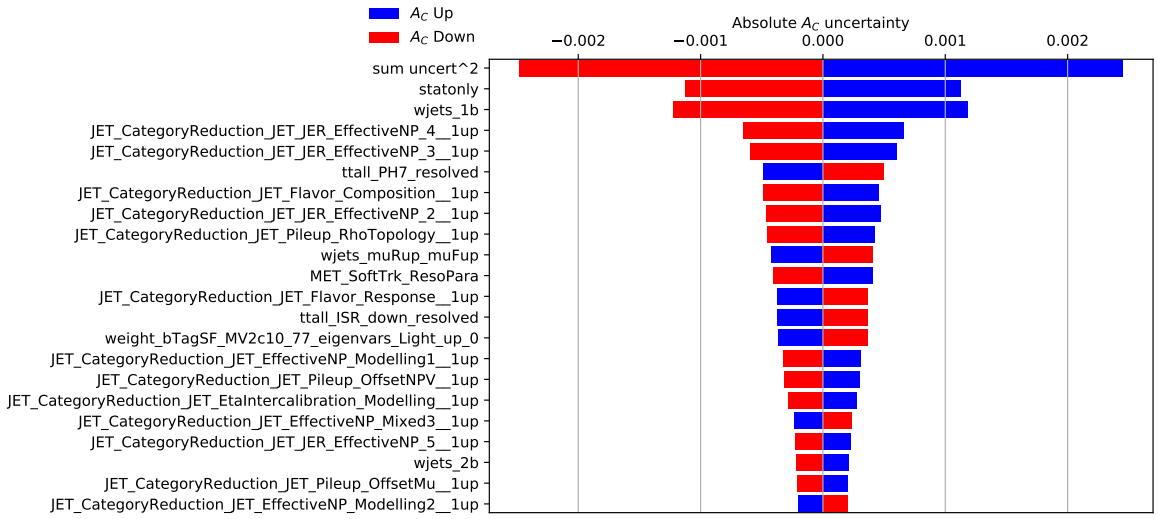

Figure 9.2: The 'stat.-only' ranking of syst. uncertainties in the inclusive A_C measurement. Only the top 20 uncertainties are shown.

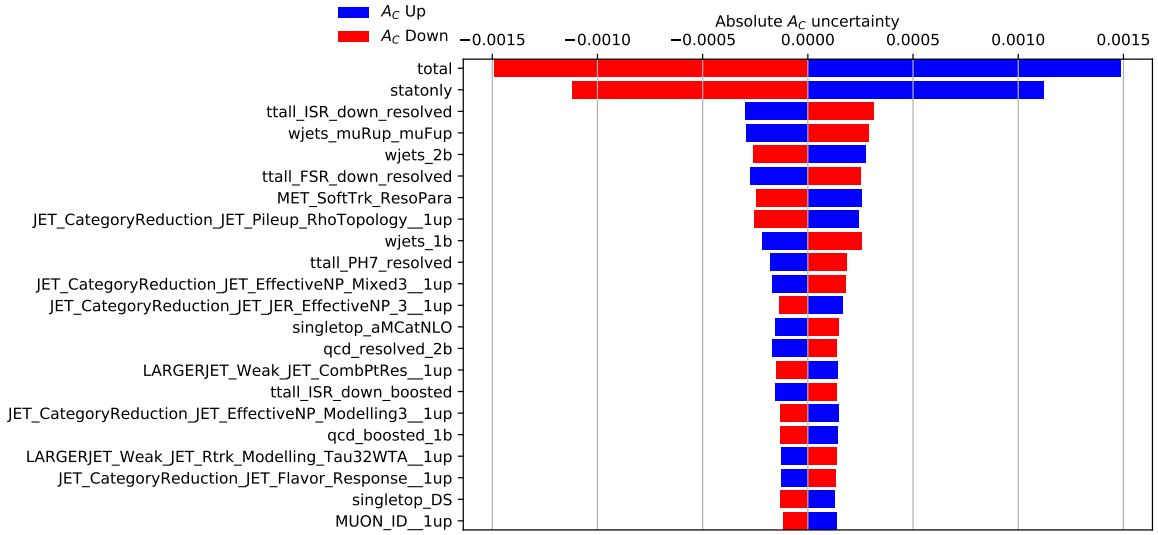

Figure 9.3: The 'full-stat.' ranking of syst. uncertainties in the inclusive A_C measurement. Only the top 20 uncertainties are shown.

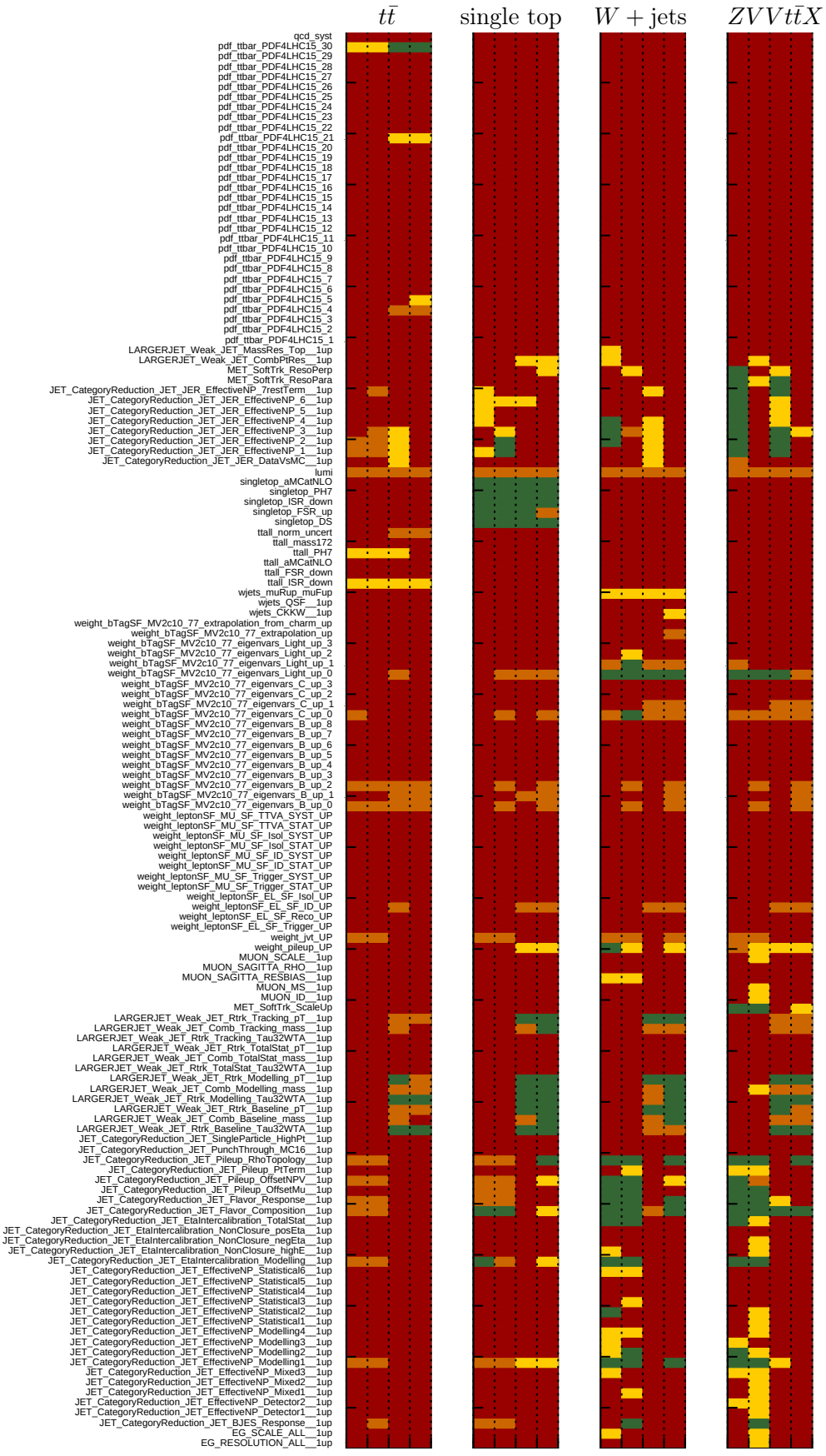

Figure 9.4: Effect of pruning on syst. uncertainties affecting the signal and background processes in the inclusive measurement. In each process, the four columns correspond to four signal regions. Red cells indicate the uncertainty is removed, orange that shape is removed, yellow that normalisation is removed and green correspond to no modifications.

Chapter 10

Results

10.1 Nuisance Parameter Pulls and Constraints

A summary of the pulls and constraints of the individual nuisance parameters in the inclusive and differential A_C measurements is shown in Figures 10.1 – 10.3. In all cases the pulls and constraints are shown for both the Asimov dataset and real data. In the case of Asimov no pulls are expected, although due to the FBU marginalisation and multi-dimensional integration there might be some unphysical pulls due to correlations between the nuisance parameters, as discussed in Section 8.7. To validate the marginalisation approach a maximum-a-posteriori estimate which directly corresponds to the mode of the FBU likelihood is also shown. A good agreement is observed between the two approaches in both Asimov and data and marginalisation is used to extract the measured A_C values.

All nuisance parameters which pass the bootstrapping and pruning criteria are shown. In the case of two-sided uncertainties only the up variation is shown as a label, but the nuisance parameter is constructed from the symmetrised up and down variations. The green band corresponds to the RMS of the prior Gaussian distributions and the yellow region represents the 2 σ CL of the prior estimate. In the case of the boosted signal normalisation NP which was introduced in Section 9.2.1 a flat prior is used and the green and yellow bands correspond to $\pm 20\%$ and $\pm 40\%$ of the central value, respectively.

In Figure 10.1 corresponding to the inclusive measurement there are few larger pulls of the NPs, including the pull of the boosted signal normalisation, which corrects for the normalisation mis-modelling in the boosted regime. In the inclusive case there are no significant constraints, except the W+jets normalisation in the 1 b-excl. channels. In Figures 10.2 and 10.3 which correspond to the $\beta_z(t\bar{t})$ and $m(t\bar{t})$ differential measurements, respectively, much more nuisance parameters are pulled and constrained. This is an expected behaviour. In the differential measurements much more bins are used and a particular systematic effect often differently affects the individual differential bins,

which leads to complex and specific shapes of the systematic variations. As a consequence, the corresponding nuisance parameters can be relatively easily constrained and pulled.

In the differential measurements there is also a higher risk that the statistical fluctuations in the MC predictions might cause unphysical spikes in the distributions of the systematic uncertainties, which might be consequently over-constrained in the unfolding procedure if they are not removed by the bootstrapping procedure. This effect is particularly apparent in the cases when the alternative MC samples have a relatively smaller number of events, e.g. in the case of the alternative sample generated with $m_{\text{top}} = 172$ GeV only about 15 million of events are used. This problem is difficult to avoid, since providing sufficiently large samples would require generating tens or hundreds of millions of new events. On the other hand, only few pulls larger than the RMS of the prior are observed and the majority of pulled nuisance parameters are still consistent with the mean of the prior, which does not indicate 'dangerous' pulls and constraints. Furthermore, as it was shown in the systematic ranking studies presented in Section 9.5, the statistical uncertainties are dominating and small imperfections in the estimation of the distributions of the systematic uncertainties are not expected to affect the result significantly.

10.2 Post-Marginalisation Correlations

All nuisance parameters enter the unfolding as decorrelated, but the FBU is capable of estimating the correlations in the particular measurement. The post-marginalisation correlations obtained from unfolding real data are summarised in the Appendix in Figures A.15 – A.17. Correlations between the parton-level $\Delta|y|$ bins are also shown, as well as correlations with the A_{C} value itself.

In the inclusive case only few nuisance parameters are significantly correlated, e.g. b-tagging scale factors and the large-R jet scale variations with the boosted signal normalisation parameter. In the differential measurements there are much more correlated parameters, with JER parameters and signal modelling uncertainties among the leading ones.

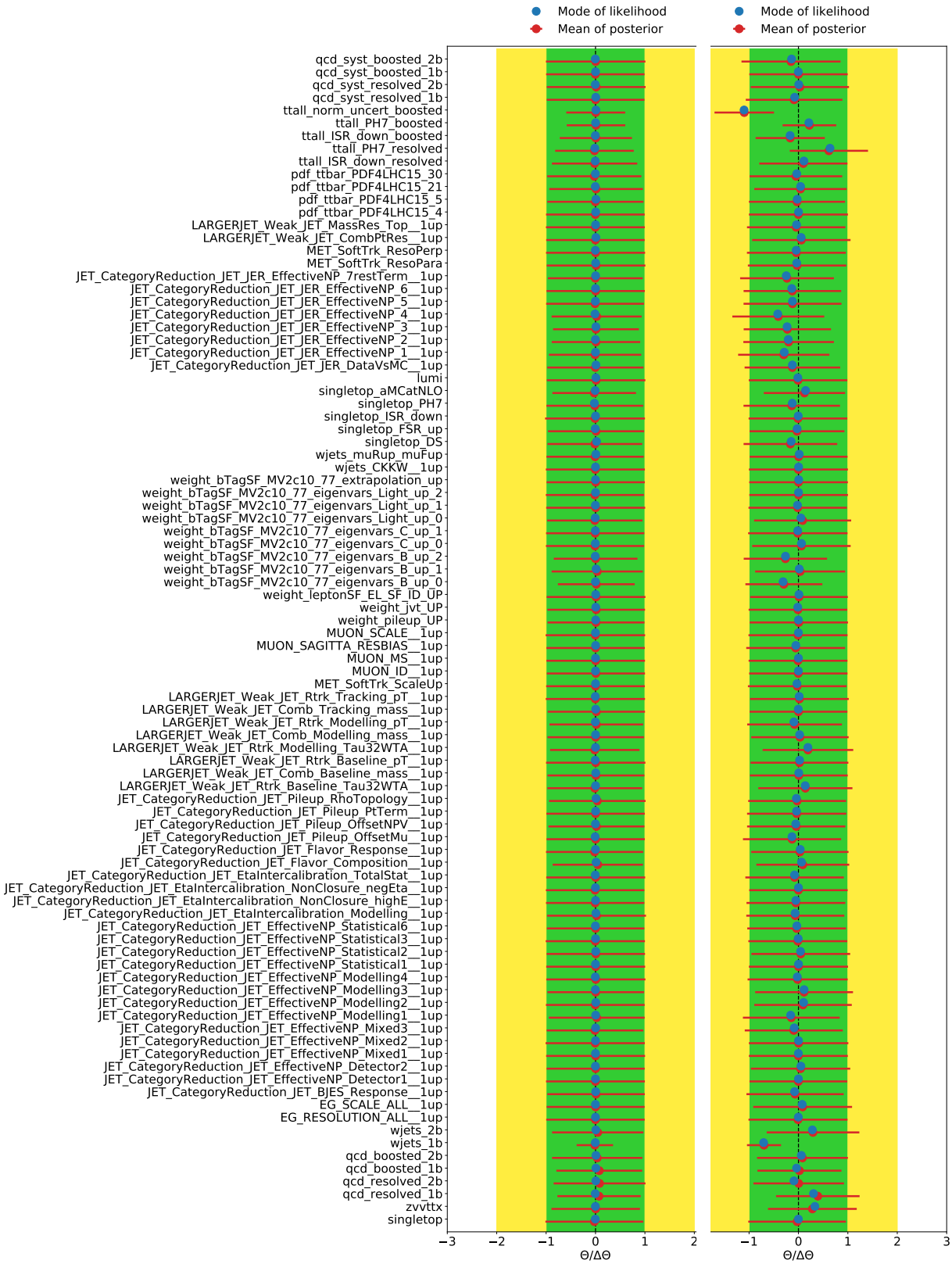

(a) Asimov. (b) Data.

Figure 10.1: Pulls and constraints of the nuisance parameters in the inclusive case for Asimov (left) and data (right). The red points correspond to the mean of the posterior and the blue ones to the mode of the likelihood approach (MAP). The green and yellow regions correspond to the 1 and 2 σ intervals of the prior probability density, respectively.

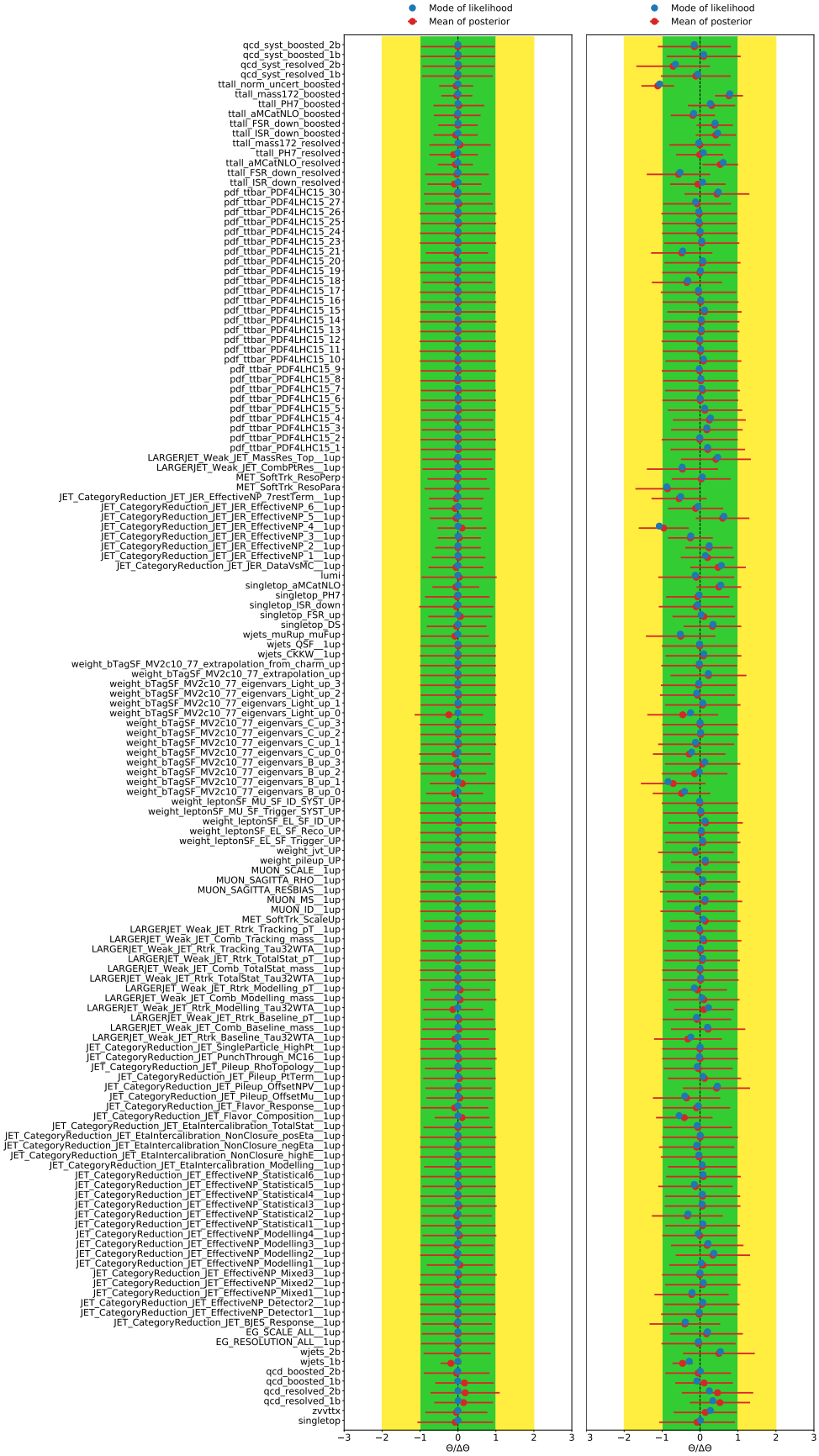

(a) Asimov. (b) Data.

Figure 10.2: Pulls and constraints of the nuisance parameters in the differential $\beta_z(t\bar{t})$ case for Asimov (left) and data (right). The red points correspond to the mean of the posterior and the blue ones to the mode of the likelihood approach (MAP). The green and yellow regions correspond to the 1 and 2 σ intervals of the prior probability density, respectively.

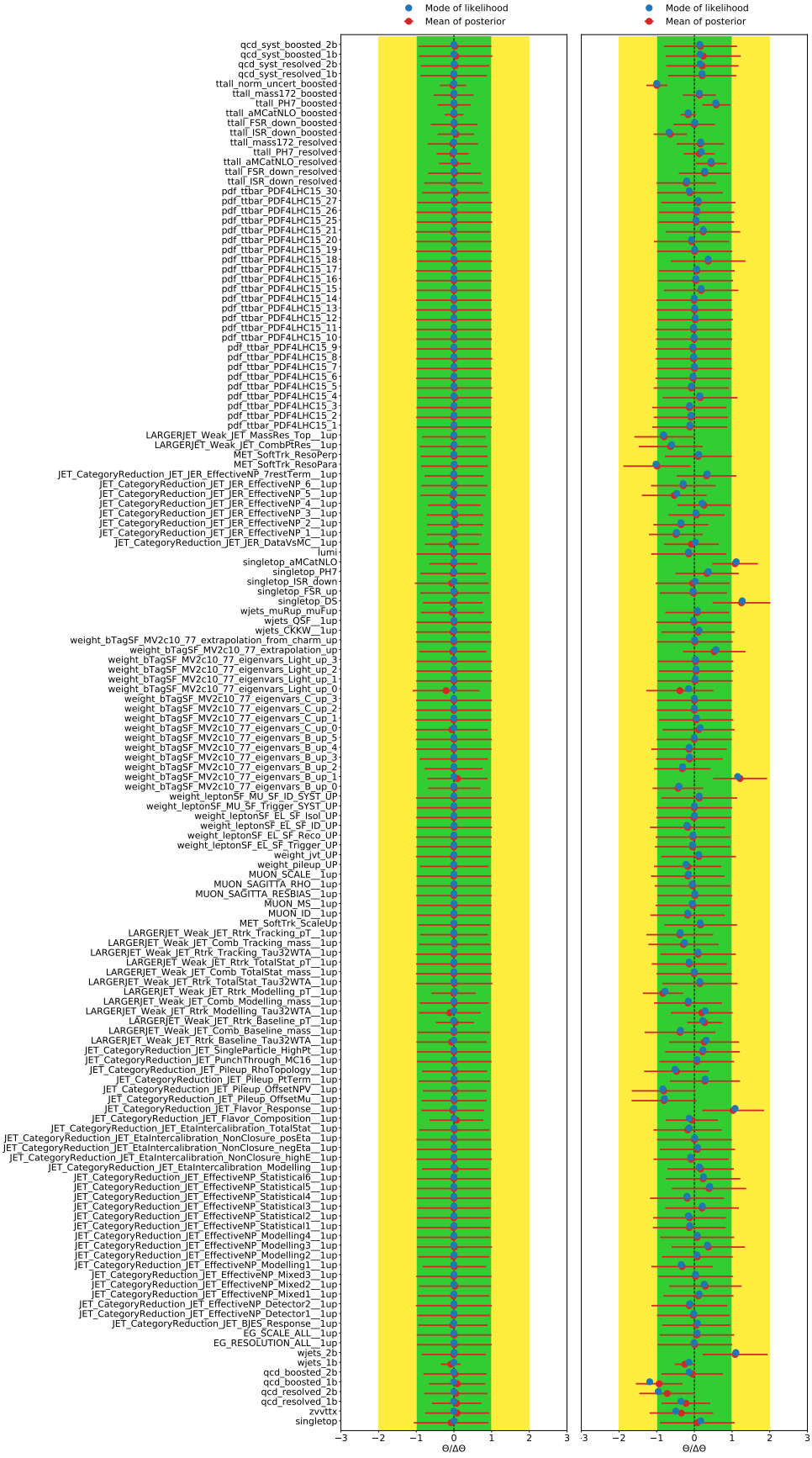

(a) Asimov. (b) Data.

Figure 10.3: Pulls and constraints of the nuisance parameters in the differential $m(t\bar{t})$ case for Asimov (left) and data (right). The red points correspond to the mean of the posterior and the blue ones to the mode of the likelihood approach (MAP). The green and yellow regions correspond to the 1 and 2 σ intervals of the prior probability density, respectively.

10.3 Post-Marginalisation Distributions

A summary of the pre-marginalisation and post-marginalisation distributions of the $\Delta|y|$ bins in the individual signal regions is provided for both the inclusive and differential A_C measurements in Figure 10.4. In the case of the differential measurements the differential bins are plotted side-by-side in each signal region. The pre-marginalisation plots show the agreement of the data and MC before the marginalisation procedure, i.e. before the FBU was performed. The normalisation difference in the boosted regime is clearly visible. In the post-marginalisation distributions the MC prediction is corrected, taking into account the pulls and constraints of the nuisance parameters, as well as the correlations between them. Consequently, the post-marginalisation uncertainties are much smaller and perfect agreement between the data and MC is observed. The improvement of the precision of the MC prediction is also visible from Table 10.1 where a comparison of total event yields before and after marginalisation is shown.

	pre-marg.	post-marg. incl.	post-marg. $\beta_z(t\bar{t})$	post-marg. $m(t\bar{t})$
$t\bar{t}$	3490000±280000	3538000± 23000	3490000± 12000	3586000± 12000
Single top	144000± 16000	143000± 6000	138800± 3100	126000± 4000
W + jets	240000±130000	159000± 16000	196000± 8000	199000± 8000
$Z + VV + t\bar{t}X$	70000± 40000	78000± 12000	76000± 6000	53000± 7000
Fakes	140000± 70000	159000± 22000	175000± 12000	113000± 11000
Total Prediction	4080000±350000	4080000± 40000	4076000± 20000	4076000± 20000
Data (139 fb^{-1})	4075855	4075855	4075855	4075855

Table 10.1: Event yields before and after marginalisation for the inclusive and differential $\beta_z(t\bar{t})$ and $m(t\bar{t})$ A_C measurements. All regions are combined.

The post-marginalisation agreement in the unfolded distributions is expected to be perfect by definition. However, if the pulls and constraints are physical, the post-marginalisation agreement should be improved also in control distributions which were not unfolded. An example of a comparison between the pre/post-marginalisation data/MC agreement is shown in the Appendix in Figures A.18 – A.21 for the reconstructed top p_T variable. In all cases the data/MC agreement is improved and the discrepancies are mostly well covered even by the reduced uncertainty band. Similar checks were performed also for other control distributions, such as jet and lepton p_T or E_T^{miss}. In all cases improvement is observed which is an important validation of the analysis setup.

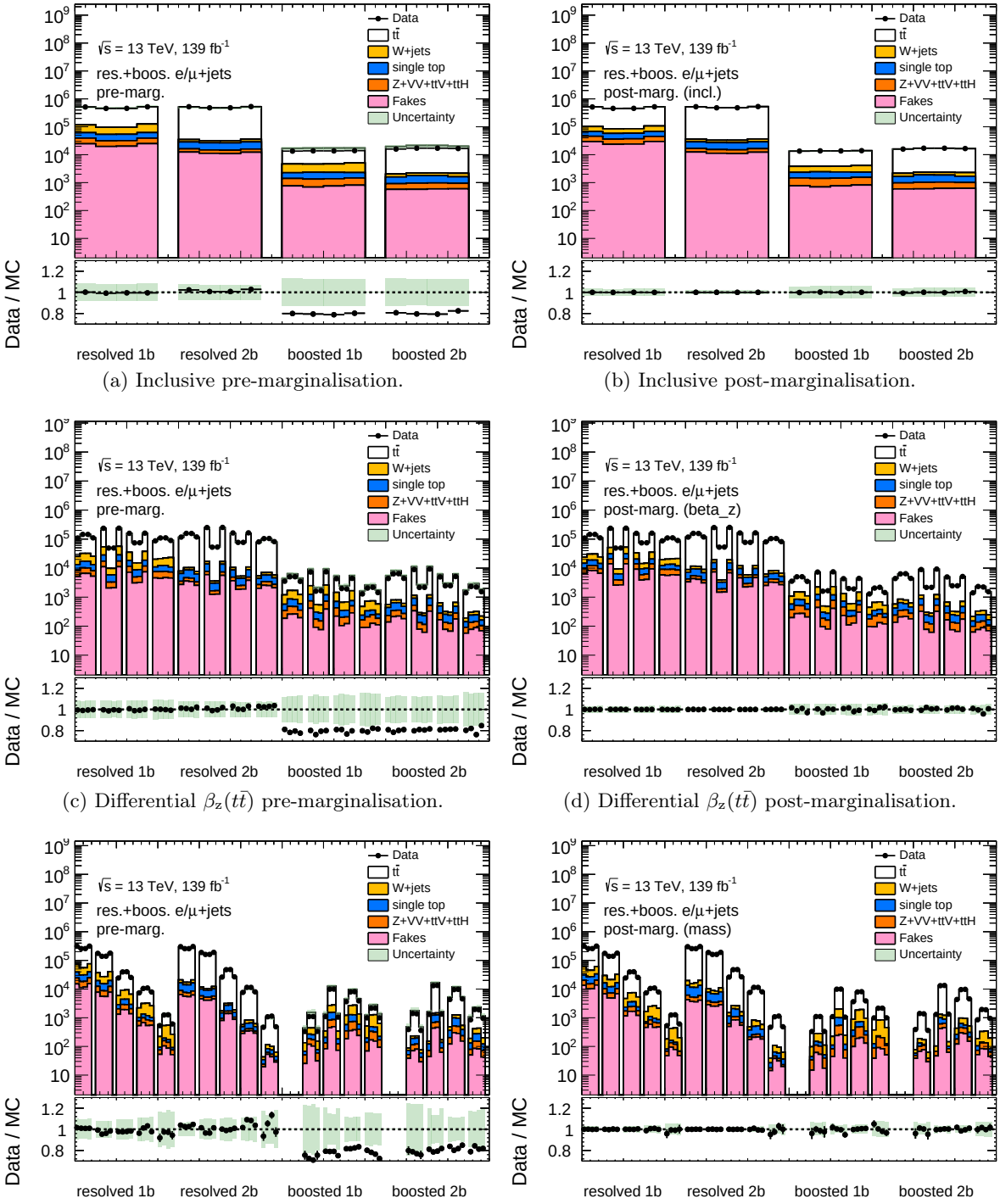

(a) Inclusive pre-marginalisation.

(b) Inclusive post-marginalisation.

(c) Differential $\beta_z(t\bar{t})$ pre-marginalisation.

(d) Differential $\beta_z(t\bar{t})$ post-marginalisation.

(e) Differential $m(t\bar{t})$ pre-marginalisation.

(f) Differential $m(t\bar{t})$ post-marginalisation.

Figure 10.4: Comparison between data and the MC prediction for bins used in the inclusive (top) and differential $\beta_z(t\bar{t})$ (middle) and $m(t\bar{t})$ (bottom) A_C measurements. This comparison is shown before (left) and after (right) marginalisation within FBU. The bottom panels show the ratio of the MC to data predictions. The light green band corresponds to the total pre/post-marginalisation uncertainty, including the normalisation and luminosity uncertainties. The binning is defined in Section 8.8.

10.4 Posterior Probability Density Distributions

The unfolded posterior probability density distributions obtained from data are shown in Figures 10.5 – 10.7. The predictions of the parton-level asymmetries obtained from the nominal POWHEG+PYTHIA 8 signal sample are also shown. In all cases the posteriors are symmetric and in very good agreement with the corresponding Gaussian fits, therefore it is reasonable to take the RMS of the distributions as a symmetric uncertainty.

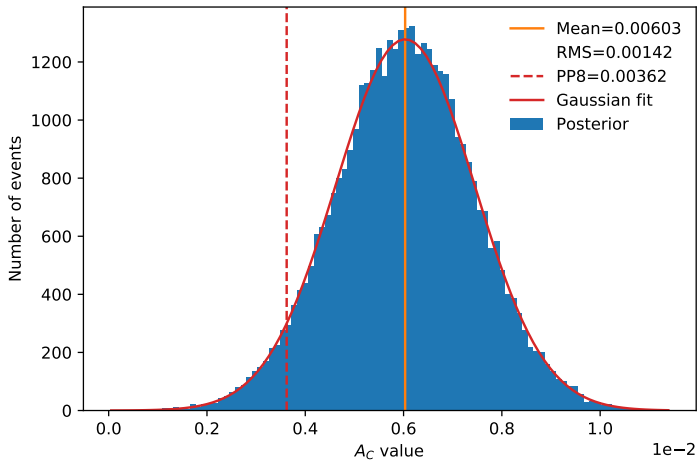

Figure 10.5: The A_C posterior probability density distribution in the inclusive measurement. The POWHEG+PYTHIA 8 parton-level asymmetry and posterior mean values are shown in red and orange, respectively.

10.5 Measured Charge Asymmetry Values

An overview of the A_C values with the corresponding uncertainties is provided in Table 10.2. The uncertainties are dominated by the RMS of the posteriors, followed by the statistical uncertainties in the response matrix and the unfolding bias, which is mostly negligible. The total uncertainty is the sum-in-quadrature of the mentioned uncertainties. Graphically, the results with the total uncertainties are presented in Figure 10.8.

A strongest to-date evidence of non-zero inclusive charge asymmetry is observed with a 4 σ confidence level. All values are consistent with the NNLO in QCD + NLO in EW SM prediction [132]. The LUXQED_PLUS_PDF4LHC15_NNLO_100 PDF set based on PDF4LHC recommendations [259] is used to calculate the SM prediction and the theoretical uncertainties are obtained by varying the renormalisation and factorisation scales. The POWHEG+PYTHIA 8 parton-level asymmetry is also shown for comparison, in this case the uncertainties are statistical only.

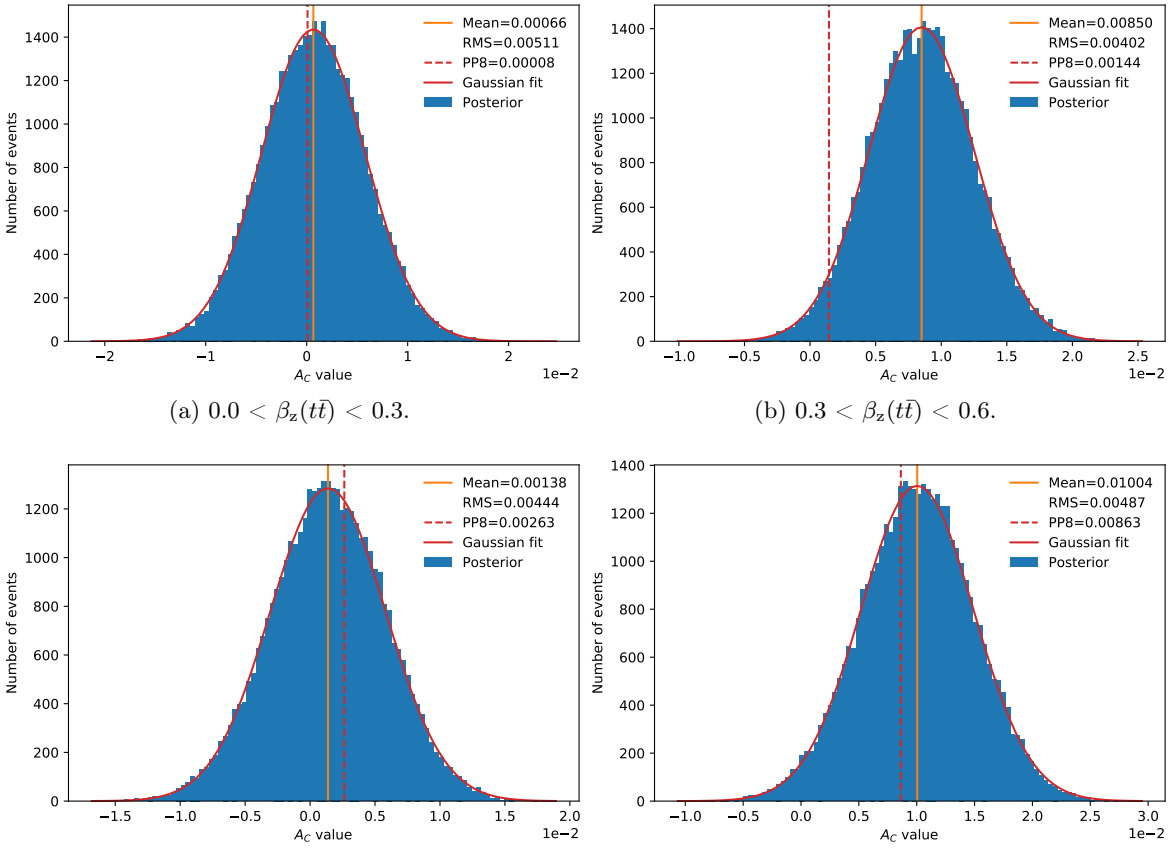

(a) $0.0 < \beta_z(t\bar{t}) < 0.3$.

(b) $0.3 < \beta_z(t\bar{t}) < 0.6$.

(c) $0.6 < \beta_z(t\bar{t}) < 0.8$.

(d) $0.8 < \beta_z(t\bar{t}) < 1.0$.

Figure 10.6: The A_C posteriors in the differential $\beta_z(t\bar{t})$ measurement. The POWHEG+PYTHIA 8 parton-level asymmetry and posterior mean values are presented in red and orange, respectively.

		SM	Data 139 fb^{-1}				
			Mean	Post-marg.	Res. mat.	Bias	Total
inclusive		$0.0064^{+0.0005}_{-0.0006}$	0.0060	0.0014	0.0005	0.0001	0.0015
$m(t\bar{t})$ [GeV]	< 500	$0.0055^{+0.0007}_{-0.0005}$	0.0045	0.0044	0.0013	0.0001	0.0045
	500-750	0.0072 ± 0.0006	0.0051	0.0029	0.0009	0.0000	0.0031
	750-1000	$0.0079^{+0.0003}_{-0.0005}$	0.0100	0.0067	0.0021	0.0001	0.0070
	1000-1500	0.0096 ± 0.0009	0.0169	0.0077	0.0029	0.0004	0.0083
	> 1500	$0.0094^{+0.0015}_{-0.0011}$	0.0121	0.0315	0.0092	0.0005	0.0329
$\beta_z(t\bar{t})$	0-0.3	0.0011 ± 0.0004	0.0007	0.0051	0.0020	0.0001	0.0055
	0.3-0.6	$0.0023^{+0.0006}_{-0.0004}$	0.0085	0.0040	0.0013	0.0003	0.0042
	0.6-0.8	0.0042 ± 0.0003	0.0014	0.0044	0.0015	0.0004	0.0047
	0.8-1.0	$0.0146^{+0.0012}_{-0.0014}$	0.0100	0.0049	0.0013	0.0007	0.0051

Table 10.2: Results with uncertainties, compared to the NNLO QCD + NLO EW SM prediction. The central unfolded values with the post-marginalisation uncertainties, uncertainties due to limited number of MC events in the response matrix, uncertainties due to the unfolding bias and the total uncertainties are shown for the inclusive and differential $A_C^{t\bar{t}}$ measurements.

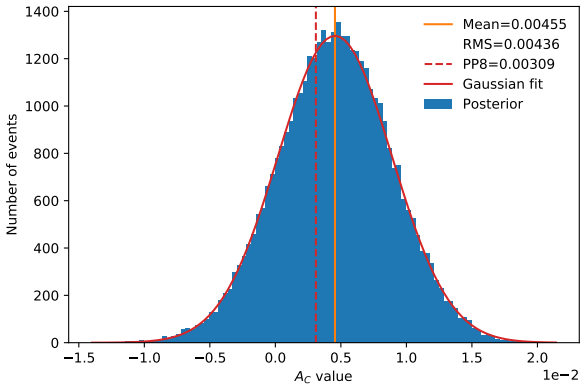

(a) $0 < m(t\bar{t}) < 500$ GeV.

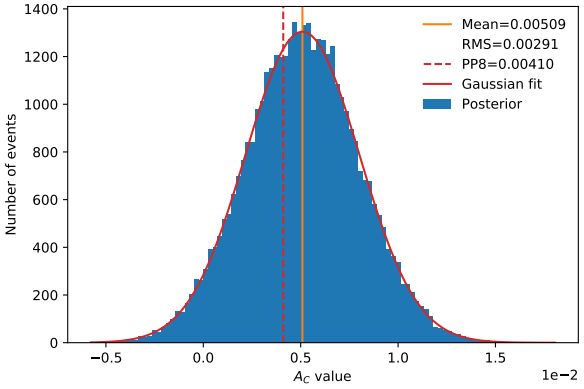

(b) $500 < m(t\bar{t}) < 750$ GeV.

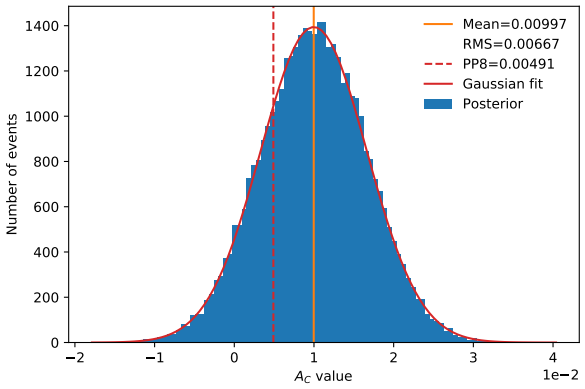

(c) $750 < m(t\bar{t}) < 1000$ GeV.

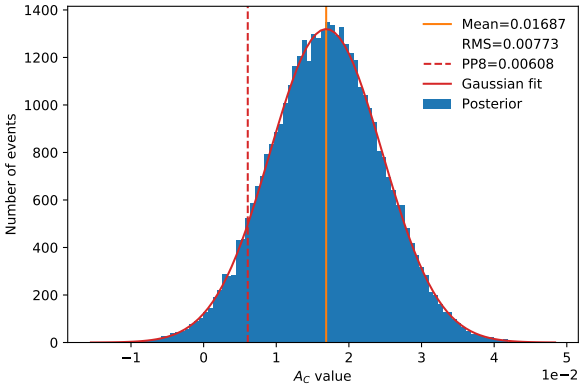

(d) $1000 < m(t\bar{t}) < 1500$ GeV.

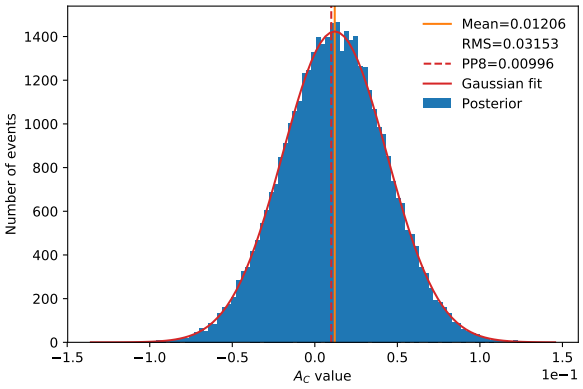

(e) $m(t\bar{t}) > 1500$ GeV.

Figure 10.7: The A_C posterior in the differential $m(t\bar{t})$ measurement. The POWHEG+PYTHIA 8 parton-level asymmetry and posterior mean values are presented in red and orange, respectively.

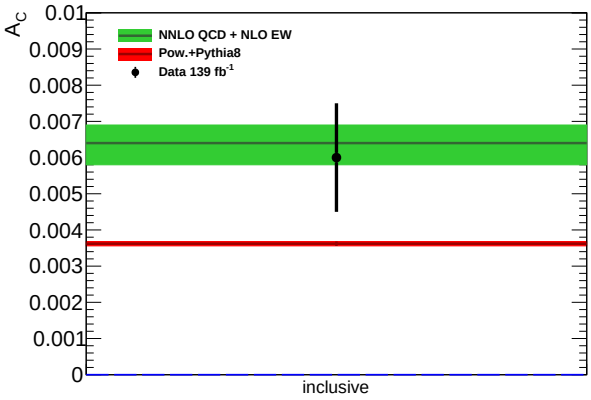

(a) Data 139 fb^{-1}, inclusive.

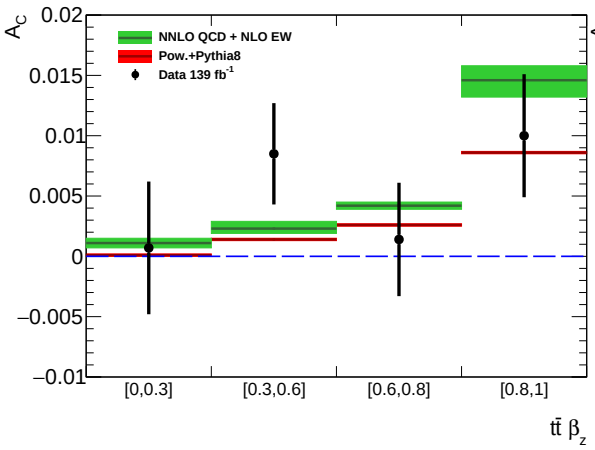

(b) Data 139 fb^{-1}, differential $\beta_z(t\bar{t})$.

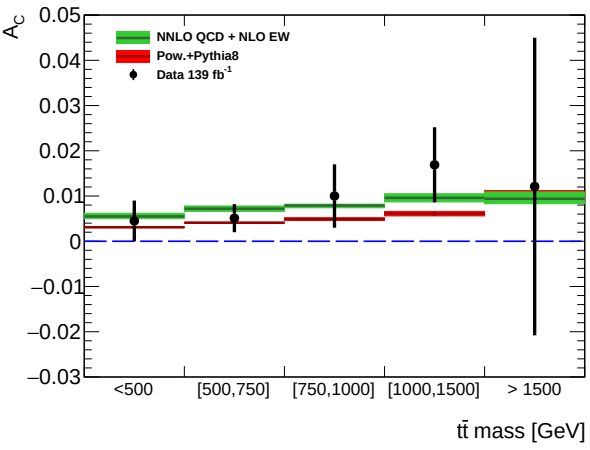

(c) Data 139 fb^{-1}, differential $m(t\bar{t})$.

Figure 10.8: The unfolded inclusive and differential ($\beta_z(t\bar{t})$ and $m(t\bar{t})$) A_C values compared to the SM prediction [132] and the POWHEG+PYTHIA 8 parton-level asymmetry. The total uncertainty is shown.

10.6 Comparison with the 8 TeV ATLAS A_C Measurements

A comparison of the measured A_C values with the ATLAS 8 TeV A_C results [150, 154] in the lepton+jets decay channel is shown in Figure 10.9. In all cases a good agreement of the measured values with the SM prediction is observed. The unfolded uncertainty is significantly reduced in the $\sqrt{s} = 13$ TeV results, especially in the case of the differential measurements. However, at the same time the SM predicts smaller asymmetry values at $\sqrt{s} = 13$ TeV due to larger fraction of top-quark pairs produced via gluon fusion.

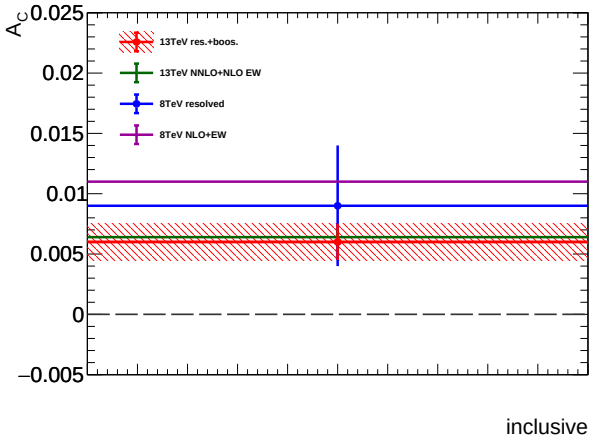

(a) Data 139 fb^{-1}, inclusive.

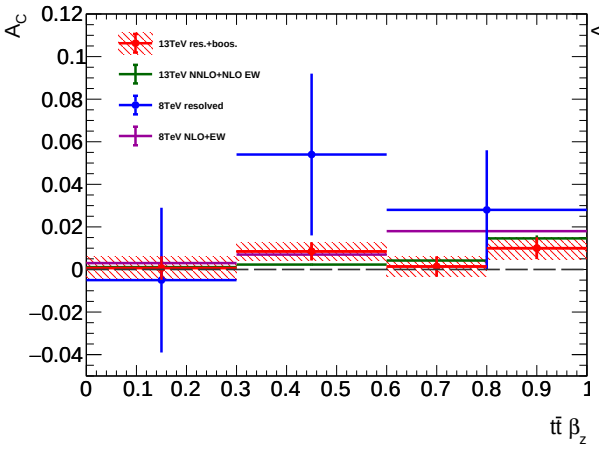

(b) Data 139 fb^{-1}, differential $\beta_z(t\bar{t})$.

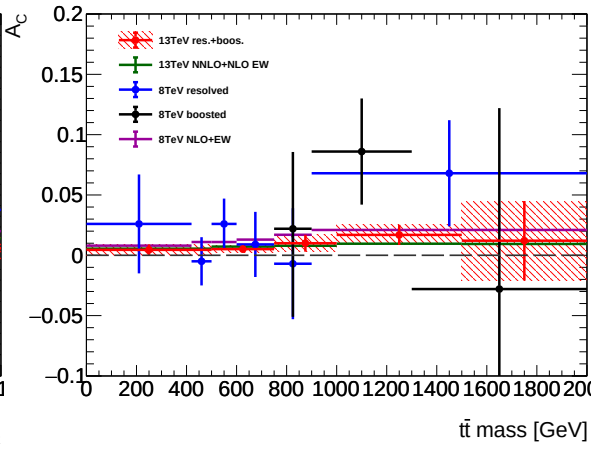

(c) Data 139 fb^{-1}, differential $m(t\bar{t})$.

Figure 10.9: A comparison of the A_C values measured by the ATLAS experiment using proton-proton collision data at $\sqrt{s} = 13$ TeV and $\sqrt{s} = 8$ TeV [150, 154]. The measured values are compared to the NNLO+NLO EW prediction [132] at $\sqrt{s} = 13$ TeV and to the NLO+EW calculation at $\sqrt{s} = 8$ TeV [117].

10.7 Discussion

This thesis was written in the final stages of the effort to obtain the first ATLAS preliminary A_C result at $\sqrt{s} = 13$ TeV. Among the last missing steps there is an effective field theory interpretation which would constrain the BSM physics in a model-independent way as proposed in Ref. [266].

The final ATLAS Run 2 A_C result is expected to benefit also from the dilepton $t\bar{t}$ decay channel and possibly even from the all-hadronic boosted channel in order to further reduce the uncertainties. A differential measurement as a function of the $p_T(t\bar{t})$ is also expected to be added. The current measurement is still dominated by statistical uncertainties and there will be no new data from the ATLAS experiment for several years. However, there are some possibilities to increase the acceptance of the selection and thus to reduce the statistical uncertainties without adding new data. In the high $m(t\bar{t})$ region there is a problem in both ℓ+jets topologies that the charged lepton gets too close to the b-jet and the event is rejected by the lepton isolation or overlap removal criteria. The currently used settings are relatively strict and the overlap removal criteria are constant, not taking into account the momenta of the studied objects. By modifying the lepton isolation and overlap removal criteria it should be possible to significantly increase the acceptance in the high $m(t\bar{t})$ region.

Conclusion

This thesis presents the first measurement of the charge asymmetry in top-quark pair production by the ATLAS experiment using full Run 2 (139 fb^{-1}) proton-proton collision data at $\sqrt{s} = 13$ TeV. The lepton+jets decay channel is investigated. Events are selected in the resolved and boosted topologies which are subsequently combined within the fully bayesian unfolding method. The charge asymmetry is measured inclusively and also differentially as a function of the top-quark pair longitudinal boost and mass. Systematic uncertainties are marginalised within the unfolding procedure. A bootstrapping method is used to remove statistically insignificant systematic uncertainties and a pruning procedure is used to remove negligible uncertainties in order to simplify the unfolding problem. The measurement is limited by statistical uncertainties in all regions and the measured values are in good agreement with the NNLO in QCD + NLO in EW Standard Model predictions. A significant improvement in the precision with respect to the 8 TeV A_{C} measurements is observed. In the inclusive case, an evidence of a non-zero asymmetry is observed at a 4 σ confidence level.

Bibliography

[1] S. Weinberg, *A Model of Leptons*, Phys. Rev. Lett. **19** (1967) 1264–1266.

[2] A. Salam, *Weak and Electromagnetic Interactions*, Conf. Proc. **C680519** (1968) 367–377, http://inspirehep.net/record/53083.

[3] H. Fritzsch, M. Gell-Mann, and H. Leutwyler, *Advantages of the color octet gluon picture*, Phys. Lett. B **47** (1973) 365 – 368.

[4] S. L. Glashow, *Partial-symmetries of weak interactions*, Nucl. Phys. **22** (1961) 579 – 588.

[5] C. S. Wu, et al., *Experimental Test of Parity Conservation in Beta Decay*, Phys. Rev. **105** (1957) 1413–1414.

[6] A. Salam and J. Ward, *Electromagnetic and weak interactions*, Phys. Lett. **13** (1964) 168 – 171.

[7] F. Englert and R. Brout, *Broken Symmetry and the Mass of Gauge Vector Mesons*, Phys. Rev. Lett. **13** (1964) 321–323.

[8] P. W. Higgs, *Broken Symmetries and the Masses of Gauge Bosons*, Phys. Rev. Lett. **13** (1964) 508–509.

[9] F. H. et al., *Observation of neutrino-like interactions without muon or electron in the gargamelle neutrino experiment*, Phys. Lett. B **46** (1973) 138 – 140.

[10] P. Musset and J.-P. Vialle, *Neutrino physics with gargamelle*, Phys. Rept. **39** (1978) 1 – 130.

[11] UA1 Collaboration, *Experimental Observation of Isolated Large Transverse Energy Electrons with Associated Missing Energy at* $\sqrt{s} = 540$ *GeV*, Phys. Lett. B **122** (1983) 103–116.

[12] UA2 Collaboration, *Observation of single isolated electrons of high transverse momentum in events with missing transverse energy at the CERN pp collider*, Phys. Lett. B **122** (1983) 476 – 485.

[13] UA1 Collaboration, *Experimental Observation of Lepton Pairs of Invariant Mass Around 95 GeV/*c^2 *at the CERN SPS Collider*, Phys. Lett. B **126** (1983) 398–410.

[14] UA2 Collaboration, *Evidence for* $Z^0 \to e^+e^-$ *at the CERN* $p\bar{p}$ *Collider*, Phys. Lett. B **129** (1983) 130–140.

[15] M. Gell-Mann, *The Eightfold Way: A Theory of strong interaction symmetry*, http://inspirehep.net/record/44998/.

[16] V. E. e. a. Barnes, *Observation of a Hyperon with Strangeness Minus Three*, Phys. Rev. Lett. **12** (1964) 204–206.

[17] M. Gell-Mann, *A schematic model of baryons and mesons*, Phys. Lett. **8** (1964) 214 – 215.

[18] G. Zweig, *An SU_3 model for strong interaction symmetry and its breaking; Version 1*, http://inspirehep.net/record/11881.

[19] W. Pauli, *Über den Zusammenhang des Abschlusses der Elektronengruppen im Atom mit der Komplexstruktur der Spektren*, Zeitschrift für Physik **31** (1925) 765–783.

[20] O. W. Greenberg, *Spin and Unitary-Spin Independence in a Paraquark Model of Baryons and Mesons*, Phys. Rev. Lett. **13** (1964) 598–602.

[21] M. Y. Han and Y. Nambu, *Three Triplet Model with Double SU(3) Symmetry*, Phys. Rev. **139** (1965) B1006–B1010.

[22] D. J. Gross and F. Wilczek, *Ultraviolet Behavior of Non-Abelian Gauge Theories*, Phys. Rev. Lett. **30** (1973) 1343–1346.

[23] H. D. Politzer, *Reliable Perturbative Results for Strong Interactions?*, Phys. Rev. Lett. **30** (1973) 1346–1349.

[24] V. N. Gribov, *The Theory of quark confinement*, Eur. Phys. J. C **10** (1999) 91–105.

[25] D. P. e. a. Barber, *Discovery of Three-Jet Events and a Test of Quantum Chromodynamics at PETRA*, Phys. Rev. Lett. **43** (1979) 830–833.

[26] Particle Data Group Collaboration, *Review of Particle Physics*, Phys. Rev. D **98** (2018) 030001.

[27] F. E. Wietfeldt and G. L. Greene, *Colloquium: The neutron lifetime*, Rev. Mod. Phys. **83** (2011) 1173–1192.

[28] J. J. e. a. Aubert, *Experimental Observation of a Heavy Particle J*, Phys. Rev. Lett. **33** (1974) 1404–1406.

[29] J. E. e. a. Augustin, *Discovery of a Narrow Resonance in e^+e^- Annihilation*, Phys. Rev. Lett. **33** (1974) 1406–1408.

[30] S. W. e. a. Herb, *Observation of a Dimuon Resonance at* 9.5 *GeV in* 400 *GeV Proton-Nucleus Collisions*, Phys. Rev. Lett. **39** (1977) 252–255.

[31] CDF Collaboration, *Observation of top quark production in $\bar{p}p$ collisions*, Phys. Rev. Lett. **74** (1995) 2626–2631.

[32] D0 Collaboration, *Observation of the top quark*, Phys. Rev. Lett. **74** (1995) 2632–2637.

[33] CDF Collaboration, *The CDF Detector: An Overview*, Nucl. Instrum. Meth. A **271** (1988) 387–403.

[34] D0 Collaboration, *The D0 Detector*, Nucl. Instrum. Meth. A **338** (1994) 185–253.

[35] S. Holmes, R. S. Moore, and V. Shiltsev, *Overview of the Tevatron Collider Complex: Goals, Operations and Performance*, JINST **6** (2011) T08001.

[36] B. Andersson, et al., *Parton Fragmentation and String Dynamics*, Phys. Rept. **97** (1983) 31–145.

[37] J. J. Thomson, *Cathode rays*, Phil. Mag. Ser.5 **44** (1897) 293–316.

[38] C. D. Anderson, *The Positive Electron*, Phys. Rev. **43** (1933) 491–494.

[39] P. A. Cherenkov, *Visible luminescence of pure liquids under the influence of γ-radiation*, Dokl. Akad. Nauk SSSR **2** (1934) 451–454.

[40] V. L. Ginzburg and I. M. Frank, *Radiation of a uniformly moving electron due to its transition from one medium into another*, J. Phys.(USSR) **9** (1945) 353–362, http://inspirehep.net/record/45474/.

[41] M. L. e. a. Perl, *Evidence for Anomalous Lepton Production in e^+e^- Annihilation*, Phys. Rev. Lett. **35** (1975) 1489–1492.

[42] C. L. Cowan, et al., *Detection of the free neutrino: A Confirmation*, Science **124** (1956) 103–104.

[43] G. Danby, et al., *Observation of High-Energy Neutrino Reactions and the Existence of Two Kinds of Neutrinos*, Phys. Rev. Lett. **9** (1962) 36–44.

[44] DONUT Collaboration, *Observation of tau neutrino interactions*, Phys. Lett. B **504** (2001) 218–224.

[45] Super-Kamiokande Collaboration, *Evidence for oscillation of atmospheric neutrinos*, Phys. Rev. Lett. **81** (1998) 1562–1567.

[46] IceCube Collaboration, *The IceCube Data Acquisition System: Signal Capture, Digitization, and Timestamping*, Nucl. Instrum. Meth. A **601** (2009) 294–316.

[47] BAIKAL Collaboration, *The Baikal underwater neutrino telescope: Design, performance and first results*, Astropart. Phys. **7** (1997) 263–282.

[48] J. C. Maxwell, *VIII. A dynamical theory of the electromagnetic field*, Philosophical Transactions of the Royal Society of London **155** (1865) 459–512.

[49] A. Einstein, *Uber einen die Erzeugung und Verwandlung des Lichtes betreffenden heuristischen Gesichtspunkt*, Annalen der Physik **322** (1905) 132–148.

[50] R. A. Millikan, *A Direct Determination of "h."*, Phys. Rev. **4** (1914) 73–75.

[51] P. A. M. Dirac and N. H. D. Bohr, *The quantum theory of the emission and absorption of radiation*, Proceedings of the Royal Society of London. Series A, Containing Papers of a Mathematical and Physical Character **114** (1927) 243–265.

[52] F. J. Dyson, *The Radiation Theories of Tomonaga, Schwinger, and Feynman*, Phys. Rev. **75** (1949) 486–502.

[53] *LEP Design Report: Vol.2. The LEP Main Ring*, http://inspirehep.net/record/203828.

[54] ALEPH, DELPHI, L3, OPAL, LEP Electroweak Collaborations, *Electroweak Measurements in Electron-Positron Collisions at W-Boson-Pair Energies at LEP*, Phys. Rept. **532** (2013) 119–244.

[55] ALEPH, DELPHI, L3, OPAL, SLD, LEP Electroweak Working Group, SLD Electroweak Group, SLD Heavy Flavour Group, *Precision electroweak measurements on the Z resonance*, Phys. Rept. **427** (2006) 257–454.

[56] N. Cabibbo, *Unitary Symmetry and Leptonic Decays*, Phys. Rev. Lett. **10** (1963) 531–533.

[57] M. Kobayashi and T. Maskawa, *CP-Violation in the Renormalizable Theory of Weak Interaction*, Progress of Theoretical Physics **49** (1973) 652–657.

[58] L. Reinders, H. Rubinstein, and S. Yazaki, *Hadron properties from QCD sum rules*, Phys. Rept. **127** (1985) 1 – 97.

[59] Y. K. Hsiao and C. Q. Geng, *Identifying Glueball at 3.02 GeV in Baryonic B Decays*, Phys. Lett. B **727** (2013) 168–171.

[60] W. Ochs, *The Status of Glueballs*, J. Phys. G **40** (2013) 043001.

[61] ATLAS Collaboration, *The ATLAS Experiment at the CERN Large Hadron Collider*, JINST **3** (2008) S08003.

[62] CMS Collaboration, *The CMS Experiment at the CERN LHC*, JINST **3** (2008) S08004.

[63] ATLAS Collaboration, *Observation of a new particle in the search for the Standard Model Higgs boson with the ATLAS detector at the LHC*, Phys. Lett. B **716** (2012) 1–29.

[64] CMS Collaboration, *Observation of a new boson at a mass of 125 GeV with the CMS experiment at the LHC*, Phys. Lett. B **716** (2012) 30–61.

[65] A. Einstein, *On the General Theory of Relativity*, Sitzungsber. Preuss. Akad. Wiss. Berlin (Math. Phys.) **1915** (1915) 778–786, http://inspirehep.net/record/42608.

[66] K. C. Freeman, *On the Disks of Spiral and S0 Galaxies*, Astrophysical Journal **160** (1970) 811.

[67] D. Walsh, R. F. Carswell, and R. J. Weymann, *0957 + 561 A, B - Twin quasistellar objects or gravitational lens*, Nature **279** (1979) 381–384.

[68] G. Bertone, D. Hooper, and J. Silk, *Particle dark matter: Evidence, candidates and constraints*, Phys. Rept. **405** (2005) 279–390.

[69] A. G. R. et al., *Observational Evidence from Supernovae for an Accelerating Universe and a Cosmological Constant*, The Astronomical Journal **116** (1998) 1009–1038.

[70] A. D. Sakharov, *Violation of CP Invariance, C asymmetry, and baryon asymmetry of the universe*, Pisma Zh. Eksp. Teor. Fiz. **5** (1967) 32–35.

[71] G. 't Hooft, *Naturalness, chiral symmetry, and spontaneous chiral symmetry breaking*, NATO Sci. Ser. B **59** (1980) 135–157.

[72] S. Dimopoulos and H. Georgi, *Softly Broken Supersymmetry and SU(5)*, Nucl. Phys. B **193** (1981) 150–162.

[73] H. P. Nilles, *Supersymmetry, Supergravity and Particle Physics*, Phys. Rept. **110** (1984) 1–162.

[74] T. Kaluza, *Zum Unitatsproblem der Physik*, Sitzungsber. Preuss. Akad. Wiss. Berlin (Math. Phys.) **1921** (1921) 966–972.

[75] O. Klein, *The Atomicity of Electricity as a Quantum Theory Law*, Nature **118** (1926) 516.

[76] N. Arkani-Hamed, S. Dimopoulos, and G. R. Dvali, *The Hierarchy problem and new dimensions at a millimeter*, Phys. Lett. B **429** (1998) 263–272.

[77] E. Witten, *String theory dynamics in various dimensions*, Nucl. Phys. B **443** (1995) 85–126.

[78] E. Farhi and L. Susskind, *Technicolor*, Phys. Rept. **74** (1981) 277.

[79] I. A. D'Souza and C. S. Kalman, *Preons: Models of leptons, quarks and gauge bosons as composite objects*. 1992. http://inspirehep.net/record/345688.

[80] G. Isidori, G. Ridolfi, and A. Strumia, *On the metastability of the standard model vacuum*, Nucl. Phys. B **609** (2001) 387–409.

[81] J. Gao, C. S. Li, and H. X. Zhu, *Top-Quark Decay at Next-to-Next-to-Leading Order in QCD*, Phys. Rev. Lett. **110** (2013) 042001.

[82] M. Czakon, P. Fiedler, and A. Mitov, *Total Top-Quark Pair-Production Cross Section at Hadron Colliders Through* $\mathcal{O}(\alpha_S^4)$, Phys. Rev. Lett. **110** (2013) 252004.

[83] M. Czakon and A. Mitov, *Top++: A Program for the Calculation of the Top-Pair Cross-Section at Hadron Colliders*, Comput. Phys. Commun. **185** (2014) 2930.

[84] ATLAS Collaboration, *Measurement of the* $t\bar{t}$ *production cross-section using* $e\mu$ *events with b-tagged jets in pp collisions at* $\sqrt{s}$ *= 7 and 8 TeV with the ATLAS detector*, Eur. Phys. J. C **74** (2014) 3109.

[85] CMS Collaboration, *Combination of ATLAS and CMS top quark pair cross section measurements in the emu final state using proton-proton collisions at 8 TeV*, http://inspirehep.net/record/1319376.

[86] CDF and D0 Collaborations, *Combination of Measurements of the Top-Quark Pair Production Cross Section from the Tevatron Collider*, Phys. Rev. D **89** (2014) 072001.

[87] CMS Collaboration, *Measurement of the inclusive* $t\bar{t}$ *cross section in pp collisions at* $\sqrt{s}$ *= 5.02 TeV using final states with at least one charged lepton*, JHEP **03** (2018) 115.

[88] *LHCTopWG Summary Plots*, https://twiki.cern.ch/twiki/bin/view/LHCPhysics/LHCTopWGSummaryPlots, 2018. Accessed 1.3.2019.

[89] D0 Collaboration, *Observation of Single Top-Quark Production*, Phys. Rev. Lett. **103** (2009) 092001.

[90] CDF Collaboration, *Observation of Electroweak Single Top-Quark Production*, Phys. Rev. Lett. **103** (2009) 092002.

[91] T. M. P. Tait and C.-P. Yuan, *Single top quark production as a window to physics beyond the standard model*, Phys. Rev. D **63** (2000) 014018.

[92] A. Giammanco, *Single top quark production at the LHC*, Reviews in Physics **1** (2016) 1 – 12.

[93] ATLAS Collaboration, *Top-quark mass measurement in the all-hadronic $t\bar{t}$ decay channel at $\sqrt{s} = 8$ TeV with the ATLAS detector*, JHEP **09** (2017) 118.

[94] CMS Collaboration, *Measurement of the top quark mass in the all-jets final state at $\sqrt{s} = 13$ TeV and combination with the lepton+jets channel*, Submitted to: Eur. Phys. J. (2018).

[95] ATLAS Collaboration, *Performance of top-quark and W-boson tagging with ATLAS in Run 2 of the LHC*, arXiv:1808.07858.

[96] ATLAS Collaboration, *Measurements of $t\bar{t}$ differential cross-sections of highly boosted top quarks decaying to all-hadronic final states in pp collisions at $\sqrt{s} = 13$ TeV using the ATLAS detector*, Phys. Rev. D **98** (2018) 012003.

[97] D. Chang, W.-F. Chang, and E. Ma, *Alternative interpretation of the Fermilab Tevatron top events*, Phys. Rev. D **59** (1999) 091503.

[98] CDF Collaboration, *Exclusion of an Exotic Top Quark with -4/3 Electric Charge Using Soft Lepton Tagging*, Phys. Rev. Lett. **105** (2010) 101801.

[99] D0 Collaboration, *Experimental discrimination between charge 2e/3 top quark and charge 4e/3 exotic quark production scenarios*, Phys. Rev. Lett. **98** (2007) 041801.

[100] ATLAS Collaboration, *Measurement of the top quark charge in pp collisions at $\sqrt{s} = 7$ TeV with the ATLAS detector*, JHEP **11** (2013) 031.

[101] CDF Collaboration, *Top quark mass measurement using the template method in the* lepton + jets *channel at CDF II*, Phys. Rev. D **73** (2006) 032003.

[102] ATLAS Collaboration, *Measurement of the top quark mass in the $t\bar{t} \to$ lepton+jets channel from $\sqrt{s} = 8$ TeV ATLAS data and combination with previous results*, Submitted to: Eur. Phys. J. (2018).

[103] A. Buckley et al., *General-purpose event generators for LHC physics*, Phys. Rept. **504** (2011) 145–233.

[104] CMS Collaboration, *Measurement of the top quark mass using proton-proton data at $\sqrt{s} = 7$ and 8 TeV*, Phys. Rev. D **93** (2016) 072004.

[105] ATLAS, CDF, CMS and D0 Collaborations, *First combination of Tevatron and LHC measurements of the top-quark mass*, arXiv:1403.4427.

[106] J. Haller, et al., *Update of the global electroweak fit and constraints on two-Higgs-doublet models*, Eur. Phys. J. C **78** (2018) 675.

[107] T. Markkanen, A. Rajantie, and S. Stopyra, *Cosmological Aspects of Higgs Vacuum Metastability*, Front. Astron. Space Sci. **5** (2018) 40.

[108] A. Salvio, *A Simple Motivated Completion of the Standard Model below the Planck Scale: Axions and Right-Handed Neutrinos*, Phys. Lett. B **743** (2015) 428–434.

[109] CMS Collaboration, *Measurement of the ratio $\mathcal{B}(t \to Wb)/\mathcal{B}(t \to Wq)$ in pp collisions at $\sqrt{s} = 8$ TeV*, Phys. Lett. B **736** (2014) 33–57.

[110] ATLAS Collaboration, *Direct top-quark decay width measurement in the $t\bar{t}$ lepton+jets channel at $\sqrt{s}$=8 TeV with the ATLAS experiment*, Eur. Phys. J. C **78** (2018) 129.

[111] G. Mahlon and S. J. Parke, *Spin correlation effects in top quark pair production at the LHC*, Phys. Rev. D **81** (2010) 074024.

[112] ATLAS Collaboration, *Observation of spin correlation in $t\bar{t}$ events from pp collisions at $\sqrt{s} = 7$ TeV using the ATLAS detector*, Phys. Rev. Lett. **108** (2012) 212001.

[113] CMS Collaboration, *Measurements of $t\bar{t}$ spin correlations and top-quark polarization using dilepton final states in pp collisions at $\sqrt{s} = 7$ TeV*, Phys. Rev. Lett. **112** (2014) 182001.

[114] ATLAS Collaboration, *Measurements of top-quark pair spin correlations in the $e\mu$ channel at $\sqrt{s} = 13$ TeV using pp collisions in the ATLAS detector*, http://inspirehep.net/record/1681226.

[115] J. H. Kuhn and G. Rodrigo, *Charge asymmetry of heavy quarks at hadron colliders*, Phys. Rev. D **59** (1999) 054017.

[116] M. T. Bowen, S. D. Ellis, and D. Rainwater, *Standard model top quark asymmetry at the Fermilab Tevatron*, Phys. Rev. D **73** (2006) 014008.

[117] W. Bernreuther and Z.-G. Si, *Top quark and leptonic charge asymmetries for the Tevatron and LHC*, Phys. Rev. D **86** (2012) 034026.

[118] V. Ahrens, et al., *Top-pair forward-backward asymmetry beyond next-to-leading order*, Phys. Rev. D **84** (2011) 074004.

[119] N. Kidonakis, *The top quark forward-backward asymmetry at approximate N^3LO*, Phys. Rev. D **91** (2015) 071502.

[120] M. Czakon, et al., *NNLO QCD predictions for fully-differential top-quark pair production at the Tevatron*, JHEP **05** (2016) 034.

[121] M. Czakon, et al., *Top-pair production at the LHC through NNLO QCD and NLO EW*, JHEP **10** (2017) 186.

[122] J. H. Kuhn and G. Rodrigo, *Charge asymmetries of top quarks at hadron colliders revisited*, JHEP **01** (2012) 063.

[123] O. Antunano, J. H. Kuhn, and G. Rodrigo, *Top quarks, axigluons and charge asymmetries at hadron colliders*, Phys. Rev. D **77** (2008) 014003.

[124] G. Rodrigo, *Axigluon signatures at hadron colliders*, PoS **RADCOR2007** (2007) 010.

[125] J. L. Rosner, *Prominent decay modes of a leptophobic Z'*, Phys. Lett. B **387** (1996) 113–117.

[126] P. Ferrario and G. Rodrigo, *Massive color-octet bosons and the charge asymmetries of top quarks at hadron colliders*, Phys. Rev. D **78** (2008) 094018.

[127] D0 Collaboration, *Measurement of the asymmetry in angular distributions of leptons produced in dilepton $t\bar{t}$ final states in $p\overline{p}$ collisions at $\sqrt{s} = 1.96$ TeV*, Phys. Rev. D **88** (2013) 112002.

[128] CDF Collaboration, *Measurement of the Inclusive Leptonic Asymmetry in Top-Quark Pairs that Decay to Two Charged Leptons at CDF*, Phys. Rev. Lett. **113** (2014) 042001.

[129] J. A. Aguilar-Saavedra, *Single lepton charge asymmetries in ttbar and ttbargamma production at the LHC*, Eur. Phys. J. C **78** (2018) 434.

[130] LHCb Collaboration, *The LHCb Detector at the LHC*, JINST **3** (2008) S08005.

[131] R. Gauld, *Measuring top quark production asymmetries at LHCb*, `https://cds.cern.ch/record/1557385`.

[132] M. Czakon, et al., *Top-quark charge asymmetry at the LHC and Tevatron through NNLO QCD and NLO EW*, Phys. Rev. D **98** (2018) 014003.

[133] R. Field and R. Feynman, *A parametrization of the properties of quark jets*, Nucl. Phys. B **136** (1978) 1 – 76.

[134] J. A. Aguilar-Saavedra, et al., *Asymmetries in top quark pair production at hadron colliders*, Rev. Mod. Phys. **87** (2015) 421–455.

[135] CDF Collaboration, *Evidence for a Mass Dependent Forward-Backward Asymmetry in Top Quark Pair Production*, Phys. Rev. D **83** (2011) 112003.

[136] D0 Collaboration, *Forward-backward asymmetry in top quark-antiquark production*, Phys. Rev. D **84** (2011) 112005.

[137] S. Frixione and B. R. Webber, *Matching NLO QCD computations and parton shower simulations*, JHEP **06** (2002) 029.

[138] CDF Collaboration, *Measurement of the top quark forward-backward production asymmetry and its dependence on event kinematic properties*, Phys. Rev. D **87** (2013) 092002.

[139] CDF Collaboration, *Measurement of the forward-backward asymmetry of top-quark and antiquark pairs using the full CDF Run II data set*, Phys. Rev. D **93** (2016) 112005.

[140] D0 Collaboration, *Measurement of the forward-backward asymmetry in top quark-antiquark production in ppbar collisions using the lepton+jets channel*, Phys. Rev. D **90** (2014) 072011.

[141] D0 Collaboration, *Simultaneous measurement of forward-backward asymmetry and top polarization in dilepton final states from $t\bar{t}$ production at the Tevatron*, Phys. Rev. D **92** (2015) 052007.

[142] CDF Collaboration, *Measurement of the leptonic asymmetry in $t\bar{t}$ events produced in $p\bar{p}$ collisions at $\sqrt{s} = 1.96$ TeV*, Phys. Rev. D **88** (2013) 072003.

[143] D0 Collaboration, *Measurement of the forward-backward asymmetry in the distribution of leptons in $t\bar{t}$ events in the lepton+jets channel*, Phys. Rev. D **90** (2014) 072001.

[144] CDF and D0 Collaborations, *Combined Forward-Backward Asymmetry Measurements in Top-Antitop Quark Production at the Tevatron*, Phys. Rev. Lett. **120** (2018) 042001.

[145] ATLAS Collaboration, *Measurement of the top quark pair production charge asymmetry in proton-proton collisions at $\sqrt{s} = 7$ TeV using the ATLAS detector*, JHEP **02** (2014) 107.

[146] CMS Collaboration, *Inclusive and differential measurements of the $t\bar{t}$ charge asymmetry in proton-proton collisions at $\sqrt{s} = 7\,TeV$*, Phys. Lett. B **717** (2012) 129–150.

[147] ATLAS Collaboration, *Measurement of the charge asymmetry in dileptonic decays of top quark pairs in pp collisions at $\sqrt{s} = 7$ TeV using the ATLAS detector*, JHEP **05** (2015) 061.

[148] CMS Collaboration, *Measurements of the $t\bar{t}$ charge asymmetry using the dilepton decay channel in pp collisions at $\sqrt{s} = 7$ TeV*, JHEP **04** (2014) 191.

[149] ATLAS and CMS Collaborations, *Combination of inclusive and differential $\mathrm{t\bar{t}}$ charge asymmetry measurements using ATLAS and CMS data at $\sqrt{s} = 7$ and 8 TeV*, JHEP **04** (2018) 033.

[150] ATLAS Collaboration, *Measurement of the charge asymmetry in top-quark pair production in the lepton-plus-jets final state in pp collision data at $\sqrt{s} = 8$ TeV with the ATLAS detector*, Eur. Phys. J. C **76** (2016) 87.

[151] CMS Collaboration, *Inclusive and differential measurements of the $t\bar{t}$ charge asymmetry in pp collisions at $\sqrt{s} = 8$ TeV*, Phys. Lett. B **757** (2016) 154–179.

[152] ATLAS Collaboration, *Measurements of the charge asymmetry in top-quark pair production in the dilepton final state at $\sqrt{s} = 8$ TeV with the ATLAS detector*, Phys. Rev. D **94** (2016) 032006.

[153] CMS Collaboration, *Measurements of $t\bar{t}$ charge asymmetry using dilepton final states in pp collisions at $\sqrt{s} = 8$ TeV*, Phys. Lett. B **760** (2016) 365–386.

[154] ATLAS Collaboration, *Measurement of the charge asymmetry in highly boosted top-quark pair production in $\sqrt{s} = 8$ TeV pp collision data collected by the ATLAS experiment*, Phys. Lett. B **756** (2016) 52–71.

[155] CMS Collaboration, *Measurement of the charge asymmetry in top quark pair production in pp collisions at $\sqrt{s} = 8$ TeV using a template method*, Phys. Rev. D **93** (2016) 034014.

[156] J. A. Aguilar-Saavedra, *Portrait of a colour octet*, JHEP **08** (2014) 172.

[157] CMS Collaboration, *Measurements of $t\bar{t}$ differential cross sections in proton-proton collisions at $\sqrt{s} = 13$ TeV using events containing two leptons*, JHEP **02** (2019) 149.

[158] CDF Collaboration, *First measurement of the forward-backward asymmetry in bottom-quark pair production at high mass*, Phys. Rev. D **92** (2015) 032006.

[159] CDF Collaboration, *Measurement of the forward-backward asymmetry in low-mass bottom-quark pairs produced in proton-antiproton collisions*, Phys. Rev. D **93** (2016) 112003.

[160] D0 Collaboration, *Measurement of the Forward-Backward Asymmetry in the Production of $B^{\pm}$ Mesons in $p\bar{p}$ Collisions at $\sqrt{s} = 1.96$ TeV*, Phys. Rev. Lett. **114** (2015) 051803.

[161] D0 Collaboration, *Measurement of the Forward-Backward Asymmetry in Λ_b^0 and $\bar{\Lambda}_b^0$ Baryon Production in $p\bar{p}$ Collisions at $\sqrt{s} = 1.96$ TeV*, Phys. Rev. D **91** (2015) 072008.

[162] C. W. Murphy, *Bottom-Quark Forward-Backward and Charge Asymmetries at Hadron Colliders*, Phys. Rev. D **92** (2015) 054003.

[163] LHCb Collaboration, *First measurement of the charge asymmetry in beauty-quark pair production*, Phys. Rev. Lett. **113** (2014) 082003.

[164] ATLAS Collaboration, *ATLAS: Detector and physics performance technical design report. Volume 1*, https://cds.cern.ch/record/391176.

[165] O. S. Bruning, et al., *LHC Design Report*. CERN Yellow Reports: Monographs. CERN, Geneva, 2004. https://cds.cern.ch/record/782076.

[166] L. Evans and P. Bryant, *LHC Machine*, JINST **3** (2008) S08001.

[167] ALICE Collaboration, *The ALICE experiment at the CERN LHC*, JINST **3** (2008) S08002.

[168] TOTEM Collaboration, *TOTEM: Technical design report. Total cross section, elastic scattering and diffraction dissociation at the Large Hadron Collider at CERN*, https://cds.cern.ch/record/704349.

[169] LHCf Collaboration, *Technical design report of the LHCf experiment: Measurement of photons and neutral pions in the very forward region of LHC*, https://cds.cern.ch/record/926196.

[170] MoEDAL Collaboration, *Technical Design Report of the MoEDAL Experiment*, https://cds.cern.ch/record/1181486.

[171] P. A. M. Dirac, *The Theory of Magnetic Poles*, Phys. Rev. **74** (1948) 817–830.

[172] D. J. Warner, *Project study for a new 50 MeV linear accelerator for the C. P. S*, https://cds.cern.ch/record/414071.

[173] K. Hanke, *Past and present operation of the CERN PS Booster*, Int. J. Mod. Phys. A **28** (2013) 1330019.

[174] A. Blas et al., *The PS complex as proton pre-injector for the LHC: Design and implementation report*, https://cds.cern.ch/record/449242.

[175] T. Linnecar, *Preparing the SPS for LHC*, Part. Accel. **58** (1997) 91–101, https://cds.cern.ch/record/327491.

[176] K. Dahlerup-Petersen, et al., *The Protection System for the Superconducting Elements of the Large Hadron Collider at CERN*, https://cds.cern.ch/record/386677.

[177] M. Bajko et al., *Report of the Task Force on the Incident of 19th September 2008 at the LHC*, https://cds.cern.ch/record/1168025.

[178] *LuminosityPublicResultsRun2*, https://twiki.cern.ch/twiki/bin/view/AtlasPublic/LuminosityPublicResultsRun2#Multiple_Year_Collision_Plots, 2019. Accessed 9.1.2019.

[179] ATLAS Collaboration, *ATLAS inner detector: Technical Design Report, 1*, http://cds.cern.ch/record/331063/.

[180] ATLAS Collaboration, *ATLAS Insertable B-Layer Technical Design Report*, https://cds.cern.ch/record/1291633.

[181] ATLAS Collaboration, *ATLAS liquid-argon calorimeter: Technical Design Report*, https://cds.cern.ch/record/331061.

[182] ATLAS Collaboration, *ATLAS tile calorimeter: Technical Design Report*, https://cds.cern.ch/record/331062/.

[183] ATLAS Collaboration, *ATLAS muon spectrometer: Technical Design Report*, https://cds.cern.ch/record/331068.

[184] ATLAS Collaboration, *ATLAS magnet system: Technical Design Report, 1*, https://cds.cern.ch/record/338080.

[185] ATLAS Collaboration, *ATLAS level-1 trigger: Technical Design Report*, https://cds.cern.ch/record/381429.

[186] ATLAS Collaboration, *ATLAS high-level trigger, data-acquisition and controls: Technical Design Report*, https://cds.cern.ch/record/616089.

[187] S. Baranov, et al., *Estimation of Radiation Background, Impact on Detectors, Activation and Shielding Optimization in ATLAS*, http://cds.cern.ch/record/814823.

[188] *Total Integrated Luminosity and Data Quality in 2015-2018*, https://twiki.cern.ch/twiki/bin/view/AtlasPublic/LuminosityPublicResultsRun2#Multiple_Year_Collision_Plots, 2019. Accessed 9.1.2018.

[189] A. Rosenfeld and J. L. Pfaltz, *Sequential Operations in Digital Picture Processing*, J. ACM **13** (1966) 471–494.

[190] E. Belau et al., *The Charge Collection in Silicon Strip Detectors*, Nucl. Instrum. Meth. **214** (1983) 253.

[191] R. Fruhwirth, *Application of Kalman filtering to track and vertex fitting*, Nucl. Instrum. Meth. A **262** (1987) 444–450.

[192] ATLAS Collaboration, *Performance of the ATLAS Track Reconstruction Algorithms in Dense Environments in LHC Run 2*, Eur. Phys. J. C **77** (2017) 673.

[193] ATLAS Collaboration, *A neural network clustering algorithm for the ATLAS silicon pixel detector*, JINST **9** (2014) P09009.

[194] R. Fruhwirth, W. Waltenberger, and P. Vanlaer, *Adaptive vertex fitting*, J. Phys. G **34** (2007) N343.

[195] ATLAS Collaboration, *Electron and photon energy calibration with the ATLAS detector using data collected in 2015 at* $\sqrt{s} = 13$ *TeV*, https://cds.cern.ch/record/2203514.

[196] W. Lampl, et al., *Calorimeter Clustering Algorithms: Description and Performance*, https://cds.cern.ch/record/1099735.

[197] ATLAS Collaboration, *Electron efficiency measurements with the ATLAS detector using the 2015 LHC proton-proton collision data*, https://cds.cern.ch/record/2157687.

[198] ATLAS Collaboration, *Muon reconstruction performance of the ATLAS detector in proton-proton collision data at* $\sqrt{s} = 13$ *TeV*, Eur. Phys. J. C **76** (2016) 292.

[199] M. Cacciari, G. P. Salam, and G. Soyez, *The anti-*k_t *jet clustering algorithm*, JHEP **04** (2008) 063.

[200] G. P. Salam, *Towards Jetography*, Eur. Phys. J. C **67** (2010) 637–686.

[201] ATLAS Collaboration, *Jet energy scale measurements and their systematic uncertainties in proton-proton collisions at* $\sqrt{s} = 13$ *TeV with the ATLAS detector*, Phys. Rev. D **96** (2017) 072002.

[202] M. Cacciari, G. P. Salam, and G. Soyez, *The Catchment Area of Jets*, JHEP **04** (2008) 005.

[203] T. Sjöstrand et al., *PYTHIA 6.4 Physics and Manual*, JHEP **0605** (2006) 026.

[204] T. Sjöstrand et al., *A Brief Introduction to PYTHIA 8.1*, Comput. Phys. Commun. **178** (2008) 852–867.

[205] T. Sjöstrand et al., *An Introduction to PYTHIA 8.2*, Comput. Phys. Commun. **191** (2015) 159–177.

[206] ATLAS Collaboration, *Performance of pile-up mitigation techniques for jets in pp collisions at* $\sqrt{s} = 8$ *TeV using the ATLAS detector*, Eur. Phys. J. C **76** (2016) 581.

[207] ATLAS Collaboration, *Local hadronic calibration*, http://inspirehep.net/record/811642.

[208] D. Krohn, J. Thaler, and L.-T. Wang, *Jet Trimming*, JHEP **02** (2010) 084.

[209] S. D. Ellis and D. E. Soper, *Successive combination jet algorithm for hadron collisions*, Phys. Rev. D **48** (1993) 3160–3166.

[210] ATLAS Collaboration, *Performance of jet substructure techniques for large-R jets in proton-proton collisions at $\sqrt{s} = 7$ TeV using the ATLAS detector*, JHEP **09** (2013) 076.

[211] ATLAS Collaboration, *Performance of b-Jet Identification in the ATLAS Experiment*, JINST **11** (2016) P04008.

[212] ATLAS Collaboration, *Optimisation and performance studies of the ATLAS b-tagging algorithms for the 2017-18 LHC run*, https://cds.cern.ch/record/2273281.

[213] ATLAS Collaboration, *Measurements of b-jet tagging efficiency with the ATLAS detector using $t\bar{t}$ events at $\sqrt{s} = 13$ TeV*, JHEP **08** (2018) 089.

[214] ATLAS Collaboration, *Measurement of b-tagging Efficiency of c-jets in $t\bar{t}$ Events Using a Likelihood Approach with the ATLAS Detector*, https://cds.cern.ch/record/2306649.

[215] ATLAS Collaboration, *Performance of missing transverse momentum reconstruction with the ATLAS detector using proton-proton collisions at $\sqrt{s} = 13$ TeV*, Eur. Phys. J. C **78** (2018) 903.

[216] G. Avoni et al., *The new LUCID-2 detector for luminosity measurement and monitoring in ATLAS*, JINST **13** (2018) P07017.

[217] ATLAS Collaboration, *Luminosity determination in pp collisions at $\sqrt{s} = 8$ TeV using the ATLAS detector at the LHC*, Eur. Phys. J. C **76** (2016) 653.

[218] D. J. Lange, *The EvtGen particle decay simulation package*, Nucl. Instrum. Meth. A **462** (2001) 152–155.

[219] T. Gleisberg, et al., *Event generation with SHERPA 1.1*, JHEP **02** (2009) 007.

[220] GEANT4 Collaboration, *GEANT4: A Simulation toolkit*, Nucl. Instrum. Meth. A **506** (2003) 250–303.

[221] E. Richter-Was, D. Froidevaux, and L. Poggioli, *ATLFAST 2.0 a fast simulation package for ATLAS*, http://inspirehep.net/record/1195280.

[222] W. Lukas, *Fast Simulation for ATLAS: Atlfast-II and ISF*, 2012. http://inspirehep.net/record/1197050.

[223] A. D. Martin, et al., *Parton distributions for the LHC*, Eur. Phys. J. C **63** (2009) 189–285.

[224] P. Nason, *A New method for combining NLO QCD with shower Monte Carlo algorithms*, JHEP **11** (2004) 040.

[225] S. Frixione, P. Nason, and C. Oleari, *Matching NLO QCD computations with Parton Shower simulations: the POWHEG method*, JHEP **11** (2007) 070.

[226] S. Alioli, et al., *A general framework for implementing NLO calculations in shower Monte Carlo programs: the POWHEG BOX*, JHEP **06** (2010) 043.

[227] NNPDF Collaboration, *Parton distributions for the LHC Run II*, JHEP **04** (2015) 040.

[228] ATLAS Collaboration, *Studies on top-quark Monte Carlo modelling for Top2016*, https://cds.cern.ch/record/2216168.

[229] *ATLAS Run 1 Pythia8 tunes*, https://cds.cern.ch/record/1966419.

[230] J. Alwall, et al., *The automated computation of tree-level and next-to-leading order differential cross sections, and their matching to parton shower simulations*, JHEP **07** (2014) 079.

[231] M. Bahr et al., *Herwig++ Physics and Manual*, Eur. Phys. J. C **58** (2008) 639–707.

[232] J. Bellm et al., *Herwig 7.0/Herwig++ 3.0 release note*, Eur. Phys. J. C **76** (2016) 196.

[233] L. A. Harland-Lang, et al., *Parton distributions in the LHC era: MMHT 2014 PDFs*, Eur. Phys. J. C **75** (2015) 204.

[234] R. Frederix, E. Re, and P. Torrielli, *Single-top t-channel hadroproduction in the four-flavour scheme with POWHEG and aMC@NLO*, JHEP **09** (2012) 130.

[235] E. Re, *Single-top Wt-channel production matched with parton showers using the POWHEG method*, Eur. Phys. J. C **71** (2011) 1547.

[236] S. Alioli, et al., *NLO single-top production matched with shower in POWHEG: s- and t-channel contributions*, JHEP **09** (2009) 111.

[237] LHC Higgs Cross Section Working Group, *Handbook of LHC Higgs Cross Sections: 4. Deciphering the Nature of the Higgs Sector*, arXiv:1610.07922.

[238] C. Anastasiou, et al., *High precision QCD at hadron colliders: Electroweak gauge boson rapidity distributions at NNLO*, Phys. Rev. D **69** (2004) 094008.

[239] J. M. Campbell and R. K. Ellis, *Update on vector boson pair production at hadron colliders*, Phys. Rev. D **60** (1999) 113006.

[240] ATLAS Collaboration, *Estimation of non-prompt and fake lepton backgrounds in final states with top quarks produced in proton-proton collisions at* $\sqrt{s} = 8$ *TeV with the ATLAS detector*, http://inspirehep.net/record/1319687.

[241] E. et al., *A likelihood-based reconstruction algorithm for top-quark pairs and the KLFitter framework*, Nucl. Instrum. Meth. A **748** (2014) 18–25.

[242] ATLAS Collaboration, *Search for* $t\bar{t}$ *resonances in the lepton plus jets final state with ATLAS using 4.7* fb^{-1} *of pp collisions at* $\sqrt{s} = 7$ *TeV*, Phys. Rev. D **88** (2013) 012004.

[243] A. Hocker et al., *TMVA - Toolkit for Multivariate Data Analysis*, arXiv:physics/0703039.

[244] *Simulation of top quark production for the ATLAS experiment at* $\sqrt{s} = 13$ *TeV*, https://cds.cern.ch/record/2120417.

[245] G.Choudalakis, *Fully Bayesian Unfolding*, arXiv:1201.4612.

[246] P. Diaconis, *The Markov Chain Monte Carlo Revolution*, Bulletin of the American Mathematical Society **46** (2009) 179–205.

[247] M. D. Hoffman and A. Gelman, *The No-U-Turn Sampler: Adaptively Setting Path Lengths in Hamiltonian Monte Carlo*, arXiv:1111.4246.

[248] R. M. Neal, *MCMC Using Hamiltonian Dynamics*, Handbook of Markov Chain Monte Carlo **54** (2010) 113–162.

[249] F. C. Salvatier J, Wiecki TV, *Probabilistic programming in Python using PyMC3*, PeerJ Computer Science **2:e55** (2016).

[250] A. Gelman and D. B. Rubin, *Inference from Iterative Simulation Using Multiple Sequences*, Statist. Sci. **7** (1992) 457–472.

[251] R. Bassett and J. Deride, *Maximum a Posteriori Estimators as a Limit of Bayes Estimators*, Mathematical Programming (2016) .

[252] J. A. Aguilar-Saavedra, *Single top quark production at LHC with anomalous Wtb couplings*, Nucl. Phys. B **804** (2008) 160–192.

[253] ATLAS Collaboration, *Jet Calibration and Systematic Uncertainties for Jets Reconstructed in the ATLAS Detector at $\sqrt{s} = 13$ TeV*, https://cds.cern.ch/record/2037613.

[254] ATLAS Collaboration, *Tagging and suppression of pileup jets with the ATLAS detector*, https://cds.cern.ch/record/1700870.

[255] ATLAS Collaboration, *Identification of boosted, hadronically decaying W bosons and comparisons with ATLAS data taken at $\sqrt{s} = 8$ TeV*, Eur. Phys. J. C **76** (2016) 154.

[256] ATLAS Collaboration, *In-situ measurements of the ATLAS large-radius jet response in 13 TeV pp collisions*, https://cds.cern.ch/record/2275655.

[257] ATLAS Collaboration, *Calibration of light-flavour jet b-tagging rates on ATLAS proton-proton collision data at $\sqrt{s} = 13$ TeV*, http://cds.cern.ch/record/2314418.

[258] ATLAS Collaboration, *Performance of Missing Transverse Momentum Reconstruction in ATLAS studied in Proton-Proton Collisions recorded in 2012 at 8 TeV*, https://cds.cern.ch/record/1570993.

[259] J. Butterworth et al., *PDF4LHC recommendations for LHC Run II*, J. Phys. G **43** (2016) 023001.

[260] S. Dulat, et al., *New parton distribution functions from a global analysis of quantum chromodynamics*, Phys. Rev. D **93** (2016) 033006.

[261] S. Frixione, et al., *Single-top hadroproduction in association with a W boson*, JHEP **07** (2008) 029.

[262] ATLAS Collaboration, *ATLAS simulation of boson plus jets processes in Run 2*, https://cds.cern.ch/record/2261937.

[263] K. Hamilton, P. Richardson, and J. Tully, *A Modified CKKW matrix element merging approach to angular-ordered parton showers*, JHEP **11** (2009) 038.

[264] G. Bohm and G. Zech, *Introduction to Statistics and Data Analysis for Physicists; 2nd rev. ed.*, http://bib-pubdb1.desy.de/record/169869.

[265] ATLAS Collaboration, *Measurement of dijet cross sections in pp collisions at 7 TeV centre-of-mass energy using the ATLAS detector*, JHEP **05** (2014) 059.

[266] M. P. Rosello and M. Vos, *Constraints on four-fermion interactions from the $t\bar{t}$ charge asymmetry at hadron colliders*, Eur. Phys. J. C **76** (2016) 200.

Appendix

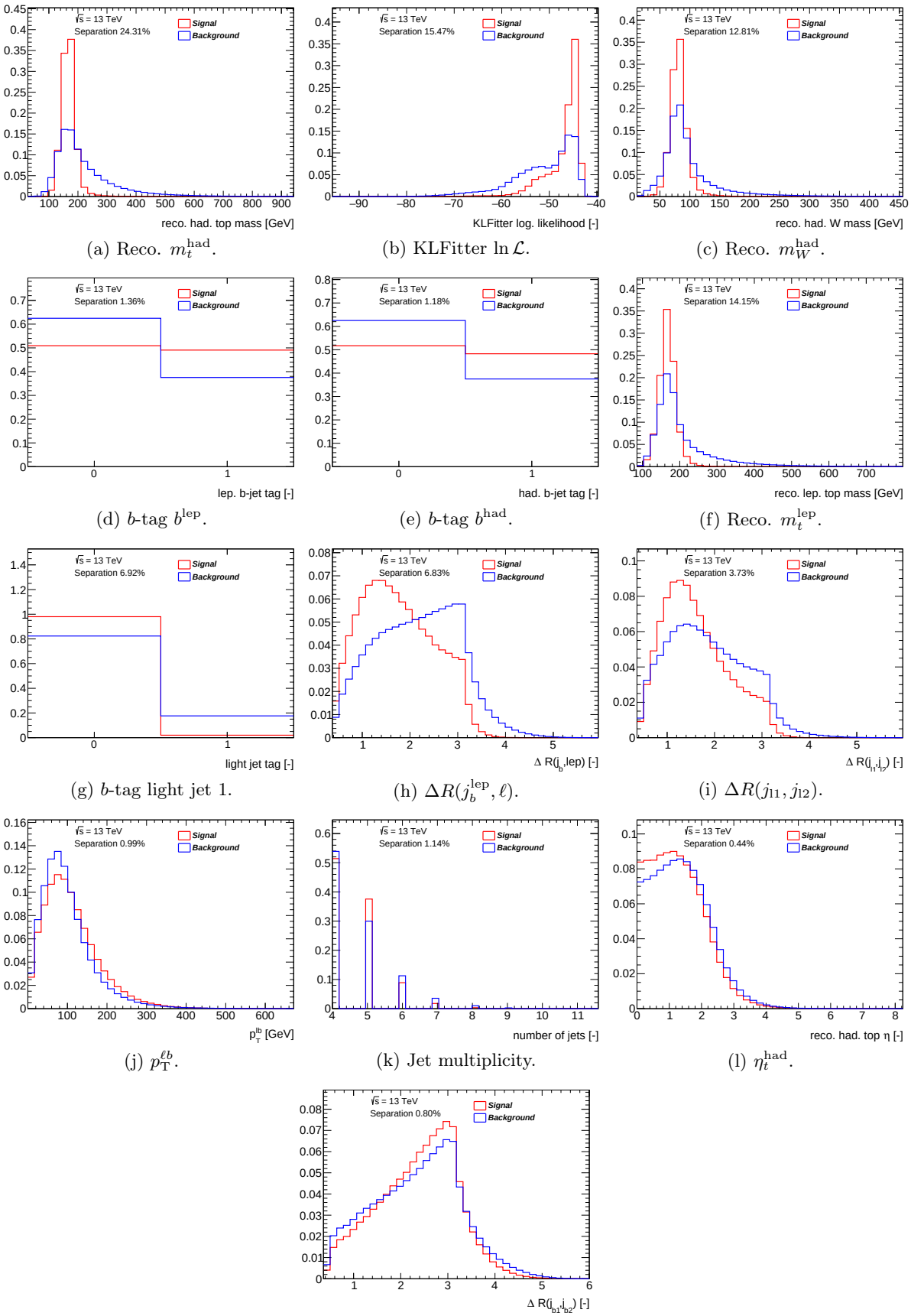

(a) Reco. m_t^{had}.

(b) KLFitter $\ln \mathcal{L}$.

(c) Reco. m_W^{had}.

(d) b-tag b^{lep}.

(e) b-tag b^{had}.

(f) Reco. m_t^{lep}.

(g) b-tag light jet 1.

(h) $\Delta R(j_b^{\mathrm{lep}}, \ell)$.

(i) $\Delta R(j_{\mathrm{l}1}, j_{\mathrm{l}2})$.

(j) $p_{\mathrm{T}}^{\ell b}$.

(k) Jet multiplicity.

(l) η_t^{had}.

(m) $\Delta R(j_b^{\mathrm{had}}, j_b^{\mathrm{lep}})$.

Figure A.1: Separation power of the BDT input variables in the 1 b-tag exclusive channel, electron and muon channels are plotted together.

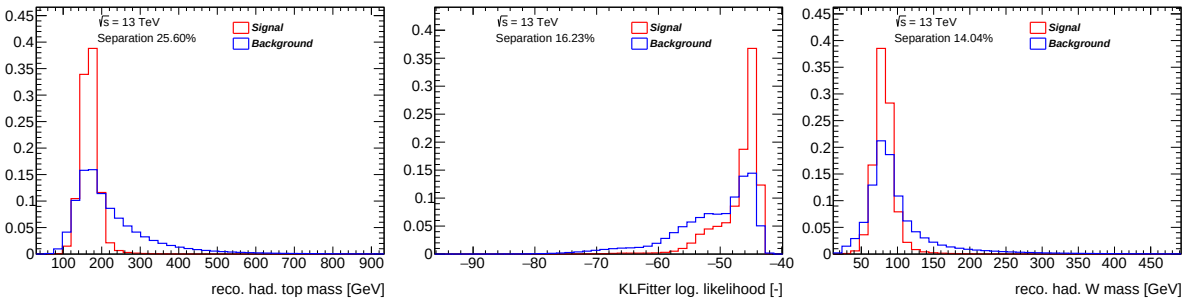

(a) Reco. m_t^{had}.

(b) KLFitter $\ln \mathcal{L}$.

(c) Reco. m_W^{had}.

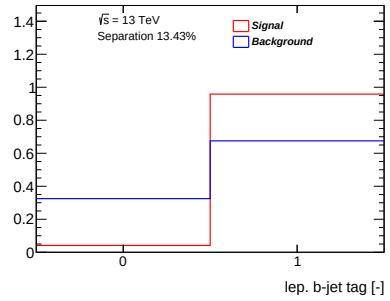

(d) b-tag b^{lep}.

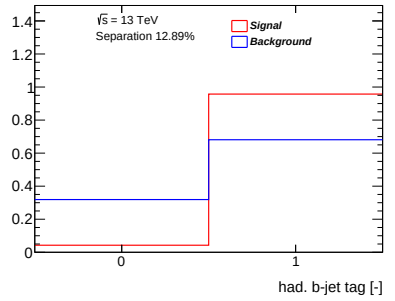

(e) b-tag b^{had}.

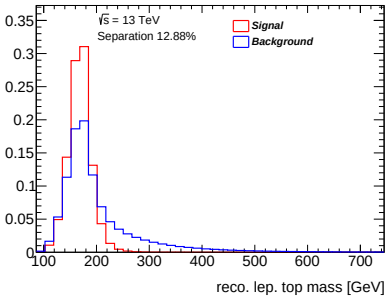

(f) Reco. m_t^{lep}.

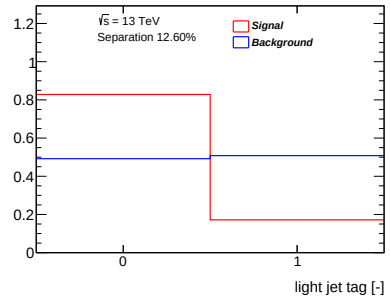

(g) b-tag light jet 1.

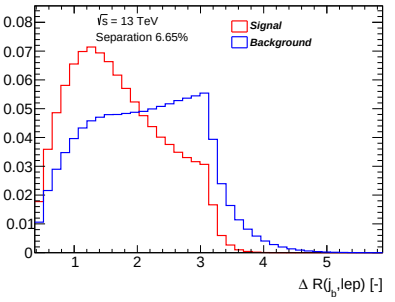

(h) $\Delta R(j_b^{\mathrm{lep}}, \ell)$.

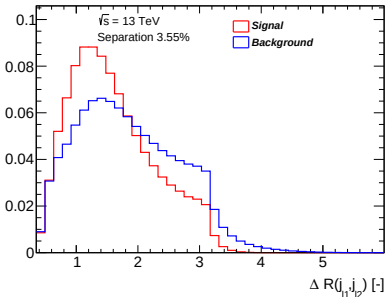

(i) $\Delta R(j_{l1}, j_{l2})$.

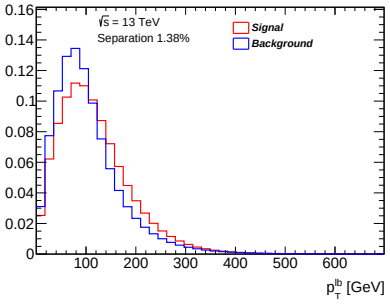

(j) $p_{\mathrm{T}}^{\ell b}$.

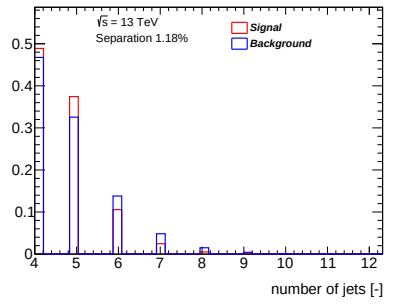

(k) Jet multiplicity.

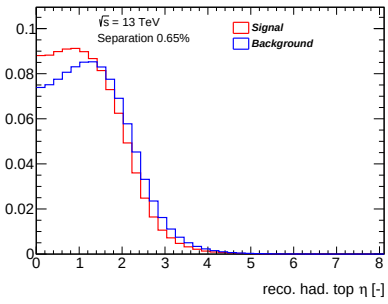

(l) η_t^{had}.

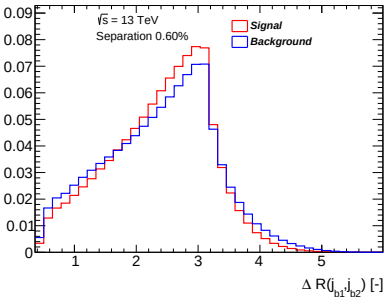

(m) $\Delta R(j_b^{\mathrm{had}}, j_b^{\mathrm{lep}})$.

Figure A.2: Separation power of the BDT input variables in the 2 b-tag inclusive channel, electron and muon channels are plotted together.

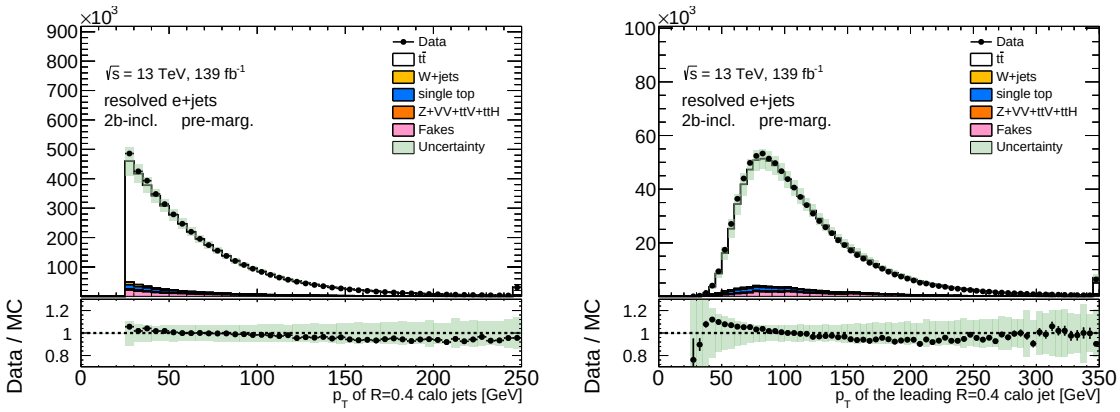

(a) Jet p_{T}.

(b) Leading jet p_{T}.

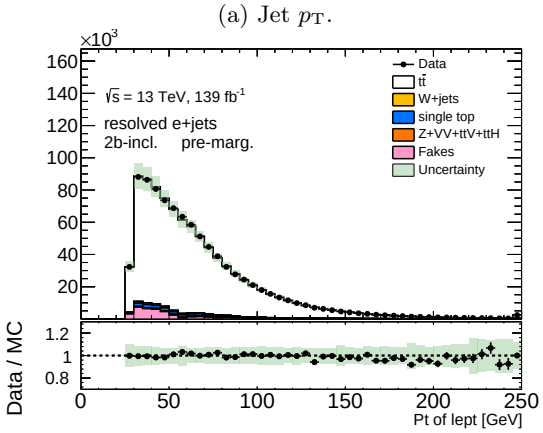

(c) Lepton p_{T}.

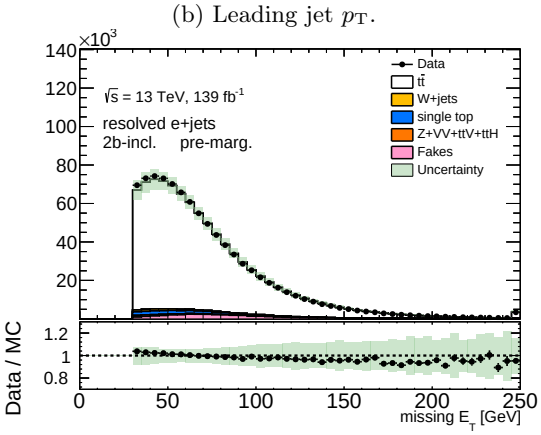

(d) $E_{\mathrm{T}}^{\mathrm{miss}}$.

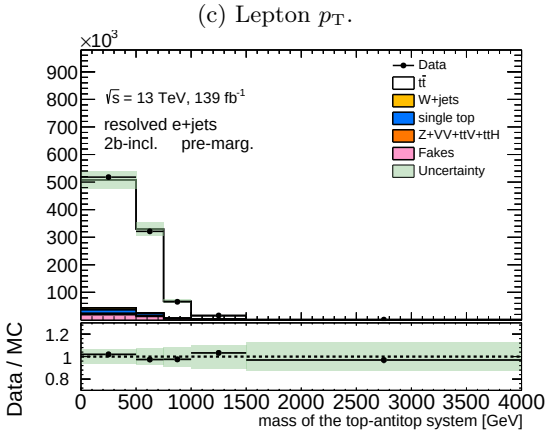

(e) $m(t\bar{t})$.

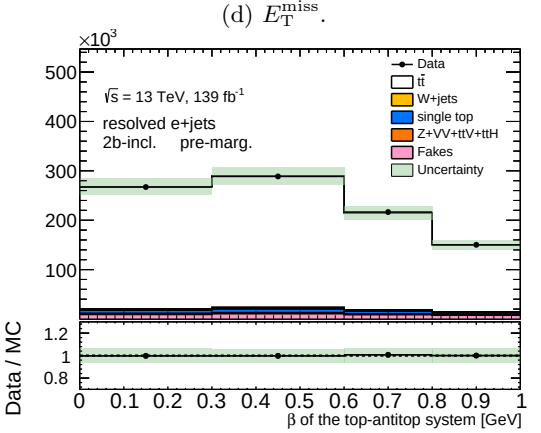

(f) $\beta_{\mathrm{z}}(t\bar{t})$.

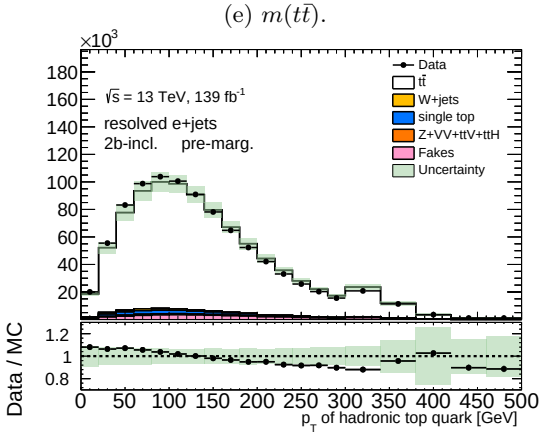

(g) BDT reco. t^{had} p_{T}.

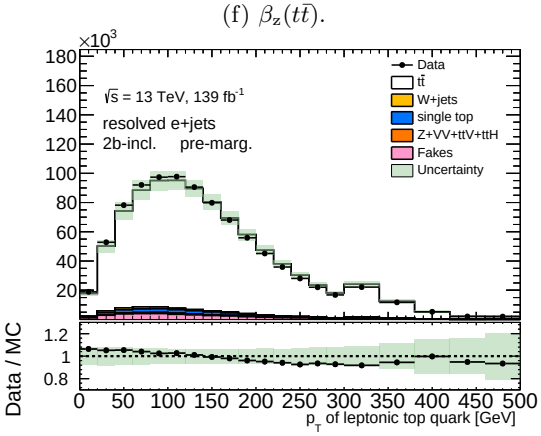

(h) BDT reco. t^{lep} p_{T}.

Figure A.3: Data to prediction comparison in resolved e+jets channel, 2incl. b-tag region. The last bin includes overflow events. The green band corresponds to the MC statistical and systematic uncertainties. Luminosity and normalisation uncertainties are not included.

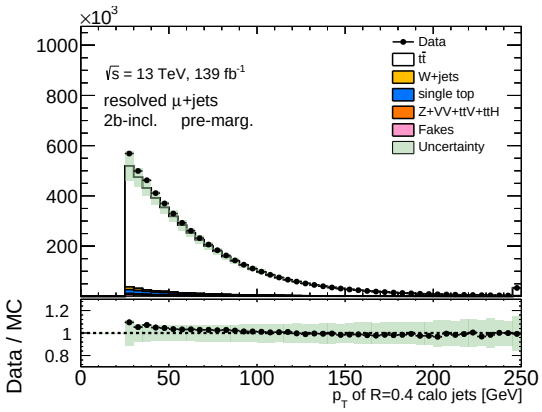

(a) Jet p_{T}.

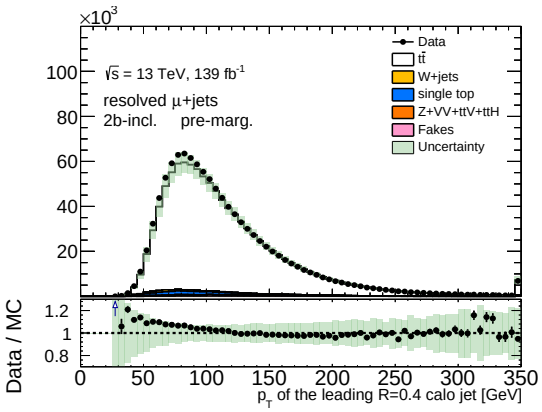

(b) Leading jet p_{T}.

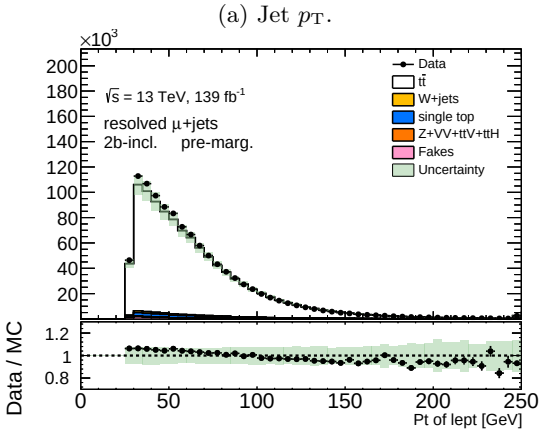

(c) Lepton p_{T}.

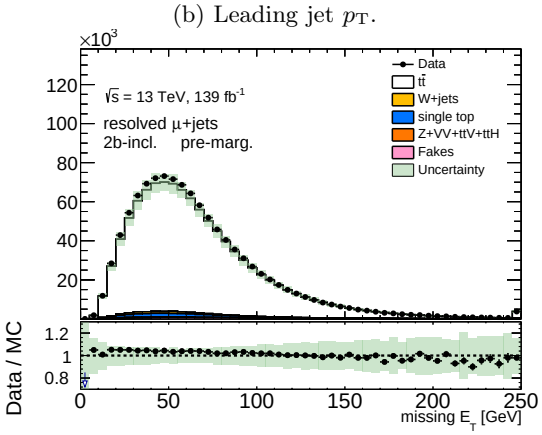

(d) $E_{\mathrm{T}}^{\mathrm{miss}}$.

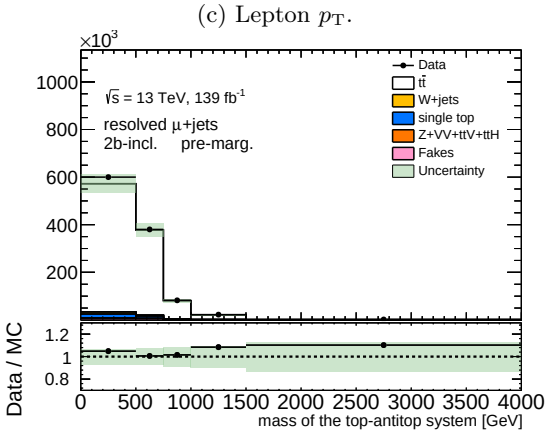

(e) $m(t\bar{t})$.

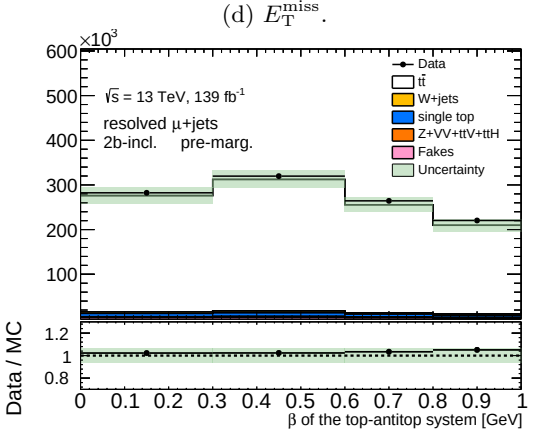

(f) $\beta_{\mathrm{z}}(t\bar{t})$.

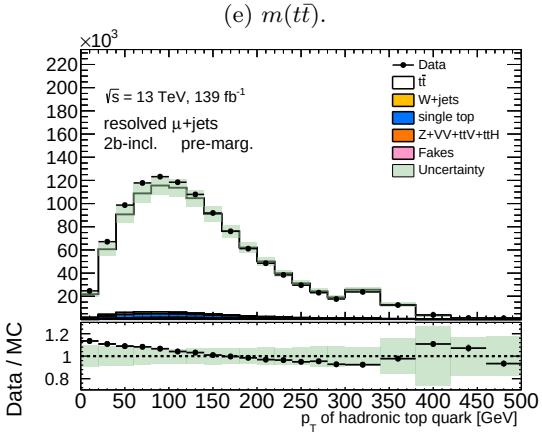

(g) BDT reco. t^{had} p_{T}.

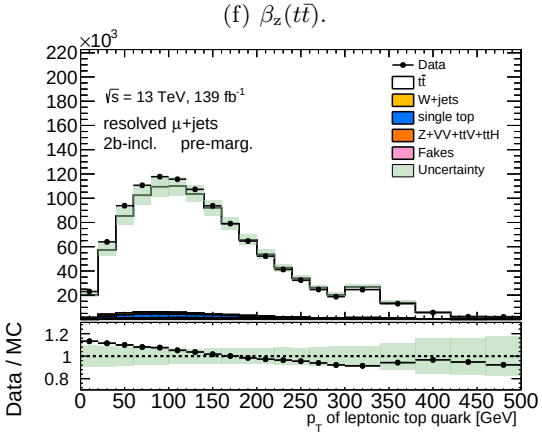

(h) BDT reco. t^{lep} p_{T}.

Figure A.4: Data to prediction comparison in resolved μ+jets channel, 2 incl. b-tag region. The last bin includes overflow events. The green band corresponds to the MC statistical and systematic uncertainties. Luminosity and normalisation uncertainties are not included.

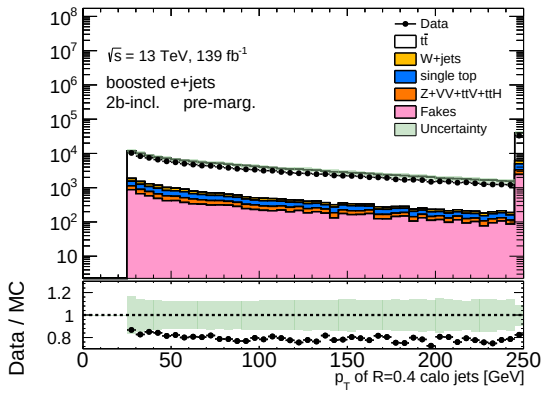

(a) Jet p_{T}.

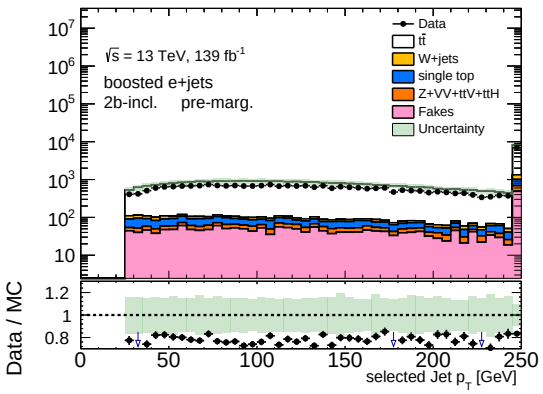

(b) Jet close to the lepton ($\Delta R(\mathrm{jet}, \ell) < 1.5$) p_{T}.

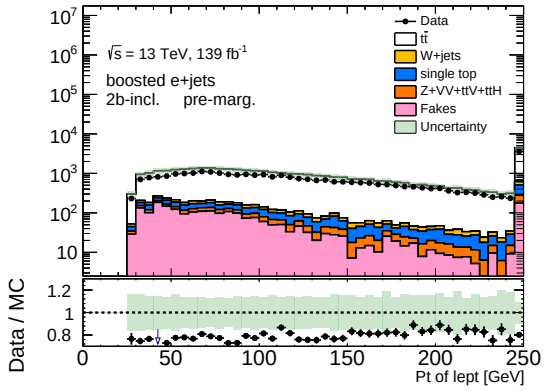

(c) Lepton p_{T}.

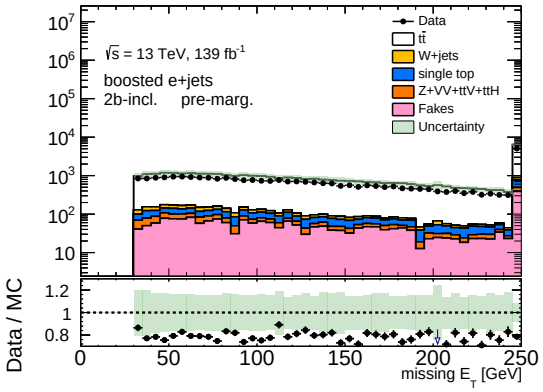

(d) $E_{\mathrm{T}}^{\mathrm{miss}}$.

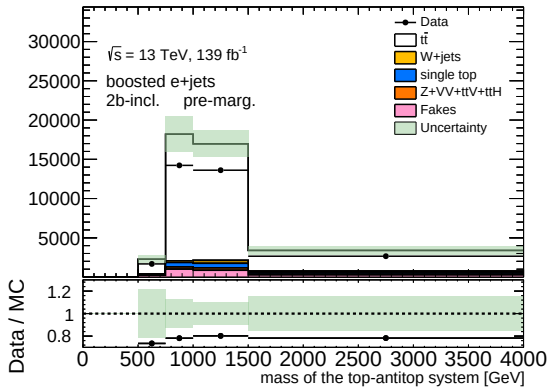

(e) $m(t\bar{t})$.

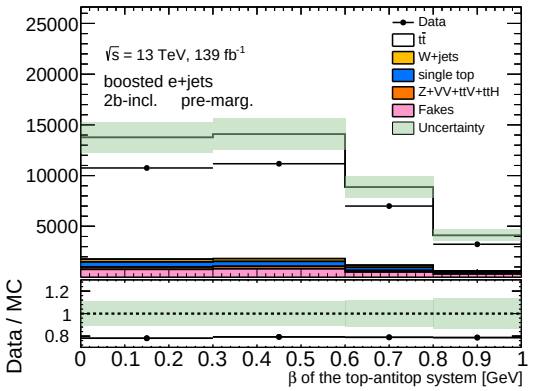

(f) $\beta_{\mathrm{z}}(t\bar{t})$.

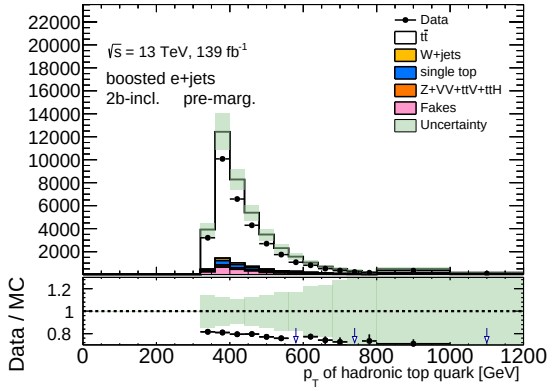

(g) Reco. t^{had} (large-R jet) p_{T}.

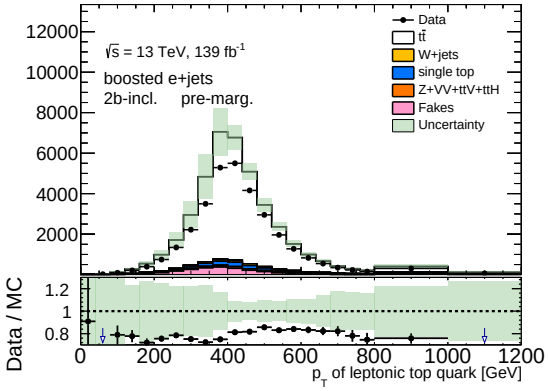

(h) Reco. t^{lep} p_{T}.

Figure A.5: Data to prediction comparison in boosted e+jets channel, 2 incl. b-tag region. The last bin includes overflow events. The green band corresponds to the MC statistical and systematic uncertainties. Luminosity and normalisation uncertainties are not included.

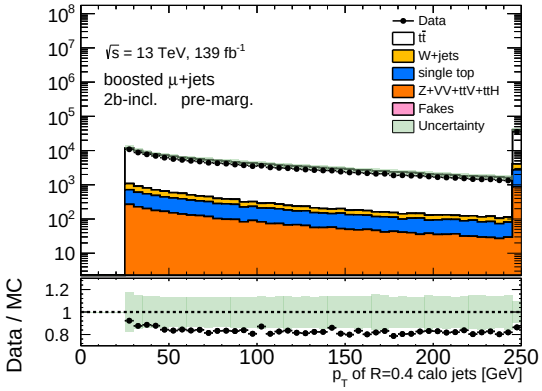

(a) Jet p_{T}.

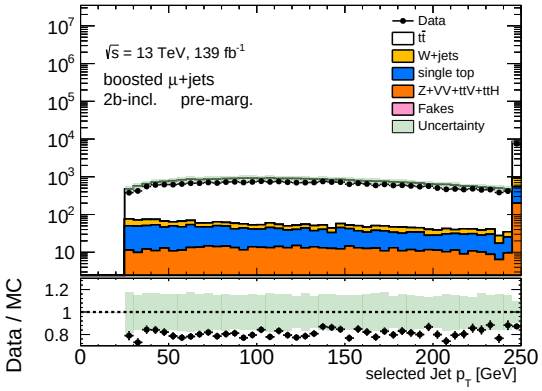

(b) Jet close to the lepton ($\Delta R(\mathrm{jet}, \ell) < 1.5$) p_{T}.

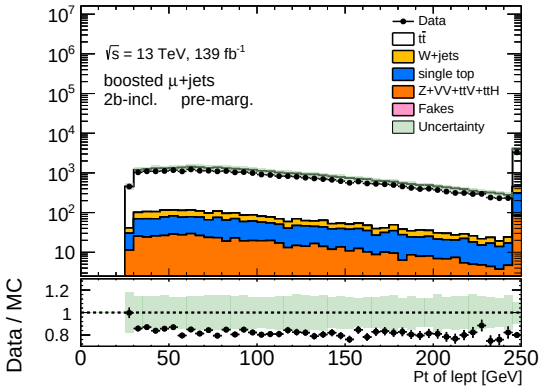

(c) Lepton p_{T}.

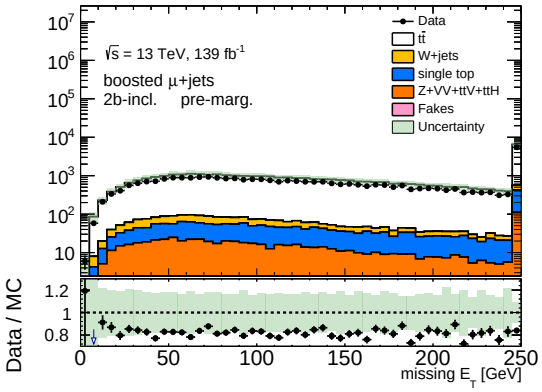

(d) $E_{\mathrm{T}}^{\mathrm{miss}}$.

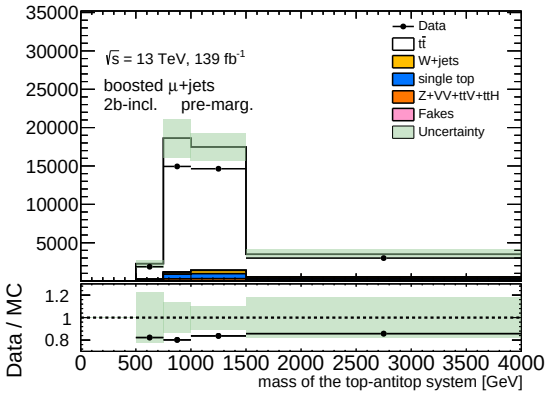

(e) $m(t\bar{t})$.

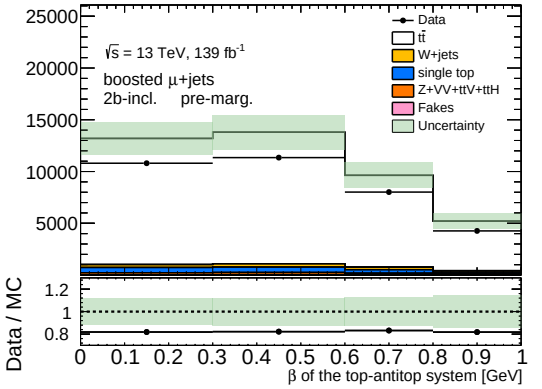

(f) $\beta_{\mathrm{z}}(t\bar{t})$.

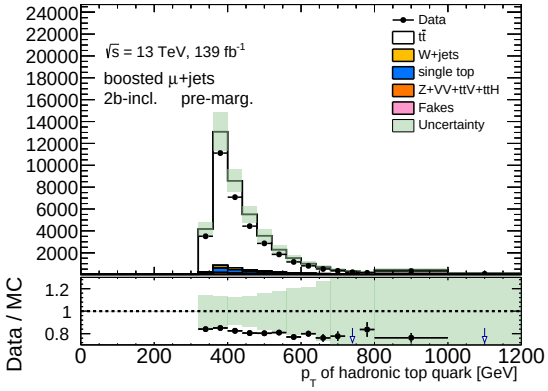

(g) Reco. t^{had} (large-R jet) p_{T}.

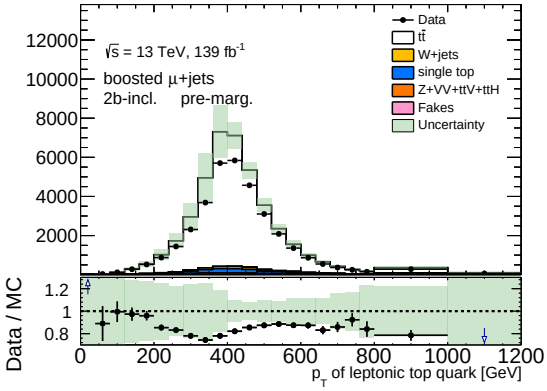

(h) Reco. t^{lep} p_{T}.

Figure A.6: Data to prediction comparison in boosted μ+jets channel, 2 incl. b-tag region. The last bin includes overflow events. The green band corresponds to the MC statistical and systematic uncertainties. Luminosity and normalisation uncertainties are not included.

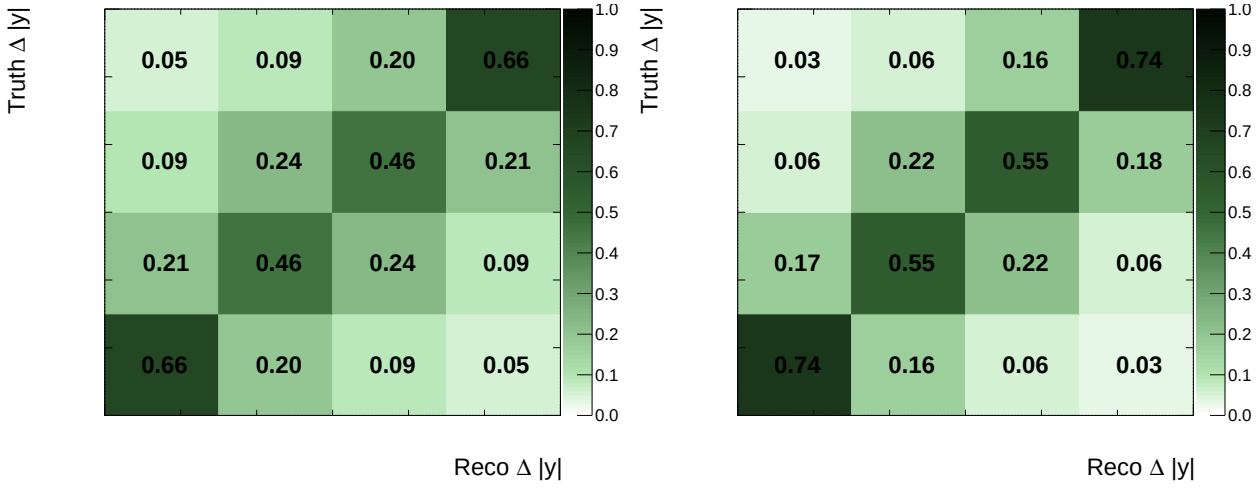

(a) Resolved 1 b-excl.

(b) Resolved 2 b-incl.

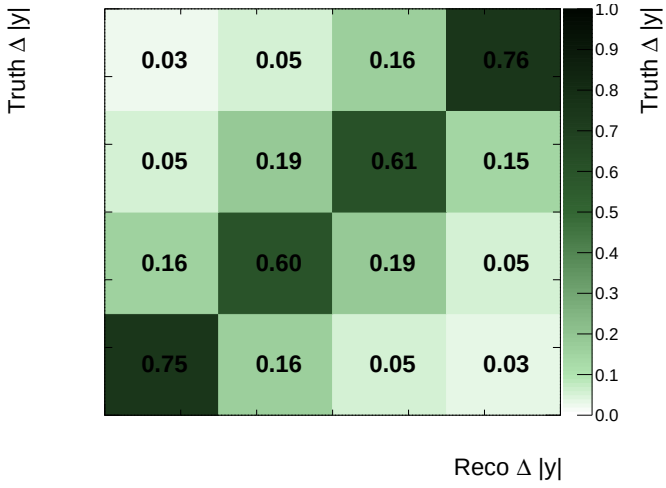

(c) Boosted 1 b-excl.

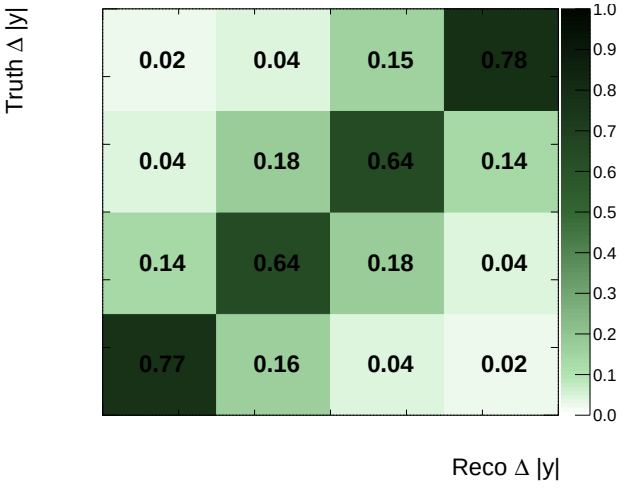

(d) Boosted 2 b-incl.

Figure A.7: Migration matrices in the four signal regions in the inclusive A_{C} measurement. Resolved (top) and boosted (bottom), 1 b-excl. (left) and 2 b-incl (right). The numbers represent the percentual propability of a truth $\Delta|y|$ bin to be reconstructed in the individual reconstruction-level bins.

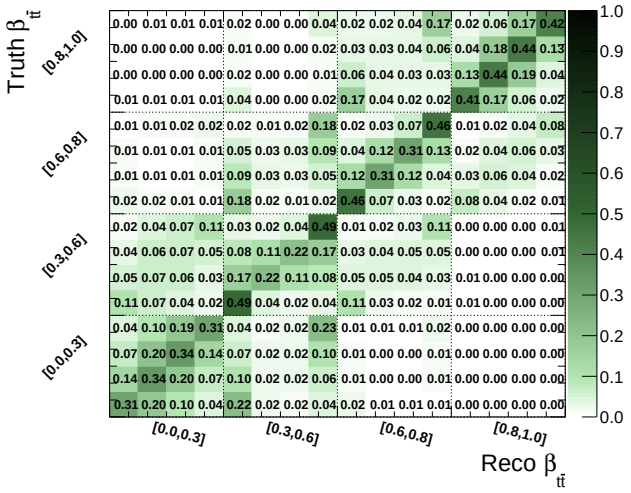

(a) Resolved 1 b-excl.

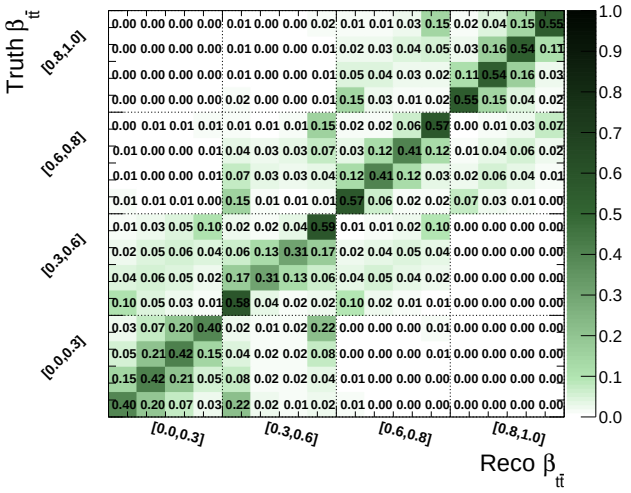

(b) Resolved 2 b-incl.

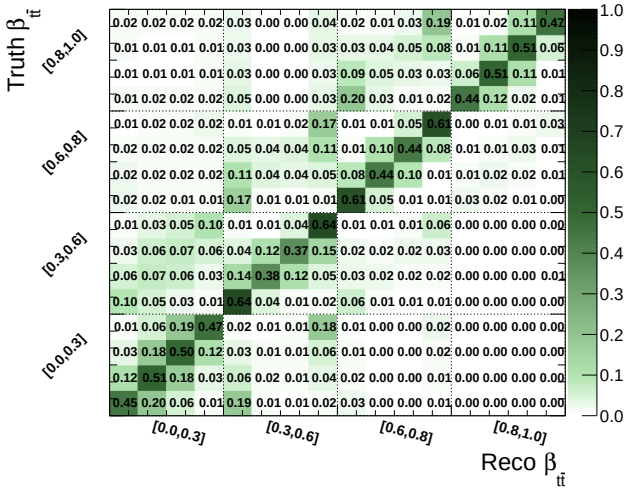

(c) Boosted 1 b-excl.

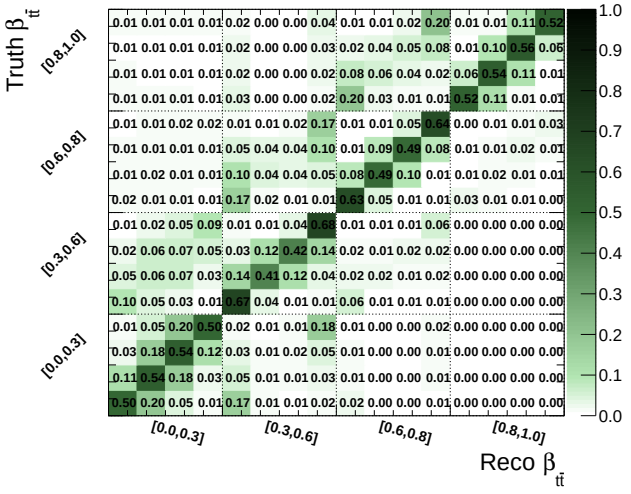

(d) Boosted 2 b-incl.

Figure A.8: Migration matrices in the four signal regions in the $\beta_z(t\bar{t})$ differential A_C measurement. Resolved (top) and boosted (bottom), 1 b-excl. (left) and 2 b-incl (right). The migrations are not only between the $\Delta|y|$ bins, but also between the bins in the differential variable. The numbers represent the percentual propability of a truth $\Delta|y|$ and $\beta_z(t\bar{t})$ bin to be reconstructed in the individual reconstruction-level bins.

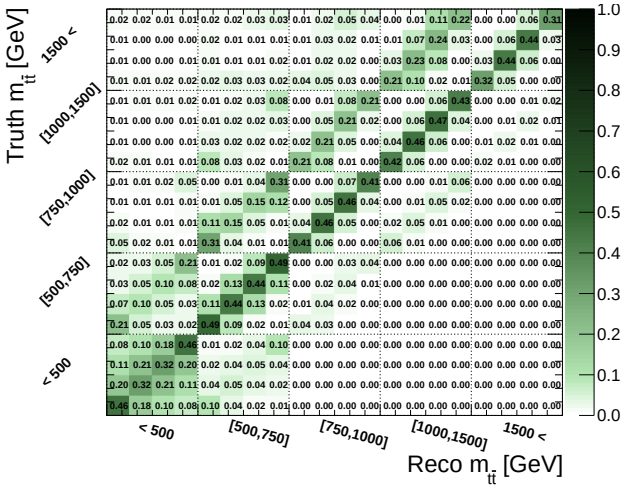

(a) Resolved 1 b-excl.

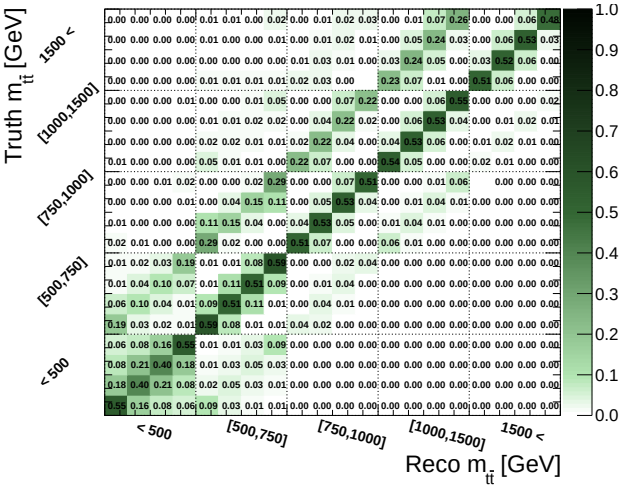

(b) Resolved 2 b-incl.

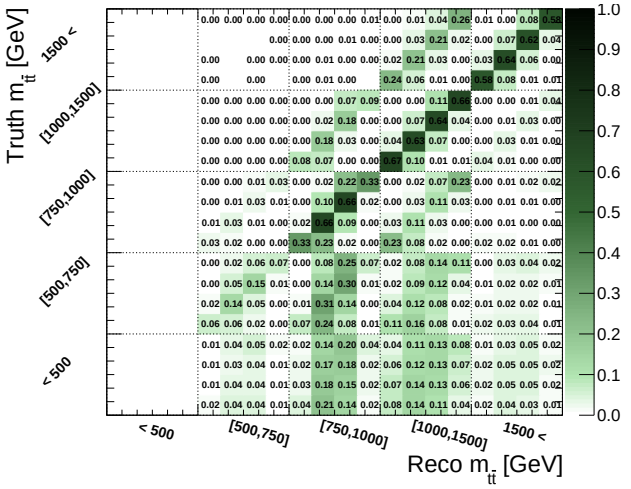

(c) Boosted 1 b-excl.

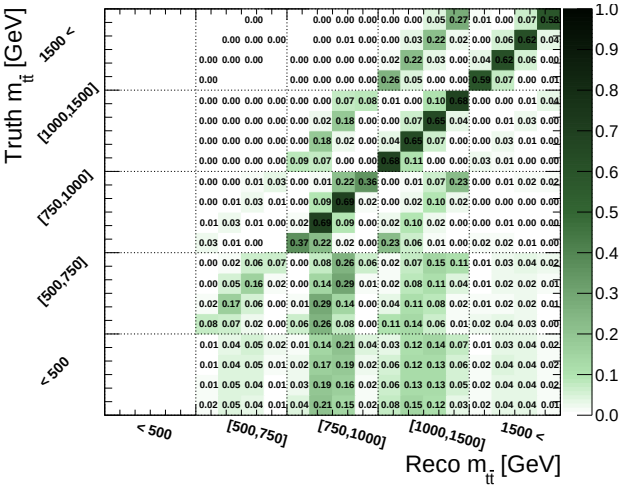

(d) Boosted 2 b-incl.

Figure A.9: Migration matrices in the four signal regions in the $m(t\bar{t})$ differential A_{C} measurement. Resolved (top) and boosted (bottom), 1 b-excl. (left) and 2 b-incl (right). The migrations are not only between the $\Delta|y|$ bins, but also between the bins in the differential variable. The numbers represent the percentual propability of a truth $\Delta|y|$ and $m(t\bar{t})$ bin to be reconstructed in the individual reconstruction-level bins. In the boosted topology there are no events below 500 GeV at the reconstruction level, since these are removed in the selection.

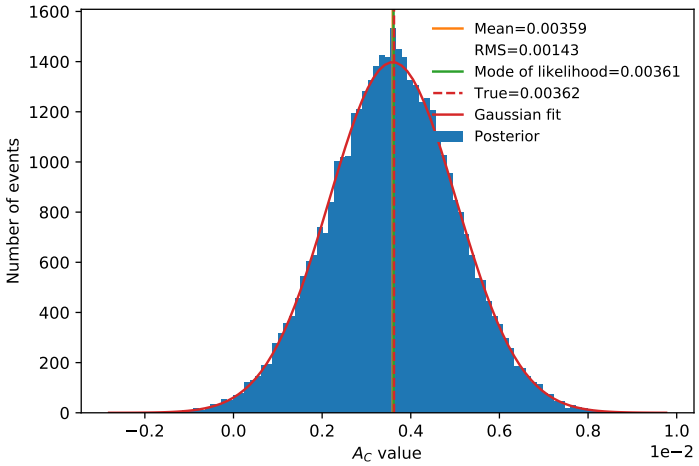

Figure A.10: The A_C posterior probability density distribution in the inclusive A_C measurement for the Asimov dataset. The POWHEG+PYHTIA 8 parton-level asymmetry, the mode of the likelihood and the posterior mean value are shown in red, green and orange, respectively.

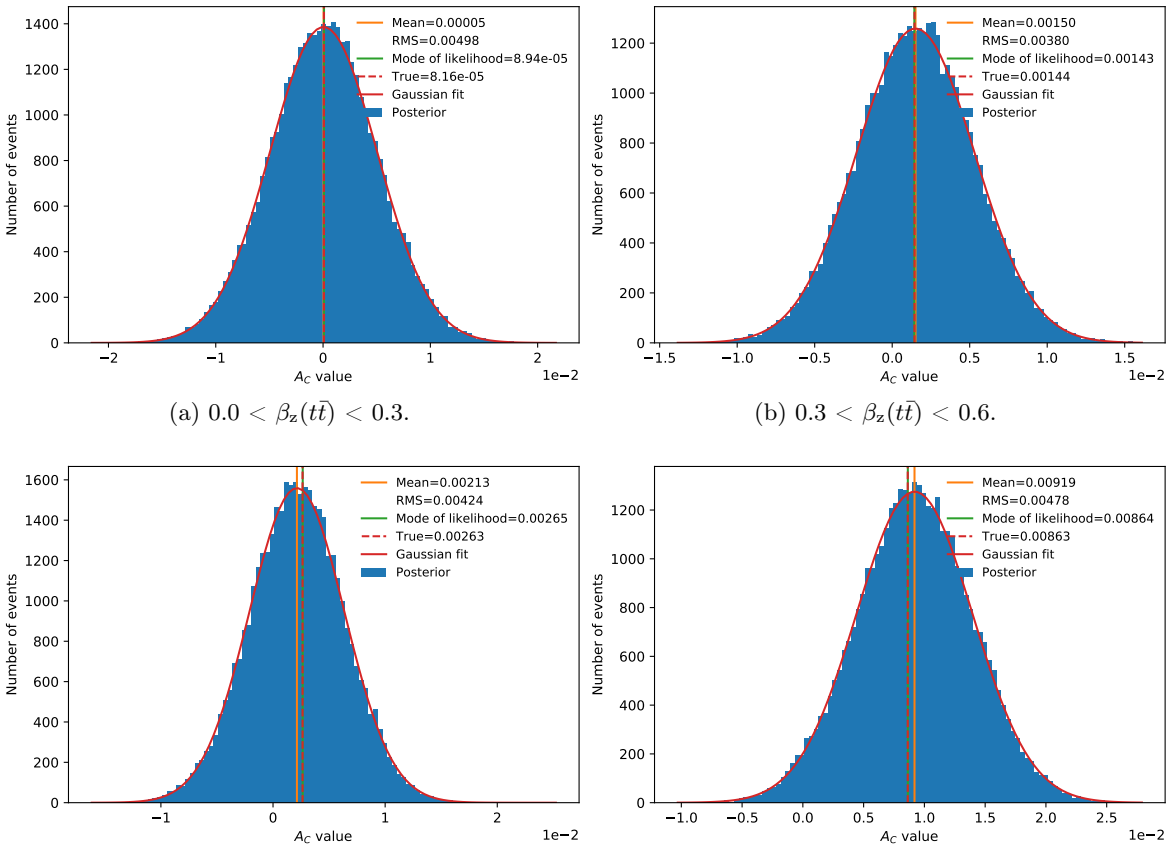

(a) $0.0 < \beta_z(t\bar{t}) < 0.3$.

(b) $0.3 < \beta_z(t\bar{t}) < 0.6$.

(c) $0.6 < \beta_z(t\bar{t}) < 0.8$.

(d) $0.8 < \beta_z(t\bar{t}) < 1.0$.

Figure A.11: The A_C posteriors in the differential $\beta_z(t\bar{t})$ A_C measurement for the Asimov dataset. The POWHEG+PYHTIA 8 parton-level asymmetry, the mode of the likelihood and the posterior mean values are presented in red, green and orange, respectively.

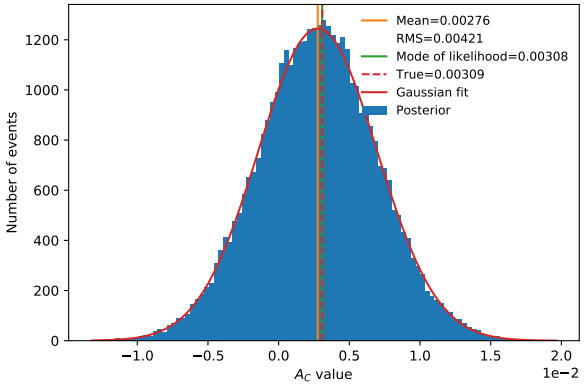

(a) $0 < m(t\bar{t}) < 500$ GeV.

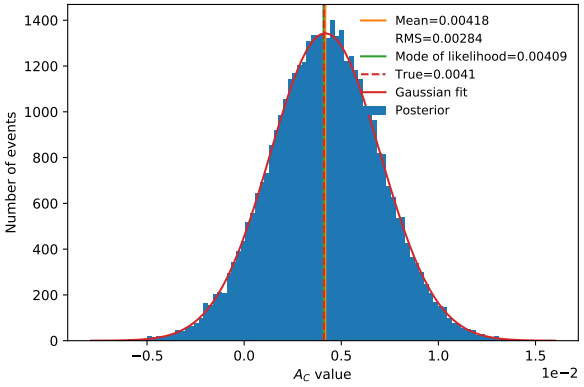

(b) $500 < m(t\bar{t}) < 750$ GeV.

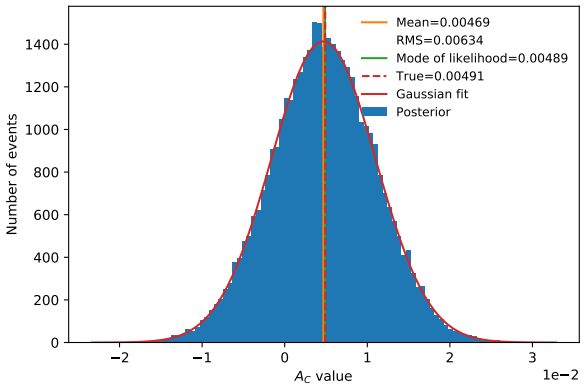

(c) $750 < m(t\bar{t}) < 1000$ GeV.

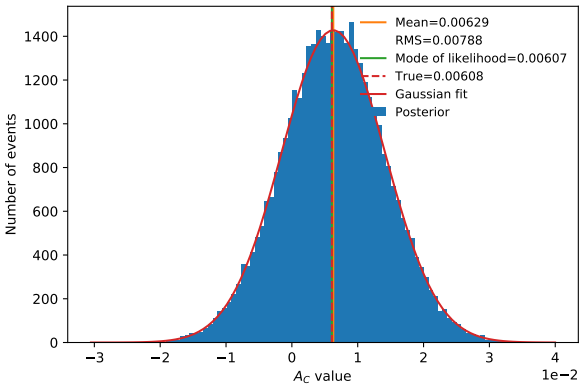

(d) $1000 < m(t\bar{t}) < 1500$ GeV.

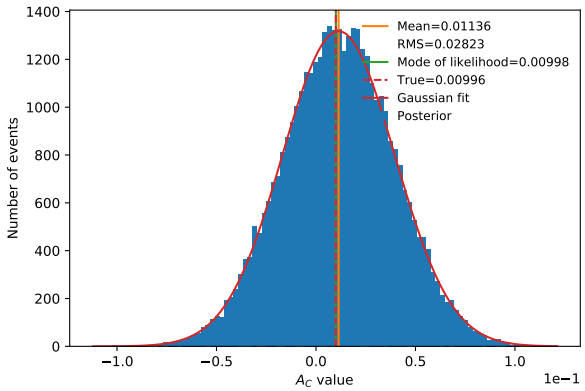

(e) $m(t\bar{t}) > 1500$ GeV.

Figure A.12: The A_C posterior in the differential $m(t\bar{t})$ A_C measurement for the ASimov dataset. The POWHEG+PYHTIA 8 parton-level asymmetry, the mode of the likelihood and the posterior mean values are presented in red, green and orange, respectively.

Figure A.13: The full 'stat.-only' ranking of the systematic uncertainties in the inclusive A_C measurement.

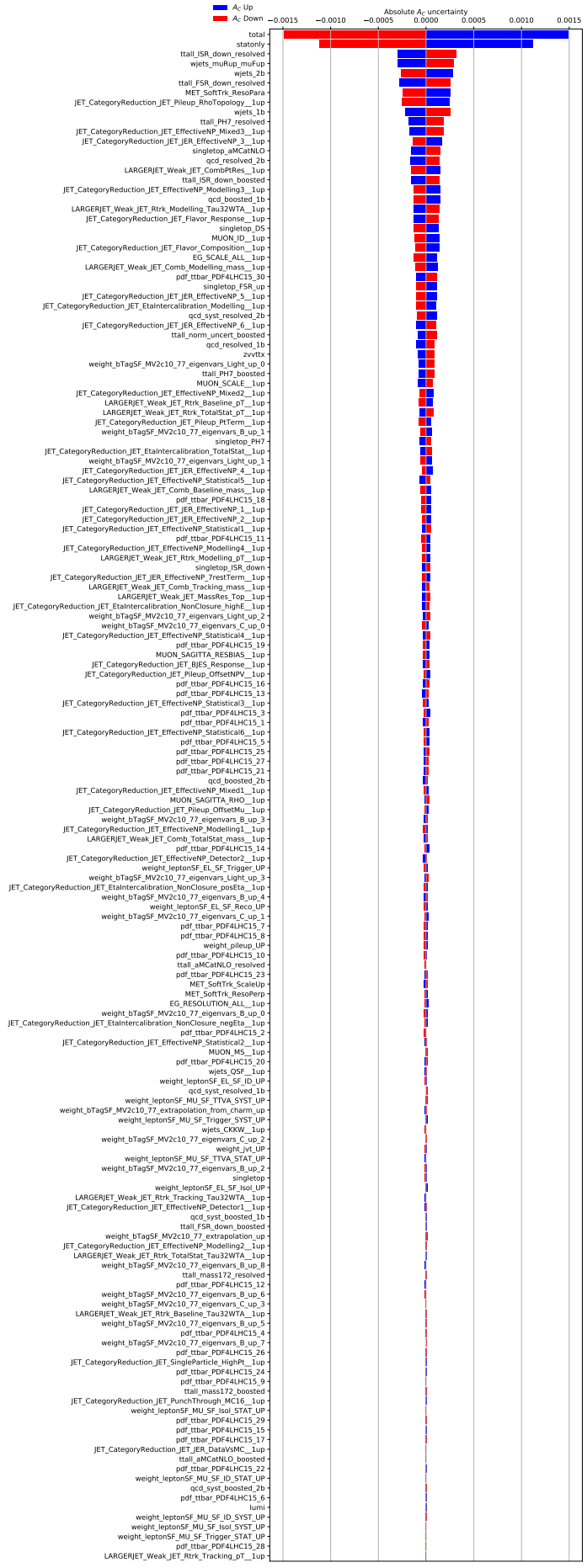

Figure A.14: The full 'full-syst.' ranking of the systematic uncertainties in the inclusive A_C measurement.

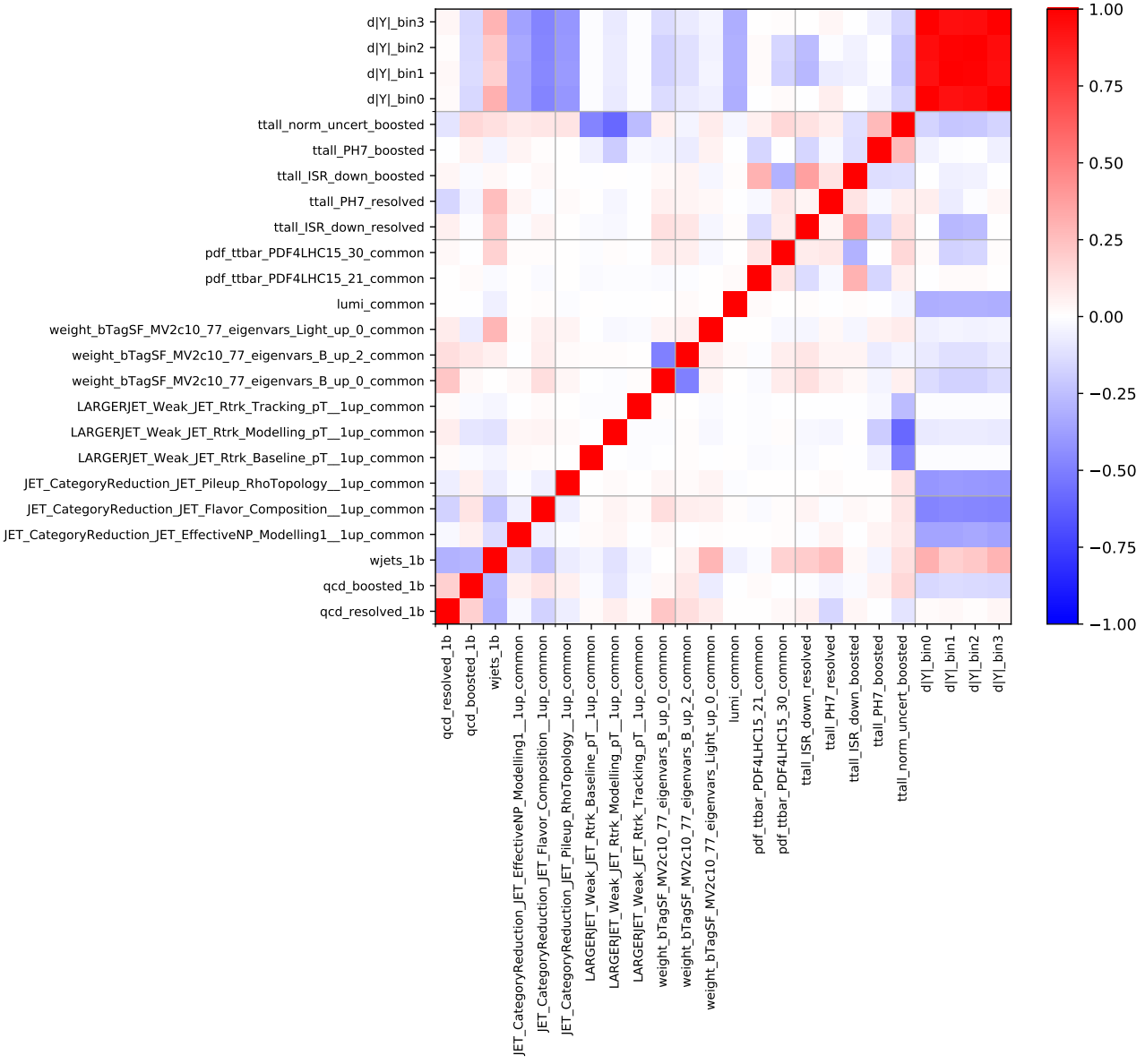

Figure A.15: Post-marginalisation correlation matrix between the nuisance parameters, parton-level $\Delta|y|$ bins and the A_C itself in the inclusive A_C measurement. Only parameters which are (anti)correlated with at least one other parameter by more than 25% are shown.

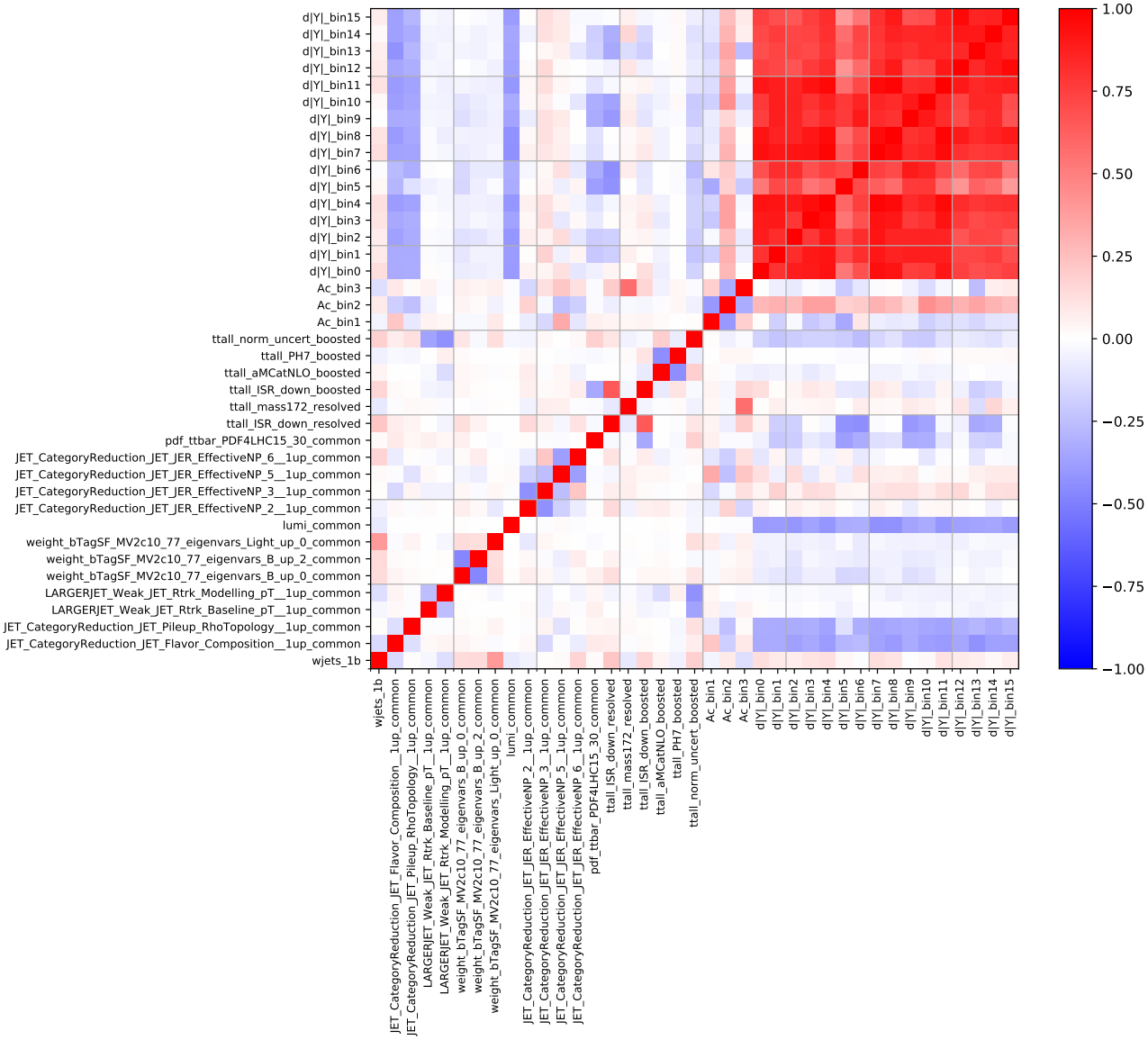

Figure A.16: Post-marginalisation correlation matrix between the nuisance parameters, parton-level $\Delta|y|$ bins and the A_{C} itself in the differential ($\beta_{\mathrm{z}}(t\bar{t})$) A_{C} measurement. Only parameters which are (anti)correlated with at least one other parameter by more than 35% are shown.

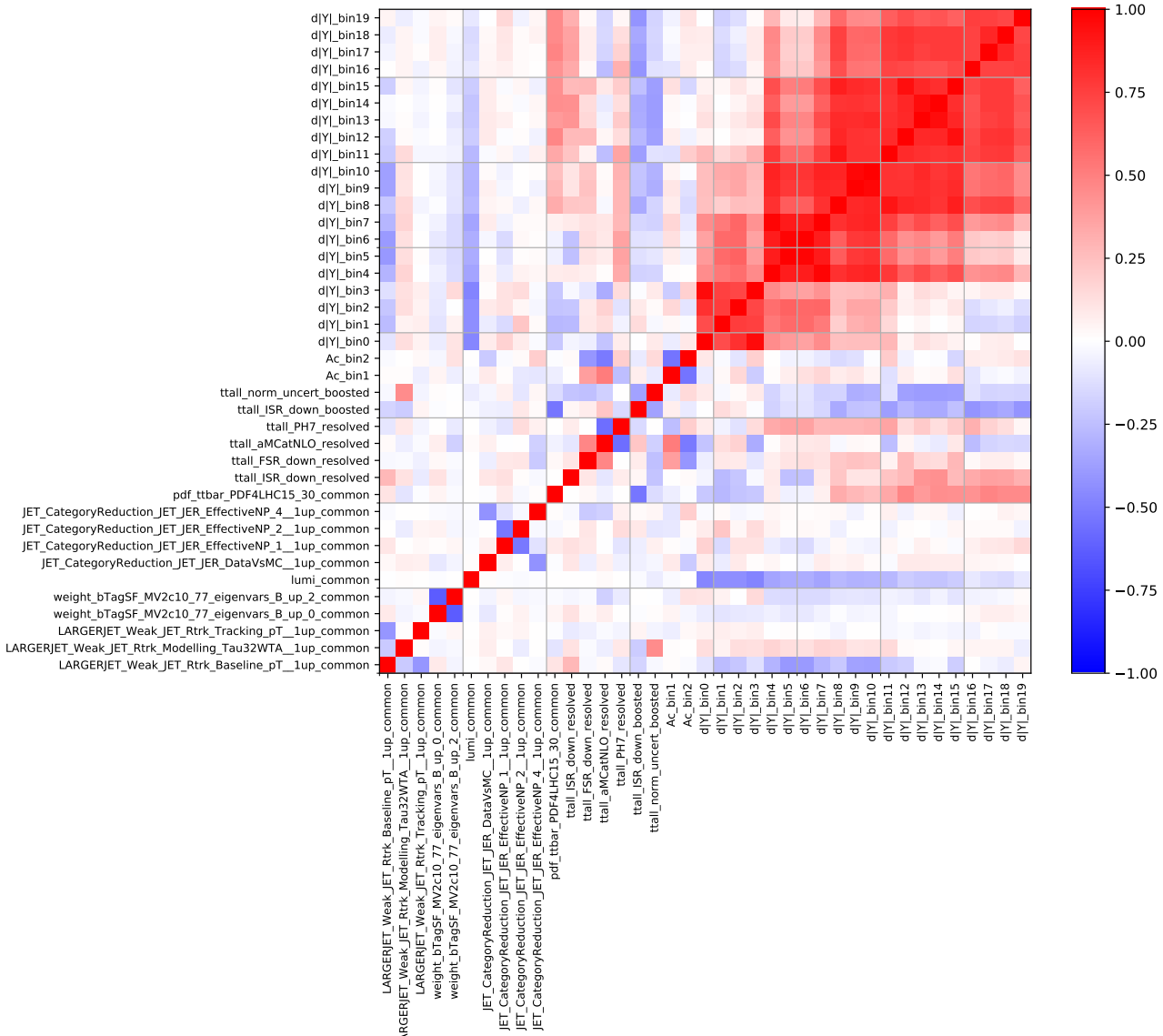

Figure A.17: Post-marginalisation correlation matrix between the nuisance parameters, parton-level $\Delta|y|$ bins and the A_{C} itself in the differential ($m(t\bar{t})$) A_{C} measurement. Only parameters which are (anti)correlated with at least one other parameter by more than 40% are shown.

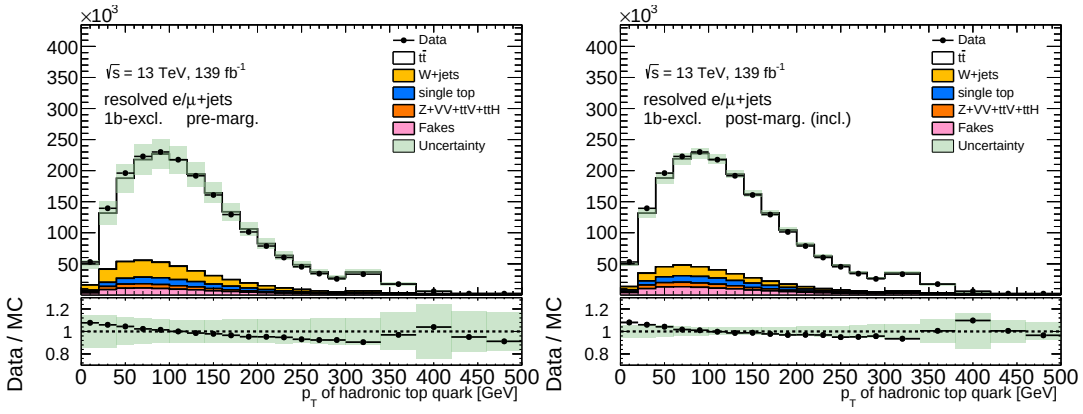

(a) Reco. t^{had} p_{T}, 1 b, pre-marg.

(b) Reco. t^{had} p_{T}, 1 b, post-marg. (incl.).

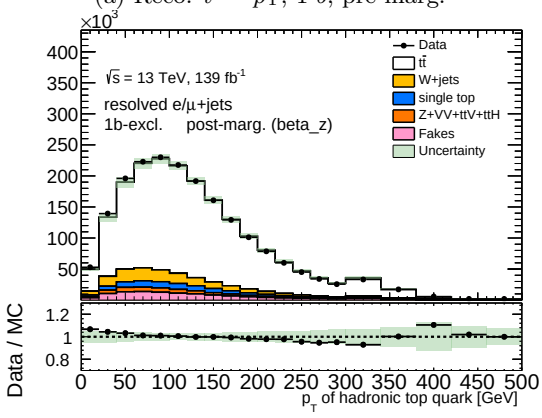

(c) Reco. t^{had} p_{T}, 1 b, post-marg. ($\beta_z(t\bar{t})$).

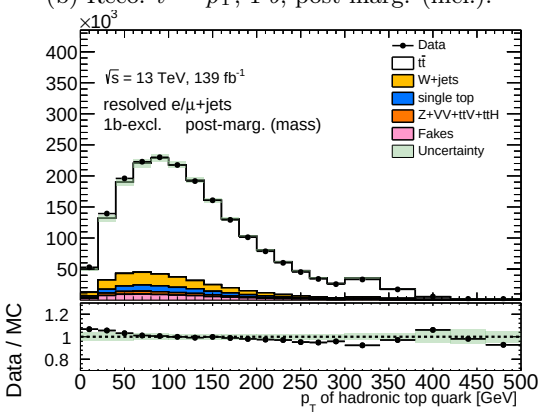

(d) Reco. t^{had} p_{T}, 1 b, post-marg. ($m(t\bar{t})$).

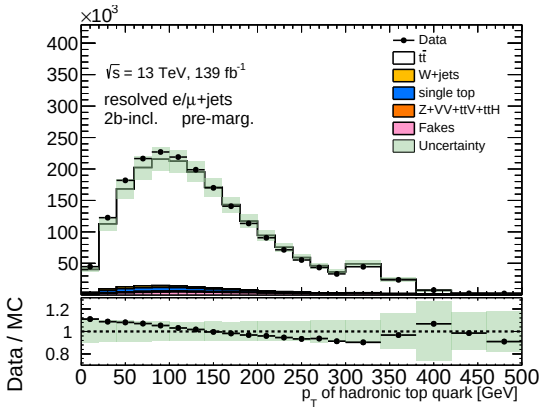

(e) Reco. t^{had} p_{T}, 2 b, pre-marg.

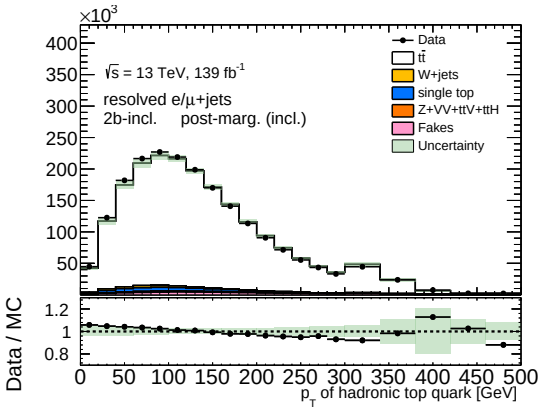

(f) Reco. t^{had} p_{T}, 2 b, post-marg. (incl.).

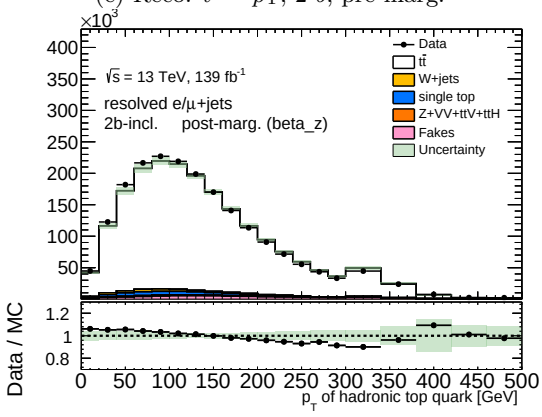

(g) Reco. t^{had} p_{T}, 2 b, post-marg. ($\beta_z(t\bar{t})$).

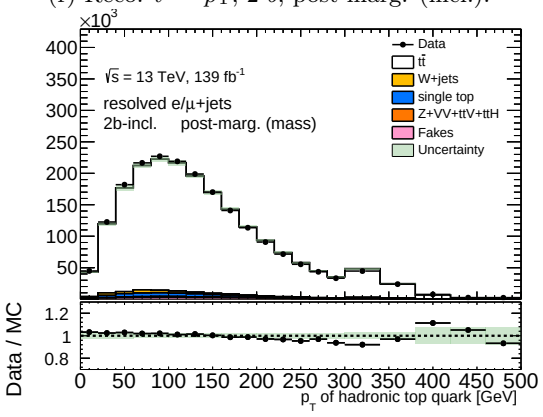

(h) Reco. t^{had} p_{T}, 2 b, post-marg. ($m(t\bar{t})$).

Figure A.18: A comparison of the reconstructed t^{had} p_{T} in the resolved topology, 1 b-excl. (top) and 2 b-incl. (bottom). Plots before and after marginalisation are shown. The light green bands correspond to the total uncertainty, including the normalisation uncertainties.

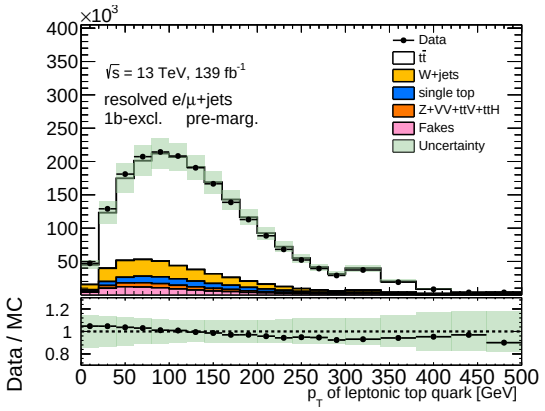

(a) Reco. t^{lep} p_{T}, 1 b, pre-marg.

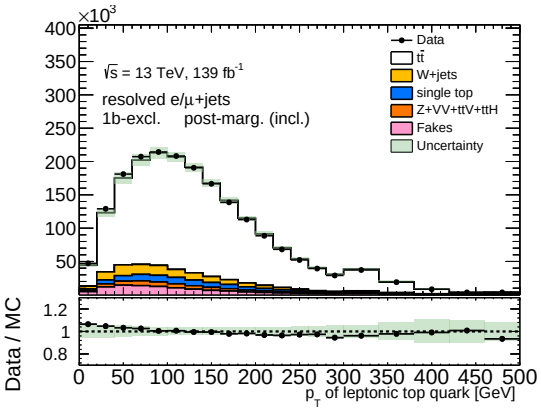

(b) Reco. t^{lep} p_{T}, 1 b, post-marg. (incl.).

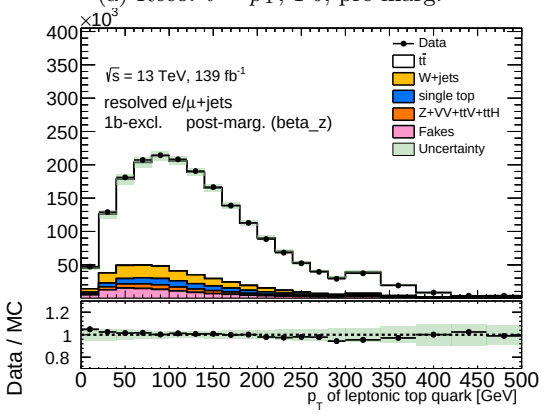

(c) Reco. t^{lep} p_{T}, 1 b, post-marg. ($\beta_{\text{z}}(t\bar{t})$).

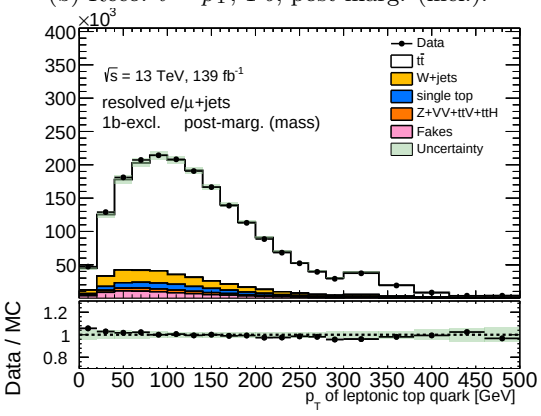

(d) Reco. t^{lep} p_{T}, 1 b, post-marg. ($m(t\bar{t})$).

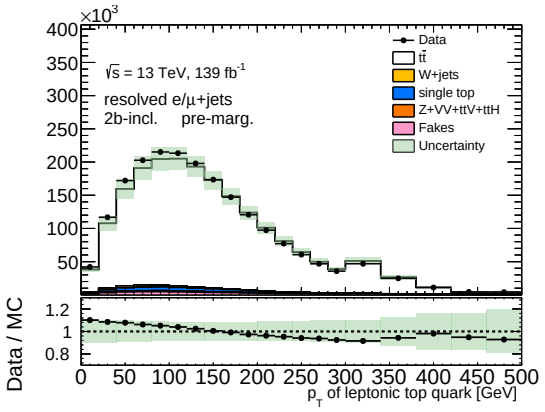

(e) Reco. t^{lep} p_{T}, 2 b, pre-marg.

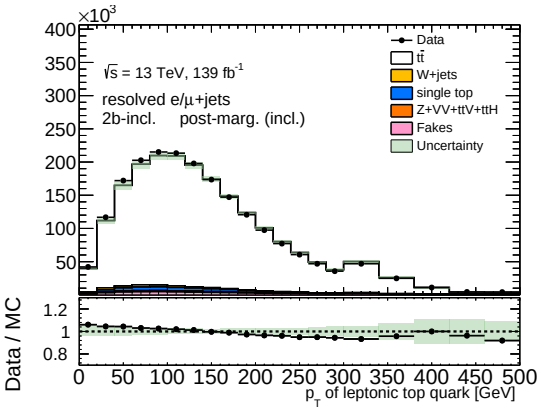

(f) Reco. t^{lep} p_{T}, 2 b, post-marg. (incl.).

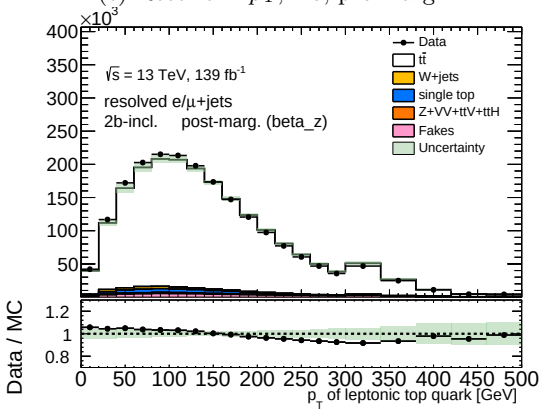

(g) Reco. t^{lep} p_{T}, 2 b, post-marg. ($\beta_{\text{z}}(t\bar{t})$).

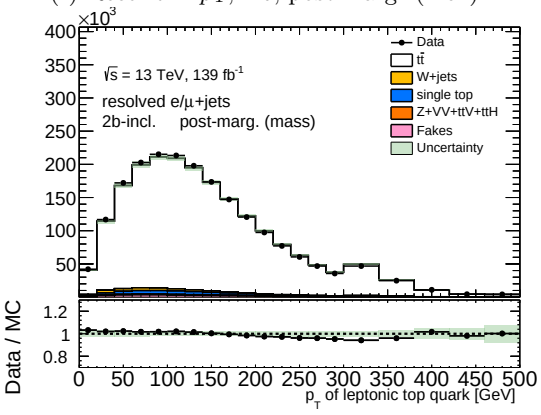

(h) Reco. t^{lep} p_{T}, 2 b, post-marg. ($m(t\bar{t})$).

Figure A.19: A comparison of the reconstructed t^{lep} p_{T} in the resolved topology, 1 b-excl. (top) and 2 b-incl. (bottom). Plots before and after marginalisation are shown. The light green bands correspond to the total uncertainty, including the normalisation uncertainties.

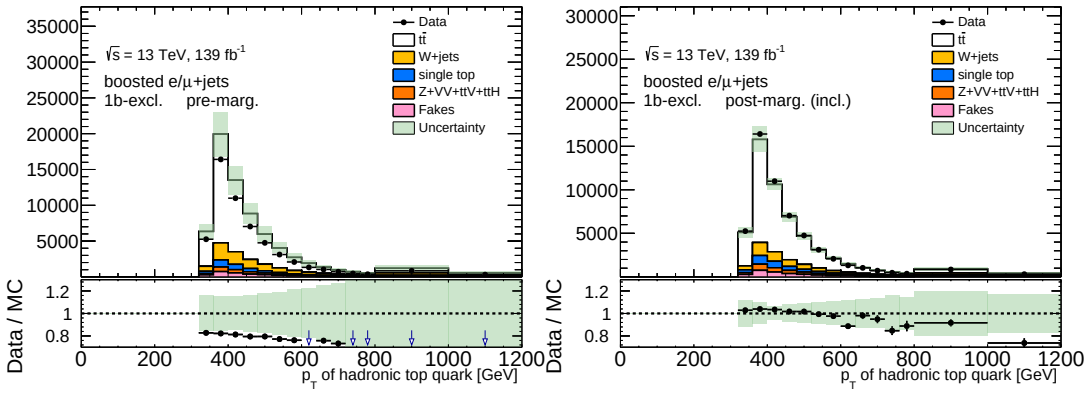

(a) Reco. t^{had} p_{T}, 1 b, pre-marg.

(b) Reco. t^{had} p_{T}, 1 b, post-marg. (incl.).

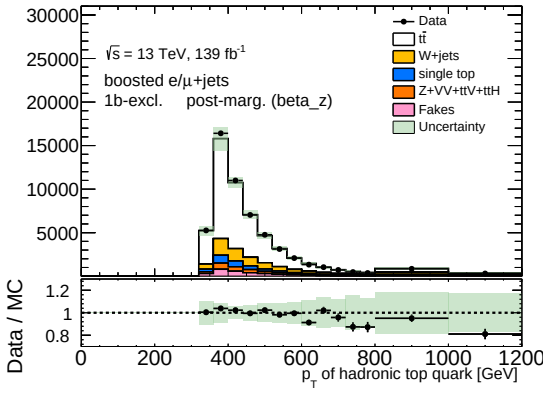

(c) Reco. t^{had} p_{T}, 1 b, post-marg. ($\beta_z(t\bar{t})$).

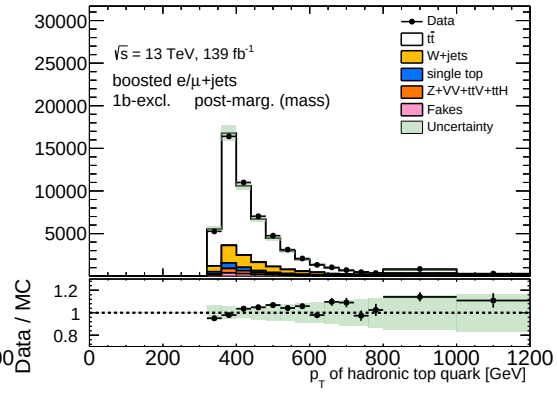

(d) Reco. t^{had} p_{T}, 1 b, post-marg. ($m(t\bar{t})$).

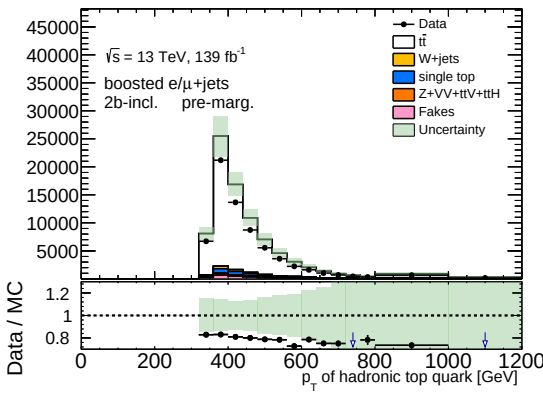

(e) Reco. t^{had} p_{T}, 2 b, pre-marg.

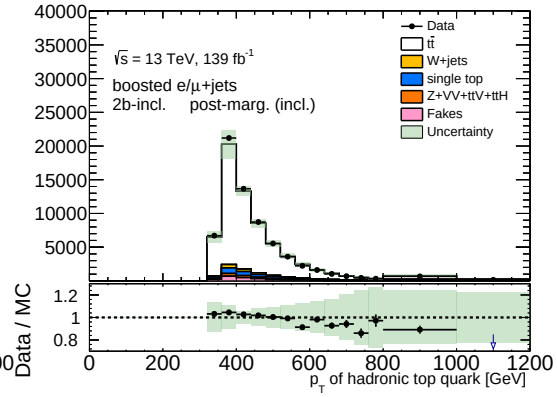

(f) Reco. t^{had} p_{T}, 2 b, post-marg. (incl.).

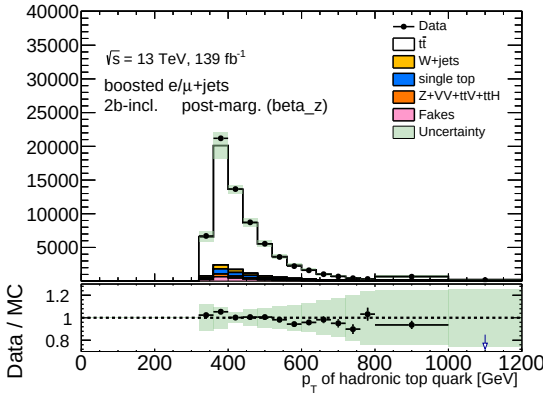

(g) Reco. t^{had} p_{T}, 2 b, post-marg. ($\beta_z(t\bar{t})$).

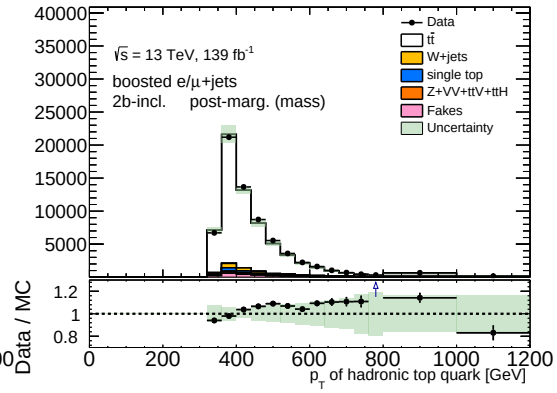

(h) Reco. t^{had} p_{T}, 2 b, post-marg. ($m(t\bar{t})$).

Figure A.20: A comparison of the reconstructed t^{had} p_{T} in the boosted topology, 1 b-excl. (top) and 2 b-incl. (bottom). Plots before and after marginalisation are shown. The light green bands correspond to the total uncertainty, including the normalisation uncertainties.

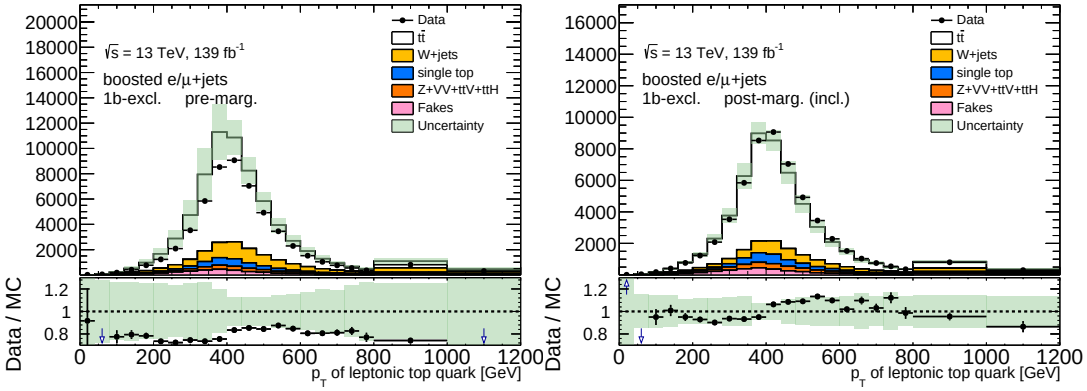

(a) Reco. t^{lep} p_{T}, 1 b, pre-marg.

(b) Reco. t^{lep} p_{T}, 1 b, post-marg. (incl.).

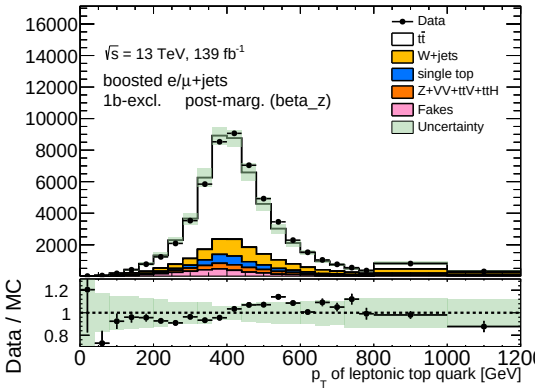

(c) Reco. t^{lep} p_{T}, 1 b, post-marg. ($\beta_{\text{z}}(t\bar{t})$).

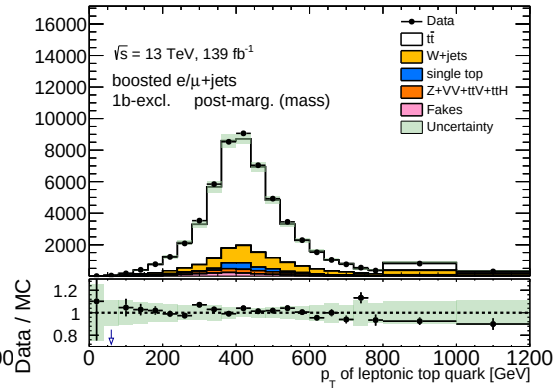

(d) Reco. t^{lep} p_{T}, 1 b, post-marg. ($m(t\bar{t})$).

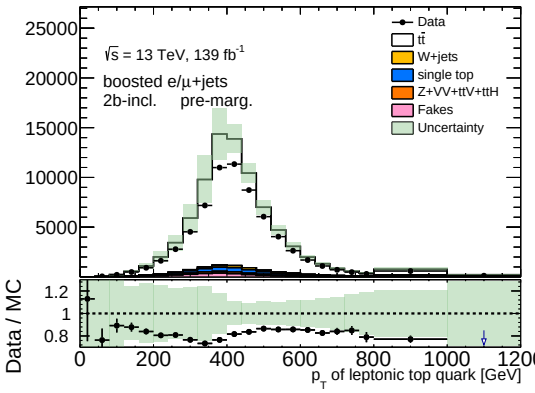

(e) Reco. t^{lep} p_{T}, 2 b, pre-marg.

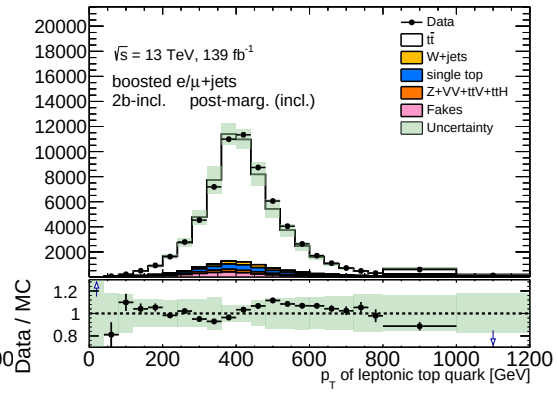

(f) Reco. t^{lep} p_{T}, 2 b, post-marg. (incl.).

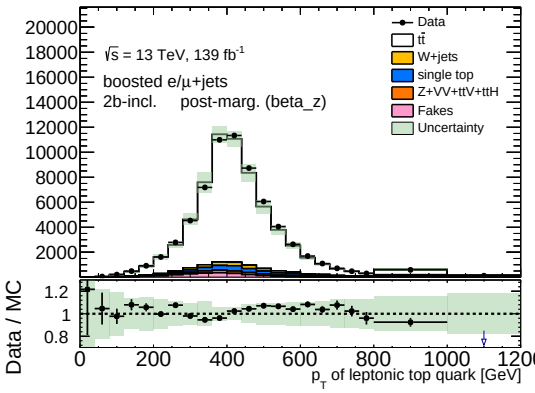

(g) Reco. t^{lep} p_{T}, 2 b, post-marg. ($\beta_{\text{z}}(t\bar{t})$).

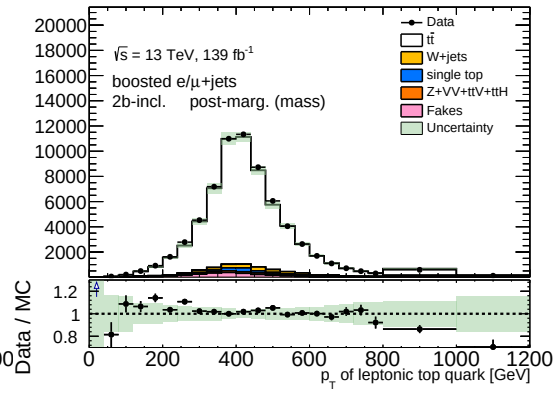

(h) Reco. t^{lep} p_{T}, 2 b, post-marg. ($m(t\bar{t})$).

Figure A.21: A comparison of the reconstructed t^{lep} p_{T} in the boosted topology, 1 b-excl. (top) and 2 b-incl. (bottom). Plots before and after marginalisation are shown. The light green bands correspond to the total uncertainty, including the normalisation uncertainties.